Experimental Search for the Decay $\pi^0 \rightarrow \nu\overline{\nu}$

Kentaro Mizouchi

January 2006

Department of Physics, Graduate School of Science
Kyoto University

Abstract

This thesis reports an experimental search for the exotic pion decay $\pi^0 \to \nu\overline{\nu}$ performed by the E949 experiment at Brookhaven National Laboratory. The decay is prohibited by angular momentum conservation if neutrinos are purely mass-less particles. However, recent evidence for neutrino mass implies the decay would occur at a certain rate. This research is a direct access to the neutrino mass and its helicity.

The E949 experiment took data for 12 weeks in 2002, and collected 1.8×10^{12} charged-kaon decays at rest. The search was performed with an optimized hermetic photon detection system using kinematically identified $K^+ \to \pi^+\pi^0$ ($K_{\pi 2}$) events in the data sample triggered for $K^+ \to \pi^+\nu\overline{\nu}$ decay. A sample of 3.0×10^9 π^0s were tagged by selecting the monochromatic π^+ from $K_{\pi 2}$ with an impurity of 10^{-9}. As a result of the analysis, a total of 99 events were observed in the signal region although they all seemed to be $\pi^0 \to \gamma\gamma$ backgrounds coming through the photon detection inefficiency. With a conservative stance, we set an upper limit of 2.7×10^{-7} at 90 % confidence level; the corresponding $\pi^0 \to \gamma\gamma$ rejection was estimated to be 3.5×10^6 with an acceptance correction. This result was a factor of three improvement from the prior experimental limit. The limit is also applicable to π^0 decay to any unknown weakly interacting particles.

This thesis also presents an improved analysis technique of photon detection. For more accurate understanding of the remaining backgrounds, single photon inefficiency of the detector was measured with a special data sample for calibration. The measurement was limited by statistics but, for looser photon-detection criteria, we succeeded in measuring the inefficiency as a function of incident photon energy and direction; we found that $\pi^0 \to \gamma\gamma$ inefficiency convoluted from the measured inefficiency well described the actual observed backgrounds when the loose criteria were imposed. Though this technique was unable to be applied to the case with tight photon-detection criteria as used in the $\pi^0 \to \nu\overline{\nu}$ search, the inefficiency study provided a reliable information on how much photon detection would be achieved with calorimeters.

As a conclusion, a factor of three improvement on the upper limit of the decay $\pi^0 \to \nu\overline{\nu}$ search was achieved. Aiming at further improvement, a new technique of measuring the detector photon inefficiency was developed for understanding the observed events in the signal region. This thesis showed validity of the new technique for an application of background subtraction.

Contents

1 Introduction 12

1.1 Theoretical overview . . . 12

1.2 Determination of neutrino type : Dirac or Majorana ? . . . 13

1.3 History of experimental search for the decay $\pi^0 \rightarrow \nu\overline{\nu}$ . . . 13

1.4 $\pi^0 \rightarrow \nu\overline{\nu}$ in astrophysics . . . 14

1.5 Physics beyond the Standard Model . . . 15

1.6 Analogous decay to $\pi^0 \rightarrow \nu\overline{\nu}$ . . . 15

2 Event Detection Strategy 16

2.1 Event detection strategy . . . 16

2.2 What kinds of measurements are required for it ? . . . 16

3 Experimental Instruments 18

3.1 High intensity K^+ beam . . . 18

3.2 The E949 detector system . . . 19

3.2.1 Beam counters and chambers . . . 22

3.2.2 Kaon stopping target . . . 28

3.2.3 Fiducial counters : I and V-Counters . . . 29

3.2.4 Drift Chamber for momentum measurement . . . 30

3.2.5 Energy and range measuring system : Range Stack . . . 30

3.2.6 Range Stack Straw Chambers . . . 34

3.2.7 Barrel photon detection system : Barrel Veto . . . 34

3.2.8 Supplemental barrel calorimeter: Barrel Veto Liner . . . 35

3.2.9 End Cap Calorimeters . . . 37

3.2.10 Other ancillary photon detectors . . . 38

3.3 Trigger and data acquisition system . . . 41

3.3.1 The level 0 and level 1 trigger systems . . . 41

3.3.2 Minimum bias trigger . . . 41

3.3.3 The $\pi^0 \rightarrow \nu\overline{\nu}$ trigger . . . 42

3.3.4 Monitor triggers . . . 43

3.4 A summary of data acquisition and running conditions . . . 48

4 Data Analyses 50

4.1 Overview of data analyses 50
4.2 Event reconstruction 50
  4.2.1 Kaon reconstruction 50
  4.2.2 Charged track reconstruction 50
  4.2.3 Identification of pion decay at rest 53
4.3 Analysis strategy 56
4.4 High purity $K_{\pi 2}$ event selection 57
  4.4.1 Background source diagnosis 57
  4.4.2 Bifurcation technique 61
  4.4.3 Comments on the development of the $K_{\pi 2}$ selection criteria 63
  4.4.4 Muon background suppression 64
  4.4.5 Single beam background suppression 68
  4.4.6 Two-beam background suppression 72
  4.4.7 Evaluation of the Kπ2 tag impurity 75
  4.4.8 The correction factor C_{dis} 76
4.5 Search for π^0 decay to nothing with kinematically tagged π^0s 77
  4.5.1 Rejection measurement of the online $\pi^0 \to \gamma\gamma$ veto 77
  4.5.2 Acceptance measurement of the online $\pi^0 \to \gamma\gamma$ veto 79
  4.5.3 Summary of the performance of the online $\pi^0 \to \gamma\gamma$ veto 80
  4.5.4 Preliminary studies for designing offline $\pi^0 \to \gamma\gamma$ cuts 81
  4.5.5 The design of the offline $\pi^0 \to \gamma\gamma$ cuts 84
  4.5.6 Optimization of the offline $\pi^0 \to \gamma\gamma$ cuts 86
  4.5.7 Determination of the offline $\pi^0 \to \gamma\gamma$ cuts 87

5 Results **87**
5.1 Opening the signal region 87
5.2 $\pi^0 \to \gamma\gamma$ backgrounds 89
5.3 Branching ratio for the decay $\pi^0 \to \nu\overline{\nu}$ 90
5.4 Discussions 92

6 Measurement of Single Photon Inefficiency with the E949 detector **94**
6.1 Motivation and goal of the study 94
6.2 A basic idea of the study and an analysis strategy 95
6.3 The data sample and the trigger conditions 96
6.4 $K_{\pi 2}$ selection criteria and the event purification 96

6.5 Photon reconstruction 96
6.5.1 Obtaining visible fractions in Barrel Veto and Barrel Veto Liner 96
6.5.2 Obtaining a z position of each photon hit 97
6.5.3 Clustering of incident photons 98
6.5.4 The reconstruction performance 99
6.6 Tagging-photon selection criteria 99
6.7 Full reconstruction of $K_{\pi 2}$ events and missing photon kinematics 100
6.7.1 Kinematical fit with the Lagrange multiplier method 101
6.7.2 Full reconstruction with Monte Carlo sample and the performance . . . 101
6.7.3 Kinematical fitting with real data 102
6.8 The measurement of the SPI denominator map 106
6.9 The measurement of the SPI numerator map 106
6.10 The measurement of the normalization factor 110
6.11 Corrections for the measurements 110
6.12 Results on the single photon inefficiency 111

7 $\pi^0 \to \gamma\gamma$ Detection Inefficiency 115
7.1 The daughter table method 115
7.2 Phase space generation with Monte Carlo simulation 115
7.3 Results 116
7.3.1 The convoluted $\pi^0 \to \gamma\gamma$ detection inefficiency 116
7.3.2 The convoluted $\pi^0 \to \gamma\gamma$ rejection as a function of π^+ dip angle 117
7.4 Background subtraction 117
7.4.1 Subtraction of the estimated $\pi^0 \to \gamma\gamma$ backgounds 117
7.4.2 Subtraction with π^+ dip angle dependence 119
7.5 Summary 121

8 Conclusion 124

A Lists of Selection Criteria 130
A.1 Run selection 130
A.2 Pass 1 selection criteria 130
A.3 Pass 2 selection criteria 131
A.4 The box cuts for selection of π^+ from $K_{\pi 2}$ 132
A.5 The box cuts for selection of μ^+ from $K_{\mu 2}$ 132

A.6 Kinematical selection criteria 132
A.7 π^+ decay sequence selection criteria 135
A.8 Beam background rejection criteria 135
A.8.1 Beam likelihood distribution 138
A.9 $K_{\pi 2}$ selection criteria 139
A.10 $K_{\mu 2}$ selection criteria 140
A.11 Loosened $K_{\pi 2}$ selection criteria for single photon inefficiency study 140

B Details on none-$K_{\pi 2}$ background suppression 143
B.1 Single beam background suppression 143
B.2 Two-beam background suppression 145
B.3 Muon background suppression 147

C Photon reconstruction and kinematical fitting 150
C.1 The fiducial cuts for tagging photons 150
C.2 Lagrange multiplier technique 151
C.3 Performance of the kinematical fitting 153
C.4 Performance checks of the denominator maps measurement 156

D Acronyms and Abbreviations 159

List of Figures

1 Schematic top view of the beam line named LESBIII 18
2 Side view of the E949 detector (full view) 21
3 Schematic side view of the upper half of the E949 detector 22
4 Schematic end view of the upper half of the E949 detector 22
5 Schematic side view of the Čerenkov counter 23
6 Number of hits in Čerenkov counter 24
7 Schematic end view of the B4 hodoscope 26
8 Cross sectional view of a single layer of the B4 hodoscope 26
9 Schematic end view of the scintillating fiber target, I-Counters and V-Counters . 28
10 Schematic side view of the scintillating fiber target, I-Counters and V-Counters 28
11 Schematic view of the Ultra Thin Chamber (UTC) 31
12 Schematic end view of the Range Stack, Barrel Veto Liner and Barrel Veto . . . 32

13 $\pi^+ \to \mu^+ \to e^+$ decay sequence recorded by the waveform digitizers in the Range Stack . . . 33

14 Schematic end view of the inner RSSC . . . 34

15 Schematic side view of the inner RSSC . . . 34

16 Visible energy fraction as a function of azimuthal angle . . . 35

17 Schematic side view of the Barrel Veto Liner around 45-degree region . . . 36

18 Radiation length with and without the Barrel Veto Liner . . . 36

19 Schematic end view and back view of the End Cap CsI calorimeters . . . 37

20 Schematic view of the CsI crystal . . . 38

21 Gain variation of fine-mesh PMTs as a function of magnetic field . . . 39

22 Typical CsI pulse-shape recorded with a CCD transient digitizer . . . 39

23 Typical timing resolution in the End Cap CsI calorimeter . . . 39

24 Radiation lengths as a function of dip angle (forward region) . . . 40

25 Range versus momentum distribution of the events collected by the $K_{\pi 2}(1)$ trigger 45

26 Momentum distributions of the pion-band events with $\pi\nu\overline{\nu}$ trigger conditions imposed sequentially . . . 46

27 Momentum distributions of the muon-band events with $\pi\nu\overline{\nu}$ trigger components imposed sequentially . . . 46

28 Inefficiency of the online BV condition as a function of visible energy . . . 47

29 Inefficiency of the online BVL condition as a function of visible energy . . . 47

30 Inefficiency of the online EC condition as a function of visible energy . . . 47

31 Number of accumulated stopped Kaons as a function of the DAQ running days 49

32 Example of a reconstructed event . . . 51

33 Distribution of the reconstructed total momentum . . . 51

34 Distribution of the reconstructed total energy . . . 52

35 Distribution of reconstructed total range . . . 52

36 An example of $\pi^+ \to \mu^+$ decay sequence fit . . . 54

37 Distribution of the ratio of χ^2's for the single and double pulse fittings . . . 55

38 Distribution of $\pi^+ \to \mu^+$ decay time by double pulse fitting. . . . 55

39 Distribution of extracted muon kinetic energy . . . 55

40 Illustration of a charge exchange background . . . 58

41 Illustration of a single pion beam background event . . . 58

42 Illustration of a single pion beam background involving kaon decay-in-flight in the beam line . . . 59

43 Illustration of a two-beam background . . . 59

44 Illustration of how the bifurcation technique works 62

45 Illustration of the outside-the-box study 63

46 π-μ separation performance by neural network 64

47 Signed maximum dE/dx deviation in the Range Stack 65

48 Likelihood distribution constructed from the dE/dx difference in the Range Stack 66

49 Confidence level distribution computed from dE/dx deviation in the Range Stack 67

50 Energy deposit in B4 hodoscope 69

51 Difference between the kaon fiber time and pion fiber time 70

52 Examples of events with an overlapping electron and photon 76

53 Photon detection performance in the BV 82

54 Observed photon hits in the BVL 83

55 Illustration of the possible mechanism of the earlier peak in the BVL 83

56 Timing distributions of single-end hits in the BV and BVL 84

57 Photon hit distribution in the End Cap calorimeter 85

58 Illustration of the optimization process to determine the photon veto parameters 86

59 Obtained profile curve in the optimization process 88

60 Kaon decay-time distribution with various levels of the photon veto 88

61 π^+ momentum distribution with various levels of the photon veto cut 90

62 Effective $\pi^0 \to \gamma\gamma$ rejection measured with the 1/3 and 2/3 sample 91

63 Energy vs timing plot of the hits observed in the BV in the survived events . . . 93

64 Distribution of the azimuthal opening angle between π^+ (ϕ_{π^+}) and photon hit (ϕ_{π^+}), which were observed in the BV in the survived events 93

65 Illustration of the idea on the measurement of single photon inefficiency 95

66 Peak position and width of the reconstructed π^0 energy as a function of the BV, BVL visible fractions. 97

67 Illustration of the photon clustering method 98

68 Reconstructed resolutions with the clustering method (MC) 99

69 Schematic view of the overlapping photon cut 100

70 Resolution (σ^{real}_{meas}) measurements with stretch functions 104

71 χ^2 probabilities from the kinematical fitting 105

72 Measured SPI denominator map 106

73 Numerator map measured with the offline photon veto used in the $\pi^0 \to \nu\overline{\nu}$ search 108

74 Numerator map measured with the relaxed photon veto 109

75 Illustration of the over-veto mechanism caused by the splitting from the tagging photon 112

76 Over-vetoing effect caused by split tagging photons 112
77 Measured single photon inefficiency 113
78 Single photon inefficiency as a function of dip angle 114
79 Single photon inefficiency as a function of energy 114
80 π^+ dip angle distribution 116
81 Convoluted $\pi^0 \to \gamma\gamma$ inefficiency 117
82 Convoluted $\pi^0 \to \gamma\gamma$ rejection with various levels of photon veto 118
83 $\pi^0 \to \gamma\gamma$ rejection as a function of π^+ dip angle 118
84 Upper limits before and after the background subtraction. 119
85 $\cos(\theta_{\pi^+})$ distribution of the observed candidates and dip angle shape function . 120
86 Likelihood distribution constructed from $\cos(\theta_{\pi^+}$ dependence 120
87 γ distribution of miss-detected $\pi^0 \to \gamma\gamma$ decays 123
88 Beam likelihood distribution 138
89 Analysis flow chart for the rejection branch in the single beam background study 143
90 Analysis flow chart for the normalization branch in the single beam background study 144
91 Analysis flow chart for the rejection branch in the two-beam background study 145
92 Analysis flow chart for the normalization branch in the two-beam background study 146
93 Analysis flow chart for the rejection branch in the muon background study . . . 147
94 Analysis flow chart for the normalization branch in the muon background study 148
95 The measured peak width in the various photon detectors. 149
96 Miscellaneous plots on the fiducial cuts for tagging photons 150
97 Resultant resolution of the tagging photons after the kinematical fitting (MC) . 153
98 Resultant resolutions of the extracted missing-photon kinematics 154
99 χ^2 probability obtained in the kinematical fitting (MC) 154
100 Obtained SPI denominator map (real data) 155
101 Measured denominator map with Monte Carlo data 156
102 Ratio of the Monte Carlo denominator map to the truth. 156
103 Stretch functions (real data) 157
104 The number of expected $\pi^0 \to \gamma\gamma$ backgrounds and candidates in the signal region 158

List of Tables

1 Summary of experimentally measured neutrino masses 13

2 Summary of the upper limits on the $\pi^0 \to \nu\overline{\nu}$ decay 14

3 Basic parameters of the LESBIII line 19

4 Various parameters on the Čerenkov counter 23

5 Properties of the Beam Wire Chamber 1 24

6 Properties of the Beam Wire Chamber 2 25

7 Properties of the beam degraders 25

8 Schematic end view of the ring veto 26

9 Schematic end view of the upstream photon veto 27

10 Properties of the Upstream Photon Veto Counter 27

11 Summary of running conditions and data acquisition 48

12 Summary of the resolutions in the kinematics reconstruction 53

13 Background sources in the $K_{\pi2}$ event selection 60

14 Summary of the bifurcation analysis in the muon background measurement . . 67

15 Rejection measurement of the delayed coincidence cut 71

16 Summary of the entries with the inverted DELC cut 71

17 Summary of the cut-2 rejection in the two-beam background measurement . . . 73

18 Summary of the cut-2 inversion in the two-beam background measurement . . 73

19 Number of none-$K_{\pi2}$ backgrounds in the signal region 75

20 Summary of the correction factor C_{dis} estimation 77

21 Rejection measurement of the HEX and the HEX-afterburner conditions in the online photon veto 78

22 Rejection measurement of the $\overline{BV}$, $\overline{BVL}$ and $\overline{EC}$ conditions in the online photon veto 78

23 Rejection of online photon veto with the Method-2 79

24 Acceptance measurement of online photon veto 80

25 Timing resolutions in various photon detection systems 81

26 Parameters for offline photon veto 89

27 Measured visible fractions of the BV and BVL 97

28 Resolutions of the reconstructed variables by the photon clustering method . . . 99

29 Input variables for kinematical fitting (Monte Carlo data) 101

30 Performance of the kinematical fitting (Monte Carlo data) 102

31 Resolutions of the measured variables (Real data) 103

32 The number of 1-gamma events produced from $K_{\pi 2}(1)$ sample 110
33 The number of 1-gamma events with sequentially imposed selection criteria . . 110
34 Rejection of the L1.1-afterburner cut 111
35 $K_{\pi 2}$ event selection criteria 139
36 $K_{\mu 2}$ selection criteria 140
37 Run conditions for the data used in the single photon inefficiency study 142

1 Introduction

1.1 Theoretical overview

The decay $\pi^0 \to \nu\overline{\nu}$ is prohibited by angular momentum conservation if neutrinos are purely left-handed particles. In the Standard Model with big success in the description of the world for elemental particles, neutrinos had been thought as massless particles, which connected to the fact that the helicity was always negative (-1) in the weak interaction. There were many experiments that measured the helicity for various neutrino flavors; none of them succeeded in detecting right-handed neutrinos. For example, the most recent measurement of the helicity of ν_τ was carried out in the CLEO experiment, which observed a parity-violating angular asymmetry in $a_1 \to \pi\pi\pi$ with the result that the ν_τ helicity was $-1.02 \pm 0.13(stat.) \pm 0.03(syst.)$ [1], and confirmed the left-handedness of the tau neutrino.

However, recent results from neutrino oscillation experiments [2, 3, 4, 5, 6, 7] show significant evidences for neutrino mass, which corresponds to the existence of a positive helicity neutrino. This is because a finite mass particle has velocity less than speed of light and helicity flip happens when one overtakes the center-of-mass frame of the particle. If the helicity positive neutrino couples to a Z^0 with standard weak interaction strength, the $\pi^0 \to \nu\overline{\nu}$ decay occurs at the rate described as a function of neutrino mass m_ν as

$$Br(\pi^0 \to \nu\overline{\nu}) = 3 \times 10^{-8} \left(m_\nu/m_{\pi^0}\right)^2 \sqrt{1 - 4\left(m_\nu/m_{\pi^0}\right)^2} \tag{1}$$

for a single Dirac-neutrino type [8].

Number of light neutrino species The most accurate measurement of the number of light neutrino species N_ν was performed by LEP experiments in studies of Z production with an e^+e^- collider, where "light neutrino" means the neutrino whose mass is less than half of the Z^0 mass. Invisible partial width of Γ_{inv}, which was obtained after subtraction of visible partial widths from that of the total Z, gave the number of possible decay channels allowed in the Z^0 decay;

$$N_\nu = \frac{\Gamma_{inv}}{\Gamma_l}\left(\frac{\Gamma_l}{\Gamma_\nu}\right)_{SM} \tag{2}$$

where Γ_l is the partial width to charged leptonic modes, and Γ_ν is that for a single neutrino species. The ratio Γ_{inv}/Γ_l was measured in the experiments and the ratio of Γ_ν/Γ_l employed the Standard Model predicted number of $(\Gamma_\nu/\Gamma_l)_{SM} = 1.991 \pm 0.001$. The resultant N_ν was 2.994 ± 0.012 with a combined fit to all the LEP data by Particle Data Group (PDG) [9]. The data highly excludes possibility of the existence of light neutrinos other than ν_e, ν_μ and ν_τ.

Neutrino masses Neutrino masses have been studied in many experiments for a long time by measuring the kinematics of charged leptons or pions associated with a neutrino production in weak interaction. However, because of their very tiny mass, upper limits are set for all three flavors. The mass of electron neutrino ν_e, whose limit is most stringent, was measured from an end point of the energy spectrum in electron emission from the tritium β-decay: ${}^3_1\mathrm{H} \to {}^3_2\mathrm{He}\ e^-\ \overline{\nu}_e$. The resultant upper limit is 3 eV/c^2 at 95 % confidence level (C.L.). The tau neutrino mass, which was measured from τ decays; $\tau^- \to 2\pi^-\pi^+\nu_\tau$ and $\tau^- \to 3\pi^-2\pi^+(\pi^0)\nu_\tau$ by the ALEPH

Table 1: Summary of experimentally measured neutrino masses. The upper limit of ν_μ mass, 190 keV/c^2, is an evaluated number by PDG with an average of data measured by experiments. More stringent upper limit of $\nu_\mu < 170$ eV/c^2 [10] is obtained from pion decays at rest in the PSI.

Neutrino flavor	Upper limit	C.L. (%)	Comment	Reference
ν_e	225 eV/c^2	95	^{163}Ho decay	[12]
$\overline{\nu}_e$	3 eV/c^2	95	^{3}H β decay	[9, 13, 14]
ν_μ	190 keV/c^2	90	π^+ decay	[9, 10]
ν_τ	18.2 MeV/c^2	95	τ decay	[11]

experiment (1991-1995 runs), set an upper limit < 18.2 MeV/c^2 [11] at 95 % C.L., which is seven orders of magnitude worse than the limit on ν_e. The upper limits of neutrino masses are summarized in Table 1. Substituting the upper limit of ν_τ mass, the equation 1 provides a theoretical upper limit on the $\pi^0 \to \nu\overline{\nu}$ branching ratio $Br(\pi^0 \to \nu_\tau\overline{\nu}_\tau) < 5 \times 10^{-10}$. Upper limits on electron neutrino and muon neutrino provide the theoretical limit of 1×10^{-23} and 6×10^{-20}, respectively.

1.2 Determination of neutrino type : Dirac or Majorana ?

There have been long standing discussions on whether neutrinos are Dirac or Majorana particles. The question is fundamental in the particle physics. After finite mass of the neutrinos has been discovered, determinations of the type of neutrinos and their mass are hot topics. Neutrino-less double β decay experiments are attracting our attentions. Observation of the neutrino-less double β decay is an evidence for neutrinos as Majorana particles, because the decay occurs if a neutrino emitted from W^+ is absorbed by W^+ again as an anti-neutrino, which indicates that the anti-neutrino and the neutrino are the same particle. The measurement of $\pi^0 \to \nu\overline{\nu}$ branching ratio also carries the same physics motivations. Firstly, branching ratio measurement is directly connected to a determination the neutrino masses. Secondly, if neutrinos are Majorana particles, ν and $\overline{\nu}$ in the final state are identical particles, which results in a branching ratio of a factor of two larger than in the Dirac neutrino case [15].

1.3 History of experimental search for the decay $\pi^0 \to \nu\overline{\nu}$

The first search for the $\pi^0 \to \nu\overline{\nu}$ decay was performed in a reanalysis of the data accumulated for a decay $K^+ \to \pi^+\nu\overline{\nu}$ by P. Herczeg and C.M. Hoffman [16]. They set an upper limit of 2.4×10^{-5} at 90% C.L.. In 1988, the CHARM collaboration improved the limit to 6.5×10^{-6} (90 % C.L.) with a measurement of prompt neutrino interaction in a beam dump experiment involving background subtraction [17]. The limit was improved by the E787 collaboration in the measurement of $K^+ \to \pi^+\nu\overline{\nu}$ experiment by imposing photon rejection cuts to the events of $K^+ \to \pi^+\pi^0(K_{\pi 2})$ decay tagged with the monochromatic π^+ at 205 MeV/c. They observed 27 events in the signal region. However, with difficulties in an accurate estimation of $\pi^0 \to \gamma\gamma$ backgrounds due to the failure of photon detection, they set a conservative upper limit of 8.3×10^{-7} at 90 % C.L. [18]. The E949 experiment is a successor to the E787 experiment

Table 2: Summary of the upper limits on the $\pi^0 \to \nu\overline{\nu}$ decay. The most stringent limit is provided by cosmological arguments. But the limit is highly model dependent, and is not used in Particle Data Group.

π^0 decay to	Upper limit	Comment	Year
$\nu\overline{\nu}$(all)	8.3×10^{-7}	$K^+ \to \pi^+\nu\overline{\nu}$ (E787 Collaboration)	1991
$\nu\overline{\nu}$(all)	6.5×10^{-6}	Beam dump experiment (CHARM Collaboration)	1988
$\nu\overline{\nu}$(all)	2.4×10^{-5}	$K^+ \to \pi^+\nu\overline{\nu}$ (LANL)	1981
$\nu\overline{\nu}$(all)	2.9×10^{-13}	Cosmic thermal backgrounds	1991
$\nu\overline{\nu}$(all)	3.2×10^{-13}	Supernova SN1987A	1991
$\nu_e\overline{\nu}_e$	1.7×10^{-6}	Beam dump experiment (CHARM Collaboration)	1988
$\nu_\mu\overline{\nu}_\mu$	1.6×10^{-6}	Beam dump experiment (LSND Collaboration)	2004
$\nu_\tau\overline{\nu}_\tau$	2.1×10^{-6}	Beam dump experiment (LANL)	1988

with an improved photon detection capability. It is expected to improve the limit by the E787 experiment and establish a new upper limit on the decay by achieving the best sensitivity in the world.

The individual measurements for the decay $\pi^0 \to \nu_l\overline{\nu}_l$, where the lepton type l was specified, were also performed by observing neutrino interactions in the final state (exclusive search). The measured upper limits were summarized in Table 2 including the inclusive measurements. $\pi^0 \to \nu_\mu\overline{\nu}_\mu$ is the mode that has the most stringent limit on the decay, which was recently published by the LSND collaboration. However any flavor specific search is less sensitive compared with the inclusive search of the E787 experiment in the past.

1.4 $\pi^0 \to \nu\overline{\nu}$ in astrophysics

In cosmology, neutrinos play an important role. For example, the anisotropy of cosmic microwave background constraints the sum of the neutrino masses $\Sigma_i m_{\mu_i}$ to be less than 0.7 eV/c^2 by taking into account the data from the galaxy redshift surveys [20]. Though the cosmological constraint involves model dependences, it provides the most stringent limit in the measurements of the neutrino masses (see Table 1). This derives a limit of 9×10^{-26} on the decay of $\pi^0 \to \nu\overline{\nu}$.

On the other hand, astrophysicists show their interests in the $\pi^0 \to \nu\overline{\nu}$ decay because the reaction $\gamma\gamma \to \pi^0 \to \nu\overline{\nu}$ could work as a cooling mechanism in the description of the Universe. Some portion of the energy carried by photons in a dense and high-energy environment are transported more effectively to outer space by converting the energy into neutrinos. The behavior of the cosmic thermal background at the temperature of the pion mass constrains the decay rate $Br(\pi^0 \to \nu\overline{\nu})$ to be less than 2.9×10^{-13} [21] throught the process of $\gamma\gamma \to \pi^0 \to \nu\overline{\nu}$ at primordial nuclear-synthesis. In other models, considering different astrophysical processes, the upper limit $Br(\pi^0 \to \nu\overline{\nu}) < 3.2 \times 10^{-13}$ [22] is extracted from the energy-loss in the Supernova SN 1987A induced by the process $\gamma\gamma \to \pi^0 \to \nu\overline{\nu}$.

In recent years, $\pi^0 \to \nu\overline{\nu}$ in the highly dense medium had improvements. In 2002, the authors in [23] showed a possibility that the $\pi^0 \to \nu\overline{\nu}$ decay would occur even if the neutrinos were massless as in the Standard Model. The possibility was also presented in the different paper [24], where the authors claimed that Goldstone modes at finite density should be collective excitations associated with deformation of the Fermi surface in the high dense matter. This indicates the Fermi surface is distorted from a spherically symmetric state if a meson has finite momentum relative to the medium, which breaks rotational invariance and therefore angular momentum is no longer good as a quantum number to describe the meson state. The paper concluded that the pion decay to massless lepton pairs would not be prohibited. As an application of the theory, in the process of neutron-star cooling in high dense environment, the medium effect in the pion-pole mechanism ($\gamma\gamma \to \pi^0 \to \nu\overline{\nu}$) was studied [25]. These descriptions are model dependent, but indicates that the $\pi^0 \to \nu\overline{\nu}$ decay does arise a broad interest on various areas of physics.

1.5 Physics beyond the Standard Model

Experimental search for $\pi^0 \to \nu\overline{\nu}$ is performed by identifying π^0 decay to invisible products with strictly keeping eye on any activity around the π^0 decay time with a powerful hermetic photon detection system. The search has a sensitivity to any decay form of $\pi^0 \to$ "nothing" as well as the $\pi^0 \to \nu\overline{\nu}$, where "nothing" is applicable to any weakly interacting hypothetical particles. For example, in a π^0 decay to light SUSY particles (photino), the branching ratio was dynamically changed as a function of the mass. The $\pi^0 \to \nu\overline{\nu}$ search provided a clean test to the theory with SUSY masses less than half of the π^0 mass. One of the important neutrino properties to be tested in the frame of π^0 to "nothing" is the decay $\pi^0 \to \nu_1\overline{\nu}_2$, where ν_1 and ν_2 are different flavors of neutrinos. This is not allowed in the Standard Model because the decay violates the lepton flavor, but exploring into the world of beyond the Standard Model, this is worth studying the decay involving a mixing angle of lepton flavor changing.

1.6 Analogous decay to $\pi^0 \to \nu\overline{\nu}$

Analogous decays of a meson to "nothing" for neutral kaon, η and B mesons also attract an interest in the recent high-energy physics for theoretical and experimental cleanness of the system. η or $K^0 \to \nu\overline{\nu}$ is experimentally much difficult compared with the π^0 decays. $B \to \nu\overline{\nu}$ decays have a significant improvements recently in the Belle and BaBar experiment using a $\Upsilon(4S)$ system to two neutral B mesons. The B to "nothing" system holds the same physics motivations as for the π^0 to "nothing", in addition, the decay to SUSY particles in the range between the π and B masses. The most recent upper limit is $Br(B \to \nu\overline{\nu}) < 22 \times 10^{-5}$ [27] given by the BaBar collaboration. The Belle collaboration also shows their interest in the letter of intent for the future experiment with the super KEKB. However their sensitivity is much poorer than that achieved in the study of π^0.

2 Event Detection Strategy

2.1 Event detection strategy

$\pi^0 \to \nu\overline{\nu}$ detection requires identification of π^0 in the detector. The decay must be caught by observation of an associate production in the π^0 generation process. A well-known kaon decay process $K^+ \to \pi^+\pi^0$ ($K_{\pi 2}$) is chosen in order to tag the π^0 existence by redundant measurements of K^+ decay at rest and π^+ (205 MeV/c) with a help of two body decay kinematics. However, one of difficulties in the technique is that various K^+ decay modes involve a π^+ in the final states; the decay channel must be identified with impurity below 8.3×10^{-7}. An observation of the final products $\nu\overline{\nu}$ is impossible due to the small cross section of neutrino interactions with materials. Hence, no observation of a final product in a hermetic photon detection system is regarded as presence of neutrinos. This implies that, any unknown particles which interacts via weak force are accepted as a signal. In summary, $K_{\pi 2}$ decay without π^0 activity observed was searched in the experiment.

2.2 What kinds of measurements are required for it ?

Intrinsic $K_{\pi 2}$ acceptance (A_0) due to $K_{\pi 2}$ selection criteria is written as follows,

$$A_0 = \frac{N(K^+ \to \pi^+\pi^0)}{N_{K^+} Br(K^+ \to \pi^+\pi^0)} \tag{3}$$

where N_{K^+} is the number of kaons collected in the experiment, $Br(K^+ \to \pi^+\pi^0)$ is the branching ratio of the $K_{\pi 2}$ decay, which is measured to be $(21.13 \pm 0.14) \times 10^{-2}$ [9], and $N(K^+ \to \pi^+\pi^0)$ is the number of events remained after the $K_{\pi 2}$ selection.

Corrected acceptance A is obtained by considering further acceptance loss;

$$A = A_0 C_{dis} \tag{4}$$

where C_{dis} is called a disruption factor, which shows how often the $K_{\pi 2}$ selection is disrupted due to the presence of π^0 decay products. For example, if electrons from π^0 Dalitz decay overlap the π^+ track of $K_{\pi 2}$, it may drive the failure of track reconstruction, while the situation does not occur in the $\pi^0 \to \nu\overline{\nu}$ decay.

The branching ratio for the decay $\pi^0 \to \nu\overline{\nu}$ is obtained by

$$Br(\pi^0 \to \nu\bar{\nu}) = \frac{N}{N_{K^+} Br(K^+ \to \pi^+\pi^0) A} \cdot \frac{1}{C_{acc}} \tag{5}$$

where N is the number of signals observed in the signal region. In case that backgrounds are dominated, the N should be replaced with N_{90}, which is from Poisson statistics, gives 90 % confidence level. C_{acc} is a correction factor aiming for a recovery of the signals lost by hermetic detection cuts due to coincidentally happened activities (accidentals).

Substituting the equation (3) and (4) to the equation (5),

$$\begin{aligned} Br(\pi^0 \to \nu\overline{\nu}) &= \frac{N}{N(K^+ \to \pi^+\pi^0)} \cdot \frac{N_{K^+}}{N_{K^+}} \cdot \frac{1}{C_{dis} C_{acc}} \\ &= \frac{N}{N(K^+ \to \pi^+\pi^0)} \cdot \frac{1}{C_{dis} C_{acc}} \end{aligned} \tag{6}$$

The first term $\frac{N}{N(K^+ \to \pi^+ \pi^0)}$ corresponds to the detection inefficiency of the hermetic detection system if the measurement is background limited; in other words, it shows an inverse of the rejection capability of the detection system. In summary, the equation (6) tells us the branching ratio or the upper limit that can be obtained by measuring rejection and acceptance of the hermetic detection system and a correction factor of C_{dis}.

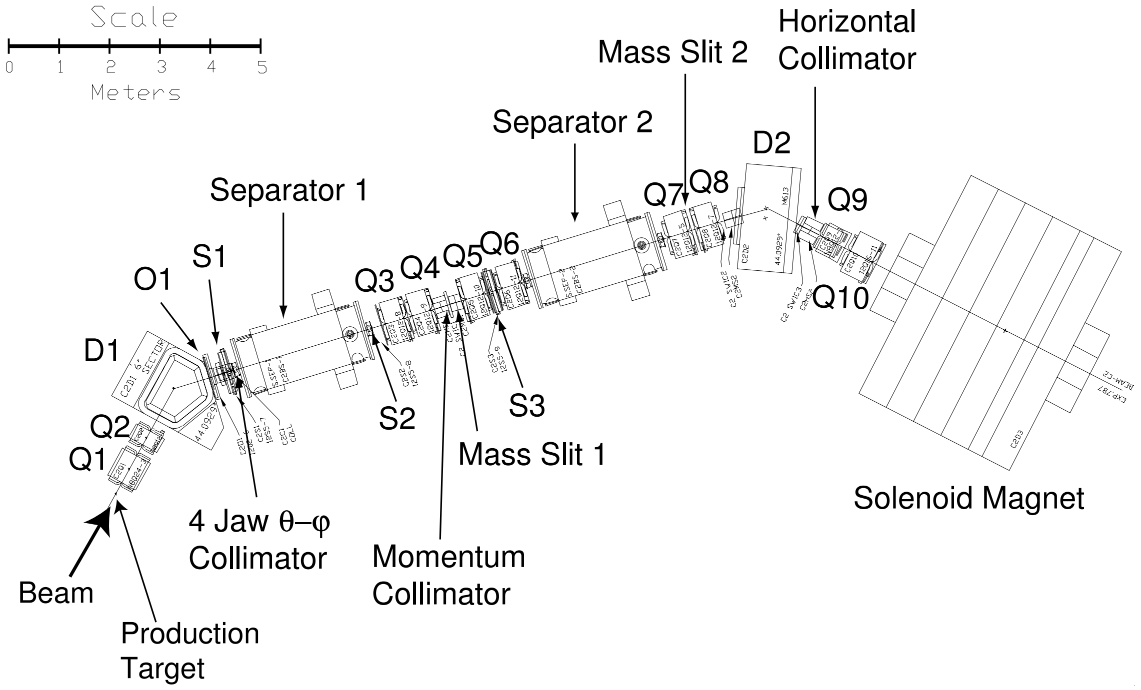

Figure 1: Schematic top view of the beam line named LESBIII. The beam line was viewing the 0 degree direction to accumulate more kaons. The bending magnet D1 and "Momentum Collimator" selected particles of 710 MeV/c and two stages of electrostatic separators and successor slits improved the beam purity. Ten quadrupole (Q1-Q10), three sextupole (S1-S3) and one octuple (O1) took care of a higher order aberration in the beam optics. "Solenoid Magnet" in the figure is a part of the E949 detector system.

3 Experimental Instruments

3.1 High intensity K^+ beam

Protons accelerated up to 21.5 GeV/c at the Alternating Gradient Synchrotron (AGS) of Broohaven National Laboratory (BNL) were extracted typically spending 2.2 seconds (spill) in 5.4-second repetition. The protons struck a 6 cm-long platinum target mounted on a copper base for water cooling. They produced 3×10^7 K^+s per every spill from collisions of 6.5×10^{13} protons on target. Accompanying ~ 500 times more π^+s, they were transported by the beam line called Low Energy Separated Beam III (LESBIII) [28] as shown in Figure 1. It was designed to produce the most intense and cleanest K^+ beam. The design concepts and performances are briefly described below and summarized in Table 3.

The highest K^+ beam intensity Aiming to collect as much kaons as possible from the production target, the first quadrupole magnet Q1 was placed close to the target, which makes the angular acceptance larger. Particles produced to the forward direction (at 0 degree angle) were viewed by the transportation line. This resulted in a success of obtaining 12 msr angular acceptance and 5×10^5 kaon yield from every 10^{12} protons on target.

Table 3: Basic parameters of the LESBIII line.

Beam Line	
Momentum range	830 MeV/c (Maximum), 710 MeV/c (Typical)
Momentum acceptance	4 % in FWHM
Production angle	forward (0 degree)
Angular acceptance	12 msr
Total Line Length	19.6 m
Particle Flux	4.8×10^6 of 800-MeV/c K^+s with 71 % purity corresponding to $\sim 10^6$ stopped K^+s in the detector (in the case of 10^{13} 24 GeV/c protons on target)
Beam Optics	Third order correction for aberration
Target	
Material	Platinum
Dimension	6-cm long
Cooling	Water cooling with an attached copper base
Max exposure rate	$\sim 30 \times 10^{12}$ MHz
Electrostatic Separators	
The first separator	Operation High Voltage : up to 625 kV Dimension : 12.7 cm (gap) × 2.0 m
The second separator	Operation High Voltage : up to 560 kV Dimension : 10.2 cm (gap) × 2.0 m

Beam purification Particles with a momentum of 710 MeV/c were selected by the bending magnet D1 and the collimator named as "Momentum Collimator" in Figure 1. They were delivered through two stages of electrostatic separators to increasing the K^+ to π^+ ratio. In the separators, kaons and pions had different deflection from the electric field while feeling the same strength of the deflection by the magnetic field, which resulted in separated spots at the collimation slits named "Mass Slit 1" and "Mass Slit 2".

The rate of "cloud pions", which were secondary pions from decays in particular from K^0, were estimated to be a few times higher than the K^+ intensity from the beam simulation. But they were effectively reduced to the ignorable level at the second mass slit. The final K^+ to π^+ ratio was 3 : 1.

3.2 The E949 detector system

The E949 detector was primarily designed for a measurement of the extremely rare kaon decay $K^+ \rightarrow \pi^+\nu\overline{\nu}$ [29, 30], whose branching ratio is expected to be around 10^{-10} in the Standard Model. Background rejection down to the 10^{-10} level was mandatory for the E949 detector. It provided accurate and redundant measurement of momentum, energy and range in plastic scintillator of charged tracks. This redundancy provided a tool for kinematic background rejection even if one of the measurements was erroneous by unexpected reasons. All of the measurements successfully achieved good resolutions of 1 % (momentum), 3 % (energy) and 3% (range). The E949 detection was also designed to have a strong discrimination against beam backgrounds by employing a technique of "delayed coincidence", which required at least a few ns between the times of an incident kaon and charged particles from the decay. Beam backgrounds, which usually occurred at prompt timing, were effectively rejected by this requirement. Hermetic detection system in the E949 detector also played a crucial role to find out the activities from kaon decays. The $K_{\pi 2}$ background to the $K^+ \to \pi^+ \nu\overline{\nu}$ decay was reduced by a factor of $\sim 10^4$ by an accurate measurement of π^+ kinematics, and the remaining 10^6 rejection was achieved by the hermetic photon detection system. This is the most valuable benefit the $\pi^0 \to \nu\overline{\nu}$ search received. But the reverse is also true. The $\pi^0 \to \nu\overline{\nu}$ studies in the thesis, in particular, maximization of the photon detection capability, will be a benefit to understand the background to $K^+ \to \pi^+ \nu\overline{\nu}$. The later sections of the thesis present key information on the photon detection inefficiency, which is indispensable to the $K^+ \to \pi^+ \nu\overline{\nu}$ analysis. In the analysis, all principal studies were performed with real data, not relying on Monte Carlo simulations, because we do not expect all pathological events can be properly simulated by Monte Carlo simulation. Online rejection in the triggers was set at proper level, not to be tightened too much, to collect enough statistics for offline analysis; they were designed to provide various control samples.

Overview of the detector The side and end view of the E949 detector are shown in Figure 3 and 4. The z-axis is defined along the beam line pointing to the downstream end, and radial and azimuthal angles are determined in the cylindrical coordinate. The E949 detector consists of four components;

- Beam counters and chambers, which were employed for beam-particle identification (K-π separation) and multi particle background rejection.
- K^+ stopping target for observation of kaon decay at rest, measurement of the decay vertex position, the decay time and detection of extra beam particle if exists.
- Spectrometer for charged particles
  - Solenoidal magnet
  - Drift chamber for momentum measurement
  - Stack of plastic scintillators, called Range Stack, for kinetic-energy and range measurements of the charged particles. Information of the particle type through the dE/dx energy loss measurement in the scintillator.
- Hermetic photon detection system for detection of extra activities, mainly electromagnetic shower of the photons from kaon decays.

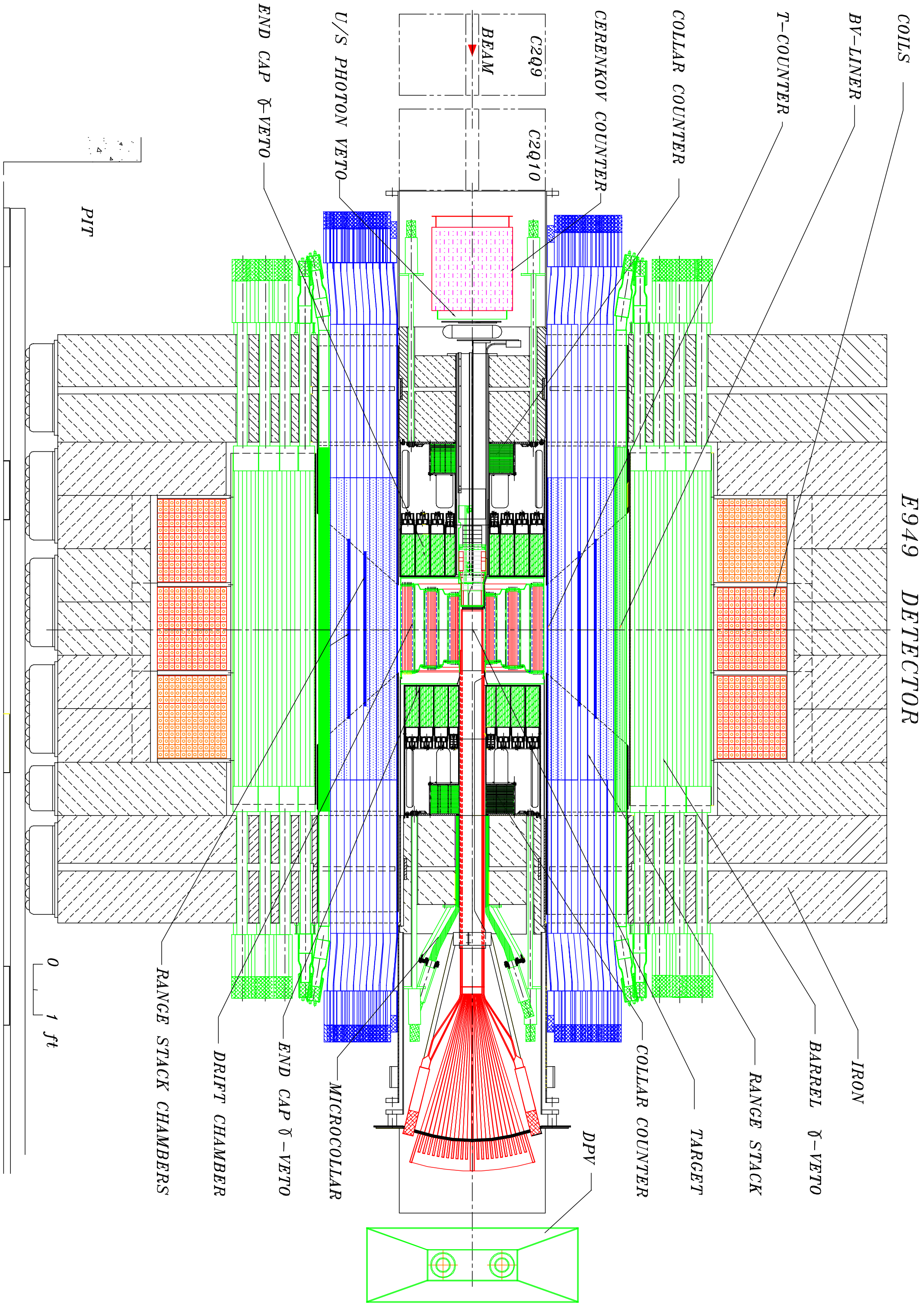

Figure 2: Side view of the E949 detector.

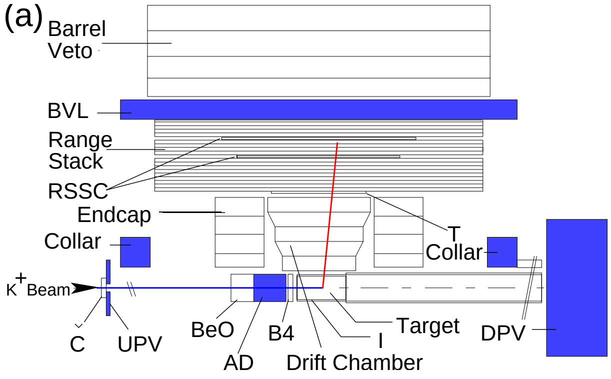

Figure 3: Schematic side view of the upper half of the E949 detector. Located from the upstream to downstream direction along the beam line are, Čerenkov counter (Č), upstream photon veto (UPV), collar detector (Collar), inactive beam degrader (BeO), active beam degrader (AD), energy loss counter (B4), scintillator fiber target (Target), downstream colloar detector and downstream photon veto (DPV). The target is surrounded by I-Counters (I) and Drift Chamber. Both ends of the detector were covered with an array of CsI crystals (Endcap).

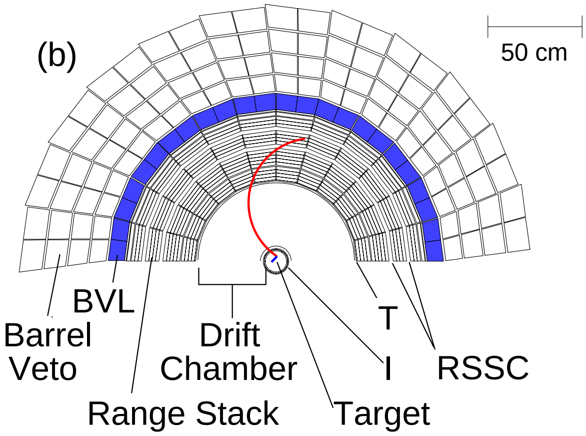

Figure 4: Schematic end view of the upper half of the E949 detector. Located from inner to outer direction, scintillating-fiber target (Target), I-Counters (I), Drift Chamber, Range Stack, barrel veto liner (BVL) and Barrel Veto. Two layers of tracking device, called range stack straw chamber (RSSC), were installed just after the layer 10 and the layer 14 scintillators.

3.2.1 Beam counters and chambers

Čerenkov counter The K^+ to π^+ ratio was typically controlled to be around 3 : 1 during the experiment. Kaons in the beam were needed to be more strictly discriminated from pions contained in the beam. The particle identification of the delivered beam was made at the entrance of the E949 detector. The Čerenkov counter, shown in Figure 5, had a 25.53-mm thick Lucite radiator with a refractive index of 1.49. In the radiator, Čerenkov light was emitted to the angle $\theta_{\check{C}}$ from the path,

$$\cos\theta_{\check{C}} = \frac{1}{n\beta} \tag{7}$$

where n is a refractive index of the radiator, and β is a velocity of an incoming particle normalized to a speed of light in vacuum. The light emitted from a π^+ with a momentum of 710 MeV/c ($\beta = 0.981$) in the radiator was totally reflected at the boundary of the radiator and reached to 14 phototubes (PMT) forming an array of the inner ring of the Čerenkov counter. On the other hand, light from a K^+ with a momentum of 710 MeV/c, passed through the boundary, reflected by the mirrors and observed in the 14 PMTs of the outer ring. Various parameters on the radiator are summarized in Table 4. The K^+ identification was performed based on the number of hits in each K and pion-PMTs in a given time window. The typical performance of the Čerenkov counter is shown in Figure 6. Each of the PMT signals was recorded with a time-

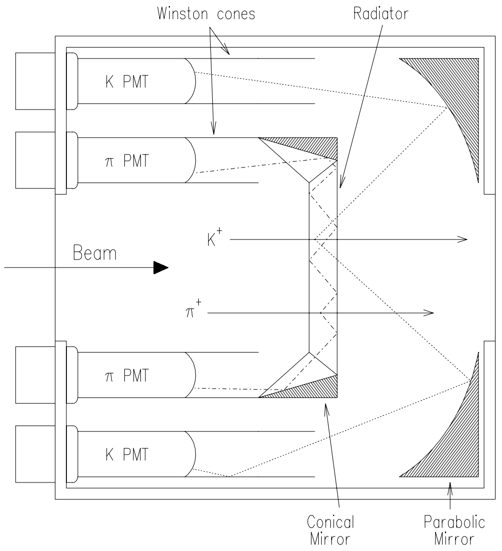

Figure 5: Schematic side view of the Čerenkov counter. Čerenkov light emitted from a π^+ in the radiator is totally reflected at the surface and reaches to the PMTs named pion PMTs (π PMT). The light originated from a K^+, which have a smaller opening angle than that of π^+, can penetrate the radiator and are delivered to "K PMT"s by a reflection of parabolic mirrors.

to-digital converter (TDC) and a 500 MHz waveform digitizer employing a gallium-arsenide (GaAs) charge coupled device (CCD) [31].

Beam wire chambers Two beam wire chambers were placed after the downstream of the Čerenkov counter for rejection of multi beam particle events. A pion accompanying a kaon might be misidentified as a signal ($K^+ \rightarrow \pi^+ +$ "nothing" event) if the K^+ was lost before it came to rest in the target. This wire chamber system ensured that no particle came into the detector at the time when the decay particles from K^+ was recorded.

The upstream chamber (BWPC 1) had active area of 17.8 cm (horizontal) × 5.08 cm (vertical) with three anode-wire planes called X, U and V. In the X plane, 144 sense wires were tensioned vertically for horizontal-position measurement, and in the U, V planes, 120 wires were positioned in every 2.54 mm. The U and V planes were tilted by $+45^\circ$ and -45° with respected to the X plane. Spatial resolution of 1.27 mm was achieved in the X plane and 2.54 mm in the U and V planes. These configurations are summarized in Table 5. Another beam wire chamber (BWPC 2) was located at 90 cm downstream of the BWPC 1. This chamber also had three planes called T, U and V, which consisted of 120 anode wires for each (see Table 6). In the BWPC 2, the number of readout channels were reduced to 32 in each plane by multiplexing the wires, and the spatial resolution was 2.4 mm at the center of the planes and 4.8 mm around the peripheral region. Each plane were tilted by 0° (T), $+120^\circ$ (U) and -120° (V) from the vertical

Table 4: Various parameters on the Čerenkov counter

Radiator (cylindrical shape)	
Diameter	203 mm
Thickness	25.53 mm
Refractive index	1.49
Čerenkov emission threshold	$\beta_{\check{C}}$ = 0.671
Total reflection threshold	$\beta_{thr} = 0.905$

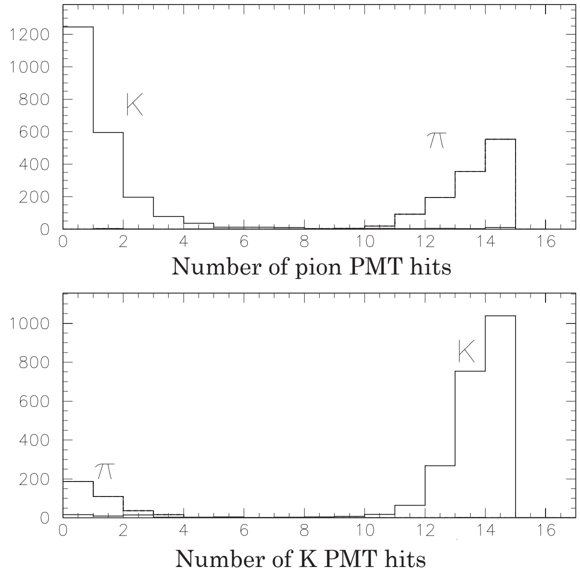

Figure 6: Number of hits in pion PMTs (above) and K PMTs (below) of the Čerenkov counter for π^+ or K^+ beam. Kaons were selected by requiring the number of hits greater than 7 in the K PMTs. π^+ beam was selected by requiring the number of hits in the pion PMTs to be more than 7.

Table 5: Properties of the Beam Wire Chamber 1

Anode wire	12 μm diameter, Au-plated tungsten
Cathode foil	25 μm Aluminized mylar
Wire spacing	3.18 mm (anode to cathode), 1.27 mm (anode to anode)
Guard wires	Au-plated Be-Cu, 8 wires at each end
X-plane	144 anode wires stretched vertically Spatial resolution of 1.27 mm
U1 and U2 planes	120 anode wires (60 readout, multiplexed $\times 2$) Tilted by +45 (U1), -45 (U2) degrees from the vertical axis 2.54 mm in the spatial resoluton
Active area	17.8 cm (horizontal) × 5.08 cm (vertical)
Total channels	264 = 144 (X) + 60 (U1) + 60 (U2)
Inert Gas	CF4 / Isobutane (80:20)

direction.

Beam degraders Two beam degraders were employed to slow down the beam particles and to enhance K^+ stopping probability. The upstream degrader called “inactive degrader” was made with 111.1-mm thick Beryllium Oxide (BeO), which had a high density with a small atomic number (less multiple scattering) with 4.76-mm thick Lucite to the end. The characteristics are detailed in Table 7. The downstream one, which was called “active degrader”, was composed of 40 layers of 2-mm thick scintillators sandwiched by 2.2-mm thick copper disks. Their thickness were optimized to maximize the number of kaons that came to rest in the scintillator target.

Energy loss counter : B4 hodoscope An energy loss counter named B4 hodoscope, located in front of the scintillation fiber target, was used for detection of beam particle position and for further K-π separation. The timing resolution was measured to be 0.58 ns in RMS, which

Table 6: Properties of the Beam Wire Chamber 2

Anode wire	12.7 μm diameter Au-plated tungsten
Cathode foil	8 μm Aluminized mylar, Carbon coated
Wire spacing	1.59 mm (anode to cathode), 0.8 mm (anode to anode)
Guard wires	Au-plated Be-Cu, 3 wires at each end
T, U and V planes	120 anode wires, 32 readout (central 72 wires multiplexed by 3, remaining 48 were by 6) Tilted by 0 (T), +120 (U) and -120 (V) degrees from the vertical axis Spatial resolution of 2.4 mm (central part), 4.8mm (edge region)
Active area	Regular hexagon with an each side having 9.6 cm in length
Total channels	96 = 32 (T) + 32 (U) + 32 (V)
Inert Gas	CF4 / Isobutane (80:20)

provided good rejection against extra particles coming at the kaon decay time. π^+s from kaon decay in flight in the middle of the beam line were identified from the dE/dx energy loss in the counter. The energy resolution of 0.43 MeV (for kaons) provided good $K^+ - \pi^+$ separation capability as shown in Figure 50 on page 69. The B4 gave accurate spatial resolutions of 0.37 cm in X and 0.36 cm in Y direction.

The B4 hodoscope consisted of two scintillator layers of 6.35-mm thick. They were rotated by $\pm 33.5^\circ$ from the horizontal axis for a measurement of two dimensional coordinates as seen in Figure 7. Each layer was composed of 16 ’Z’-shaped scintillator tips (see Figure 8), and was read-out through three wavelength shifter fibers embedded in each tips.

Ring veto counter The Ring veto counter, which was made of plastic scintillators (BC404), covered the B4 outer radius for detection of escaping particles from the beam line with dimensions of 119 mm (inner raidus) to 145.5 mm (outer radius) and 3.27-mm thickness. The counter was horizontally segmented into two pieces.

Table 7: Properties of the beam degraders

Inactive degrader	
Material	111.1-mm thick Beryllium Oxide with 4.76-mm thick Lucite
Dimension	Cylindrical shape with a radius of 136 mm
Active degrader	
Material	Alternative 40 layers of 2.2-mm thick copper disk and 2-mm thick scintillator (Bicron BC404)
Dimension	Cylindrical shape with a radius of 136 mm
Segmentation	12 in azimuthal angle
Readout	Embedded 14 WLS fibers (BCF99-29-AA-MC) for each segment, multiplexed into single channel
Phototube	Hamamatsu R1924 × 1

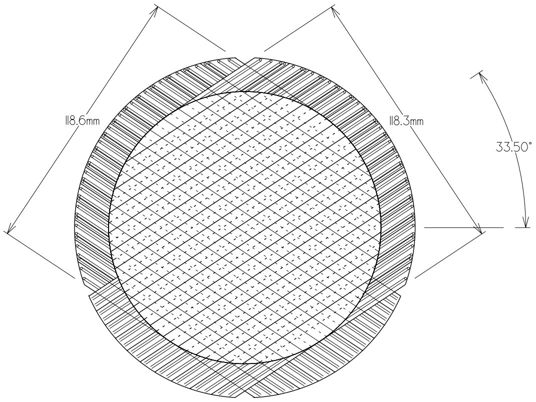

Figure 7: Schematic end view of the B4 hodoscope, which was composed of two layers of segmented scintillator plates for U and V-axis measurements. Each layer was rotated by + (or -) 33.5° with respect to the horizontal axis.

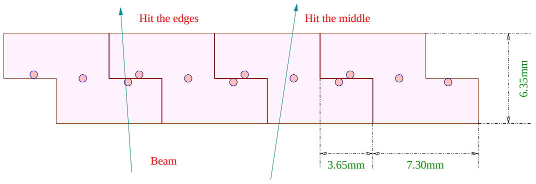

Figure 8: Cross sectional view of a single layer of the B4 hodoscope. Each layer consisted of 16 elements of 'Z'-shaped scintillator tips. Combination of the Z-shape could reduce a detection inefficiency by preventing particles to passing through the gap between tips. "○"s in the figure indicate wavelength shifter fibers.

Upstream Photo Veto Counter The upstream photon veto counter was one of the ancillary photon-detection systems covering small dip angle with respect to the beam line, and was located between the Čerenkov counter and the BWPC 1. The detector was made of 12 layers of lead (1 or 2 mm thick) and plastic scintillator (2 mm thick) alternatively stacked along the z direction. It formed a square-shape with a dimension of 28.4 cm × 28.4 cm in X-Y plane, and had a beam hole at the center. The parameters of the counter are summarized in Table 10.

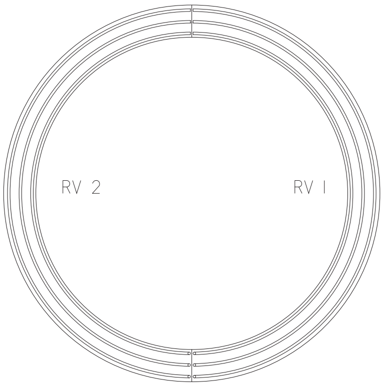

Table 8: Schematic end view of the ring veto.

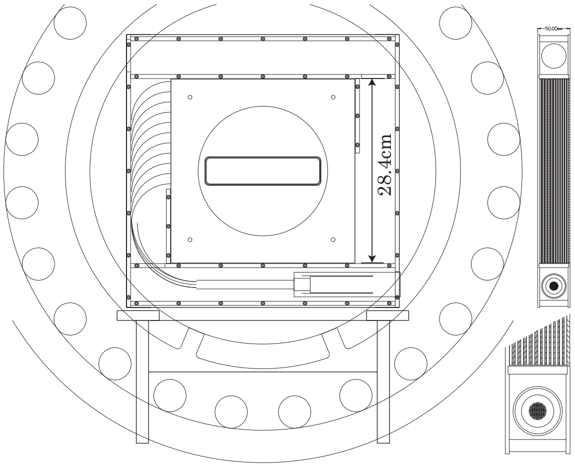

Table 9: Schematic end view of the upstream photon veto.

Table 10: Properties of the Upstream Photon Veto Counter

Type	12 layers of lead and plastic scintillators
Material	2 mm-thick scintillator plates (Bicron BC404)
	1 mm-thick (1 to 6 layer) and 2 mm-thick (other) lead sheets
Dimension	28.4 cm × 28.4 cm shape
Upstream face	3.175 mm-thick aluminum plate
Downstream face	2.2 mm-thick copper plate

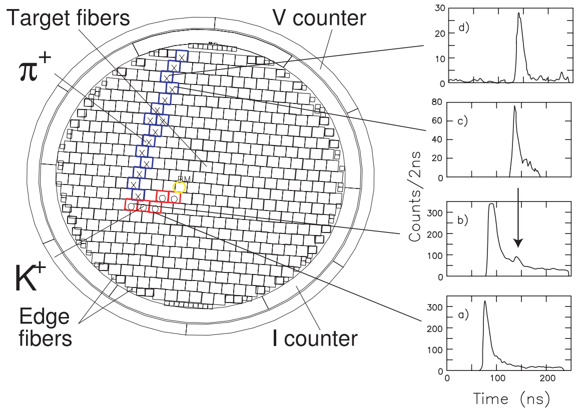

Figure 9: Schematic end view of the scintillating fiber target, I-Counters and V-Counters. Fibers with '○' indicate the fibers of kaon passage, and had the dE/dx energy deposit consistent with kaons coming to rest as shown in the waveform "a)". The Kaon decay produces a double pulse in the waveform as seen in "b)". A kaon decay product deposits energy as "c)" along the trajectory denoted with 'x' in the figure.

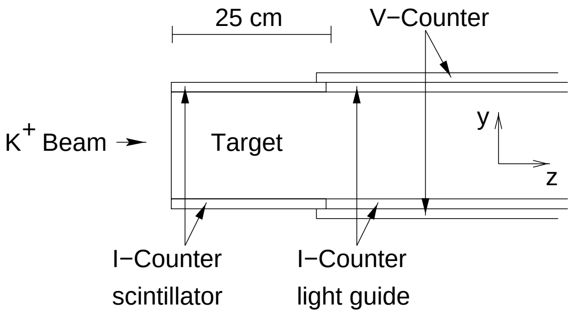

Figure 10: Schematic side view of the scintillating fiber target, I-Counters and V-Counters. I-Counters, which surrounded the target in the azimuthal direction, determined the fiducial region along the Z direction. The V-Counters, which covered the light guide of the I-Counter, removed charged particles passing through the light guides.

3.2.2 Kaon stopping target

Kaons, which were slowed down in the degraders, came to rest in a fine-segmented scintillator target. This arrangement brought us great benefits in the experiment: (1) Particles from two body decays had monochromatic momentum in the detector frame, and provided an easy way of rejecting or collecting the events in the online level. This resulted in better purity or higher rejection against various backgrounds. (2) Waiting at least 2 ns between the time of the particle entering the target and the secondary particles decaying from the target provided good rejection against prompt beam backgrounds and kaon decay-in-flight events.

The target was made of a bundle of 413 plastic scintillating fibers. Each fiber had a cross-section of 5 mm $\times$ 5 mm in X-Y plane and a length of 3.1 m in the beam direction. Having assembled together, they formed a cylindrical shape with 12-cm diameter as shown in Figure 9, for the end view. The side view is shown in Figure 10. Each fiber was readout by a PMT at the downstream end and its energy and timing as well as the waveform were recorded by an ADC, a TDC and a 500 MHz sampling CCD. The gaps at the peripheral region were stacked with $\sim$ 200 thinner (1$\sim$3 mm) fibers called "edge fiber"s. The edge fibers were grouped into 12 bundles and read by 12 PMTs.

Energy deposit in a fiber ranged from ~ 1 MeV of minimum ionizing particles (MIP) to ~ 80 MeV of kaons at the very end of stopping process. Typical waveforms are shown in Figure 9. To deal with this large dynamic range, not only high-gain CCD channels but also that of low-gain (84 in total) were prepared for multiplexed signals. Using these CCD waveforms, the fiber placed at kaon decay position was identified by a double pulse fitting at the offline analysis. Kinetic energy of the secondary particle in the fiber was extracted from the kaon stopping signal for better energy resolution. Thanks to the target's fine segmentation, it was possible to reconstruct kaon and pion track precisely and calculate an accurate pion path length. It also guaranteed that the pion came from the decay vertex by confirming there were no gap between the trajectories.

3.2.3 Fiducial counters : I and V-Counters

Fiducial counters named "I-Counters" surrounded the target for detection of charged particles from kaon decay in the target. They determined the fiducial area (= allowed region where kaon decays take place) through a requirement that the decay product must pass through the counter. The timing was used as the kaon decay time in the online trigger for delayed coincidence. The I-Counters were azimuthally segmented into six counters of 6.4-mm thick plastic scintillators and were 25-cm long in the beam direction (see Figure 9 and 10). Each scintillator was readout by a PMT with an ADC, a TDC and a 500 MHz flash ADC based waveform digitizer (TD) [32].

V-Counters, which were made of 5.0-mm thick and 1.96-mm long plastic scintillators, surrounded the light guides of the I-Counters. They rejected events with unwanted signals in the light guide due to Čerenkov ratidation. The V-Counters were located so as to have a 6-mm overlap in the Z direction with the I-Counter scintillators. This determined the fiducial region to be $\sim$ 24.2-cm long along the beam direction. Each scintillator was read by a PMT and recorded with an ADC and a TDC.

3.2.4 Drift Chamber for momentum measurement

A cylindrical drift chamber, located outside of the I-Counters, reconstructed a charged track trajectory based on the drift distances from the corresponding sense wires. The track curvature in the X-Y plane, produced in a 1 T magnetic field, was measured to determine the momentum of the charged particle.

The chamber was designed to minimize its amount of material to reduce multiple scatterings and improve the energy resolution by reducing dead materials. The chamber, called “Ultra Thin Chamber” (UTC) [33], was formed with inflating thin foils shaped by gas pressure; it had no supporting material inside it. It had a dimension of 51-cm long in the beam direction and an inner (outer) radius of 7.85 cm (43.31 cm). The total thickness was 2×10^{-3} radiation lengths along typical particle passage.

Anode and cathode structure in the UTC The UTC consisted of three active cylindrical superlayers and two inactive volumes between them. Each radial end of a superlayer had a 25-μm thick Kapton foil and it was supported by differential gas pressure. The superlayers, each with four layers of square drift cell, were filled with a mixture of argon (49.6 %), ethane (49.6 %) and ethanol (0.8 %). The inactive volumes were filled with nitrogen gas. In the active superlayers, wires were arranged in a rectangular cell structure with a dimension of 11 mm × 19 mm in X-Y cross sectional view. Each cell was made of an anode sense wire of gold-coated Tungsten (20 μm diameter) and surrounding eight aluminum cathode wires (100 μm diameter). The innermost superlayer had 192 ($= 48 \times 4$) cells, where 48 cells were aligned in the azimuthal direction and 4 layers in the radial direction, while the middle and the outermost superlayers had 384 (= 96 × 4) and 576 (= 144 × 4) cells, respectively. The cells in the radial direction were staggered by a half cell to resolve the left-right ambiguity.[1] Each anode wire was operated at the high voltage of ∼2 kV, which gave a gain of 8.0×10^4 and a drift velocity of 5 cm/μs.

On the Kapton foils, a helical array of copper strips (7-mm wide, 120-nm thick) was laminated with a 1 mm gap between strips. They were tilted at 45 degrees with respect to the beam direction. The strip, coated with 30-nm thick nickel, collected the induced charges from an incident particle and determined the track Z-positions with a help of the reconstructed track in X-Y plane. The number of strips varied with the foil radius from 72, 108, 144, 180 to 216.

3.2.5 Energy and range measuring system : Range Stack

The Range Stack (RS), which was a cylindrical array of plastic scintillators placed outside the drift chamber (see Figure 12), measured energy and range of charged particles. It was thick enough to stop π^+ originated from the kaon decay at rest. It fully covered the acceptance in the azimuthal direction, and had 45.08 cm in the inner radius, 84.67 cm in the outer radius and ∼ 2 m in the beam direction. The Range Stack was segmented into 24 sectors in the azimuthal direction and 19 layers (stacked) in the radial direction; thus, 456 scintillator plates were used in total. The counters of all radial layers in four successive sectors (76 counters in total) were grouped into a single set called “hextant”.

---

[1] Sense wires can measure the drift length but can not measure the drift direction, so that, any single wire cannot decide if a particle passed on its left or right side from its own information.

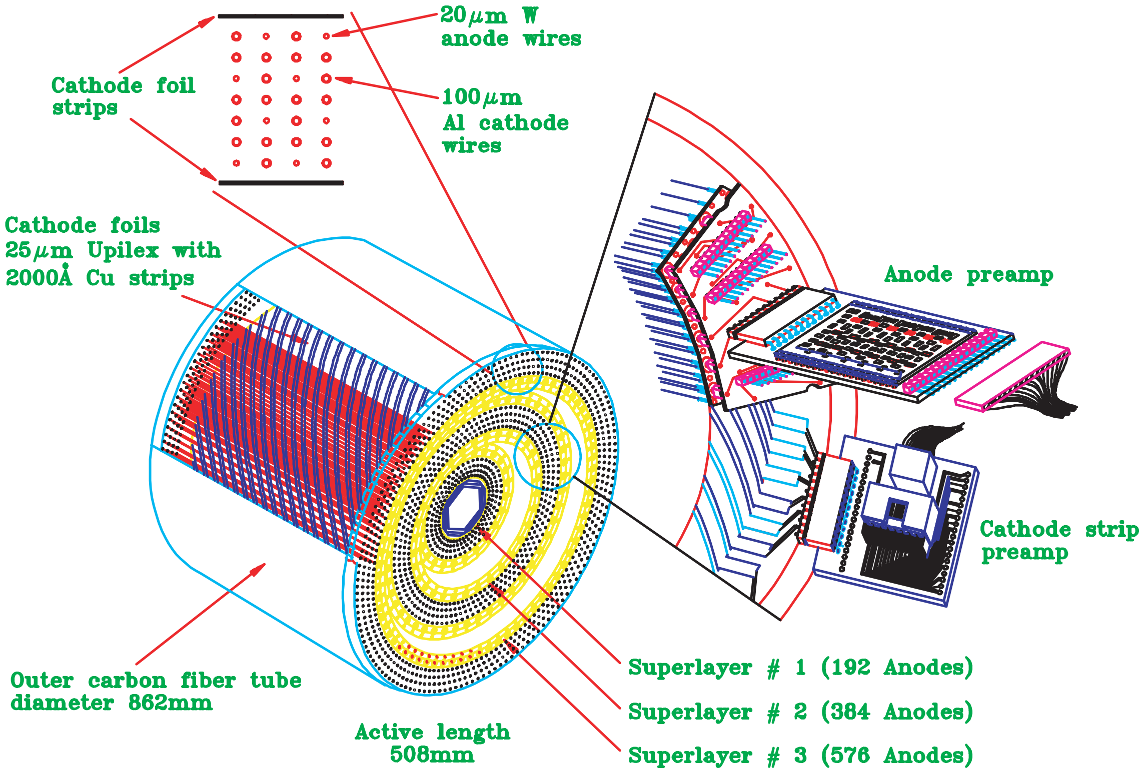

Figure 11: Schematic view of the Ultra Thin Chamber (UTC). The drift chamber consisted of three active cylindrical superlayers and two inactive volumes.

The 24 counters in the innermost layer, called the T-Counters, had a thickness of 6.35 mm in the radial direction and a length of 52 cm in the beam direction; the hits of these counters were used in the trigger. In each of the T-counters, 17 wavelength shifting (WLS) fibers were embedded and readout by the PMTs attached at both ends. The counters in the second to the 18th layers had a thickness of 1.905 cm in the radial direction and a length of 182 cm in the beam direction. The counters in the layer 19 were made of 24 1-cm thick × 182-cm long scintillators. They were used as a veto, confirming that charged particles stopped before the layer 19. The longer range tracks, which mainly came from μ^+ of $K_{\mu 2}$, were rejected with the layer 19 signals. The counters in layer 2 to 19 were readout by two PMTs on both ends through light guides.

Signal readout Each PMT was instrumented with its own dedicated channel of an ADC and a TDC; in addtion, every four PMTs in the same layer and the same hextant were fed into an analog multiplexer and connected to a waveform digitizer called Transient Digitizer (TD). The TD with a 500-MHz sampling rate recorded the waveform up to 2 μs, and the stored waveform was used to identify $\pi^+ \to \mu^+$ decay chain at the offline analysis. Positron emission from μ^+ decay was not in the range of TD, in many cases, due to the muon lifetime of $\sim 2.2\mu$s, but the positron signals were recorded by multi-hit TDCs with a longer gate-window of 10 μs. An example of the waveforms recorded by the TDs is shown in Figure 13. One can see the whole

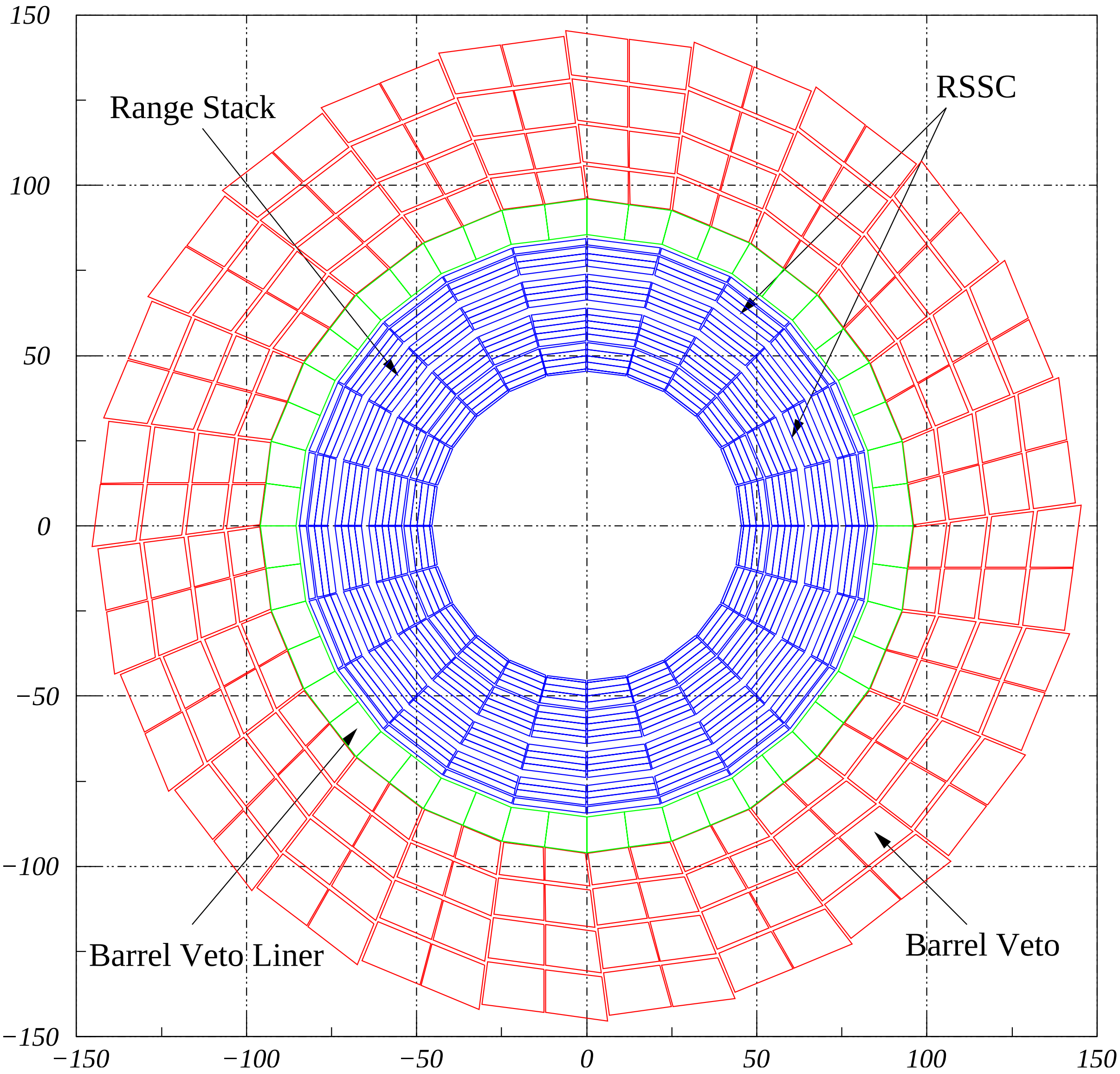

Figure 12: Schematic end view of the Range Stack, Barrel Veto Liner and Barrel Veto.

decay sequence of π^+ that came to rest in layer 12, a signal of μ^+ from the pion decay as a bump, and a positron emitted from the muon decay. The ADC gate were set to be 100 ns; the muon energy of 4 MeV was usually included within the ADC gate. This should be subtracted in the offline energy reconstruction. The particle identification with the $\pi^+ \to \mu^+ \to e^+$ decay sequence is one of key issues in this analysis; it will be described later in the analysis section.

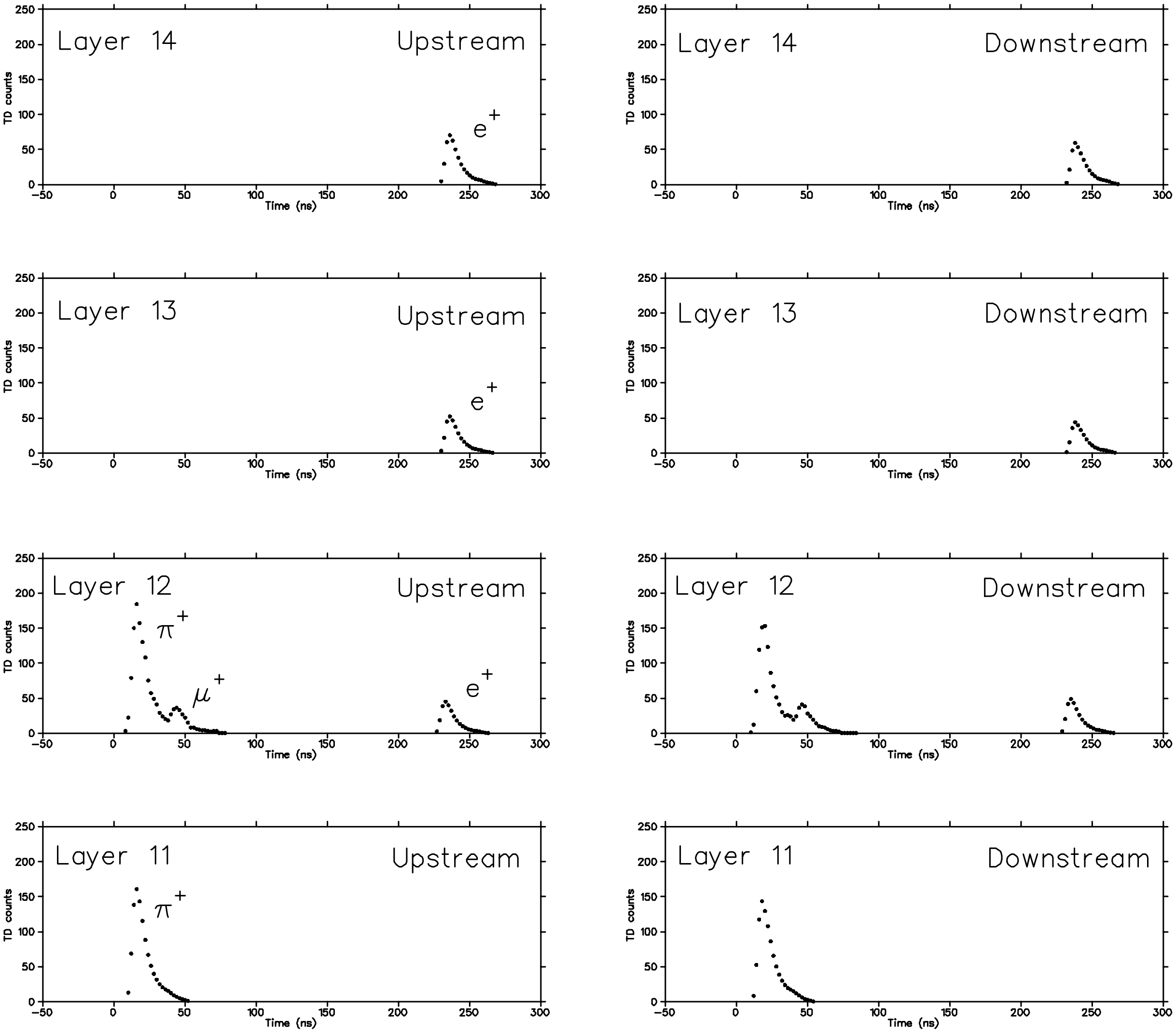

Figure 13: $\pi^+ \to \mu^+ \to e^+$ decay sequence recorded by the waveform digitizers in the Range Stack. π^+ from the kaon decay passed layer 11 and came to rest at layer 12 (no π^+ signal in layer 13 or above.). π^+ decayed into μ^+ and ν_μ. The monochromatic 4 MeV muon made a bump on the pion signal tail. 4 MeV muon came to rest in the same counter, and a positron was emitted and reached layer 14.

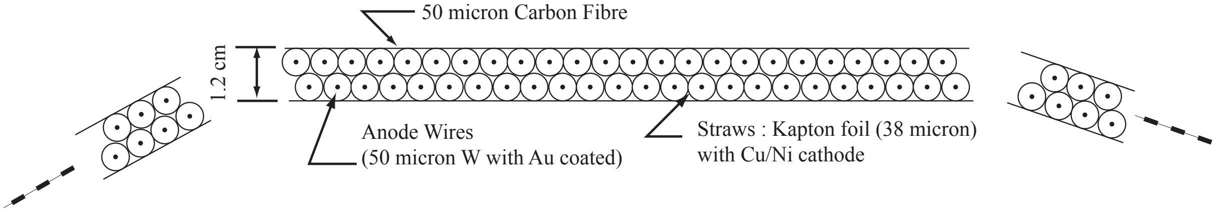

Figure 14: Schematic end view of the inner RSSC. The tubes run through the beam direction.

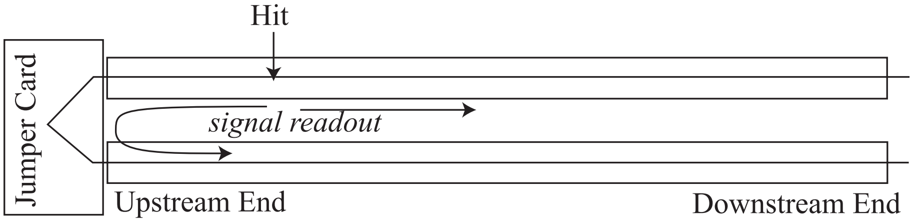

Figure 15: Schematic side view of the inner RSSC. For reduction of the number of readout channels, two adjacent RSSC anode-wires were connected together with a jumper card.

3.2.6 Range Stack Straw Chambers

Range Stack Straw Chambers (RSSCs) were placed between the layers 10 and 11 and the layers 14 and 15 in the Range Stack, aiming for accurate trajectory reconstruction of charged particles. The RSSCs between 10 and 11 had two sub-layers of 24 straw tubes as shown in Figure 14. Each tube, with 3.4 mm in radius, was formed with a 38-μm thick Kapton foil with the inner surface of Cu/Ni coated cathode. A gold coated Tungsten anode wire (50-μm diameter) was strung at the center. The two sub-layers were stacked with an offset by a half cell from each other as shown in Figure 14, and the total mass per unit area kept as small as 0.054 g/cm^2. The anode wires were tensioned along the beam direction for X-Y position measurement, and Z-position was measured from the end-to-end time difference of the signal arriving times. The outer RSSCs, located between the RS layer 14 and 15, aligned two superlayers of 28 tubes for every sector in the same way. For reduction of readout channels, every two anode wires were connected together at the upstream end and the signals were read on the downstream ends as shown in Figure 15.

Operating condition The RSSCs, filled with a gas mixture of 25 % argon and 75 % isobutane, were operated in the limited-streamer mode at 3450 V. The obtained time resolution was $\sim$ 50 ps with a time-streacher-circuit, which allowed us to determine the Z position with a resolution of 1.5 cm in RMS.

3.2.7 Barrel photon detection system : Barrel Veto

Barrel Veto (BV), a sandwich calorimeter of lead sheets and plastic scintillators, detected photons and other extra activities. It had the solid angle of $2/3 \times 4\pi$, and fully surrounded the Range Stack and Barrel Veto Liner, which will be explained later. The detector was segmented

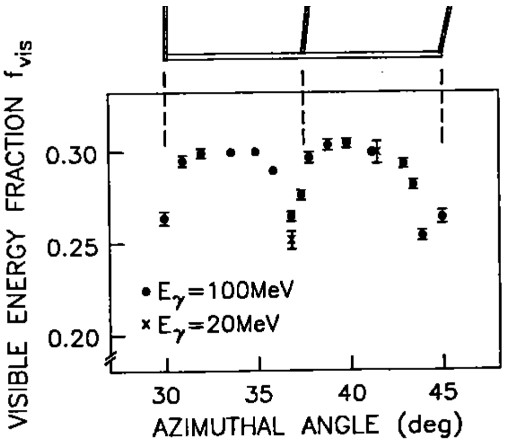

Figure 16: Visible energy fraction as a function of the azimuthal angle. The upper schematic figure shows the support frame of the Barrel Veto. The lower plot shows the visible energy fraction vs azimuthal angle.

into 48 modules in the azimuthal direction and into four in the radial direction (192 modules in total). Each module was made up of 16 (the innermost modules), 18, 20 and 21 (the outermost modules) of lead-scintillator layers, with each layer being composed of a 1-mm thick lead sheet and a 5-mm thick plastic scintillator plate (BC408, Bicron Corp.). The total radiation length in the radial direction was 14.3, and the length in the beam direction was 1.9 m. The attenuation length of the scintillator lights was measured to be 1.2 m from the ratio of light output at both ends.

Signal Readout Both ends of the scintillator were attached to a 150 mm-long acrylic light mixer, which was in turn coupled to a UV transparent acrylic light pipe (67 mm in diameter and 850 mm in length) via a flexible wafer made of silicone dielectric gel (Dow Corning SYLGARD 527), and to a 77 mm-diameter PMT (EMI 9821KB) through a hole in the end-plate of the spectrometer. The PMTs were shielded with μ-metal sleeves. The fraction of light emission reached to the photocathode varied from 30 % (for the inner modules) to 17 % (for the outer modules) and the average light yield was ~ 10 photoelectrons per 1 MeV of visible energy deposit.

Supports of the Modules 1.5 mm-thick stainless steel-plates formed a web-like frame structure, as shown in Figure 12 in the cross sectional view. They were fixed onto the four aluminum plates attached to the magnet yoke. The support frame was tilted from the radial line, so that any module boundary would not point to the fiducial region of the scintillator fiber target directly. Although the frame was designed to minimize the dead material, it was unavoidable to see a drop in the visible energy if particles passed through it. The variation was estimated with Monte Carlo simulation, and the results were shown in Figure 16.

3.2.8 Supplemental barrel calorimeter: Barrel Veto Liner

Barrel Veto Liner (BVL) was a lead-scintillator sandwich calorimeter; it was newly introduced into the E949 detector to increase the photon detection capability by adding more radiation lengths at the cost of removing the outermost layers 20 and 21 of the Range Stack in E787. From earlier studies [34] the direction of 45 degrees from the beam axis was found to be the

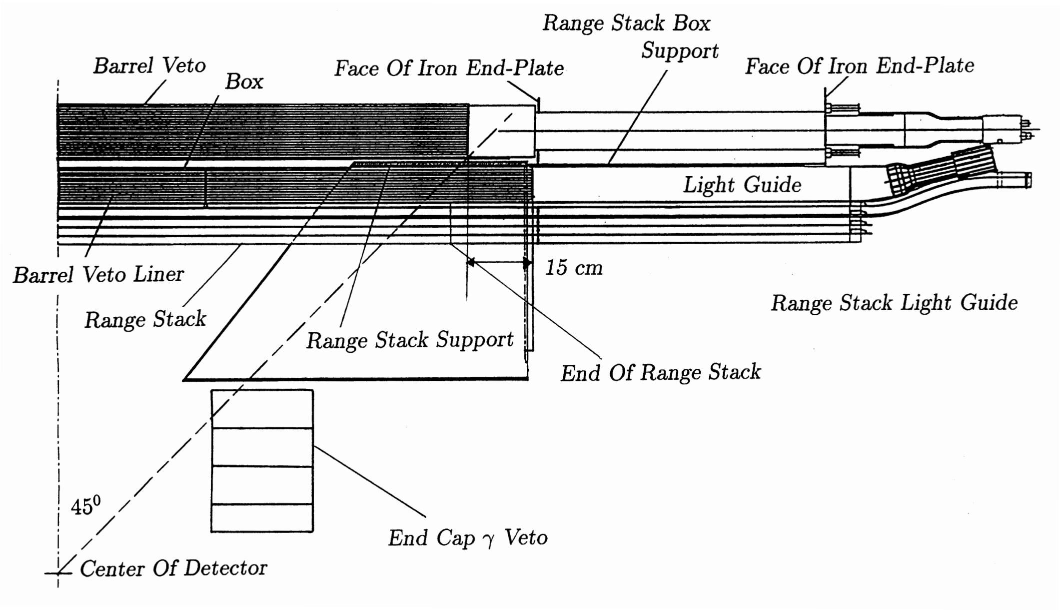

Figure 17: Schematic side view of the Barrel Veto Liner around 45-degree region. The BVL rod was extended to the inner face of the magnet end-plate.

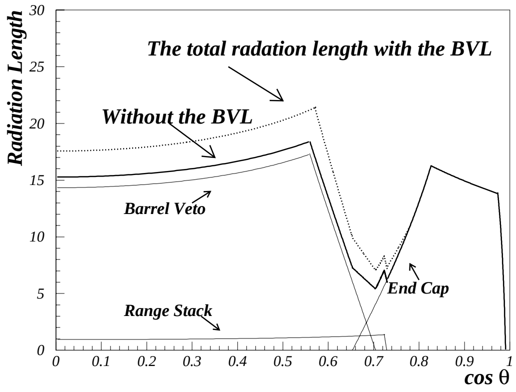

Figure 18: Radiation length with and without the Barrel Veto Liner. Solid line shows the total radiation length without the Barrel Veto Liner (BVL). The radiation length steeply drops at the dip angle θ of $45°$ (around the boundary of Barrel and End region) which corresponds to 0.71 in $\cos\theta$.

region where the total radiation lengths were not enough. The new Barrel Veto Liner had a longer active region (220 cm) in the beam direction, 30 cm longer than the original Barrel Veto.

The Barrel Veto Liner was segmented to 48 sectors in the azimuthal angle; there was only one module in the radial direction. Each module was 220 cm long in the beam direction, 10 cm wide in the azimuthal direction and 7.79 cm high in the radial direction, where 13 plates of 5 mm-thick plastic scintillators (BC403, Bicron Corp.) and 12 sheets of 1 mm-thick leads were stacked alternatively. The total radiation length in the radial direction was 2.29; it increased to 3.2 for the photons emitted in the direction of the $45°$. Since there was no room to attach a light mixer, a 70 cm-long UV-transparent light guide was directory attached to the rod. Also, due to the spatial limitation, the light guide covered only the half area of the cross section of the rod. Signals from PMT at each end were fed to an ADC, a TDC and a TD.

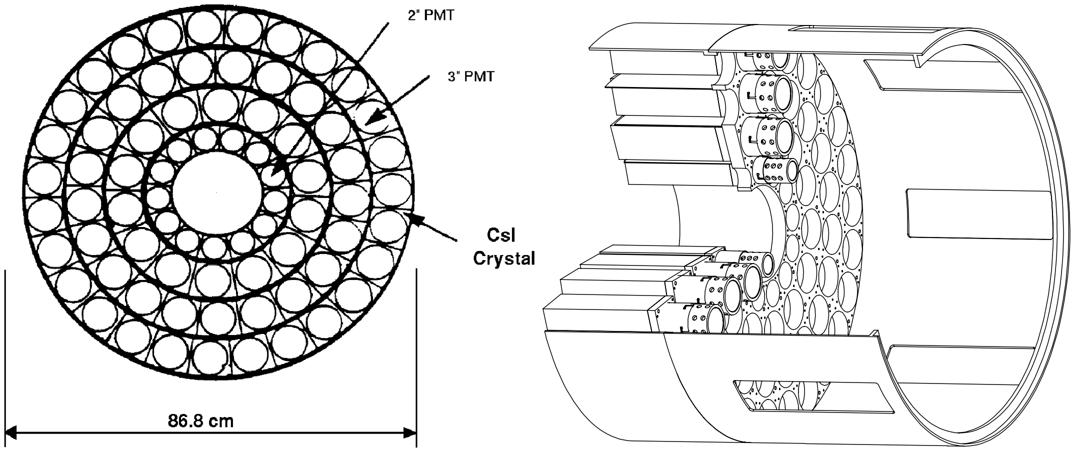

Figure 19: Schematic end view and back view of the End Cap CsI detectors. PMTs were directly connected to the crystals to maximize the light output.

3.2.9 End Cap Calorimeters

The calorimeters covering the outermost region where the opening angle of less than $\pi/4$ from the beam direction are called the "End Caps". Since the regions were exposed to the halo of high intensity beam; the acceptance loss due to the accidental hits might be crucial. Thus, undoped Cesium Iodide (CsI) calorimeters [35] for better timing resolution were used. Larger visible fraction, which is a ratio of the observed energy in the detector to the actual deposited energy, was realized by the full active material of CsI, and resulted in significant improvements in the detection efficiency for low energy photons.

As shown in Figure 2, there were two End Caps located at the upstream and downstream ends of the detector. The upstream End Cap consisted of a cylindrical array of 75 crystals grouped into four rings, which were formed with 13 (the innermost ring), 14, 21, and 27 (the outermost) crystals. The downstream End Cap consisted of four rings where 12, 13, 19 and 25 crystals were used, respectively (see Figure 19).

CsI crystals The CsI ingots manufactured by the Crismatec (Saint-Gobain Ceramics & Plastics Inc. [36]) were cut to a right-pentagonal-polyhedron shape as shown in Figure 20 with a dimension of A = 7.8 $\sim$ 8.0 cm, B = 6.1 cm, C = 25.0 cm (Ring 1) and A = 9.9 $\sim$ 11.2 cm, B = 8.6 cm, C = 25.0 cm (Other rings) for minimization of gaps between each modules in a cylindrical assembly. The scintillators had a density of $\rho = 4.5$ g/cm^3, a short radiation length of 1.86 cm, and the Moliere radius (R_M) of 3.8 cm. They gave good light yields with relatively fast response; their averaged light yield was 255 pe/MeV by a direct PMT readout assuming full photocathode coverage and the quantum efficiency of 16 %. The undoped CsI crystals were known to emit two components of scintillation light with a different time scale. The fast component with the time constant of ~ 45 ns had a peak emission at a wavelength of ~ 310 nm and the slow component (~ 600 ns) had a smaller peak at ~ 450 nm in the wavelength. Fast-to-Total (F/T) factor defined as a ratio of "energy deposit in 100 ns ADC gate"(F) to "energy in 1 μs gate"(T), a representative fraction of the fast component, was found to be around 75 to 90 %, typically 80 %. The slow component was removed for high rate tolerance by a 2.5 mm-thick

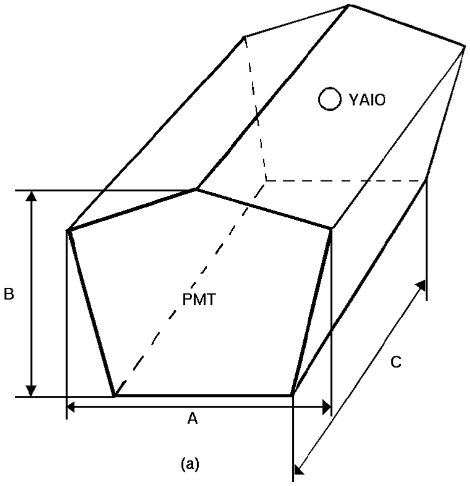

Figure 20: Schematic view of the CsI crystal for the End Cap calorimeters. The crystal was cut to right-pentagonal polyhedron shape for efficient packing in a cylindrical assembly.

UV band pass filter "Kenko U330", whose transmitting band was $230 - 395$ nm (FWHM). It suppressed the slow component an order of magnitude while transmitted ~ 90 % of the fast component.

High field fine-mesh phototubes A fine-mesh phototube [37] developed by Hamamatsu Photonics were attached to the crystal. The PMT had a UV-transmitting glass window and a Bialkali photocathode with a quantum efficiency of 17 % at a wavelength of 310 nm. A diameter of 52 mm (2 in.) tubes were used for smaller crystals in the innermost ring, and 78 mm (3 in.) tubes for others. Both had 19 stages of special dynodes made with a fine Bialkali mesh (1500 wires/in.); this dynode structure allowed operation in a strong magnetic field up to 1 T. The gain drop was significantly reduced, for example, in a $B = 0.96$ T of the E949 axial magnetic field; they kept a gain of $2 - 5 \times 10^5$ corresponding to $1/40 - 1/100$ of a typical gain of 2×10^7 at zero magnetic field. The relative gain as function of magnetic field is shown in Figure 21.

Readout electronics The signal from the fine-mesh PMT was split to three ways. The first output was fed into an 8-bit 500 MHz CCD transient digitizer having a maximum range of 256 ns for multiple hit recognition. The second one was delivered to an 11-bit ADC for energy measurement and the last one was multiplexed with three lines from other PMTs and used for online photon veto in a level 1 trigger logic. The typical pulse shape monitored by the CCD is shown in Figure 22. The fast rising time of 9.9 ns gave a good timing resolution as shown in Figure 23 and the short tail of 44.1 ns helped to reduce a blindness effect brought by an overlapping tail from an earlier hit.

3.2.10 Other ancillary photon detectors

Collar detector was installed to detect photons emitted with a small dip angle θ; it converted $0.970 < |\cos\theta| < 0.997$ in both upstream and downstream regions. The detector consisted of 24 2-mm thick lead sheets and alternatively stacked 25 layers of 5-mm thick scintillator plates of BC404 (Bicron). It provided ~ 9 radiation lengths to the beam direction as shown in Figure 24. The downstream side collar detector was supplemented by a smaller counter called Micro Collar detector.

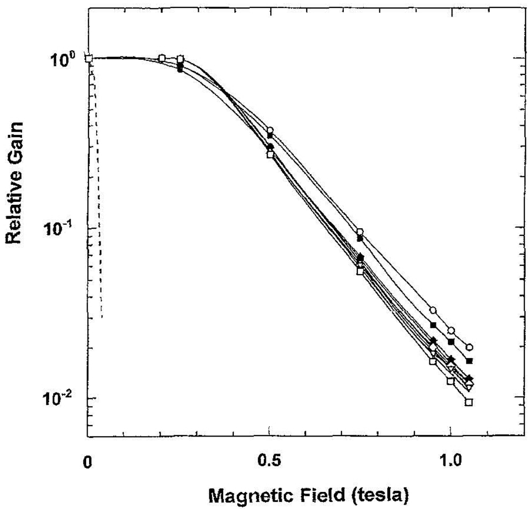

Figure 21: Gain variation of fine-mesh PMTs as a function of magnetic field. The relative gains, normalized by the gain at null magnetic field, as a function of the field parallel to the PMT axis were plotted for a sample of ten 3-in. fine-mesh tubes. Compared with a nominal wire-mesh PMT (shown by a dashed line), the fine-mesh PMTs showed significant improvement.

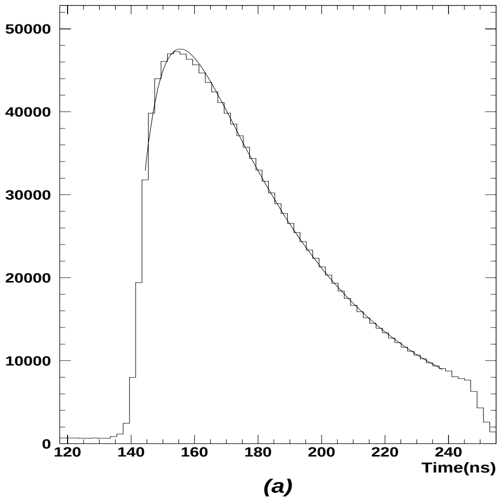

Figure 22: Typical CsI pulse shape recorded with a CCD transient digitizer.

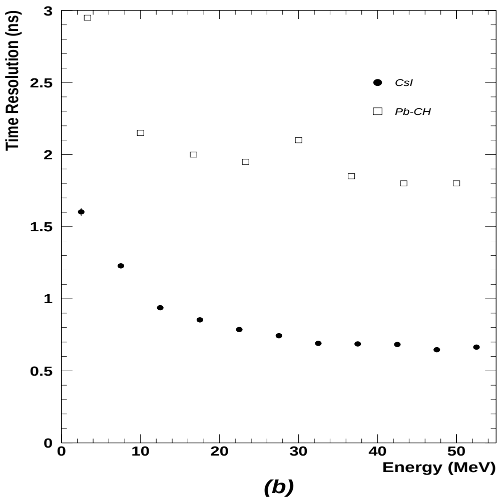

Figure 23: Typical timing resolution (rms) as a function of the energy deposited in the End Cap CsI single module. Solid circles show the End Cap time resolution and open rectangles show that of the obsolete Pb-scintillator sandwich detector.

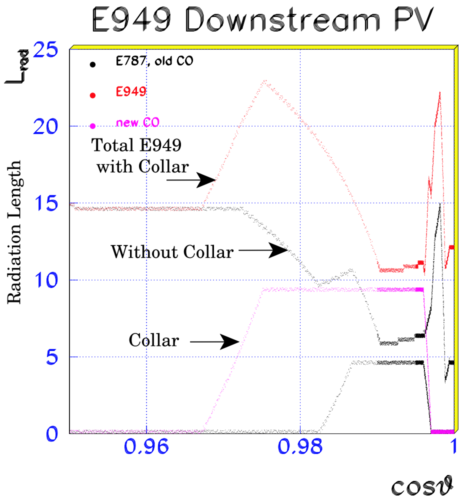

Figure 24: Radiation lengths plotted as a function of $\cos\theta$, where θ is the dip angle from the beam direction. The angle $\theta = 0$ is pointing the beam downstream direction. Collar detector provided ~ 9 radiation length in the region of $0.970 < \cos\theta < 0.995$.

3.3 Trigger and data acquisition system

The E949 trigger consisted of two-stage hardware systems. The first stage, called “level 0”, performed event selection based on *AND* / *OR* logic with discriminated signals from each detector. The next stage, called “level 1”, involved two functions of more complexed hardware processing named “level 1.1” and “level 1.2”.

3.3.1 The level 0 and level 1 trigger systems

The level 0 trigger was a demand for a kaon in the beam followed by a single charged track into the RS. A kaon was identified by a coincidence of hits from the Čerenkov counter, energy-loss counter and target. A charged track was required at this level to have a coincidence of the hits from the I-Counters and the first layer (T-Counter) and second layer in the same RS sector. The trigger made a decision within ~ 38 ns based on the combination of logic signals (the actual combination varied according to the physics mode). When it was satisfied, then the level 1.1 trigger followed; at this stage, dedicated electric circuits selected a π^+ track based on the pulse shape information in the RS stopping counter. It needed additional 10 to 20 μs for judgment. The level 1.2 (explained later) took time up to 100 μs for the decision. The events, which passed this level, were stored with their ADC, TDC, and TD or CCD information.

A unique character of the E949 trigger was that the trigger and DAQ were governed by two different time strobes. The experiment involved kaon decays at rest; since the decay time is different event-by-event, the trigger must wait the kaon decay up to several tens of nano second. Thus, the two strobes were separately required for the counters related to the beam line, and the counters related to the kaon decay products.

3.3.2 Minimum bias trigger

A trigger condition, named $K_{\pi2}(1)$, was installed to collect $K_{\pi2}$ decays with the minimum trigger constraints. The $K_{\pi2}(1)$ trigger actually consisted of logic AND’s of the signals from the discriminators:

$$K_{\pi2}(1) \equiv K_B \cdot T2 \cdot (6_{ct} + 7_{ct}) \cdot \overline{19_{ct}} \tag{8}$$

where K_B was a coincidence of the kaon Čerenkov counter, the B4 Hodoscope counter and the target, ensuring a kaon in the beam. The $T2$ required a coincidence of hits from the first and second layer counters in the same RS sector, demanding the decay product to go into the Range Stack. The term $(6_{ct} + 7_{ct})$ was a requirement of hits either in the layer 6 or 7 in the same Range Stack sector as that of T2. [2] The $\overline{19_{ct}}$ was a requirement for the charged track to stop within the Range Stack by confirming that the layer 19 had no hit. This requirement removed μ^+s from $K_{\mu2}$ decays almost completely.

Figure 25 shows the π^+ range versus momentum plot for the events collected by the $K_{\pi2}(1)$ trigger, where the momentum was measured by the drift chamber and the range by the range counter. The momentum in the figure was corrected for the π^+ loss in the target, and the range was equivalent to the track length in the scintillator. Two bands observed in the plot, caused by

---

[2] The ’+’ symbol indicated *logic-OR*. We defined “N_{ct}” as the N-th layer in the Range Stack has a hit from a charged track (ct).

the dE/dx difference in the RS, was a key to separate π^+ from μ^+ in the experiment. The band with shorter range was originated from π^+s, and was called "pion band". There is a prominent dense spot in the band; the monochromatic π^+s from $K_{\pi 2}$ decays. The tail hanging down from the $K_{\pi 2}$ peak was "$K_{\pi 2}$ range tail", which was caused by multiple scatterings or nuclear interactions of π^+ in the RS. The other band, which was named "muon band", had a dense spot from $K_{\mu 2}$ decays with "$K_{\mu 2}$ range tail" events.

3.3.3 The $\pi^0 \rightarrow \nu\overline{\nu}$ trigger

The $\pi^0 \rightarrow \nu\overline{\nu}$ trigger, denoted as $\pi\nu\overline{\nu}$ in this thesis, was defined as below,

$$\begin{aligned} \pi\nu\overline{\nu} \quad \equiv \quad & K_{\pi 2}(1) \cdot DC \cdot L11 \cdot RNG \cdot NRSSC \\ & \cdot HEX \cdot L12 \cdot \overline{BV} \cdot \overline{BVL} \cdot \overline{EC} \end{aligned} \tag{9}$$

where $K_{\pi 2}(1)$ is from Equation 8. To explain how each trigger condition worked, the background rejection in the pion and muon bands are presented in Figure 26 and 27, where events are projected onto the momentum axis. Each band was defined with the selection criteria of

- $|R - 0.30 \times P + 32| < 4.0$ cm for the pion band
- $|R - 0.38 \times P + 37| < 5.0$ cm for the muon band

respectively, where P represented the momentum and R represented the range.

The "DC" conditions required a delayed coincidence of the I-Counter and the kaon Čerenkov counter; the delay of ~ 2 ns effectively removed prompt beam scattering events coming from π^+s contaminated in the beam. The "L11" was a hardware-based identification of $\pi^+ \rightarrow \mu^+$ decay chain in the π^+ stopping counter. A dedicated algorithm embedded in a custom chip made a decision with the pulse height and area of the waveform recorded in the RS. Smaller ratio of the pulse height over the area indicated a double pulse. The trigger condition accepted the events with smaller ratio, assuming the double pulse came from π^+ decay. Figure 26 and 27 indicated that the L11 had large rejection (~ 10) against muons at a cost of $\sim 50\%$ acceptance loss to pions (compare the solid circle points of the two). Note that the trigger also removed decay-in-flight π^+s or pion-nuclear interaction events by requiring that π^+ came to rest in the stopping counter. The refined range mask "RNG" was another condition to remove $K_{\mu 2}$. The trigger condition made a refined range estimation with a Z hit position in the RS stopping counter (by calculating the end-to-end time difference) with the path length in the target (by counting the number of hits in the target fibers). By rejecting events with significant long range tracks, this condition provided $\sim 10^2$ rejection against $K_{\mu 2}$ with a negligible acceptance loss of $K_{\pi 2}$ as shown by the cross points in Figures 26 and 27. The requirement "NRSSC" was to remove a charged track which stopped within the RSSC, and ensured the particle came to rest in an active region of the Range Stack. The trigger had a 10^3 rejection against $K_{\mu 2}$ peak events (see $P = 236$ MeV/c in Figure 27) with a 50% acceptance loss of $K_{\pi 2}$ (see $P = 205$ MeV/c in Figure 26) collected by the $K_{\pi 2}(1)$ trigger.

The prior upper limit of the $\pi^0 \rightarrow \nu\overline{\nu}$ decay is 8.3×10^{-7}; thus, 10^8 or more π^0s from $K_{\pi 2}$ events must be collected to improve the limit. $\pi^0 \rightarrow \gamma\gamma$ decays were rejected online with the conditions of "$HEX \cdot L12 \cdot \overline{BV} \cdot \overline{BVL} \cdot \overline{EC}$", called online photon veto.

Online photon veto The momentum of the π^+s from $K_{\pi 2}$ decays in the 1 T magnetic field implied the π^+ tracks in the RS were fully contained within one or two adjacent *hextant*s. The events with activities in more than three *hextant*s or separated two *hextant*s have an extra particle other than the π^+. Such events were rejected by the trigger condition denoted as HEX.

The L12 had two components. One of them, called "L11 afterburner" was unrelated to photon veto.[3] The condition rejected events with an accidental hit near the stopping counter because it might defeat the L11 with an artifact double pulse. The other component, which was used for photon veto, rejected an event when the event had hits in both of the two adjacent hextants while the T2 counter and the stopping counter are found in the same hextant. This implied that single hextant fully contained the trajectory and hits, observed in the other hextant, came from an another particle. Since the component dealt with the hextant more refined way, it was called "HEX afterburner".

The "$\overline{BV}$" rejected events if the analog sum of the BV signals was over the discriminator threshold in a given window. The time window was typically ~ 10 ns, which was significantly narrowed from that of 20 ns in the E787 experiment, by introducing Digital Mean-Timer Modules [40].[4] The rejection capability was checked with the "trigger inefficiency" (I_{BV}) which is defined as the ratio of

$$I_{BV} = \frac{N_{\overline{BV}}(E)}{N_{\text{Total}}(E)} \tag{10}$$

where $N_{\text{Total}}(E)$ is the number of entries used in the check, E is the total visible energy in the BV in the time range of ± 5 ns from the kaon decay time. $N_{\overline{BV}}(E)$ is the number of entries, where the BV trigger was not asserted (= $\overline{BV}$). The trigger occupancy is defined as $1 - I_{BV}$. Figure 28 [5] shows the trigger occupancy and inefficiency as a function of the E in the BV. The threshold, which is defined as the point giving 50 % inefficiency, was 5.2 MeV. The "$\overline{BVL}$" rejected an event with the signal sum over the threshold, as in the $\overline{BV}$. The threshold was lowered to be 1.1 MeV. The condition "$\overline{EC}$" was made from End Cap CsI signals. The corresponding threshold was 19.2 MeV. The performance of the online photon veto will be detailed later in the thesis.

3.3.4 Monitor triggers

Monitor triggers to collect control samples were prepared for trigger studies, DAQ performance check, detector calibration and background studies. $K_{\pi 2}(2)$ was defined as

$$K_{\pi 2}(2) \equiv K_{\pi 2}(1) \cdot DC \cdot L11 \cdot HEX \cdot L12 \tag{11}$$

for partial measurement of online photon-veto rejection. The $K_{\mu 2}(1)$ was a trigger to collect $K_{\mu 2}$ sample by requiring charged tracks with longer range as below

$$K_{\mu 2}(1) \equiv K_B \cdot T2 \cdot (6_{ct} + 7_{ct}) \cdot (17_{ct} + 18_{ct} + 19_{ct}) \tag{12}$$

---

[3] The rejection should be subtracted when one measures the rejection of the online photon veto.

[4] Signal arrival time would change depending on the photon z hit position. The timing resolution was determined by the variation of the propagation time in the BV rod. But by constructing the mean time of both ends, the resolution is improved to $\sim$ 10 ns in the online level.

[5] Note that the x axis is "visible energy". Inefficiency due to narrow gaps or photonuclear interactions in dead material can not be seen in the plot, because they might be invisible (*i.e.* visible energy = 0.).

where $(17_{ct}+18_{ct}+19_{ct})$ required a hit at least in one of the layers 17th, 18th, 19th in the Range Stack. The data were used for photon-veto acceptance measurement because $K_{\mu 2}$'s should have no activity other than single μ^+. Beam pions scattered into a detector (denoted as π_{scat}) were also collected by

$$\pi_{scat} \equiv \pi_B \cdot \overline{DC} \cdot T2 \cdot (6_{ct} + 7_{ct}) \cdot HEX \cdot \overline{BV} \cdot \overline{BVL} \cdot \overline{EC} \qquad (13)$$

where π_B is a requirement of coincident hits in the pion Čerenkov counter, the B4 hodoscope and the target fiber. The delayed coincidence requirement (DC) was inverted to collect prompt timing events.

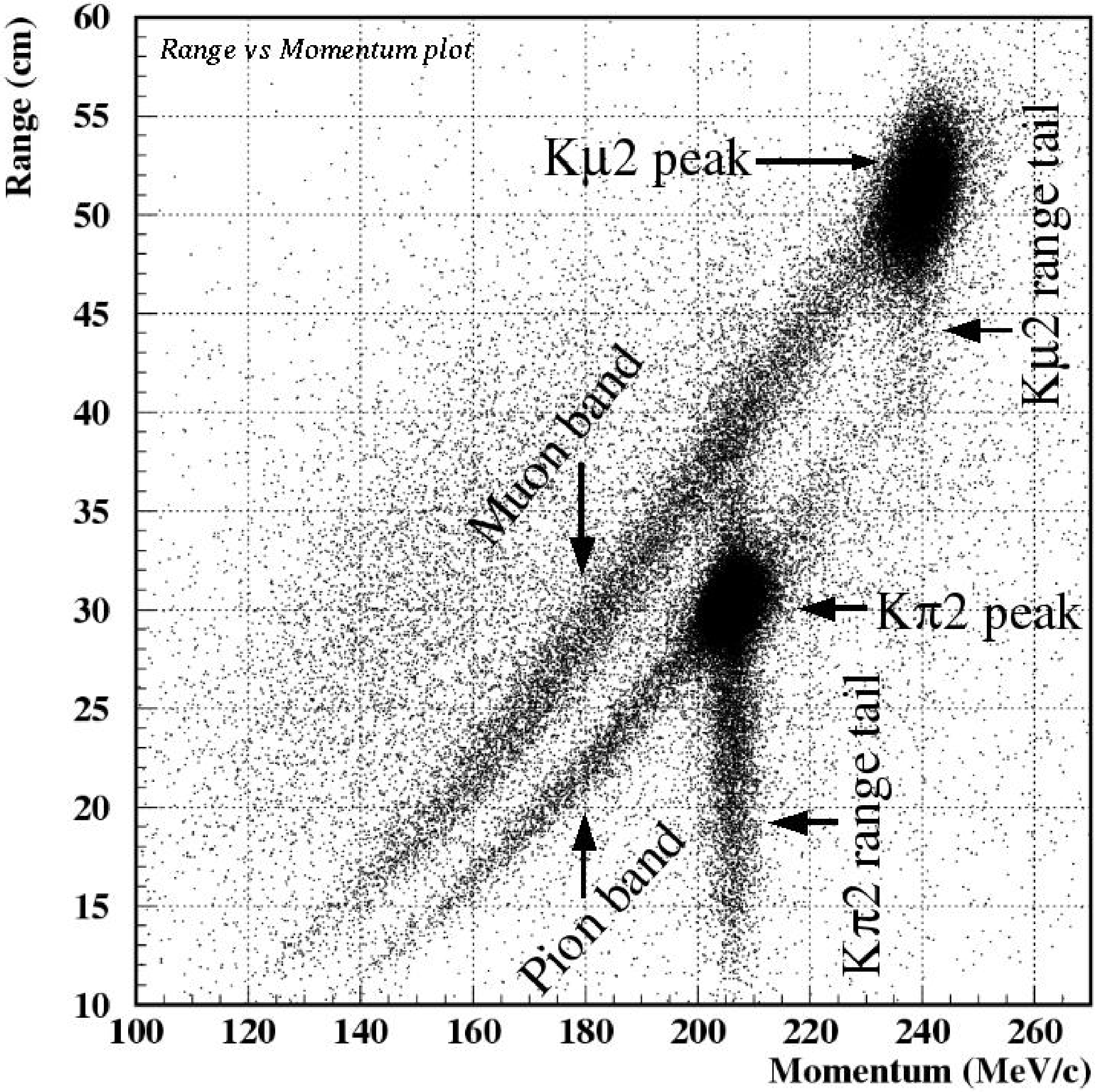

Figure 25: Range versus momentum distribution of the events collected by the $K_{\pi 2}(1)$ trigger. The band of events with longer range in the same momentum was made of μ^+ samples and called "muon band". The band of events with shorter range was from π^+s and called "pion band".

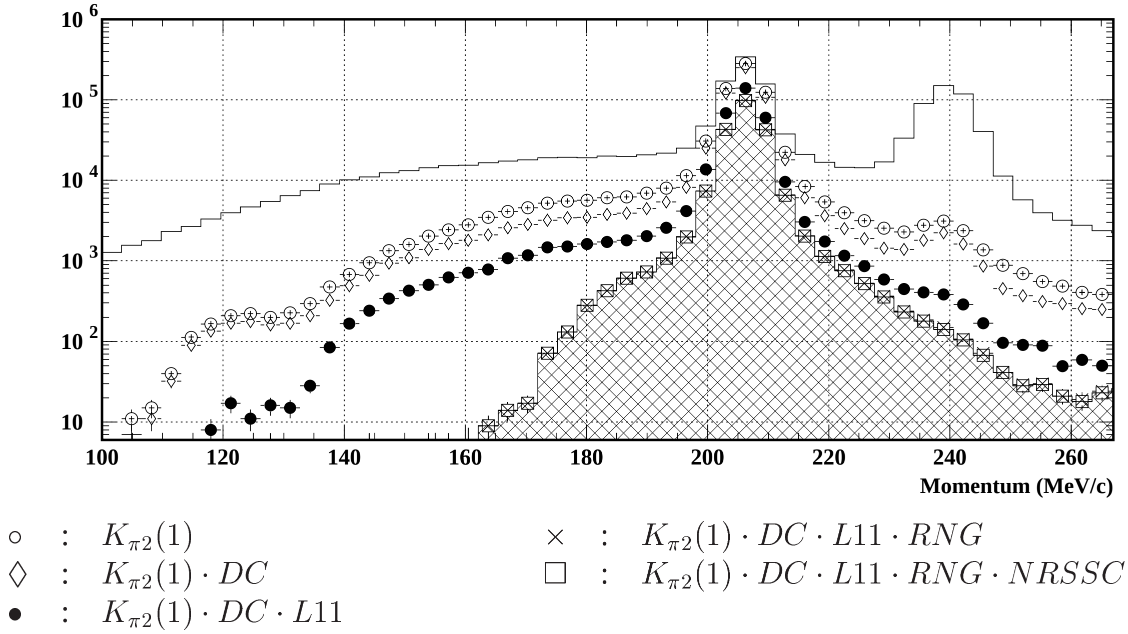

Figure 26: Momentum distributions of the pion-band events with $\pi\nu\overline{\nu}$ trigger conditions imposed sequentially. The open histogram is a projection of the events in Figure 25 to the momentum axis, and each symbol is the same distribution with the specific condition(s). The hatched histogram shows the momentum distribution of the events collected by the $\pi\nu\overline{\nu}$ trigger without photon-veto trigger conditions.

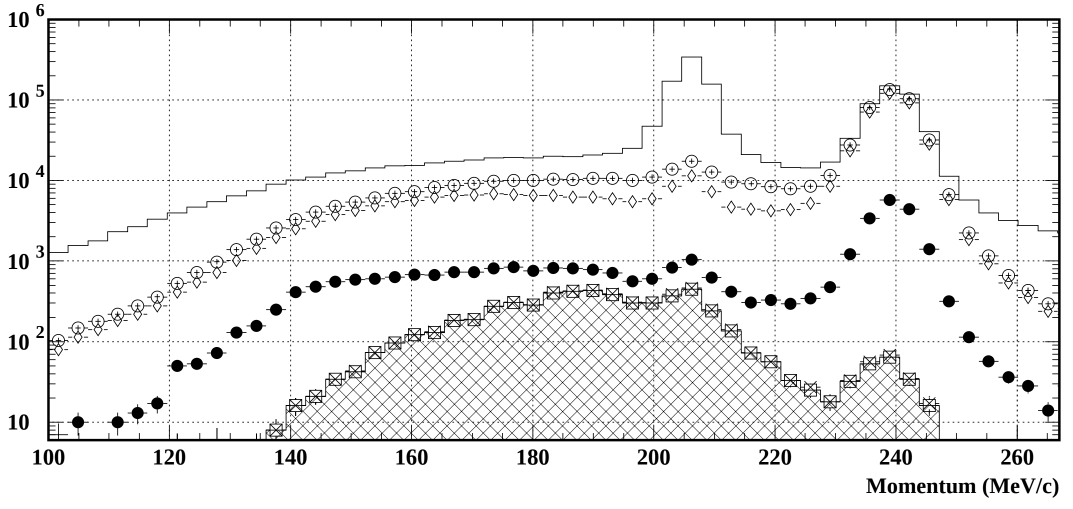

Figure 27: Momentum distributions of the muon-band events with $\pi\nu\overline{\nu}$ trigger conditions imposed sequentially. The open histogram is a projection of the events in Figure 25 to the momentum axis, and each symbol is the same distribution with the specific condition(s). The symbol definitions are in Figure 26. The hatched histogram shows the momentum distribution of the muon band events in the $\pi\nu\overline{\nu}$ data set without photon-veto conditions.

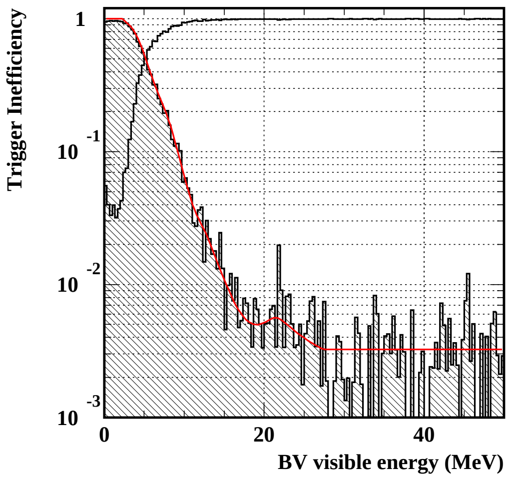

Figure 28: Inefficiency of the online BV condition as a function of energy sum observed in the BV (visible energy) within ± 5 ns around the kaon decay time. The hatched histogram is the inefficiency and the open histogram is the trigger occupancy. The energy threshold which gave 50% hit occupancy was 5.19 MeV. The red line shows the fitting curve to the inefficiency histogram.

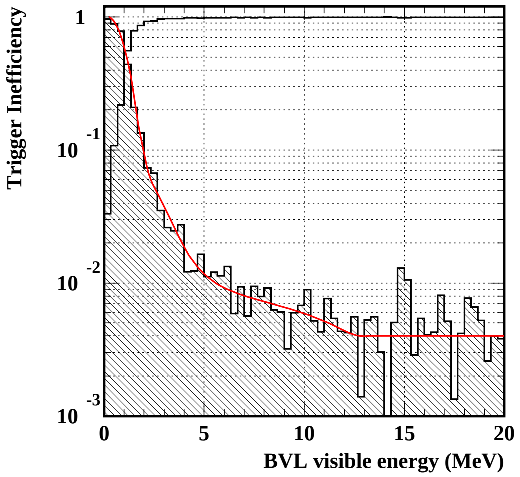

Figure 29: Inefficiency of the online BVL condition as a function of visible energy in BVL within ± 5 ns around the kaon decay time. The hatched (open) histogram is the inefficiency (trigger occupancy). The energy threshold was 1.14 MeV. The red line shows the fitting result to the inefficiency histogram.

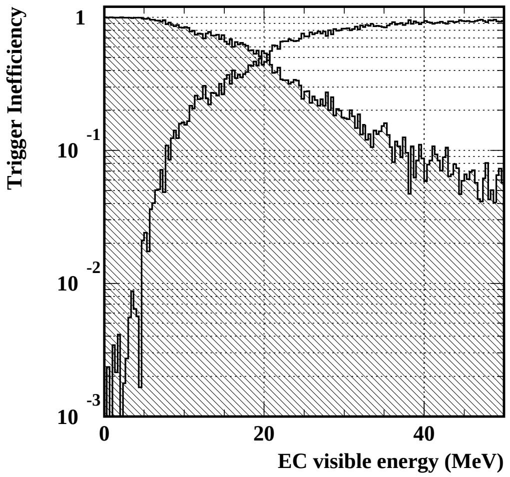

Figure 30: Inefficiency of the online EC condition as a function of visible energy in EC within ± 5 ns around the kaon decay time. The hatched (open) histogram is the inefficiency (trigger occupancy). The energy threshold was 19.19 MeV.

Table 11: Summary of running conditions and data acquisition.

Run condition		
AGS proton momentum	21.5 GeV	
Number p^+ per spill on target	4.7×10^7	(average)
AGS spill length	2.2 sec	
Spill duty factor	41 %	
Total running hours	1600 hr	
Average "beam on" fraction	81 %	
Average "DAQ live" fraction	87 %	
K^+ momentum	710 MeV/c	(at LESBIII)
K to π ratio	3 - 4	(depend on separator)
Number of K^+ per spill	12.8×10^6	(at Čerenkov counter)
Number of K^+ accumulated	1.8×10^{12}	(in the stopping target)
Data acquisition		
Trigger type	# events	Data size (GB)
$\pi\nu\overline{\nu}$	1.4×10^8	7000
$K_{\pi 2}(1)$	4.3×10^6	295
$K_{\pi 2}(2)$	2.7×10^6	262
$K_{\mu 2}(1)$	1.0×10^7	721

3.4 A summary of data acquisition and running conditions

The E949 experiment was originally approved by the U.S. Department of Energy's Division of High Energy Physics to run for 60 weeks, concurrent with RHIC [39] operations, over three years from U.S. FY2001 to FY2003. However, the experiment was forced to finish in 12 weeks. This analysis was based on the data collected in the period of April 24 to June 9 in 2002, by removing some earlier runs for trigger tuning.

The E949 detector worked well in the physics run, but the beam line condition was not optimal. Occasional discharge in electro-static separators required to lower the high voltage, which caused a worse K^+ to π^+ ratio. Shorter spill length at the beam extraction caused negative effects on efficient data collection due to dead time. The data acquisition (DAQ) itself ran smoothly, without any crucial trouble, even though the beam intensity was two times higher than that of the E787, thanks to a successful update of triggers [40] for rate tolerance. Table 11 is a summary of running conditions and data acquisition. The experiment accumulated 1.8×10^{12} kaons in the target. The data accumulation is presented in Figure 31.

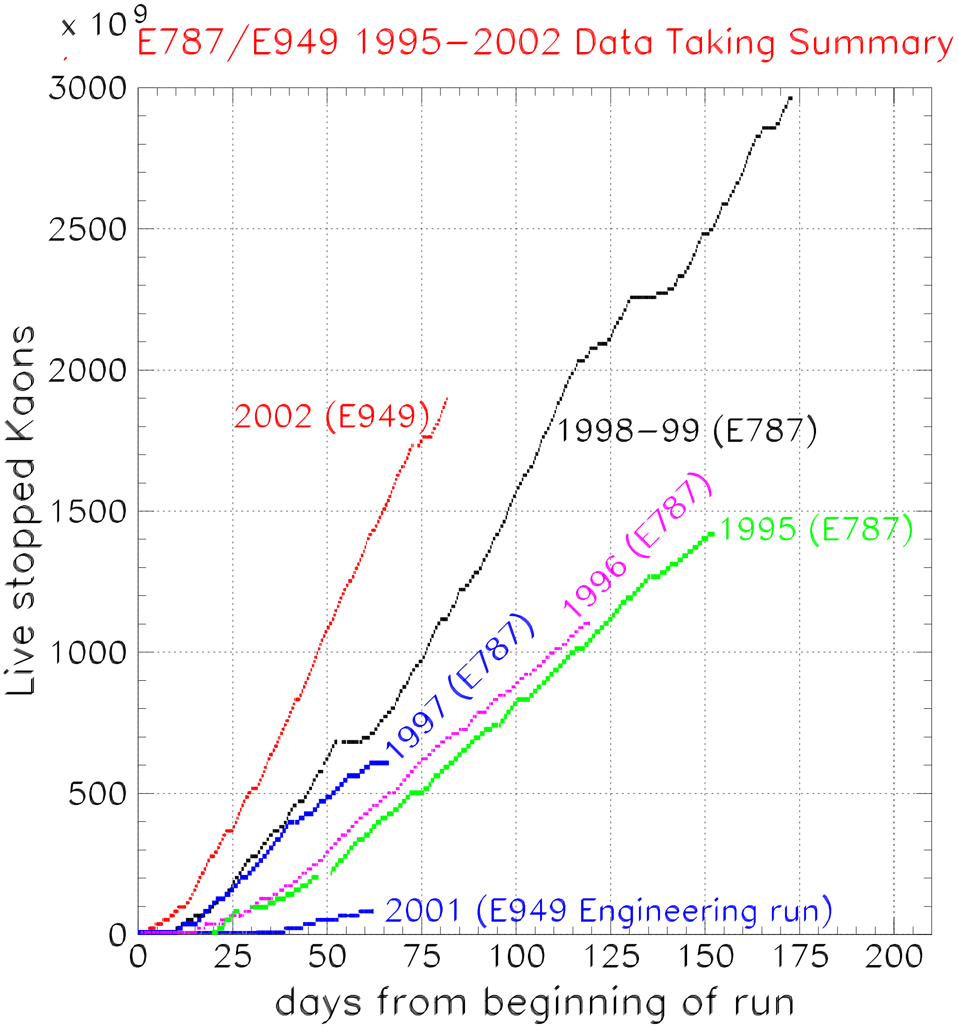

Figure 31: Number of stopped kaons accumulated while the data acquisition systems was alive, plotted as a function of running days.

4 Data Analyses

4.1 Overview of data analyses

A brief description of the analysis procedures is explained in this section. The E949 FY-2002 runs recorded 140 millions of $\pi^0 \rightarrow \nu\overline{\nu}$ triggers to 575 DLT tapes including other monitor triggers. First of all, the data were skimmed out according to the trigger bit in the process called "pass0". In the next stage named "pass1", the energy, momentum, and other kinematic variables of the charged track were obtained by a reconstruction routine. The reconstructed events were examined with some loose selection criteria and apparent background events were discarded. In the last stage named "pass2", the final selection criteria were imposed and the results were used for the physics analysis. In the subsequent sections, we explain (1) how the events were reconstructed and (2) what kinds of analysis methods and techniques were taken. After that, we describe (3) criteria for high-purity $K_{\pi2}$ event selection, and (4) methods for reliable background estimation without depending on Monte Carlo simulation. We explain (5) criteria for the best photon rejection to maximize the event sensitivity, and (6) the final results after opening the signal region.

4.2 Event reconstruction

The process of event reconstruction was composed of three stages : (1) kaon reconstruction with beam detectors, (2) reconstruction for charged tracks from a kaon decay and (3) π^+ identification in the stopping counter. In some studies, (4) photon reconstruction in the photon detector systems was included.

4.2.1 Kaon reconstruction

In the kaon reconstruction, kaon hit times in the Čerenkov counter, BWPC1-2, B4 hodoscope were reconstructed and the energies in the B4 hodoscope were summed for the $K-\pi$ separation. The B4 hit position was employed for a check of matching quality with the kaon decay vertex in the target. For rejection of multi-beam backgrounds, hits were examined around kaon decay time with a double pulse fitting routine.

4.2.2 Charged track reconstruction

A charged track from kaon decay was reconstructed in the target, drift chamber and Range Stack, making a contact with each other. The schematic view of a reconstructed event is shown in Figure 32.

Track reconstruction in the drift chamber The trajectory of a charged track was firstly reconstructed in the drift chamber. A circle fit to anode-wire hit positions with iterations was performed until the χ^2 of the fitting was minimized. After a candidate trajectory in the X-Y plane was obtained, a track fitting in the R-Z plane was performed with a linear fit to the hit

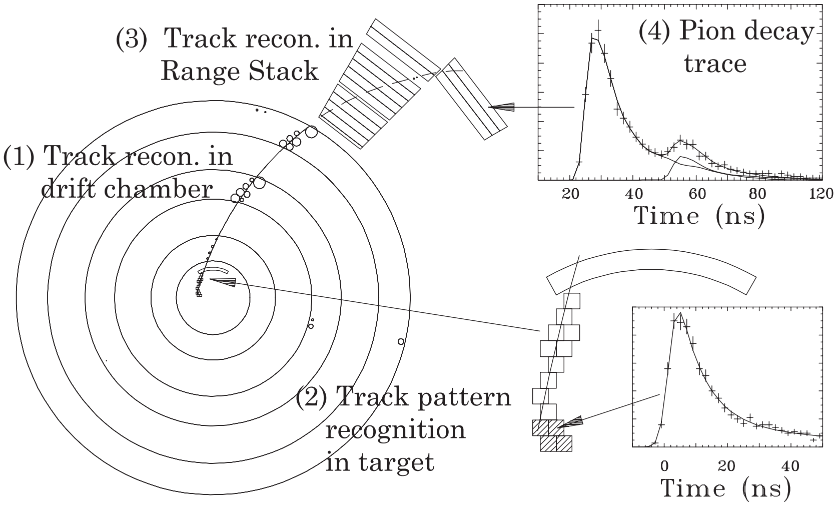

Figure 32: Example of a reconstructed event. A particle trajectory was reconstructed with the target, the drift chamber and the Range Stack. The pion decay sequence was searched in the particle stopping counter.

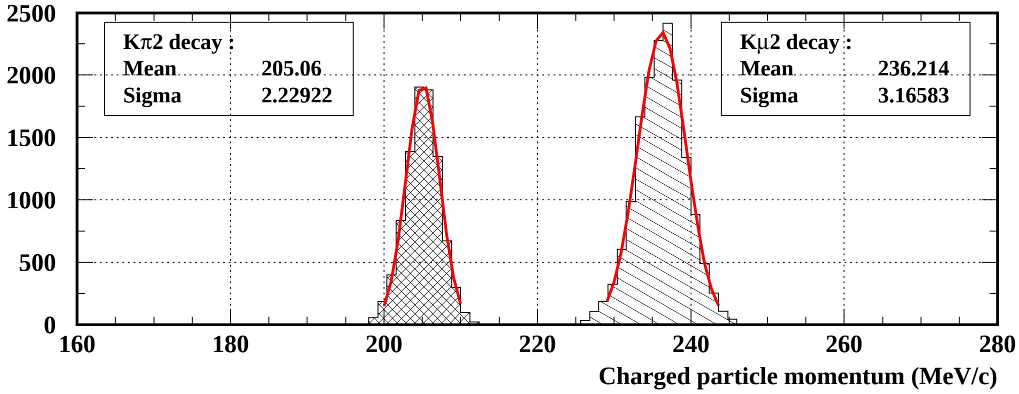

Figure 33: Distribution of the reconstructed total momentum of $K_{\pi 2}$ and $K_{\mu 2}$.

position in the helical strips on cathode foils.[6]

Track recognition in the target The candidate track in the drift chamber was extrapolated to the target. The intersection provided an initial point of the pattern recognition. The fibers, where a pion passed through, were named as *pion fiber*s. All the hits in the target were categorized into three as, kaon, pion and photon hits from the energy and timing characteristics using a likelihood technique. The average times of the pion fibers were regarded as the kaon decay time. By double-pulse fitting to the waveform of the target fiber at the kaon decay vertex, the pion energy in the fiber was extracted. By summing up all the energy in the pion fibers and the extracted energy, total energy deposit of the charged product was obtained. The pion fibers were

---

[6] The track in the X-Y plane must be determined before this R-Z fit. Since the cathode strips are running in a helical way, without X-Y hit positions, there is no way to determine the z-position.

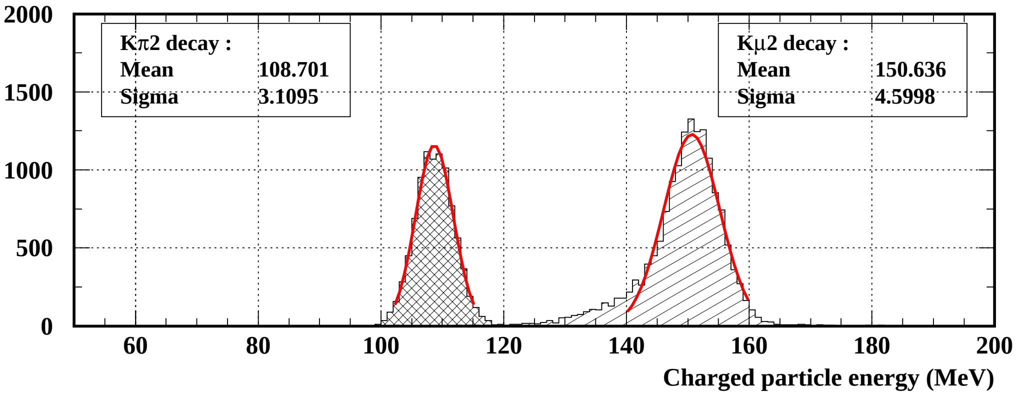

Figure 34: Distribution of the reconstructed total energy of $K_{\pi 2}$ and $K_{\mu 2}$. The $K_{\mu 2}$ events had a lower tail in the distribution; this was due to the events in which the muon did not come to rest in the Range Stack.

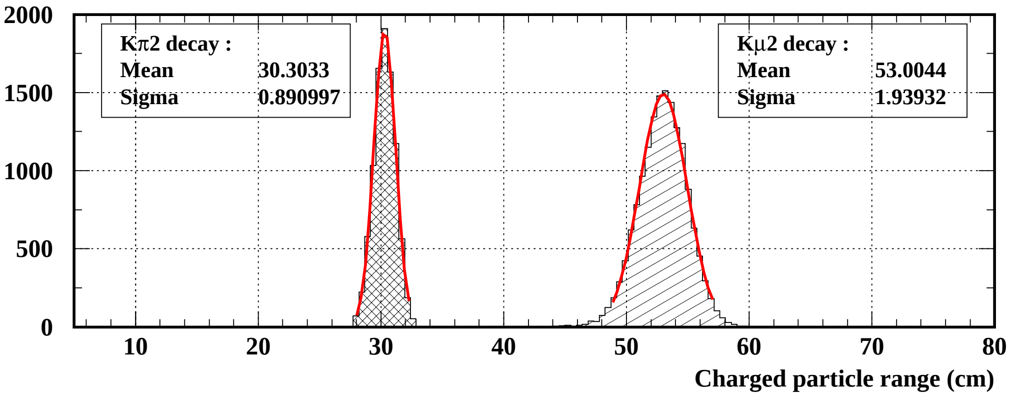

Figure 35: Distribution of the reconstructed total range of $K_{\pi 2}$ and $K_{\mu 2}$.

fitted to a circle, in the same way as the drift chamber, and the path length was computed. Hits of the fibers that neither belonged to the kaon track nor pion track were recognized as hits due to the electromagnetic shower of the photon or extra particles from the kaon decay. They would be analyzed by a routine for hermetic photon detection. After the target pattern reconstruction was performed, track fitting in the drift chamber was performed once again with the information of the pion fibers to improve the matching.

Track reconstruction in the Range Stack Track reconstruction in the Range Stack started with a search for coincident hits in the innermost two layers in the same sector called T·2. Then, it was checked if the adjacent counter in the clockwise direction[7] had a hit at the prompt timing. If there, the adjacent counter was assigned as a track counter, and if not, further search for a hit in the one outer layer in the original sector was performed. This algorithm continued whenever a hit counter was found and until no candidate was found. The outermost and the most clockwise

---

[7] The positively charged particle is bent to the clockwise direction by the magnetic field.

counter was assigned as the stopping counter, where a pion decay at rest should be recorded. At this point, it was not certain whether the decay occurred after the pion came to rest or it occurred in flight; the $\pi^+ \to \mu^+ \to e^+$ decay sequence was confirmed in the counter. The time of the charged track in the Range Stack (track time) was calculated from the hits by averaging their timing. The total energy was obtained by summing up their energy with a correction of muon kinetic-energy in the pion stopping counter[8].

Track fitting in the X-Y plane was performed by using the information of sector-crossing points, if existed, and the RSSC hits with a circle. A Monte Carlo-based track propagator found the best track giving the minimum χ^2. Fitting in the R-Z plane was performed separately, as in the drift chamber, with the information of the end-to-end time difference in each counter. Involving the extrapolated track from the drift chamber and RSSC Z information, a linear fit was performed and the best track was determined.

Total momentum, energy and range The total kinetic energy of a charge track was reconstructed by summing up all the energy in the target, I-Counter and Range Stack with corrections of expected energy-deposit in the gas volume and foils of the drift chamber. The total range[9] was reconstructed by adding the ranges in the target, I-Counter and Range Stack with corrections of the inactive material along the path of the particle. The total momentum was calculated by a track curvature in the drift chamber with corrections of the energy loss in the target, I-Counter, and other material along the path. The calibration and performance were checked by the reconstructed momentum, energy and range of the monochromatic decay products from two-body decays $K_{\mu 2}$ and $K_{\pi 2}$. Figure 33, 34 and 35 are the reconstructed momentum, energy and range distributions and Table 12 is a list of the resolutions (in rms).

Table 12: Summary of the resolutions in the kinematics reconstruction.

Measurement	$K_{\pi 2}$		$K_{\mu 2}$	
	peak	resolution	peak	resolution
momentum	205 MeV/c	1.1 %	236 MeV/c	1.3 %
energy	109 MeV	2.9 %	151 MeV	3.1 %
range	30 cm	2.9 %	53 cm	3.6 %

4.2.3 Identification of pion decay at rest

The sequence of pion decay at rest in the stopping counter

$$\pi^+ \to \mu^+ \ \nu_\mu \tag{14}$$

$$\mu^+ \to e^+ \nu_e \overline{\nu}_\mu \tag{15}$$

was identified by the triple pulses induced by the pion itself, a muon appearance and a positron from the muon decay at rest, in order to discard the events of pion decay in flight, which would

---

[8] The muon kinetic energy was contained in the given ADC gate (100 ns window), because π^+ lifetime is short. On the other hand, positron kinetic energy from the muon decay was not contained because of the longer lifetime of μ^+.

[9] equivalent to the flight range in plastic scintillator

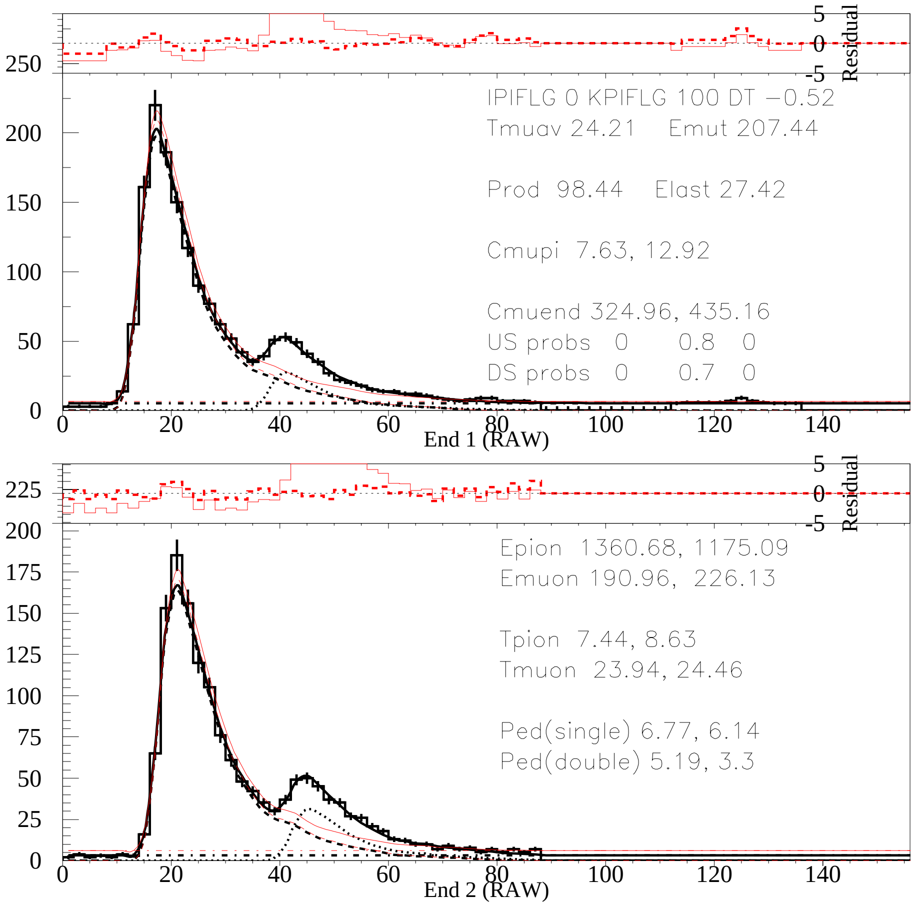

Figure 36: An example of $\pi^+ \to \mu^+$ decay sequence fit. The waveform in the upper plot is from the downstream PMT (End 1). That of the lower plot is from the upstream PMT (End 2).

cause range mis-measurement, and to reject muon backgrounds. The muon kinetic energy from the $\pi^+ \to \mu^+\nu_\mu$ decay at rest was monochromatic and 4.2 MeV. The corresponding muon range in plastic scintillator was around 1 mm. The positron appearance should be observed in the same stopping counter. The kinetic energy of the positron ranged from 0 to 53 MeV, and it usually runs through some adjacent counters. Since the pion lifetime is 26 ns, the muon signal tended to overlap a large signal from the pion dE/dx energy loss. For the $\pi^+ \to \mu^+$ decay search, both of double-pulse and single-pulse fittings, using a template pulse shape, were performed to the waveform recorded by the 500MHz transient digitizers with the pion decay time and muon kinetic energy as free parameters. Figure 36 illustrates the fitting. If the χ^2 of double-pulse fitting was significantly better than that of single-pulse fitting, the pulse was judged to be composed of two pulses. The distribution of the ratio of single-pulse fitting χ^2 over double-pulse fitting χ^2 is shown in Figure 37. The fitter extracted the $\pi^+ \to \mu^+$ decay time (Figure 38), muon energy (Figure 39). The average of observed muon energy was 3.1 MeV, which was understood by a saturation effect of scintillators due to large energy deposit from a stopping pion. This was corrected with the Birks constant [41] .

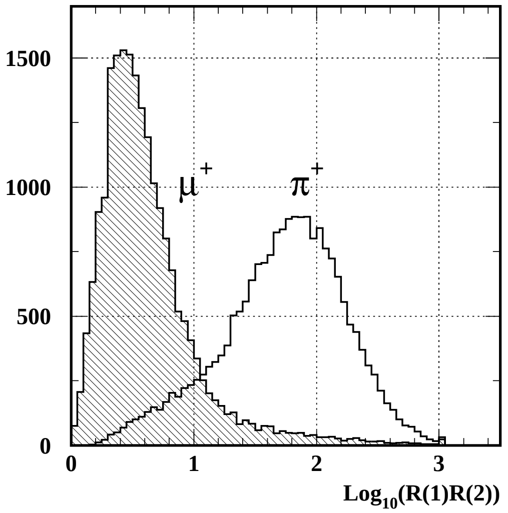

Figure 37: Distribution of the ratio of χ^2's for the single and double pulse fittings. R(i) is defined as the ratio, where i = 1 for downstream and i = 2 for upstream ends. The open histogram was produced with kinematically tagged $K_{\pi 2}$ events, and the hatched one was from $K_{\mu 2}$ events.

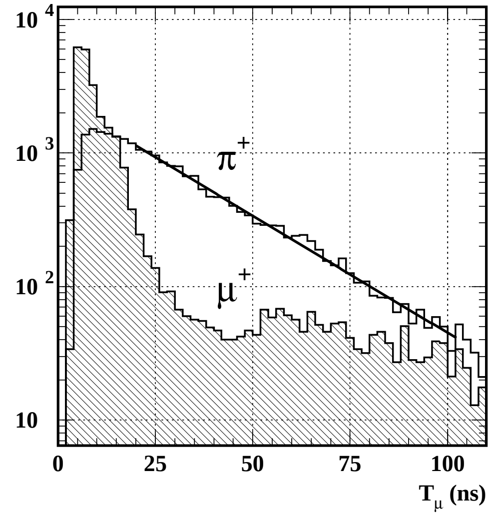

Figure 38: Distribution of $\pi^+ \rightarrow \mu^+$ decay time by double pulse fitting. The open histogram was produced with $K_{\pi 2}$ events, and the hatched one was from $K_{\mu 2}$ events. Both were kinematically tagged. In the $K_{\pi 2}$ sample, pion decay time of 25 ns was obtained. In the $K_{\mu 2}$ sample, second pulses were extracted from tail fluctuations of muon stopping dE/dx.

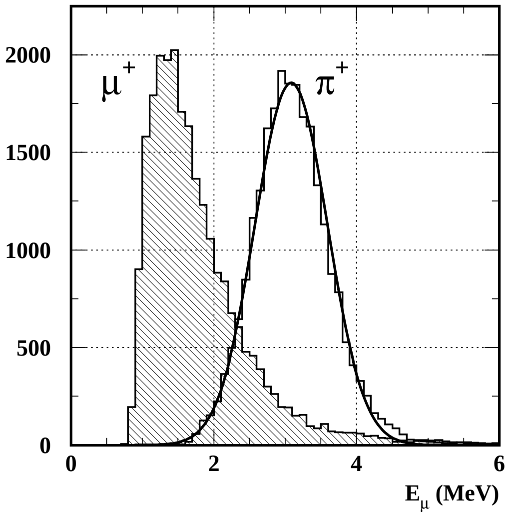

Figure 39: Distribution of muon kinetic energy. The open histogram was from $K_{\pi 2}$ events and the hatched was $K_{\mu 2}$. In the $K_{\pi 2}$ sample, a peak was at 3.1 MeV and the sigma was 0.5 MeV.

4.3 Analysis strategy

The measurement of the $\pi^0 \to \nu\overline{\nu}$ branching ratio was composed of two stages of analysis: (1) π^0 tag by selecting $K_{\pi 2}$ events with sufficient purity, and (2) maximization of photon detection capability to remove the $\pi^0 \to \gamma\gamma$ backgrounds, with parameter tuning for the best sensitivity to the $\pi^0 \to \nu\overline{\nu}$. Throughout the analysis, we set two rules; (A) the candidate events in the signal region should not be examined until the analysis is finished, and (B) developments and tunning of the selection criteria (cuts) must be made with one third portion of the data uniformly sampled from the whole data ("1/3 sample"). The remaining two-third sample ("2/3 sample") is kept untouched for an independent measurement of backgrounds. The analysis procedures were determined as follows.

1. $K_{\pi 2}$ event selection

   The monochromatic π^+ from the $K_{\pi 2}$ decay was selected to tag π^0 in the detector.

   (a) Diagnosis of none-$K_{\pi 2}$ background sources (1/3 sample)

   By listing up possible background sources from particles in beam line (kaon and pion) or from kaon decays, it was studied that how the particles became background candidates with the signature of the $\pi^0 \to \nu\overline{\nu}$, and considered that what kind of cuts were effective to the rejection.

   (b) Establishment of the $K_{\pi 2}$ selection criteria (1/3 sample)

   $K_{\pi 2}$ selection criteria were developed based on the diagnosis with the 1/3 sample. The criteria were optimized with control samples and/or the 1/3 sample. The cut positions were determined based on the background estimation with the 1/3 sample. Once the criteria were established, their parameters were fixed in the following steps.

   (c) Measurement of the tag impurity (2/3 sample)

   The number of backgrounds was measured with the 2/3 sample. Measurement with independent sample made the estimation more reliable, and helped to avoid underestimation from over-tuning in the cut optimization.

   Since we did not expect all the types of backgrounds, in particular "pathological events" (described later), could be reproduced by Monte Carlo simulation. Background measurements had to be made with real data using a special technique named "bifurcation method". (This will be explained later.)

2. Maximization of photon detection capability

   We sought the most effective criteria to reject predominant decays $\pi^0 \to \gamma\gamma$ and $\pi^0 \to e^+e^-\gamma$ in the $K_{\pi 2}$.

   (a) Scanning of the parameters in the photon detection cuts to find the optimum rejection (1/3 sample)

   Measurements of the background rejection and signal acceptance were made simultaneously in every parameter set. A profile curve, which consisted of the best rejection at every given acceptance, was produced (as illustrated in Figure 58 on page 86). The profile curve shows a trade-off between rejection gain and acceptance loss, and plays an important role in deciding the final selection criteria. All the cuts were determined at this point and were not changed anymore.

(b) Count the number of candidate events in the signal region. (2/3 sample)

After applying the photon rejection cut, the events in the signal region were examined. By checking the properties of the candidate events, we made sure they were not artifact due to a loop hole of the analysis. We calculated the branching ratio or upper limit of the decay $\pi^0 \to \nu\overline{\nu}$.

4.4 High purity $K_{\pi 2}$ event selection

4.4.1 Background source diagnosis

Many types of background events can arise from kaon decay, beam particles and other miscellaneous reasons.

Kaon backgrounds Among various kaon-decay channels, the most possible and the most crucial one is the $K_{\mu 2}$ decay. Since the $K_{\mu 2}$ has no activities other than μ^+ in the final state, if the μ^+ is misidentified as the π^+ from $K_{\pi 2}$, the event passes all the photon rejection cuts and fakes the signal signature. Precise momentum, energy and range measurements of the charged track suppress the background. Even when a scattering in material lowers the kinematics of μ^+, the identification of the pion decay rejects the muon background. The $K_{\mu 2}$s are, therefore, suppressed by at least two independent cuts. The radiative decay $K^+ \to \mu^+\nu\gamma(K_{\mu 2}\gamma)$ is another candidate. Since the $K_{\mu 2}\gamma$ has one photon in the final state, the possibility that the $K_{\mu 2}\gamma$ events survives the selection criteria and regarded as the $K_{\pi 2}$ decay with $\pi^0 \to \nu\overline{\nu}$ is much smaller than the possibility of the $K_{\mu 2}$ events.

Backgrounds arise from neutral kaon decay generated via a charge exchange (CEX) process, $K^+n \to K^0_L p$. One of such backgrounds is $K^0_L \to \pi^+ l^- \overline{\nu}_l$, where l^- indicates negative charged lepton (e^-, μ^-). A schematic view of the event is shown in Figure 40. If the charged lepton escapes away to the beam direction, it is recognized as a signal when the pion kinematics satisfies the selection criteria. Confirmation of no spatial gap between the pion fibers and the kaon fibers at the kaon decay vertex is one way to remove the background. However, if K^0_L decay occurs right after the CEX reaction, it does not make the gap. In this case, such events can be rejected by requiring delayed coincidence between the kaon and pion fibers. These are summarized in Table 13.

Beam backgrounds Single charged pion in the beam, scattering into the detector acceptance, becomes a signal candidate ("single beam background"), as shown in Figure 41. The π^+ tracks of this background broadly distribute in momentum phase space. If the events are located around the $K_{\pi 2}$ kinematics region, the final state exactly meets to the event signature of "π^+ + nothing". Stringent beam-particle identification suppresses the background, but secondary π^+s from kaon decays in flight are unavoidable (see Figure 42). A requirement on the time difference between pion fibers and kaon fibers[10] can reject the scattering event. However, two (or multiple) beam particles can defeat the requirement when the first particle makes the kaon

---

[10] This time, kaon hits are mimicked by a pion

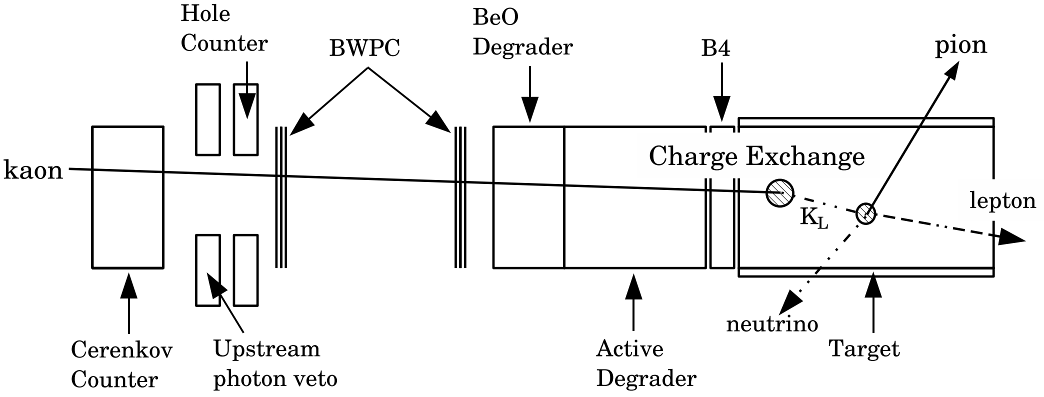

Figure 40: Illustration of a charge exchange background. This event has the same signature as $\pi^0 \to \nu\overline{\nu}$ if the charged lepton is undetected.

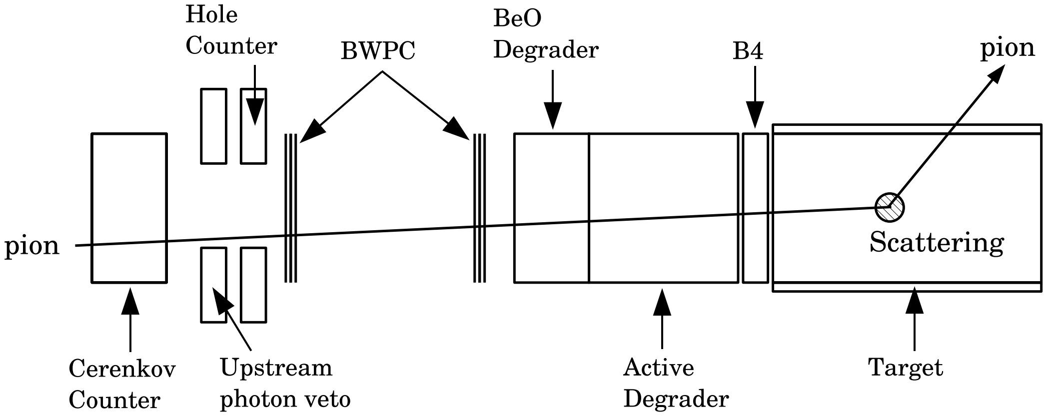

Figure 41: Illustration of a single pion background event. π^+ in kaon beam is scattered by target materials and observed in the detector.

time and the next particle makes the pion time ("two-beam background"). Suppose that a kaon comes to rest in the target but another π^+ comes into the target before the kaon decays. This events gives the $\pi^0 \to \nu\overline{\nu}$ signature as shown in Figure 43. To discard such backgrounds, any hit around the pion time should be examined in all beam counters. Beam wire chambers, which have smaller spatial granularity, make sure the entering particle is only one.

Other backgrounds Some backgrounds may arise from a hardware problem or a loophole in the selection criteria, or pathological events which we do not think about. Those events are rare and may not be found in the background studies, hiding behind more dominant backgrounds. We have a technique to find them out by extending a "bifurcation technique", as described in the section 4.4.2.

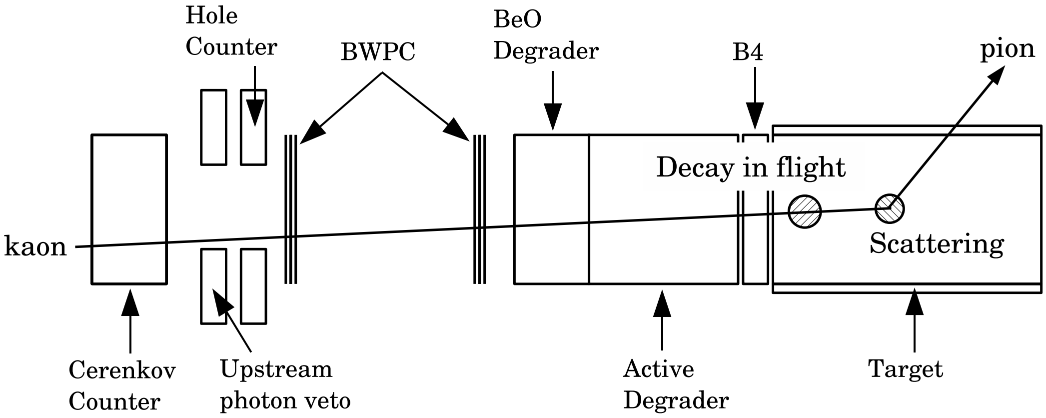

Figure 42: Illustration of a single pion beam background involving kaon decay-in-flight in the beam line.

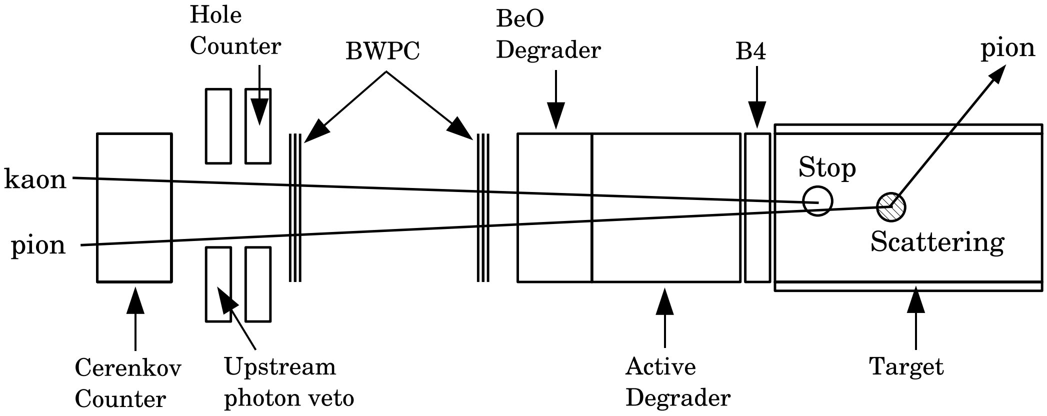

Figure 43: Illustration of a two-beam background.

Table 13: Background sources in the $K_{\pi 2}$ event selection. The check mark "$\surd$" indicates that the cut is effective to the background. Abbreviations include KIN : kinematics cuts with range versus momentum relation, PID(RS) : particle identification with $\pi^+ \to \mu^+ \to e^+$ sequence trace in the RS stopping counter, BTIME : Beam activity around kaon decay time, BMULTI : multiple particles in beam line, PID(beam) : beam particle identification with Čerenkov and B4 dE/dx, DC : time difference between kaon fibers and pion fibers in the target.

Background	KIN	PID(RS)	BTIME	BMULTI	PID(beam)	DC	gap
(1) Kaon decay category							
$K^+ \to \mu^+\nu_\mu$	$\surd$	$\surd$					
$K^+ \to \mu^+\nu_\mu\gamma$	$\surd$	$\surd$					
CEX, $K_L \to \pi^+ l^- \nu$						$\surd$	$\surd$
(2) Beam category							
Single beam background					$\surd$	$\surd$	
Two-beam background			$\surd$	$\surd$			
(3) Others ...							
Hardware problems, loopholes in selection criteria, pathological events $\cdots$.							

4.4.2 Bifurcation technique

"Bifurcation method" is a special technique, developed in the E949/E787 experiments, to measure a background level from real data sample using two uncorrelated cuts, without looking at the signal region. Figure 44 illustrates the idea how the technique works in the background measurements. In this section, we describe the technique. To make the explanation simple, we consider the case of developing cuts for a certain type of background and we have already imposed cuts to suppress all the other backgrounds to an ignorable level. In the figure, we define a two dimensional space with axes of "cut-1" and "cut-2". Each axis shows the tightness of the cut from the hardest point (= null acceptance, corresponding to the origin in the coordinate) to the loosest one (= no acceptance loss, corresponding to the maximum in the coordinate). Both axes will have the "standard cut positions" which will be used as the final cuts. The region A is accepted by the two cuts, and thus, corresponds to the signal region (box). If the cut-1 and the cut-2 are uncorrelated, the ratio of event A to B should be equal to C to D, because the rejection of cut-1 does not depend on the tightness of the cut-2. We have

$$A/B = C/D \tag{16}$$

$$A = BC/D \tag{17}$$

Equation 17 shows the number of backgrounds in the signal box can be estimated from measurements of B, C and D without looking into the signal region A. Since the rejection (R) of the cut-2 is written as $R = (C + D)/C$, if we re-write the equation in terms of R, we have,

$$A = \frac{B}{(C + D)/C - 1} \tag{18}$$

$$A = \frac{B}{R - 1} \tag{19}$$

The equation tells that the number of estimated backgrounds in the signal region (A) is obtained from the rejection of the cut-2 (R) and the number of events (B) in the region where the cut-2 is inverted.

Correlation check The bifurcation technique is correct mathematically if the two cuts are uncorrelated. The correlation check is a key to get a correct estimation. There are several methods to show that the cuts are uncorrelated, but here we take the simplest method : we confirm the cut-1 rejection doesn't change at the various tightness of the cut-2 and vice versa, or more generally, we change the tightness of both cuts simultaneously and see how the background estimates changes (and check the consistency with the expectation from each rejection factor). This study is called the "outside-the-box study".

Outside-the-box study After masking out the signal region, the two cuts are relaxed (as illustrated in Figure 45), and we perform the bifurcation technique again. The number of events in the extended region (N_{ext}) is expected to be

$$N_{ext} = \frac{B'}{R' - 1} - N_{sig} \tag{20}$$

where, N_{sig} is the number of backgrounds expected in the signal box, B' is the number of events in the loosened area, and R' is the rejection of the loosened cut-1. Since it is allowed

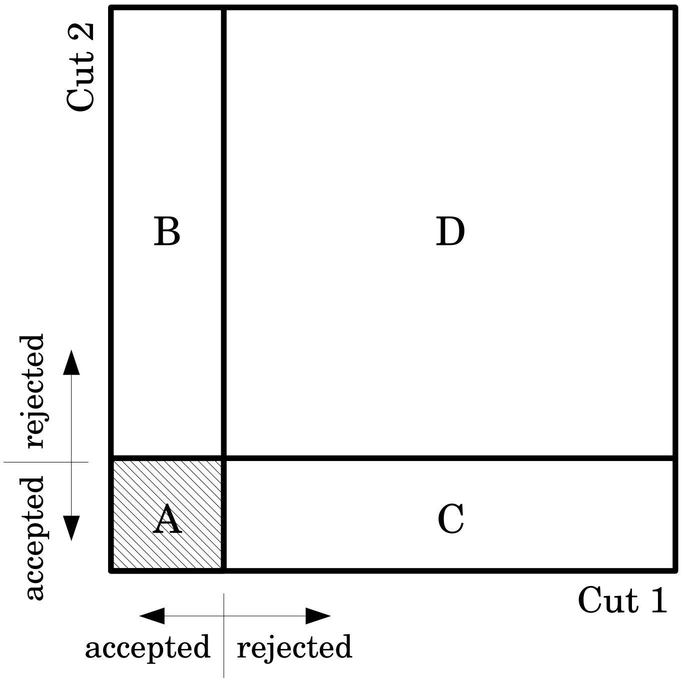

Figure 44: Illustration of how the bifurcation technique works. The region A which is accepted by both cuts is the signal region.

to see the events in the outside-the-box region, we can directly count up the actual number of backgrounds in the region. Changing the loosening factor (sometime loosening only one cut, and sometime changing both cuts), the consistency of the expected numbers is examined with the actual counted numbers. This is the basic idea of the "outside-the-box" study. The technique is applicable to decide the signal region, if the signal box is not yet defined: starting from looser cut, getting to tighter the cuts until acceptable background level is achieved. The process brings us a benefit of finding out the best balance of the tightness between two cuts.

Single cut failure event In the table 13, all types of backgrounds, except for (3), are expected to be rejected by two independent cuts. However, understanding of pathological events, which does not have an ordinary event topology and do pass one (or both) of the cuts without seeing any suppression, is critical for correct background estimation. Such events are not dominated in usual sample and hard to find out. However, in the bifurcation study, they become observable if we look at the region around the signal box. This is because, in the study, all backgrounds are suppressed by the setup cuts[11] except for the one being studied, and the backgrounds are also suppressed by the two cuts around the signal region. Events that fail a single cut (which corresponds to region B or C) is the good test bed to find out such events.

If the outside-the-box study does not have good agreement around the signal region, there exist pathological events or background events that have not been taken into account. This detection capability is an another benefit of the "outside-the-box" study.

---

[11] For example, when we perform the bifurcation study for single beam backgrounds, we need to remove other type of backgrounds (two-beam, muon backgrounds) from the samples. To reject them, crude setup cuts are prepared in advance.

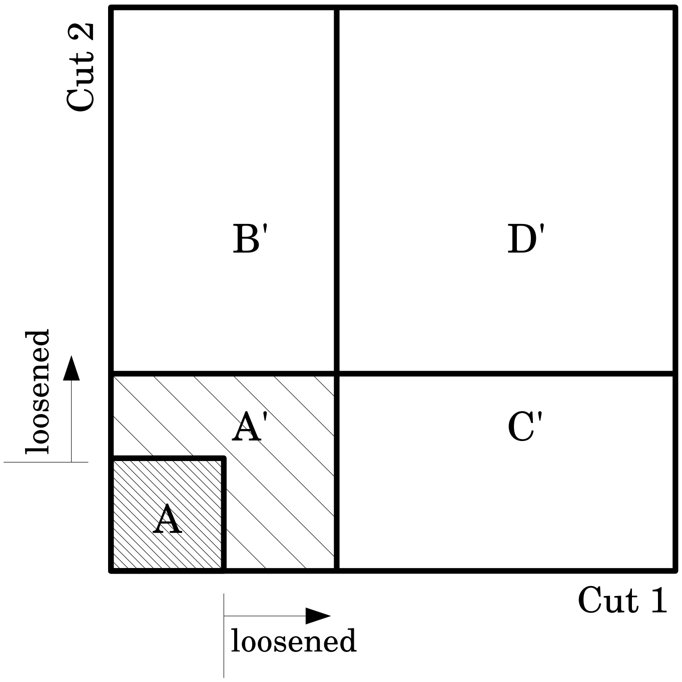

Figure 45: Illustration of the idea on the “outside-the-box study”. Loosening cuts allow us to see the backgrounds in the peripheral area of the signal box. Comparison between the expectation from the loosening factor and the actual counted backgrounds proves the cut-1 and the cut-2 are uncorrelated.

4.4.3 Comments on the development of the $K_{\pi 2}$ selection criteria

Since we aimed to achieve a better result than the current upper limit of Br($\pi^0 \rightarrow \nu\overline{\nu}$) $< 8.3 \times 10^{-7}$, the tagging impurity of 10^{-7} level in $K_{\pi 2}$ sample was crucial. The sample had to be purified as clean as possible, so that the surviving backgrounds in the signal box could be dominated by $\pi^0 \rightarrow \gamma\gamma$ backgrounds. This was the primarily requirement for the selection criteria. In addition to this, the criteria should be independent of photon rejection as much as possible. This was because, if the selection criteria had photon rejection, $\pi^0 \rightarrow \gamma\gamma$ decays were suppressed and the number of π^0 would be underestimated.

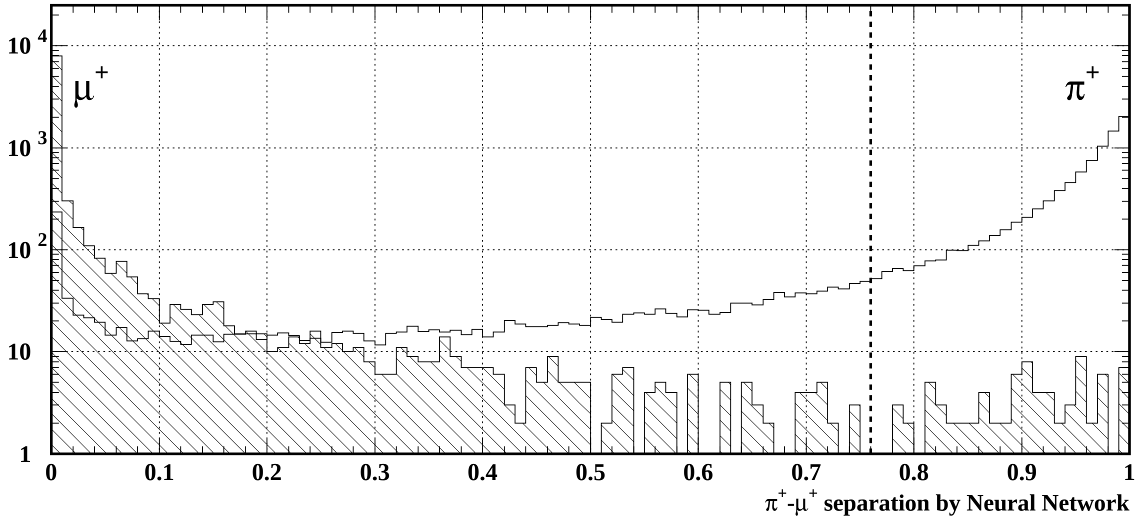

Figure 46: Performance of the π-μ separation by neural network. Muon distribution (hatched histogram) is from kinematically tagged $K_{\mu 2}$ events and pion distribution is from pion scattering events. The neural network was tuned with the $K_{\mu 2}$ and pion events using several extracted variables from π^+ decay pulse fitter. Above plot was produced with independent data sets to avoid the tuning bias. Events with the neural network output less than 0.76 is discarded as backgrounds.

4.4.4 Muon background suppression

Kaon decays $K^+ \to \mu^+\nu$ or $K^+ \to \mu^+\nu\gamma$ should be rejected by the $K_{\pi 2}$ selection criteria, since they had no or less photon in the final state, compared with $\pi^0 \to \gamma\gamma$, and could fake the $\pi^0 \to \nu\overline{\nu}$ signature easier. Cuts for the π^+ decay sequence, dE/dx in the Range Stack were employed for their rejection.

CUT-1 : Pion decay sequence cut Pion decay sequence cut consists of the following requirements :

1. $|T_{\pi,TD} - T_{RS}| \leq 2.5$ ns, where $T_{\pi,TD}$ is the time of π^+ coming to rest, and T_{RS} is the track time in the Range Stack.

   This confirms that the extracted pion time is consistent with the track time.

2. Waveforms of the prior two layers to the pion stopping counter is fitted with a double-pulse finder. If they have a coincident secondary pulse at the extracted muon timing, i.e. $|T - T_{\mu,TD}| < 5$ ns where T is the coincident hit time and $T_{\mu,TD}$ is the extracted muon time, the event is rejected by assuming the muon hit comes from accidental activities.

3. Cut on the $\pi^+ \to \mu^+$ pulse fitting quality with neural network.

   The decay pulse fitter for the stopping counter in the RS provided us the χ^2, muon time, and so forth, as described in the section 4.2.3. However, it was difficult to set the individ-

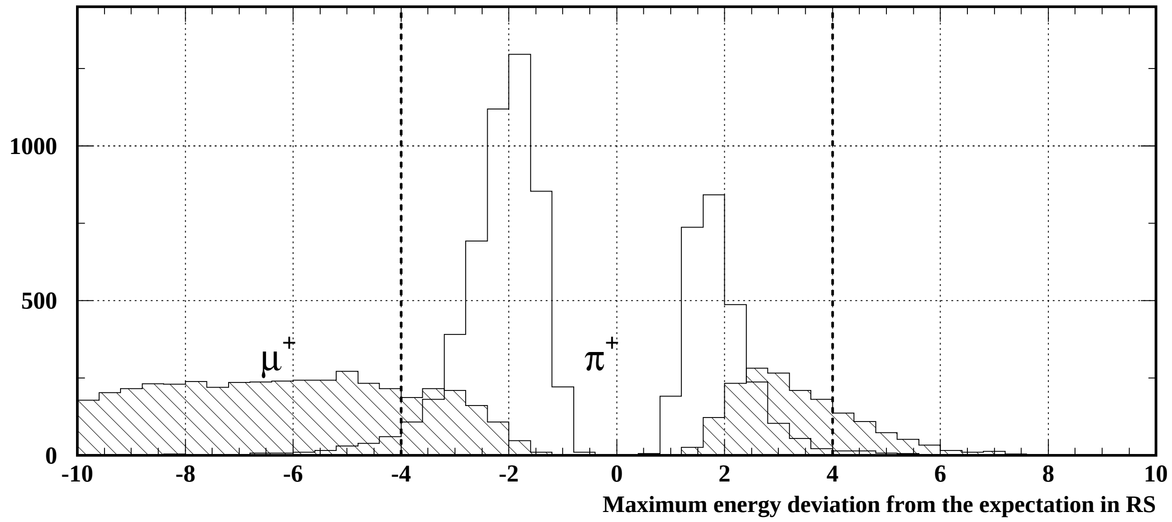

Figure 47: Signed maximum dE/dx deviation in the Range Stack. The hatched histogram is a muon sample and the open histogram is pions. The sign ($+$ or $-$) is from $\log E_{exp}^{i_{max}} - \log E_{meas}^{i_{max}}$. Events with the maximum deviation is less than 4.0 are accepted as signals

ual cut position with proper balance of the tightness. Neural network was built with six variables from the fitter outputs;

(a) $\log_{10}(\chi^2(1) \cdot \chi^2(2))$, where $\chi^2(i)$ is from the single-pulse fit at the end i.

(b) $\log_{10}(R(1) \cdot R(2))$, where $R(i)$ is a χ^2 ratio of the single-pulse fit to that of double-pulse at the end i.

(c) extracted muon energy

(d) extracted muon time

(e) $z_\pi - z_\mu$; z position difference between the pion coming to rest (z_π) and that of muon appearance (z_μ). The z position is reconstructed from the energy ratio of both ends.

(f) time difference between both ends

The neural network was trained with two control samples; pion scattering events (as signal sample) and $K_{\mu 2}$ events (as background sample). The performance was evaluated with an independent sample as shown in Figure 46. The cut position was set at 0.76, which provided a rejection ~ 500 against muon backgrounds at the cost of 15 % acceptance loss.

CUT-2 : Particle identification cut with dE/dx in the Range Stack As shown in Figure 25 on page 45, the Range Stack dE/dx provided large rejection against muons. The cut-2 was built with a series of the Range Stack dE/dx cuts;

1. Maximum allowed deviation from the expected energy.

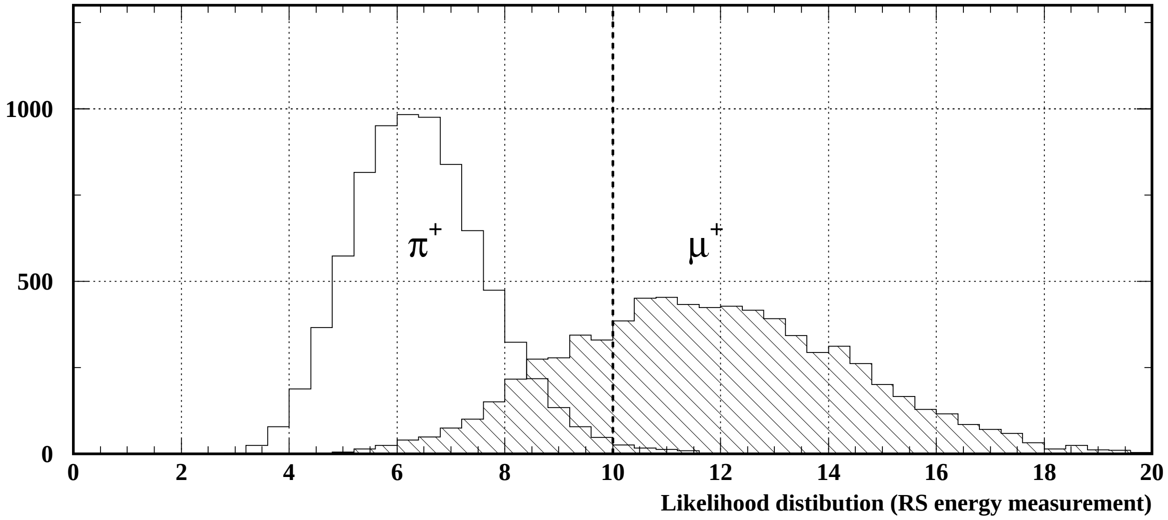

Figure 48: Likelihood distribution constructed from the dE/dx difference in the Range Stack. The cut position is set at 10.

In each counter, expected energy deposit can be calculated from the incident pion energy. Deviation (χ^i) of measured energy from that of expected

$$\chi^i \equiv \frac{\log E^i_{exp} - \log E^i_{meas}}{\sigma^i} \tag{21}$$

is computed by assuming the particle is pion[12], where E^i_{exp}, E^i_{meas} is the expected and measured energy deposit in the i-th counter. Logarithm is computed to avoid the divergence of χ^2 even with the events in the Landau tail. σ^i is the resolution of $\log E^i_{meas}$, which is varied depending on the E^i_{meas}. If the maximum energy deviation MAX($|\chi^i|$), where i runs through 1 to #counters, is greater than or equal to 4.0, the event is discarded as a muon event. The maximum deviation distribution is plotted with muon and pion samples in Figure 47.

2. Likelihood cut for dE/dx difference. A likelihood is constructed from the energy difference ($\log E^i_{exp} - \log E^i_{meas}$) using all track counters except for the stopping counter. The constructed peaks are well separated between the pion and muon samples as shown in Figure 48. Events with the likelihood less than 10 is accepted as pions.

3. Confidence level cut for the deviation. Confidence level is computed with all χ^i's except for that of T-counter, the stopping counter and the counters with the sector crossing track. The confidence level is plotted for both pion and muon samples in Figure 49. It shows good discrimination capability against the muon sample. The cut position is set at the confidence level > 0.04 for normal events. For a safety reason, if the signed maximum deviation (see Figure 47) is positive, the cut position is tightened to 0.2.

---

[12] Even if the charged track is muon, the pion assumption is used

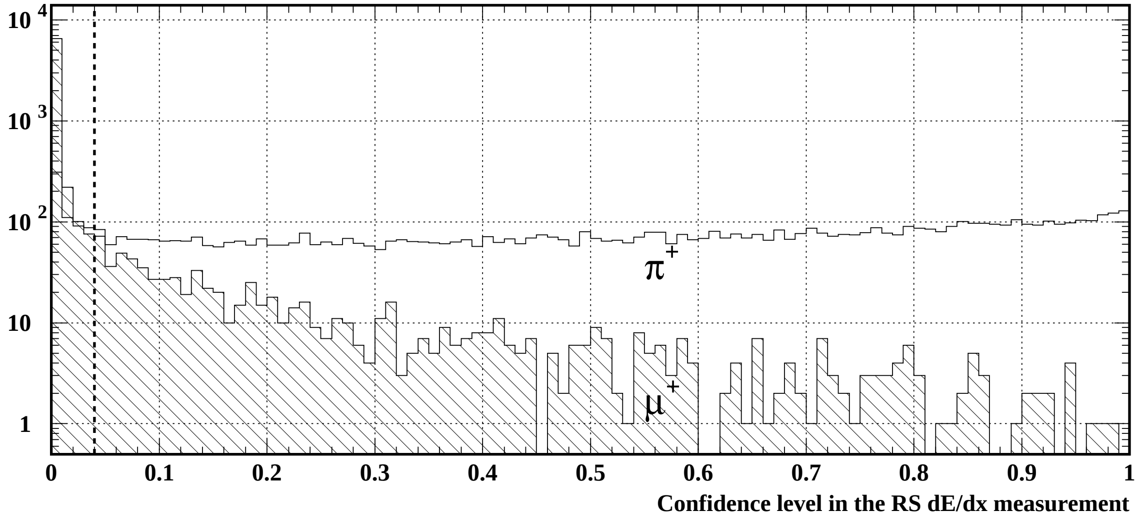

Figure 49: Confidence level distribution computed from dE/dx deviation in the Range Stack. The open (hatched) histogram is produced with pion (muon) sample. The cut position is set at 0.04. If the signed maximum energy deviation is positive, the cut is tightened to 0.2.

Table 14: Summary of the bifurcation analysis in the muon background measurement. The rejection of pion decay sequence cut (R_{TD}) was measured with the sample collected with the inverted Range Stack dE/dx selection. $N_{\overline{TD}}$ was the number of entries measured with the inverted TD cut.

	1/3 sample	2/3 sample
Before TD cuts	28597	56675
After TD cuts	27	75
Rejection	$1.06^{+0.23}_{-0.18} \times 10^3$	$0.75^{+0.09}_{-0.08} \times 10^3$
$N_{\overline{TD}}$ (inversion)	169	277

The number of muon backgrounds in the signal region The rejection of the π^+ decay sequence cut (R_{TD}) was measured with the 2/3 sample with all $K_{\pi 2}$ selection criteria except for the inversion of the Range Stack dE/dx cuts (the cut-2). The measured rejection was $R_{TD} = 0.75^{+0.09}_{-0.08} \times 10^3$. The result is summarized in Table 14. The number of entries ($N_{\overline{TD}}$) surviving after all cuts except for the inversion of π^+ decay sequence cuts was measured as shown in the table. The resultant number was 277 events with 2/3 sample.

Based on the bifurcation technique, the number of muon backgrounds (N_{muon}) in the signal region was estimated to be

$$\begin{aligned} N_{muon} &= \frac{N_{\overline{TD}}}{R_{TD} - 1} \\ &= \frac{277}{0.75^{+0.09}_{-0.08} \times 10^3 - 1} = 3.67^{+0.69}_{-0.60} \times 10^{-2} \end{aligned} \qquad (22)$$

4.4.5 Single beam background suppression

E949 ran under the beam condition of 4/1 K^+ to π^+ ratio, which was down to 3/1 later due to the separator problems. The number of π^+ in the beam are expected to be the same order of magnitude as that of kaon at the E949 detector entrance. As explained in section 4.4.1, π^+ scattered into the detector volume must be well identified with the Cerenkov counter, the B4 hodoscope and delayed coincidence. We defined two independent cuts for the single beam background suppression.

CUT-1 : dE/dx cut in the B4 hodoscope Figure 50 shows K / π separation capability from dE/dx energy loss in the B4 hodoscope counter. The average velocity at the B4 hodoscope was estimated from Monte Carlo simulation to be around $\beta \approx 0.57$ for kaons and $\beta \approx 0.97$ for pions, which resulted in a fairly good separation of the dE/dx distributions as shown in the figure. The cut position was set at 1.1 MeV (indicated by the vertical dotted line). Although the cut did not work to the pion's Landau tail flowing into the kaon distribution, it could significantly reduce pions. Note that primary pions [13] were also suppressed by the Čerenkov counter.

CUT-2 : Delayed coincidence cut in the target Figure 51 shows a distribution of $T_\pi - T_K$, which is difference between the kaon fiber time (T_K) and the pion fiber time (T_π). As shown in the figure, pion scattering events made a sharp peak at a prompt timing. This provided strong discrimination capability against the beam induced backgrounds. Normally, the cut position was set at $T_\pi - T_K > 2$ ns, which was four sigma away from the pion background peak. But for a safety reason, the cut position was tightened depending on the quality of the timing strobes. For example, events with longer range in the target had more pion fibers, which resulted in the better timing accuracy in the strobe reconstruction. On the other hand, kaon decay near the target edge provided less pion fibers (sometimes no fiber was available.), which caused much worse resolution in the reconstruction. The delayed coincidence cut was composed of 9 sub-sets including the nominal one.

1. $T_\pi - T_K > 2$ ns for the normal case.
2. $T_\pi - T_K > 3$ ns if the number of pion fibers is less than four.
3. $T_\pi - T_K > 3$ ns if "beam likelihood" is less than 200. The likelihood distribution is shown in Figure 88 on page 138 in Appendix.
4. $T_\pi - T_K > 4$ ns if there is a kaon fiber (i) whose timing (T_K^i) is more than 2 ns away from the averaged kaon fiber time (T_K); $|T_K^i - T_K| > 2$ ns.
5. $T_\pi - T_K > 4$ ns if there is a pion fiber (i) whose timing (T_π^i) is more than 3.5 ns away from the averaged fiber time; $|T_\pi^i - T_\pi| > 3.5$ ns.
6. $T_\pi - T_K > 4$ ns if the kaon energy deposit in the target is less than or equal to 50 MeV.
7. $T_\pi - T_K > 5$ ns if the kaon hit time in the B4 hodoscope (T_{B4}) is more than 1 ns away from the kaon fiber time; $|T_K - T_{B4}| > 1$ ns.

---

[13] pions existed in beam before the Čerenkov counter.

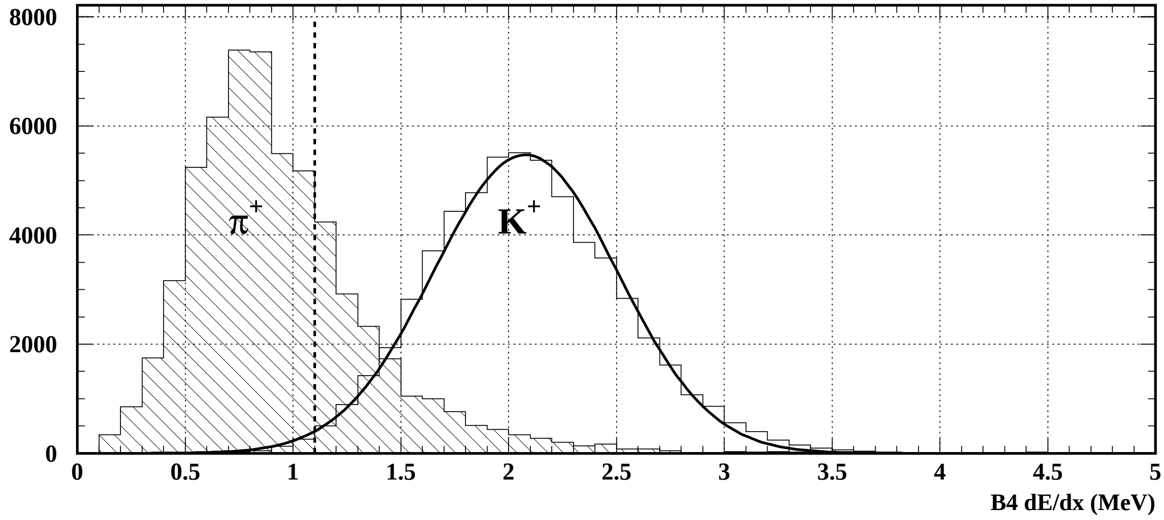

Figure 50: Energy deposit in the B4 hodoscope. The hatched histogram was made with pion scattering events by requiring a hit in the pion Čerenkov counter and no delay in the pion fiber time. Kaon distribution (open histogram) was produced with kinematically tagged $K_{\mu 2}$ events. The Landau distribution was fitted with an gaussian function. The sigma was 0.43 MeV. Events with the B4 energy smaller than 1.1 MeV were discarded.

8. $T_\pi - T_K > 5$ ns if no pion fiber is found. T_π is borrowed from the I-counter hit time.
9. $T_\pi - T_K > 6$ ns if the discrepancy is more than 1.5 ns between the pion fiber time and the pion track time (T_{RS}) in the Range Stack; $|T_\pi - T_{RS}| > 1.5$ ns.

The number of single beam backgrounds in the signal region The number of the single beam backgrounds was estimated with the bifurcation technique in the 2/3 sample. The bifurcation study started with imposing setup cuts (see Appendix B.1 on page 143) to isolate the single beam backgrounds. Rejection of the delayed coincidence (DELC) was measured with the sample which was selected with the inverted B4 dE/dx cut (the cut-1). This is equivalent that the DELC rejection was measured with the background dominated sample with the inversion of the B4 dE/dx cuts. The resultant rejection R_{DELC} is listed in Table 15. The DELC was found to be so powerful that there was no event observed after its imposition. Some of the setup cuts, which were apparently uncorrelated with the DELC, were removed to gain more statistics. Turning off the π^+ decay trace cut and several kinematics cuts, the DELC rejection of $R_{DELC} = 1.53^{+0.35}_{-0.27} \times 10^3$ was obtained (see the rightmost column in the table). By comparing the number with other rejections measured with tight setup cuts in the table, it seemed low. This is considered that none-single beam backgrounds might contaminate the sample. Since we wanted to stand on a safety side in the background measurement, we assumed the contamination actually happened, and used the value for the rejection. As a check, the consistency of the rejection factor was compared with that of the 1/3 sample (which was used for cut design); No significant discrepancy was observed.

The number of observed events after application of the inverted DELC cut ($N_{\overline{DELC}}$) was 50

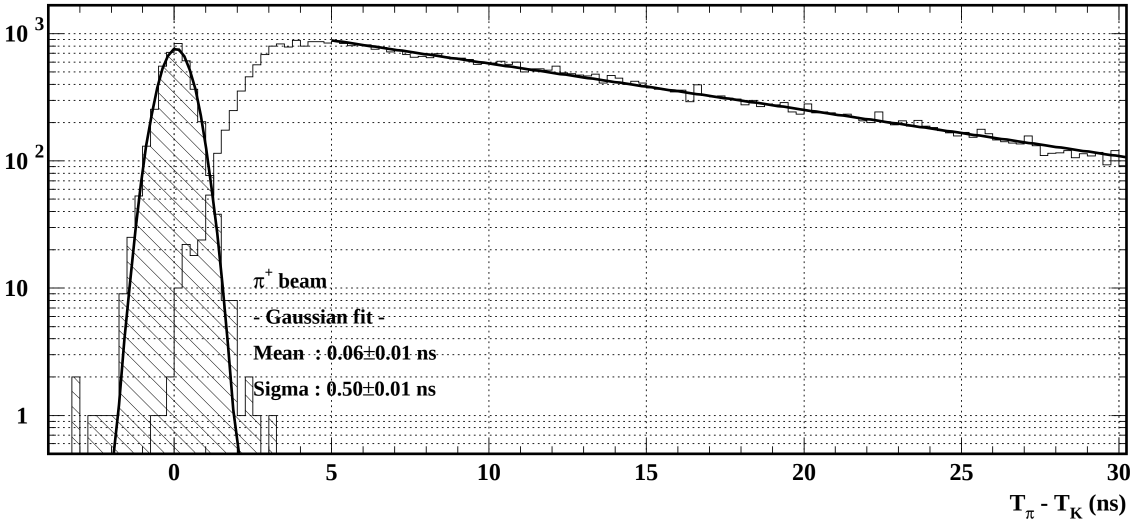

Figure 51: Difference between the kaon fiber time (T_K) and pion fiber time (T_π). The hatched histogram was produced with pion scattering events tagged with a requirement of pion-like dE/dx in the B4 hodoscope. The open histogram was produced with kinematically tagged $K_{\mu 2}$ events. The pion scattering events made a sharp peak at prompt beam timing ($T_\pi = T_K$). The resolution was 0.5 ns with a gaussian fit. Decay-time fit to the $K_{\mu 2}$ events was performed. The obtained lifetime τ_K was ~ 12 ns, which was consistent with the Kaon lifetime of 12.384 ± 0.0024. The cut position varied depending on the reconstruction quality of the timing strobes.

in the 2/3 sample (see Table 16). By following the bifurcation technique, the number of single beam background ($N_{\pi^+ beam}$) was

$$\begin{aligned} N_{\pi^+ beam} &= \frac{N_{\overline{DELC}}}{R_{DELC} - 1} \\ &= \frac{50}{1.53^{+0.35}_{-0.27} \times 10^3 - 1} = 3.27^{+1.26}_{-0.99} \times 10^{-2} \end{aligned} \tag{23}$$

in the 2/3 sample. The corresponding number in the 1/3 sample was 1.87×10^{-2}, which is consistent with that of the 2/3 sample.

Table 15: Rejection measurement of the delayed coincidence (DELC). The table contains the number of entries before and after the DELC in the 1/3 and 2/3 sample. There was no event observed after the DELC imposition with all setup cuts in the 2/3 sample.

	All setup cuts	All setup cuts but for - π^+ decay trace cuts	All setup cuts but for - π^+ decay trace cuts - some kinematics cuts
	1/3 sample measurement		
Before DELC	4172	12258	19241
After DELC	1	1	12
Rejection	$4.17^{+1.14}_{-0.25} \times 10^3$	$1.23^{+3.34}_{-0.74} \times 10^4$	$1.64^{+0.57}_{-0.39} \times 10^3$
	2/3 sample measurement		
Before DELC	8283	24546	38290
After DELC	0	1	25
Rejection	—	$2.45^{+6.69}_{-1.47} \times 10^4$	$1.53^{+0.35}_{-0.27} \times 10^3$

Table 16: Summary of the entries with the inverted DELC cut.

	1/3 sample	2/3 sample
After $\overline{DELC}$ cut	30	50

4.4.6 Two-beam background suppression

Single beam backgrounds were found to be suppressed by the DELC design as shown in the previous section. However, the DELC might be defeated if two beam particles came in, and the first particle was missed after giving the kaon fiber time, and then the second particle provided the pion fiber time. For rejection of such events, it should be confirmed that the entering particle was only one. Close examination on the beam wire chambers and Čerenkov counter around the charged track time determined by the Range Stack was the most effective way to reject these events.

CUT-1 : Extra particle cut by the B4 hodoscope The B4 hodoscope placed in front of the target was the best counter to detect an extra particle entering the target. The cut 1 was composed of following sub-sets. If any of the sub-sets was satisfied, the event was rejected.

1. Events with a hit in $|T_{B4,TDC} - T_{RS}| < 2.5$ ns, where $T_{B4,TDC}$ is the B4 hit timing from the TDCs and T_{RS} was the track time reconstructed in the Range Stack.
2. Events with a hit in $|T_{B4,TD} - T_{RS}| < 1.5$ ns, where $T_{B4,TD}$ is timing of the hit, whose energy is greater than 0.7 MeV, measured with the CCD-based transient digitizer (TD).
3. Events with a hit in $|T_{B4,CLS} - T_{RS}| < 3.5$ ns, where $T_{B4,CLS}$ is the cluster hit timing. The cluster is reconstructed with the second pulses extracted from the TD waveforms by double-pulse fitting. Second pulse is found when the χ^2 ratio of single-pulse fitting to that of double-pulse fitting is greater than 2.5.

CUT-2 : Extra particle cut by the Čerenkov counter and Beam wire chambers The cut 2 was composed of following sub-sets. If any of the sub-sets was satisfied, the event was rejected.

1. Event with a hit in $|T_{BW1} - T_{RS}| < 4.5$ ns or $|T_{BW2} - T_{RS}| < 4.5$ ns, where T_{BW1}, T_{BW2} are hit times in the Beam wire chamber 1 and 2, respectively.
2. Event with a hit in $|T_{cK} - T_{RS}| < 2.0$ ns, where T_{cK} is the hit time from kaon Čerenkov counter, and more than four K-PMTs were fired.
3. Event with a hit in $|T_{cK,TD} - T_{RS}| < 2.0$ ns and more than four K-PMTs have the hit in CCD-based TD waveforms. The TD is used for multiple hit detection.
4. Event with a hit in $|T_{cK,trail} - T_{RS}| < 3.0$ ns when $T_\pi - T_K < 15$ ns and more than five K-PMTs are fired. Here, $T_{cK,trail}$ means TDC trailing-edge time.
5. Event with a hit in $|T_{cK,trail} - T_{RS}| < 3.5$ ns when $15 < T_\pi - T_K < 25$ ns and more than one K-PMT is fired.
6. Event with a hit in $|T_{cK,trail} - T_{RS}| < 2.0$ ns when $T_\pi - T_K > 25$ ns and more than five K-PMTs are fired.
7. Event with a hit in $|T_{c\pi} - T_{RS}| < 2.0$ ns, where $T_{c\pi}$ is the hit time from the pion Čerenkov counter, and more than four pion-PMTs are fired.

Table 17: Summary of the cut-2 rejection in the two-beam background measurement.

	Kaon branch		Pion branch	
	1/3 sample	2/3 sample	1/3 sample	2/3 sample
Before the cut-2	264	473	9023	18268
After the cut-2	5	11	2	11
Rejection	$5.28^{+3.31}_{-1.78} \times 10^1$	$4.30^{+1.60}_{-1.07} \times 10^1$	$4.51^{+5.93}_{-0.22} \times 10^3$	$1.66^{+0.63}_{-0.42} \times 10^3$

Table 18: Summary of the entries with the cut-2 inversion in the two-beam background measurement.

	Kaon branch		Pion branch	
	1/3 sample	2/3 sample	1/3 sample	2/3 sample
After the cut-2 inversion	67	98	304	644

8. Event with a hit in $|T_{c\pi,TD} - T_{RS}| < 2.0$ ns and more than four pion-PMTs find the hit in CCD-based TD waveforms.
9. Event with a hit in $|T_{c\pi,trail} - T_{RS}| < 2.0$ with more than five pion-PMTs are fired. $T_{c\pi,trail}$ is the TDC trailing-edge time in the pion Čerenkov counter.

The first sub-set is called “BWTRS”. The combination of the second to sixth (seventh to ninth) sub-sets is called “CK2BM” (“Cπ2BM”). [14]

The number of two-beam backgrounds in the signal region The number of two-beam background was measured with the bifurcation technique. The two-beam backgrounds were isolated with the setup cuts. The concrete cut list are shown in Appendix B.2 on page 145.

The measurement of the two-beam backgrounds was branched on the basis of the second particle type. This was because the situation drastically changed with the type. The characteristics are summarized as follows,

- **Pion branch :**

  The first particle was K^+ and the second particle was π^+ which was originally in the beam.

  Characteristics :

  1. Huge number of entries in the beam.
  2. Stringent rejection with the pion Čerenkov counter.

- **Kaon branch :**

  The first particle was K^+ and the second particle was π^+ which was from kaon decay-in-flight occurred downstream of the Čerenkov counter.

---

[14] CK2BM, Cπ2BM : “C” stands for Čerenkov and “2BM” tells that these cuts are for Two-BeaM background suppression.

Characteristics :

1. Not so many entries in the beam.
2. Lower rejection with the kaon Čerenkov counter.

   The second particle, K^+, could be vetoed by the kaon Čerenkov counter, but, frequently it could pass through unvetoed due to the detector dead-time caused by the preceding particle.

The kaon branch was tagged by the Cπ2BM[15] and the pion branch was tagged with CK2BM[16]. Each type of the backgrounds was individually dealt with. The rejection of the cut-2 for each branch was measured with the inverted cut-1. The obtained results were $R_{2beam,kaon} = 4.30^{+1.60}_{-1.07} \times 10^1$ for the kaon branch and $R_{2beam,pion} = 1.66^{+0.63}_{-0.42} \times 10^3$ for the pion branch, respectively. The results are summarized in Table 17. The numbers of entries with the cut-2 inversion were measured to be 98 for the kaon branch ($N_{\overline{2beam,kaon}}$) and 644 for the pion branch ($N_{\overline{2beam,pion}}$) as shown in Table 18.

Following the bifurcation method, the number of backgrounds in the kaon branch ($N_{2beam,kaon}$) in the signal region was

$$\begin{aligned} N_{2beam,kaon} &= \frac{N_{\overline{2beam,kaon}}}{R_{2beam,kaon} - 1} \\ &= \frac{98}{4.30^{+1.60}_{-1.07} \times 10^1 - 1} = 2.33^{+1.11}_{-0.801} \end{aligned} \tag{24}$$

and the number of backgrounds in the pion branch ($N_{2beam,pion}$) was

$$\begin{aligned} N_{2beam,pion} &= \frac{N_{\overline{2beam,pion}}}{R_{2beam,pion} - 1} \\ &= \frac{644}{1.66^{+0.63}_{-0.42} \times 10^3 - 1} = 3.88^{+1.51}_{-1.17} \times 10^{-1} \end{aligned} \tag{25}$$

The measurements with the 2/3 sample gave consistent results with the expected numbers in the 1/3 sample analysis.

---

[15] No pion activity in the Čerenkov counter

[16] No kaon activity in the Čerenkov counter

Table 19: Number of none-$K_{\pi 2}$ backgrounds in the signal region. The number of each background is listed in the third column. That of 1/3 sample, which was obtained in the preliminary study of designing the selection criteria, is listed in the rightmost column.

Background type	Sub category	# events (2/3)	# events (1/3)
Muon background	—-	$0.04^{+0.01}_{-0.01}$	0.12
Beam background	single beam	$0.03^{+0.01}_{-0.01}$	0.02
	two-beam (kaon branch)	$2.33^{+1.11}_{-0.80}$	1.26
	two-beam (pion branch)	$0.39^{+0.15}_{-0.12}$	0.07
Total		$3.12^{+1.33}_{-0.99}$	1.47

4.4.7 Evaluation of the K$\pi 2$ tag impurity

With combining all results of the bifurcation analysis, the measured number of none-$K_{\pi 2}$ backgrounds in the signal region was $3.12^{+1.33}_{-0.99}$. For reference, the number of each background was listed up in Table 19. As seen, the most dominated background was the two-beam background of $2.33^{+1.11}_{-0.80}$ with π^+s from kaon decay-in-flight events. After applying the $K_{\pi 2}$ selection criteria, the number of accumulated $K_{\pi 2}$ events was 3.02×10^9. [17]

Summary of the $K_{\pi 2}$ selection A sample of 3.02×10^9 π^0s (N_{π^0}) were collected with the 1.8×10^{12} stopped kaons. The expected none-$K_{\pi 2}$ backgrounds in the sample was $3.12^{+1.33}_{-0.99}$, which corresponded to the impurity of $\sim 10^{-9}$. Assuming the $\pi^0 \to \nu\overline{\nu}$ search is not be limited by the inefficiency of $\pi^0 \to \gamma\gamma$ background, a sensitivity level of 10^{-9} would reached.

---

[17] The number took into account the $\pi^0 \to \gamma\gamma$ suppression factor in the online trigger. The trigger suppression factor will be detailed later.

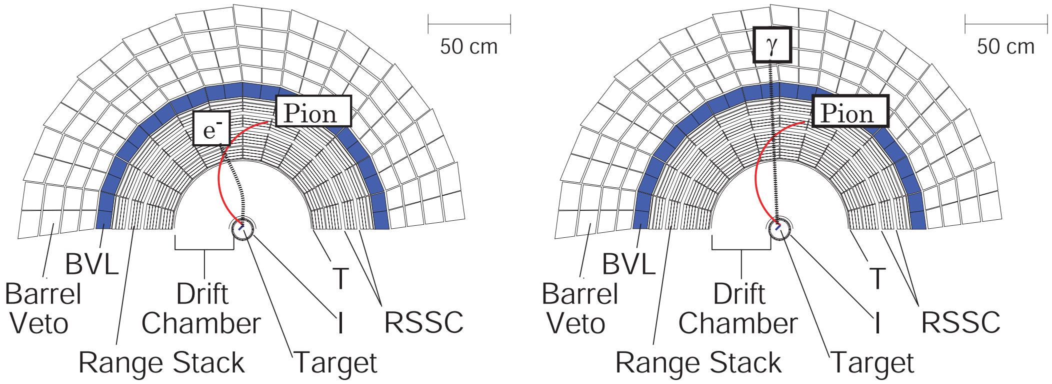

Figure 52: Examples of events with an overlapping electron and photon. When electrons or photons originated from $\pi^0 \to \gamma\gamma$, $\pi^0 \to e^+e^-\gamma$ decays overlapped with the π^+ track, they might cause a problem in the reconstruction. The electron overlapping event (left) interrupted the track counter finding and that of photon overlapping (right) might make the π^+ energy overestimated with the photon energy. Both cases resulted in acceptance drop when the $K_{\pi 2}$ selection.

4.4.8 The correction factor C_{dis}

The disruption correction, denoted as C_{dis}, was a correction factor introduced to compensate for unintentionally rejected $\pi^0 \to \gamma\gamma$ events during the $K_{\pi 2}$ selection process. Photon activities by $\pi^0 \to \gamma\gamma$ around or on the π^+ track would interfere in the reconstruction with a fake counter or anomalous dE/dx hit[18] as shown in Figure 52. Such events would fail to reconstruct the π^+ track properly, and result in acceptance loss. Even if the reconstruction succeeded, a part of e/γ energy was added to the reconstructed π^+ energy. They were then rejected by the energy cut for the monochromatic π^+.

In the offline $K_{\pi 2}$ selection, the cuts were carefully designed not to cause photon rejection, since it would underestimate the number of π^0. However, online trigger conditions did have the photon rejection. For example, the muon rejection condition RNG (see the definition on page 42), which rejected long range tracks, had unwanted rejection against $K_{\pi 2}$ events with a photon radiated in the outer layer of the Range Stack. This should be also corrected.

The correction factor C_{dis} was estimated with two sets of Monte Carlo data. One was a set of standard $K_{\pi 2}$ events, where all π^0s decayed into the predominant channels of $\gamma\gamma$ or $e^+e^-\gamma$. The other was a set of non-standard $K_{\pi 2}$ events, where all π^0s were assumed to undergo $\pi^0 \to \nu\overline{\nu}$ decay. Difference in the π^+ reconstruction efficiency and rejection of the $K_{\pi 2}$ selection criteria were examined[19] and the results were shown in Table 20. The observed difference was $1.1582 \pm 0.0007 (= 446491/385506)$. In the rightmost column of the table, one can see a tiny fraction of events were rejected by photon rejection cuts, although they had no photon in the final state. The over-rejection factor was $0.9810 \pm 0.0003 (= 257715/262719)$. Taking into

---

[18] It prevented from linking the trajectory

[19] Only the relevant cuts were investigated.

Table 20: Summary of the correction factor C_{dis} estimation. The numbers of entries are listed in the order of imposed cuts. The "KP2BOX" is the monochromatic momentum, energy and range cuts in the $K_{\pi 2}$ selection process. Other trigger definitions are shown on the page 42 in the trigger section. The L1.1, which required pulse shape of $\pi^+ \to \mu^+$ decay, and the L1.2, had photon rejection, were not included in the simulation.

	Nominal $K_{\pi 2}$ events	$K_{\pi 2}$ with $\pi^0 \to \nu\overline{\nu}$
# of generated events	2.8×10^6	2.8×10^6
+ $K_{\pi 2}(1)$ trigger	1036482	1007045
+ ID · DC	882227	852338
+ L1.1 · L1.2	—	—
+ RNG	484895	521401
+ NRSSC	477289	518411
+ KP2BOX	385506	446491
Additional setup cuts	—	262719
Online photon rejection	—	262715
Offline photon rejection	—	257715

account the over-rejection, the C_{dis} was measured to be $C_{dis} = 1.14 \pm 0.01$ $(= 1.1582 \times 0.9810)$.

4.5 Search for π^0 decay to nothing with kinematically tagged π^0s

In this section, cuts to reject π^0 decay to $\gamma\gamma$ or other visible final states are described. Since the most dominant π^0 decay is $\pi^0 \to \gamma\gamma$, the cut was named "photon veto". The photon veto was composed of two parts; online and offline photon veto. The online photon veto was described in the trigger section on page 43. In this section, its performance (rejection and acceptance) is presented. The offline photon veto will be considered in section 4.5.5 based on studies of photon detector performance (section 4.5.4). Its rejection was maximized with optimization process described in section 4.5.6.

4.5.1 Rejection measurement of the online $\pi^0 \to \gamma\gamma$ veto

Online photon veto was composed of the following conditions : HEX, HEX-afterburner, $\overline{BV}$, $\overline{BVL}$ and $\overline{EC}$ (see the trigger section on page 43). The rejection was measured with two different methods.

1. **Method-1 :** Starting from the minimum bias event sample, taken by $K_{\pi 2}(1)$ trigger, we simulated $\pi\nu\overline{\nu}$ trigger without the online photon veto in the offline. Actually, these events which satisfied the conditions $DC \cdot L11 \cdot RNG \cdot NRRSC$ were selected among the $K_{\pi 2}(1)$ events. The event sample, denoted as "$\pi\nu\overline{\nu}_{\text{NOPV}}$", was then purified with the $K_{\pi 2}$ selection criteria. The online rejection was measured with the number of entries before and after applying the online photon veto conditions.

   This is a reliable and robust way. However, due to statistical limitation of the $K_{\pi 2}(1)$

Table 21: Rejection measurement of the HEX and the HEX-afterburner conditions in the online photon veto.

	# events	Rejection
$K_{\pi 2}(1)$ sample	—	—
+ $DC \cdot L11 \cdot RNG \cdot NRSSC$	—	—
+ $K_{\pi 2}$ selection criteria	36680	—
+ HEX	12194	3.008 ± 0.022
+ HEX afterburner (simulation)	10986	1.110 ± 0.003
+ L1.2	10491	(1.047 ± 0.002)
Total		3.339 ± 0.027

Table 22: Rejection measurement of the $\overline{BV}$, $\overline{BVL}$ and $\overline{EC}$ conditions in the online photon veto.

	# events	Rejection
$K_{\pi 2}(2)$ sample	—	—
+ $RNG \cdot NRSSC$	—	—
+ $K_{\pi 2}$ selection criteria	176098	—
+ $\overline{BV} \cdot \overline{BVL} \cdot \overline{EC}$	97	1815 ± 184

events, the resultant number would have large error. [20]

2. **Method-2 :** Both $\pi\nu\overline{\nu}$ and $\pi\nu\overline{\nu}_{\text{NOPV}}$ events were purified with the $K_{\pi 2}$ selection criteria. The rejection was measured from the ratio of the numbers of $\pi\nu\overline{\nu}_{\text{NOPV}}$ events to that of $\pi\nu\overline{\nu}$ with taking into account the trigger prescale factors of $K_{\pi 2}(1)$.

   Since the method did not need to apply the photon veto to the $K_{\pi 2}(1)$ events, the statistical error would be small. However, any unknown data loss in one of the samples would become a source of systematic errors.[21]

The two measurements were individually performed. When both measurements gave the consistent results, the result of the Method-2, the result of the smaller statistical error, would be accepted. If inconsistent, that of the Method-1 would be accepted.

Measurement with the Method-1 Table 21 shows the resultant rejections of the HEX and HEX-afterburner conditions with the Method-1. Since the HEX-afterburner was embedded in the L1.2 condition, the rejection was estimated with the software-based emulation. The rejection of the combined two conditions was 3.339 ± 0.027 ($= 3.008 \times 1.110$). The rejection of the L1.1-afterburner ($R_{L1.1after}$), which was embedded in the L1.2 with the HEX-afterburner,

---

[20] Online photon veto was primarily designed to have a rejection of $\sim 10^4$. If we want to measure the rejection with 10 % statistical error (= 100 events observation after the cut imposition), more than 10^7 events (= 10^4 $\times 100$ events $\times$ other trigger rejection $\times$ acceptance loss at the $K_{\pi 2}$ selection) are required.

[21] Storage full, data corruption, DAQ problem in hardware/software level $\cdots$, everything. No data loss in the physics trigger of $\pi\nu\overline{\nu}$ was confirmed with various ways. However the calibration trigger of $K_{\pi 2}(1)$ was not.

Table 23: Rejection of online photon veto with the Method-2. The third column shows the number of offline events after the $K_{\pi 2}$ selection criteria. Forth column shows the number of entries with prescale factors. Although the $\pi\nu\overline{\nu}$ data were collected with no prescale, the $K_{\pi 2}(1)$ data were collected with various run-dependent prescale factors.

Trigger type	Selection	# events	#events × prescale
$K_{\pi 2}(1)$	+ $DC \cdot L11 \cdot RNG \cdot NRSSC$		
	+ $K_{\pi 2}$ selection criteria	24523	0.3161×10^{10}
$\pi\nu\overline{\nu}$	+ $K_{\pi 2}$ selection criteria	476441	0.4764×10^{6}
	Trigger ratio		6635 ± 52

was $R_{L1.1after} = 1.047 \pm 0.002$. The $R_{L1.1after}$ was used as a correction factor in the Method-2. The rejection of the $\overline{BV} \cdot \overline{BVL} \cdot \overline{EC}$ condition was measured as shown in Table 22. Combining the both results, the total rejection of online photon veto was 6060 ± 663.

Measurement with the Method-2 The number of the $\pi\nu\overline{\nu}_{\mathrm{NOPV}}$ events, after application of the $K_{\pi 2}$ selection criteria as well as the prescale correction, was 0.3161×10^{10} as shown in Table 23. The corresponding number for the $\pi\nu\overline{\nu}$ trigger was 0.4764×10^{6}. The ratio gave rejection of 6635 ± 52 ($= 0.3161 \times 10^{10}/0.4764 \times 10^{6}$). The number included the L1.1-afterburner rejection ($R_{L1.1after} = 1.047 \pm 0.002$) embedded in the L1.2. By subtracting the contribution, the actual rejection of the online photon veto was measured to be 6337 ± 62 ($= 6635/1.047$).

Summary of the rejection measurements By comparing the rejections, 6060 ± 663 in Method-1 and 6337 ± 62 in Method-2, they were found to be consistent within the errors. Thus, the number of 6337 ± 62 was used as the total rejection factor of the online photon veto in the further analysis.

4.5.2 Acceptance measurement of the online $\pi^0 \to \gamma\gamma$ veto

Online photon veto rejected events with accidental hits even if the events did not have a photon in the final state. This effect, resulting in apparent acceptance loss, should be corrected. In this section, the acceptance measurement with the $K_{\mu 2}$ sample is described. The $K_{\mu 2}$ sample have no photon in the final state, and whose signature is close to that of $\pi^0 \to \nu\overline{\nu}$ of $K_{\pi 2}$ decay, *i.e.* two body decay with one charged track.

The $K_{\mu 2}$ selection criteria $K_{\mu 2}$ events were skimmed out from $K_{\mu 2}(1)$ sample, whose trigger definition is shown in the trigger section on page 43. The $K_{\mu 2}$ selection criteria should have a impurity below 10^{-3}. This purity was achieved with the selection criteria shown in Appendix A.10, where beam background cuts (from the $K_{\pi 2}$ selection criteria) and the monochromatic μ^+ selection cuts were employed.

Contamination of the backgrounds $K^+ \to \mu^+\nu\gamma$ was crucial because they were always rejected by the photon veto and their contamination would cause underestimation of the acceptance. However, thanks to their small branching ratio (0.5 %) and the suppression by the

Table 24: Acceptance measurement of online photon veto. HEX-afterburner condition was simulated with software codes. The $\overline{L20ct} \cdot \overline{L21ct}$, which were originally prepared for the layer 20th and 21th counters in the Range Stack in the E787, seemed to caused acceptance loss. Although the acceptance loss was negligible, we decided to include it as a part of the online photon veto.

	# events	Acceptance
$K_{\mu2}(1)$ + Additional trigger bits + $K_{\mu2}$ selection criteria	15183	
+ HEX	14168	0.933±0.002
+ HEX afterburner (simulation)	13869	0.979±0.001
+ $\overline{EC}$	13711	0.987±0.001
+ $\overline{BV}$	13562	0.989±0.001
+ $\overline{BVL}$	13308	0.978±0.001
+ $\overline{L20ct} \cdot \overline{L21ct}$	13220	0.993±0.001
Total acceptance		0.871±0.003

monochromatic μ^+ selection, it could be negligible. Another backgrounds of $K^+ \to \mu^+\pi^0\nu$, whose branching ratio is 3.27 %, was also negiligible, because its μ^+ momentum differed significantly from the monochromatic μ^+ of $K_{\mu2}$.

The resultant acceptance Table 24 shows the measured acceptance of each condition in the online photon veto. In the measurements, the condition of no hit in the layer 19 of the Range Stack was imposed as a setup cut to confirm muons did not reach the BVL. Each acceptance loss was measured with the number of entries before/after the application of each trigger condition. The total acceptance was 0.871±0.003.

4.5.3 Summary of the performance of the online $\pi^0 \to \gamma\gamma$ veto

$K_{\pi2}$ events with π^0 to $\gamma\gamma$ decays or other visible final states were suppressed by the online photon veto with a rejection factor of 6337 ± 62. Its acceptance for $K_{\pi2}$ events with $\pi^0 \to$ "nothing" was measured to be 0.871 ± 0.003.

Table 25: Timing resolutions in various photon detection systems. Difference in the resolution between the BV and BVL was due to the TDC performance. (Abbreviations; BV = Barrel Veto, BVL = Barrel Veto Liner, EC = End cap calorimeter, RS = Range Stack, TG = Target, IC = I-Counters, VC = V-Counters, CO = Collar counters, CM = Micro-Collar counters.)

System	Resolution (ns)	System	Resolution (ns)	System	Resolution (ns)
BV	1.2	RS	0.7	VC	1.3
BVL	0.7	TG	1.8	CO	1.2
EC	1.6	IC	1.1	CM	1.0

4.5.4 Preliminary studies for designing offline $\pi^0 \to \gamma\gamma$ cuts

To design offline photon veto, we investigated what kind of cuts were required and/or effective to suppress the $\pi^0 \to \gamma\gamma$ backgrounds. The photon veto was determined with studies on the performances of the photon detectors.

Timing resolutions of the photon detectors Timing resolution of each photon detection system was key information to determine the timing window of photon veto. Better resolution provided a good rejection even with narrower windows, which could reduce the acceptance loss. The upper left plot in Figure 53 shows the photon timing distribution in the BV. The resolution of 1.2 ns (RMS) was obtained in the BV. Timing resolutions for other photon detection systems are summarized in Table 25. All the detectors achieved timing resolutions better than 2 ns. To improve the detection inefficiency, stringent rejection against low energy photon was important. Timing resolution with low energy photon should be checked. The upper right plot in Figure 53 shows the resolution as a function of energy in the BV. As shown in the plot, the resolution got worse as the visible energy became smaller. A factor of two worse resolution was observed at the visible energy of 0.2 MeV. This kind of plots for other systems are shown in Figure 95 on the page 149 in Appendix. They indicated necessity of the wider time windows for rejection of low energy photons, not only lower energy thresholds.

Blind effects by early accidentals Multi-hit TDCs were employed for determination of the photon hit timing at the data acquisition. Thus, there was, basically, no problem to detect the second pulse even if more than two hits came after the TDC start gate. However, when successive two particles came in with very close timing, the pulse of the second hit was hidden in the tail of the first pulse. This resulted in only one hit recorded in the TDCs (masked hits) and made us mis-measure the timing of the on-time real photon to be earlier. Such events would increase as the beam instantaneous rate. The lower left plot of Figure 53 shows the existence of the masked TDC hits in the BV. Events in the region of $-(10 \sim 50)$ ns had an excess of events with a similar energy distribution with that of prompt events, although the timing was significantly early. On the other hand, no excess in early time was observed in the $K_{\mu2}$ sample (hatched histogram). The same phenomenon was also seen in the BVL timing distribution. For the rejection of the masked hits, photon veto of wide window with higher energy threshold[22] was required for the BV and BVL.

---

[22] Since wide veto window caused large acceptance loss, the energy threshold should be loosened.

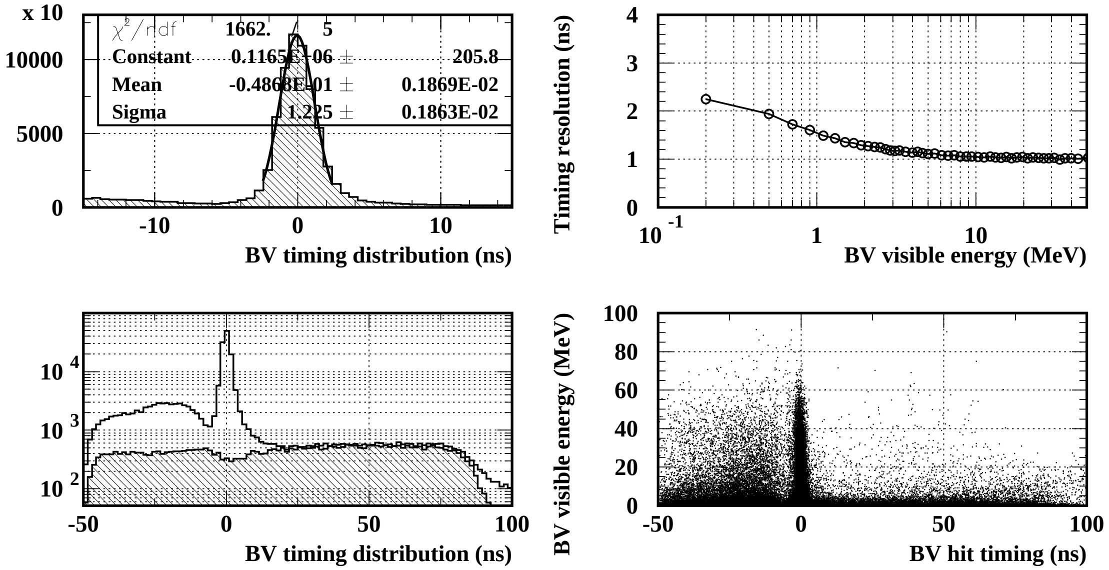

Figure 53: Photon detection performance in the BV. The upper left figure shows a photon timing distribution. The peak was standing at the prompt timing of 0 ns with the width (RMS) of 1.2 ns. The width varied as a function of energy as shown in the upper right figure. It indicated that wider veto window was required for the rejection of low energy photons. In the lower left plot, $K_{\pi 2}$ decay (the open histogram) showed a significant excess at the time range of (-50 ns : -10 ns) compared with that of $K_{\mu 2}$ decays (the hatched histogram). To check the excess, a scatter plot of the energy vs timing in the BV was made (the lower right plot). The earlier hits had significant energy and were not regarded as noises nor accidentals. Their energy distribution shows a similar shape with that of the prompt peak.

Micro-structure of two timing peaks in the BVL It was found that the timing distribution in the BVL had a micro-structure of two peaks as shown in the left plot of Figure 54. It was checked that the earlier peak was from neither any particular counter nor any particular run as one suspected a possible mistake in calibration. Since the earlier peak had higher energy distribution than that of the prompt peak, a mechanism of double photon hitting in the same BVL rod was considered. The mechanism, illustrated in Figure 55 (left side), involved two photons impinging simultaneously. In the mechanism, since each photon made a hit near the each end, the averaged time of both ends was shifted to early time due to the small propagation length. A phenomenon, supporting this interpretation, was observed in the end-to-end time difference distribution as shown in the right plot of Figure 55. Unnaturally localized spot of the earlier peak was seen at the zero time difference. Offline photon veto should deal with the earlier peak with wide veto window. The cuts with wide window and loose energy threshold, which was suggested in the study of masking effect, would help the rejection.

Single-end (unpaired) hits A “single-end” hit is an unpaired hit, where a hit is observed at only one end. Such an event was caused, most likely, by low energy photons with small polar angle, hitting one of the far-end of the Barrel rod. In such a case, a hit could be observed at the closer end, but not at the opposite end due to light attenuation with much longer propagation length. This was considered as one of the photon missing processes. Thus, the offline photon

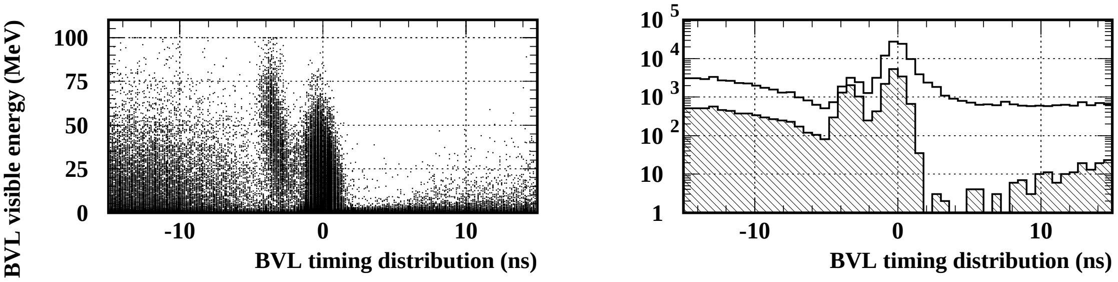

Figure 54: Observed photon hits in the BVL. The BVL had a micro structure of two peaks in the timing distribution (left figure). The earlier peak had higher energy. The peak distribution with the energy cut of $E_{visible}^{BVL} > 30$ MeV was plotted in the right plot. The open histogram is the timing distribution before the cut, and the hatched histogram is that with the energy cut. Smaller suppression was seen in the earlier peak compared with the later peak.

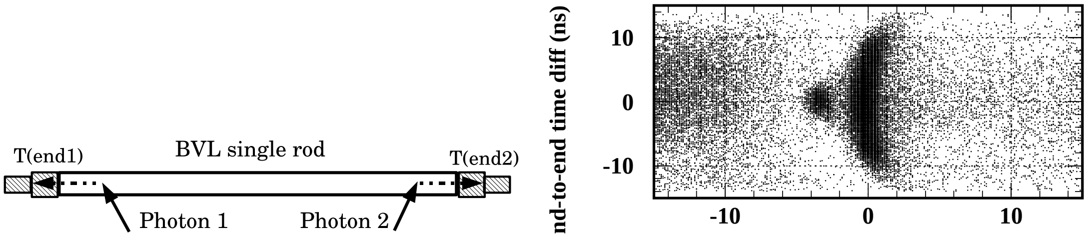

Figure 55: Illustration of the possible mechanism of the earlier peak in the BVL. The earlier peak was generated with events with whose two photons of $\pi^0 \to \gamma\gamma$ hit the same BVL rod (left figure). The right figure is a scatter plot of the BVL hit timing vs end-to-end time difference of the hit; T(upstream) - T(downstream). The localized spot gave the supporting evidence of the BVL double-hit mechanism.

veto included the rejection of single-end hits. The observed timing distribution of the single-end hits in the BV was plotted in Figure 56 (left side) and that of the BVL was shown in the figure (right plot). As seen in the plot, the timing resolutions were worse compared with both-end hits, because they were not able to reconstruct the averaged timing with both ends.

Influence of high intensity beam exposure In the offline photon veto, balance of the cut tightness should take into account the “signal to noise ratio” of the observed hits. For example, Figure 57 shows the hit timing distribution of four counters in the different ring of the End cap calorimeter at the upstream end (see the assembly configuration in Figure 19 on page 37). In the upper left plot, which shows the hit timing distribution of the most inner and upstream ring, the prompt peak by photons was buried in the high rate accidentals. If the same width of veto window was applied to the innermost ring as in the other rings, it would caused significant acceptance loss due to the accidentals. It indicated necessity of the individual treatment for the upstream innermost ring.

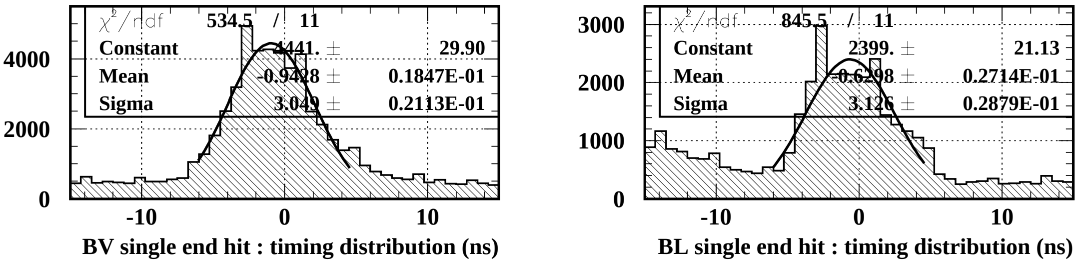

Figure 56: Timing distributions of single-end hits in the BV (left) and BVL (right). Both plots were made with a sample of 10^5 $K_{\pi 2}$ events. Since they were not able to reconstruct the average timing, the timing varied depending on the Z-hit position. This resulted in worse timing resolution of 3.0 ns (BV) and 3.1 ns (BVL) in RMS.

4.5.5 The design of the offline $\pi^0 \to \gamma\gamma$ cuts

The results of the prior studies, presented in the previous sections, are summarized, and the actual $\pi^0 \to \gamma\gamma$ cuts are presented below.

- The study of the timing resolution for low energy photons indicated a requirement of proper balance with the time window and energy threshold. The cut should have the window size and energy threshold as a free parameter. This type of cut was introduced to each of 9 systems; BV, BVL, EC, RS, TG, IC, VC, CO and CM (9 cuts).
- The study of the masking effects suggested that the BV and BVL should have additional cuts with wide windows and loose energy thresholds, intended to reject early hits. The cut, named “Early hit veto”, was introduced for each (two cuts, in total).
- The study of the signal-to-noise (S/N) ratio in the End Cap calorimeter indicated the counters in the upstream innermost ring should be treated separately. In addition, to deal with multiple hits, the double pulse fitting was performed to the waveforms for all counters in the calorimeter. An additional cut was introduced for the observed second pulses (two cuts).
- The study of the single-end hits indicated necessity of the cut for unpaired hits. Without this cut, they were considered to be one of the photon missing processes.

  There were four categories for single-end hits.

  1. BAST category : A hit was found at the both ends in the ADC records. However, in the TDC records, the hit was found at only one end.

     Other three categories are defined in the same way, where “S”(“B”) stands for single-end (both-end) and “A” (“T”) stands for ADC (TDC). “N” means that no hit was found at both ends.
  2. SAST category
  3. SABT category
  4. NABT category

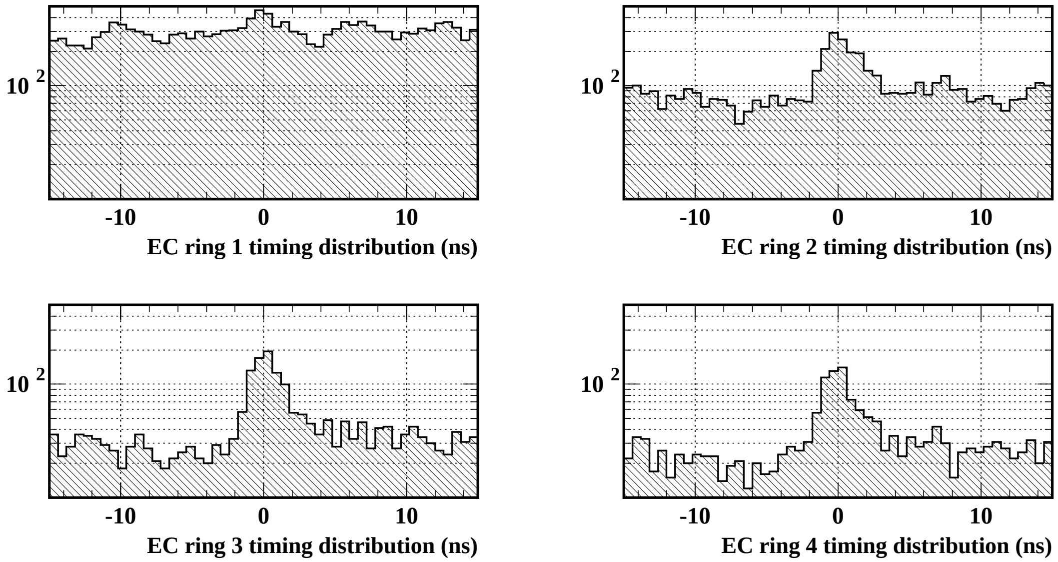

Figure 57: Photon hit distribution in the End Cap calorimeter (EC). One counter was chosen from each ring at the upstream end. All plots were made with a sample of 10^5 $K_{\pi 2}$ events. The innermost ring (upper left plot) was exposed to high accidental rates by the beam, and it was hard to identify the prompt peak. However, being away from the beam line, clear peaks with better signal to noise ratio could be seen.

> These four cuts were introduced to each of the BV, and Range Stack. For the BVL, only BAST was introduced (9 cuts in total).

In summary, 22 cuts in total were introduced for the offline photon veto. As shown in the EC hit study, the balance of the cut tightness needed to be optimized based on the S/N ratio. Thus, the cuts were designed to be simple for the optimization.[23] The designed algorithm was :

- Events are rejected if the total energy in the timing window of $T^i_{off} \pm T^i_{win}$ is greater than E^i_{Thr}, where T^i_{off} is the timing offset of the window, T^i_{win} is the half width, and E^i_{Thr} is the energy threshold. The superscript i is the index to address the cut category, which runs through 1 to 22.

The offline photon veto was applied regardless of whether the photon came from π^0 or not. The acceptance loss could be lightened if the offline photon veto was applied only to the reconstructed π^0 events. However, the rejection was limited by a poor detection efficiency of low energy photons or photons escaping to the beam line direction. The inefficiency was revealed later, but with rough estimation, it was $10^{-3} \sim 10^{-2}$. This was disastrous for the $\pi^0 \to \nu\overline{\nu}$ search.

---

[23] If the algorithm is complicated and involves many degree of freedom, the optimization is captured in the local minimum, since we handles many free parameters with 22 categories.

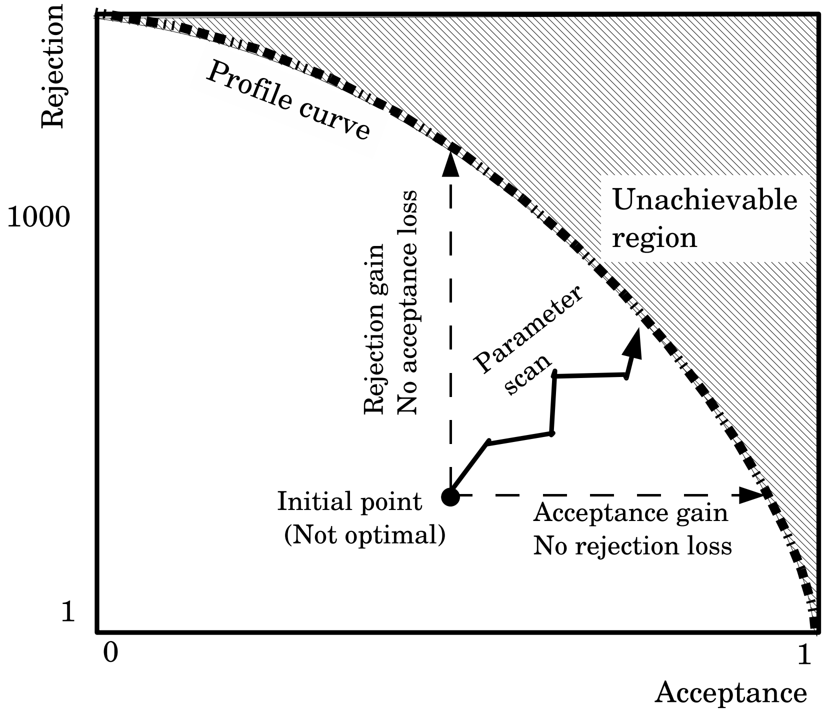

Figure 58: Illustration of optimization process to determine the photon veto parameters.

4.5.6 Optimization of the offline $\pi^0 \to \gamma\gamma$ cuts

The sensitivity to the $\pi^0 \to \nu\overline{\nu}$ search is proportional to "$\pi^0 \to \gamma\gamma$ rejection (equivalent to photon veto rejection)" × "$\pi^0 \to \nu\overline{\nu}$ acceptance". It was worthwhile to search for the best parameters that gave the most efficient rejection by measuring rejection and acceptance simultaneously.

There were 22 cuts in the the offline photon veto, each of which had three free parameters; the offset of time window, half width of the window, and the energy threshold. The optimization procedure handled 66 free parameters during the parameter scan.

Optimization process The optimization process started from the initial set of cut parameters. They were not required to be optimal. $K_{\pi 2}$ events from the 1/3 sample were used for the rejection measurement. Kinematically tagged $K_{\mu 2}$ events were used for the acceptance measurement. The $K_{\mu 2}$ events should not have any activity other than the muon track, and the event signature was close to the $K_{\pi 2}$ decay with $\pi^0 \to \nu\overline{\nu}$.[24] Every time a new set of parameters was introduced, the rejection and acceptance were re-measured with them. This sequence was performed for all the cut categories ($1 \sim 22$) with a rule that when one category was perturbed, all the other categories were kept unchanged. If the rejection successfully increased without losing the acceptance or the acceptance increased without losing rejection, this would be a candidate of the next tuning point. More preferable case was that both rejection and acceptance improved. This is illustrated in Figure 58. In the candidates, the most preferable cuts, which corresponds

---

[24] Any unknown systematics error, which might be from the charged track and not relevant to photon veto, was canceled out by taking the ratio of them.

to an movement to the 45-degree direction in the figure, was chosen as the next tuning point.

This algorithm always involved a risk that the parameters fell into a local optimum. However, the simplified cut design would help to reduce the risk. This was because there were straightforward relations. The relations are described as follows,

- Lower energy threshold would give larger rejection.
- Wider veto window would give larger rejection.
- Window offset should always be around the peak position. (Not changed so much.)

The optimization process continued until no more gain was obtained in the rejection without losing the acceptance. The boundary point was measured at every given acceptance position. As a result, a profile curve, which gave the most effective rejection, was obtained.

4.5.7 Determination of the offline $\pi^0 \to \gamma\gamma$ cuts

The profile curve from the optimization process is shown in Figure 59. In the figure, total $\pi^0 \to \gamma\gamma$ rejection and $\pi^0 \to \nu\overline{\nu}$ acceptance are shown with multiplication of the online rejection and acceptance. The open triangles show the profile curve of the best achievable performance, and the closed triangles show the net rejection to $\pi^0 \to \gamma\gamma$ by subtracting acceptance loss due to accidental activities. At the smallest acceptance point around 0.1, the optimization was stopped with a rising curve even though there seemed to be a room to obtain further rejection with sacrificing the acceptance. This was due to the small number of the remaining entries (21 events) after all the offline cut imposition. When the number of remaining entries was small, the tuning results might be biased by the small sample. [25] However, we decided to use the parameters (which corresponds to the point placed in the left end in Figure 59) in the final offline photon veto, by assuming the point gave the largest effective rejection. The finalized parameters were listed in Table 26. The remeasured acceptance (C_{acc}) with independent $K_{\mu 2}$ sample with the finalized cut was $C_{acc} = 0.117 \pm 0.002$.

5 Results

5.1 Opening the signal region

After the development of the cuts by using the 1/3 sample, all the offline cuts, including the final photon veto cuts, were imposed to the untouched 2/3 sample. As a result, a total of 99 events were observed in the signal region. Properties of the observed candidates were examined.

The contamination of the two-beam backgrounds, which were the most dominated non-$K_{\pi 2}$ backgrounds (see Table 19 on page 75), tended to have a flat distribution in the time difference between the pion time and the kaon time. The kaon decay-time distribution was plotted in

---

[25] For example, if two events in the remaining ~ 20 events have in reality a hit due to accidental, the effective rejection has a significant improvement by setting a veto window to remove the accidental hits. This situation can be reduced when the statistics is enough large. However when the statistics is small, this kind of the bias appears.

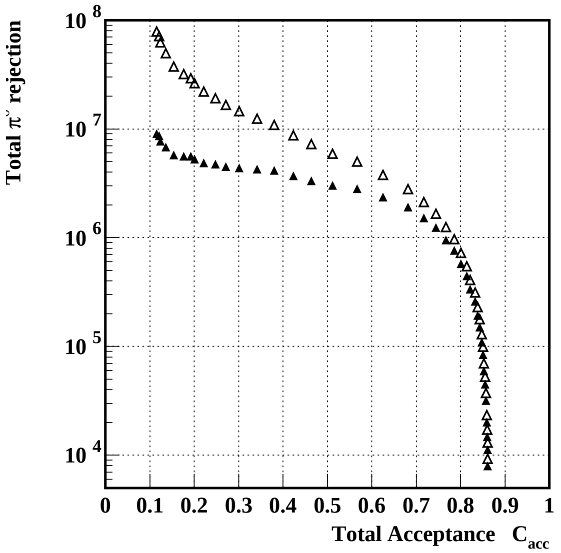

Figure 59: Obtained profile curve in the optimization process. The plot with open triangles was measured with the 1/3 sample. The closed triangle showed the total $\pi^0 \rightarrow \gamma\gamma$ rejection $\times$ total acceptance as a function of total acceptance. It indicates the effective $\pi^0 \rightarrow \gamma\gamma$ rejection (net rejection) where over-rejection caused by accidentals was corrected.

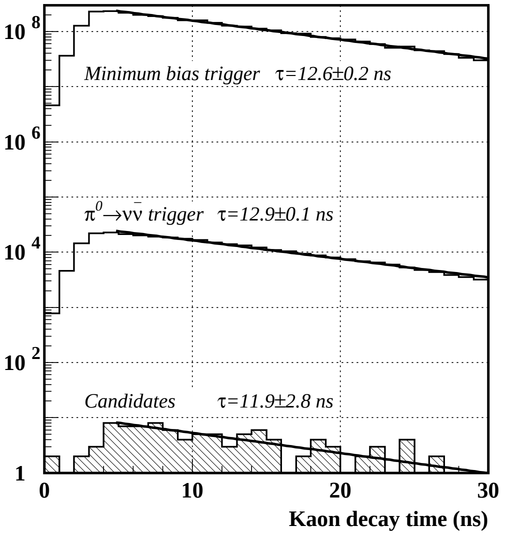

Figure 60: Kaon decay-time distribution with various levels of the photon veto. All the other cuts except the offline delayed-coincidence cut were imposed. The distribution was found not to be distorted by the photon veto, confirming that the sample was dominated by kaon decays. The depletion of events near time zero was due to trigger requirements to suppress single beam particle backgrounds. Decay-time fits were performed for each plot in the time range of [4ns:30ns]; no evidence of two-beam background was found.

Figure 60 to see the contamination of the two-beam backgrounds. There was no evidence of the apparent two-beam backgrounds in the plot. A fitted lifetime of 11.9 ± 2.8 ns was consistent with the kaon lifetime of 12.4 ns. In order to see the existence of other non-$K_{\pi 2}$ backgrounds, momentum distribution was plotted without the monochromatic π^+ box cuts (see Figure 61). Again, there was no indication of the apparent single beam backgrounds, and other non-monochromatic backgrounds. Therefore, these events did not stem from the impurity of the $K_{\pi 2}$ tagging. The remaining possibility was that they came from $\pi^0 \rightarrow \gamma\gamma$ decay due to the incompleteness of the photon veto.

Table 26: Parameters for offline photon veto from the optimization process.

Category ID	System	Attribute	T_{Offset} (ns)	T_{Win} (ns)	$E_{Thr.}$ (MeV)
1	BV		6.198	11.500	0.400
2	BVL		1.200	2.300	0.000
3	BV	Early hit veto	-9.000	28.400	29.600
4	BVL	Early hit veto	-22.600	26.400	7.300
5	EC		6.062	16.800	0.109
6	RS		10.895	26.275	0.200
7	TG		-0.600	2.300	1.690
8	IC		2.250	4.950	0.200
9	VC		0.650	2.500	1.200
10	CO		3.150	3.350	1.400
11	CM		-1.000	3.000	0.800
12	EC	Ring 1	8.180	16.200	0.192
13	BV	SAST	-10.700	9.500	1.800
14	RD	SAST	0.400	4.800	14.000
15	RD	SABT	2.500	5.500	0.000
16	RD	NABT	0.750	2.000	0.400
17	RD	BAST	12.900	1.200	10.200
18	BV	SABT	3.700	3.000	0.000
19	BV	NABT	0.300	2.400	4.800
20	BV	BAST	13.100	11.400	0.300
21	EC	Second pulse	-5.300	1.200	18.600
22	BVL	BAST	-0.200	14.400	11.400

5.2 $\pi^0 \to \gamma\gamma$ backgrounds

The primary reasons for failure to detect photons from π^0 decay in the $K_{\pi 2}$ events were (1) the sampling fluctuations in the electromagnetic shower of low energy photons around 20 MeV and (2) the photonuclear interactions of high energy photons with undetected products, such as neutrons. While the effects of electromagnetic interactions can be well simulated, there were large uncertainties due to photonuclear processes in the simulation, associated with the detailed modeling of detection inefficiencies. Therefore, the overall background contribution from $\pi^0 \to \gamma\gamma$ decays, in which both photons went undetected, was difficult to estimate in the Monte Carlo simulation reliably. Instead, we developed a way to measure the photon missing probability with real data. The technique and its validity will be described in the subsequent chapters. At this point, we considered all the 99 events were backgrounds from $\pi^0 \to \gamma\gamma$ decay, but, with a conservative attitude, we set an upper limit on the decay by assuming they were all signals.

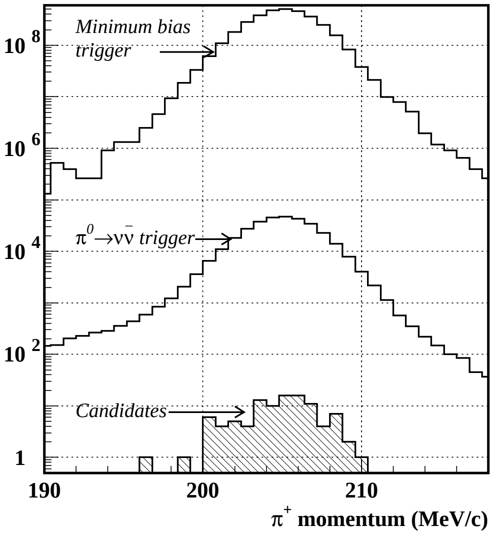

Figure 61: π^+ momentum distribution with various levels of the photon veto cut. All the other cuts except for the signal box cuts were imposed. No evidence of the single beam background, which would make a broad distribution in the momentum plot, was observed.

5.3 Branching ratio for the decay $\pi^0 \to \nu\overline{\nu}$

By rewriting Equation 6 in section 2.2, the 90 % confidence level (C.L.) upper limit of the $Br(\pi^0 \to \nu\overline{\nu})$ is represented by

$$Br(\pi^0 \to \nu\overline{\nu}) < \frac{N_{90}}{N_{\pi^0}} \cdot \frac{1}{C_{dis} \times C_{acc}} \tag{26}$$

where N_{90} indicates the 90 % C.L. upper limit for the mean of Poisson statistics when N events are observed. Based on the 99 events observation, the number of signal events was limited to be < 113 at 90 % C.L. Subtracting the non-$K_{\pi 2}$ background of approximately three events, N_{90} resulted in 110. Number of recorded π^0 (N_{π^0}), and correction factors (C_{dis} and C_{acc}) were evaluated in previous sections (4.4.7, 4.4.8 and 4.5.7) to be 3.02×10^9, 1.14, and 0.117, respectively. By substituting these values, the upper bound on the $Br(\pi^0 \to \nu\overline{\nu})$ was obtained as :

$$\begin{aligned} Br(\pi^0 \to \nu\overline{\nu}) &< \frac{110}{3.02 \times 10^9} \cdot \frac{1}{1.14 \times 0.117} \\ &= 2.7 \times 10^{-7} \end{aligned} \tag{27}$$

As a result of the analysis, the new upper limit of $Br(\pi^0 \to \nu\overline{\nu}) < 2.7 \times 10^{-7}$ has been obtained. The result is three times better than the previous best result [18]. The upper limit obtained above is sensitive to any hypothetical weakly-interacting particles, whose masses are less than half of the π^0 mass.

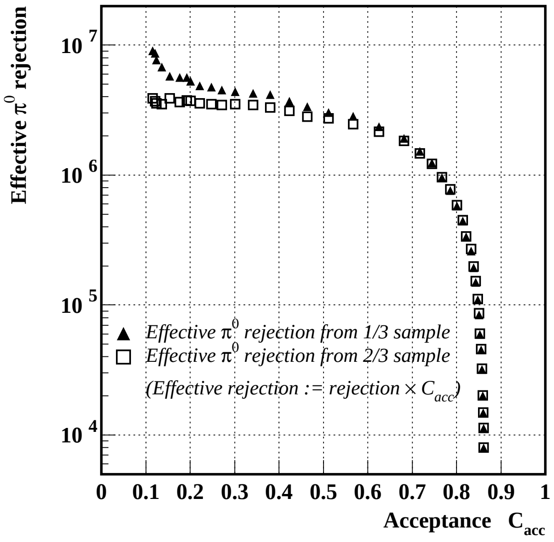

Figure 62: Effective $\pi^0 \to \gamma\gamma$ rejection measured with the 1/3 and 2/3 sample. The closed triangle shows the effective rejection of the 1/3 sample and the open rectangle shows that of the 2/3 sample. Although the plot of the 1/3 sample shows steady increment at the low acceptance region, the plot with the 2/3 sample shows saturation at acceptance < 0.35. The saturation indicates the best performance of the E949 photon detector. The net $\pi^0 \to \gamma\gamma$ rejection is 3.5×10^6.

5.4 Discussions

Photon distribution of the surviving events To see a possibility for further improvement, ADC and TDC records of the survived events were closely examined. Typically, there were activities, which had low energies below the threshold and/or whose timings were out of the window, in the barrel photon detectors : BV and BVL (see Figure 63). Figure 64 shows the correlation between photon hits in the BV and the π^+ direction of the survived events. In case of $\pi^0 \to \gamma\gamma$ decay in $K_{\pi 2}$, the photon direction tends to correlate with the π^+ direction, while it would be uniform in case of pure accidental hits. The photon hits from the survived events seemed to have a non-uniform distribution, and thus, some fraction of the hits could be considered as photons from $\pi^0 \to \gamma\gamma$. The reason to screw up the timing measurement of the real photons from $\pi^0 \to \gamma\gamma$ might be the incompleteness of the treatment of "masking" effect (see section 4.5.4) and/or the delayed activities from the photonuclear interactions.

$\pi^0 \to \gamma\gamma$ **background subtraction** Assuming all the remaining events were $\pi^0 \to \gamma\gamma$ backgrounds, the effective $\pi^0 \to \gamma\gamma$ rejection was plotted in Figure 62. The plots with the 1/3 and 2/3 sample showed a good agreement in the high acceptance region of $0.7 < C_{acc} < 1.0$. However, the discrepancy was enlarged at small acceptance. The steep curve, observed at the low acceptance region with the 1/3 sample, came from over-tuning effect caused by the small number of remaining events. The observed discrepancy between the curves of the 1/3 and 2/3 samples indicated that we succeeded to avoid biased results by using independent samples for the tuning and the branching ratio measurement.

The saturation in the plot of the 2/3 sample at the acceptance of less than 0.35 indicated that the sensitivity to the $\pi^0 \to \nu\overline{\nu}$ was limited by the E949 detector performance. There was less room to improve the rejection with improvement of the offline photon veto. To achieve further improvement, the apparent $\pi^0 \to \gamma\gamma$ backgrounds, which were from the detector inefficiency, should be subtracted. However, the Monte Carlo simulation was not reliable to reproduce the inefficiency due to the photonuclear interactions. This was because the time constant of the evaporation and the kinetic energy of the evaporated particle in the interactions had an uncertainty. Based on this discussion, the new technique to measure the detector photon inefficiency with real data was developed in the next section.

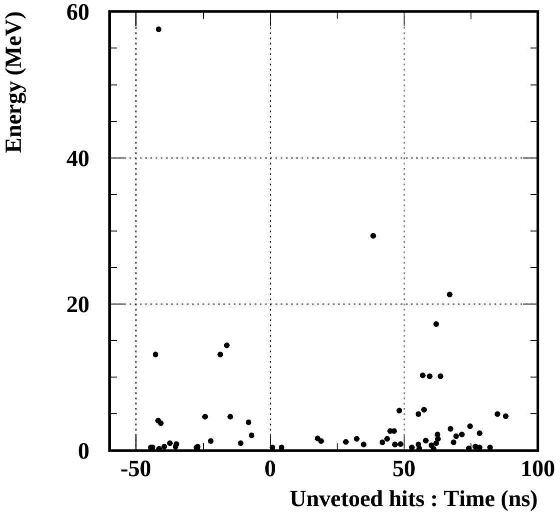

Figure 63: Energy vs timing plot of the hits observed in the BV in the survived events. These were not used for the veto since their energies were below the threshold (0.4 MeV) and/or their timings were not on-time (-5.3 ns $< t_{window} <$ 17.7 ns).

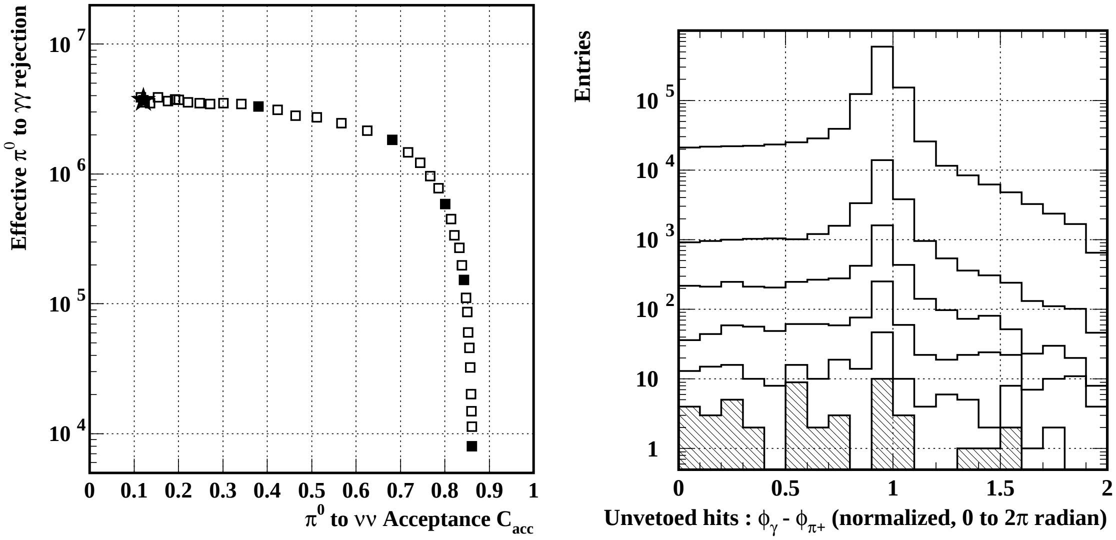

Figure 64: Distribution of the azimuthal opening angles between π^+'s (ϕ_{π^+}) and photon hits (ϕ_γ), which were observed in the BV in the survived events. Six photon veto cuts with different levels of tightness were selected from the left figure (denoted with five closed squares and a star) and the opening angle distributions "ϕ_γ - ϕ_{π^+}" of the survived events were plotted in the right figure. The photon veto cut used in the $\pi^0 \rightarrow \nu\overline{\nu}$ search is indicated with a star in the left figure and a hatched histogram in the right figure.

6 Measurement of Single Photon Inefficiency with the E949 detector

The study of single photon inefficiency was carried out for the purpose of understanding the surviving events in the signal region, and for further improvement by $\pi^0 \to \gamma\gamma$ background subtraction in the $\pi^0 \to \nu\overline{\nu}$ search.

6.1 Motivation and goal of the study

There are several known mechanisms causing photon inefficiency; (1) dead materials, (2) detector hole, (3) lack of radiation length, (4) sampling fluctuation, (5) photo-nuclear interaction, (6) masking effect from preceding accidentals and so on. Some are well studied and the contribution can be estimated precisely but some are not. The goal of this study is to quantify each contribution as much as possible with actual data, and if possible, to subtract the $\pi^0 \to \gamma\gamma$ backgrounds accurately without using Monte Carlo estimation. These motivations are elaborated as follows.

1. Where and how do the $\pi^0 \to \gamma\gamma$ backgrounds come from ? The mechanism and geometrical distribution should be investigated. If energy dependence of photon inefficiency is measured, it would allow us to discriminate the inefficiency of photo-nuclear interaction from that of sampling fluctuation. Also if geometrical dependence is measured, the existence of dead materials and inefficiency caused by the beam hole may be revealed.

2. How much are they ? We want to determine the number of the $\pi^0 \to \gamma\gamma$ background events accurately and reliably. If this is done, we are able to subtract them in the signal region, and to improve the sensitivity of $\pi^0 \to \nu\overline{\nu}$.

3. Is there any characteristics or signature to discriminate the $\pi^0 \to \gamma\gamma$ backgrounds from the $\pi^0 \to \nu\overline{\nu}$ decays ? If the photon inefficiency has a geometrical dependency, the distribution of the $\pi^0 \to \gamma\gamma$ backgrounds would reflect the dependency. On the other hand, since $\pi^0 \to \nu\overline{\nu}$ decays have no photon in the final state, they will not. The difference may provide a discrimination capability.

4. Is there better way to kill the backgrounds more effectively? Once we make clear the inefficiency mechanism, there is a chance to invent a better cut against the inefficient part.

5. Any possible feedback for next coming experiments.

   The study could provide a lot of interesting information in the techniques of the photon veto. Following studies were performed with the technique developed in this study, though we do not go into the specifics in this thesis.

   - Case 1; To parameterize the effect of dead materials placed in front of the photon detector, the study was performed with a modification of turning off a few inner plates of the Range Stack. The results, changing the number of masked scintillator plates, provided the reliable inefficiency by dead materials as a function of scintillator equivalent length. The results was used as Monte Carlo inputs.

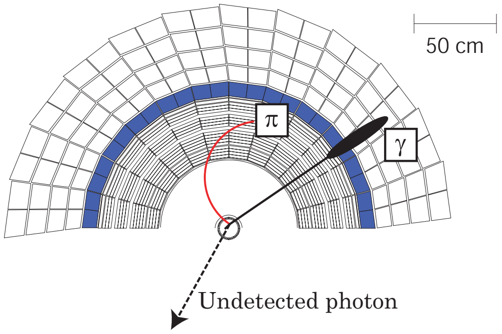

Figure 65: Illustration of the idea on the measurement of single photon inefficiency. The left figure shows an event signature of a $K_{\pi 2}$ decay with $\pi^0 \to \gamma\gamma$ from a kaon at rest. The kinematics of the mis-detected γ can be computed from that of all other particles by momentum balance. The rate of the one-photon missing events tells the mis-detection probability of the photon detectors.

- Case 2 : The single photon inefficiency was measured with common energy thresholds. This was used for the tuning of Monte Carlo simulation at the design stage of photon veto in other experiment.
- Case 3 : Rejection loss with shorter radiation length was studied.

6.2 A basic idea of the study and an analysis strategy

In the section below, the concept of the inefficiency measurement and outline of its analysis will be briefly explained.

The idea of the measurement of single photon inefficiency In this study, the kaon decays at rest, $K^+ \to \pi^+\pi^0$ with $\pi^0 \to \gamma\gamma$, were employed. Even if one photon was undetected, the kinematics of the missing particle could be extracted from the momentum balance with other particles as explained schematically in Figure 65. The reconstruction of the missing photon could tell us its flight direction and energy on an event-by-event basis, and the rate could tell how often a photon was missed in the detector. The combined information provided a map of photon inefficiency as a function of detector geometry and photon energy.

Analysis strategy The inefficiency was measured by comparing distribution of detected photons with that of missed photons. The former was obtained from the events with $K_{\pi 2}(1)$ trigger while the latter was collected with special trigger called “1-gamma”. From the $K_{\pi 2}(1)$ events, photons were identified and classified according to their polar angle θ and energy E. The number of photons $N^{\text{denom}}(\theta, E)$ was called “SPI denominator map”. From the 1-gamma events, kinematic variables of undetected photons were calculated and binned in the same as detected photons. The number of missed photons $N^{\text{numer}}(\theta, E)$ was called “SPI numerator map”. By introducing a normalization factor A_{norm}, which compensated the trigger scale factor, the photon inefficiency map was obtained as

$$\frac{N^{\text{numer}}(\theta, E)}{N^{\text{denom}}(\theta, E)} \times A_{\text{norm}} \tag{28}$$

Note that the azimuthal angle of ϕ is not parameterized in the map because the E949 detector had an axial symmetry.

6.3 The data sample and the trigger conditions

As explained in the previous section, the study used two data sets which were obtained with different triggers: the minimum-bias $K_{\pi 2}(1)$ trigger and a special 1-gamma trigger. The 1-gamma trigger was based upon $K_{\pi 2}(1)$ with additional conditions on photons, and was defined by

$$\text{1-gamma} \quad \equiv \quad K_{\pi 2}(1) \cdot DC \cdot L1.1 \cdot BV \cdot \overline{NG2} \cdot HEX \cdot L1.2 \cdot \overline{EC} \qquad (29)$$

In the definition, "BV" is a requirement of photon hit in the BV, and $\overline{NG2}$[26] is a requirement of the observed photon cluster being less than 2 in the BVL. The condition of "$HEX \cdot L1.2 \cdot \overline{EC}$" is to reject second photons. A total of 1.7×10^6 events were collected with the trigger condition.

6.4 $K_{\pi 2}$ selection criteria and the event purification

The single photon inefficiency study required a very large number of events because the inefficiency was expected to be very small and, in addition, the data were binned with θ and E. On the other hand, the purity of $K_{\pi 2}$ was less stringent than that for the $\pi^0 \to \nu\overline{\nu}$ case. Therefore, the $K_{\pi 2}$ criteria were relaxed to increase usable events. The details of the re-designed $K_{\pi 2}$ criteria will be explained in the Appendix A.11 on page 140. In the 1-gamma sample, the dominated backgrounds came mostly from $K^+ \to \mu^+\nu_\mu\gamma$ and $K^+ \to \mu^+\nu_\mu$ decays with an accidental hit in the BV. In the selection criteria, π^+-μ^+ identification with π^+ decay trace cuts and dE/dx cuts in the Range Stack were used for the rejection.

The decay of $\pi^0 \to e^+e^-\gamma$, which has a photon in the final state, meets the condition of the 1-gamma trigger. If the reconstruction is performed with an assumption of $\pi^0 \to \gamma\gamma$, a faulty missing photon was made. This backgrounds were well suppressed because the charged particles e^+ and e^- make the tracks in the target and the probability of missing two charged tracks was smaller than the case of one-photon missing. The events were never observed in the SPI numerator map.

6.5 Photon reconstruction

6.5.1 Obtaining visible fractions in Barrel Veto and Barrel Veto Liner

To retrieve absolute photon energy,[27] the visible fractions of the BV and BVL were calibrated with the π^0 total energy (246 MeV) of the $K_{\pi 2}$ decay. After rejecting events with any activity in other photon detectors, the energy of π^0 was reconstructed by changing the BV and BVL visible fractions. Figure 66 shows the plots of reconstructed peak position (left plot) and the peak width (right plot). The BV and BVL visible fractions were determined at a point where

---

[26] $\overline{NG2}$ is an abbreviation that the Number of Gamma cluster must be less than 2.

[27] Partial energy observed in the scintillator plates in the BV and BVL was calibrated with "punch-through" muons.

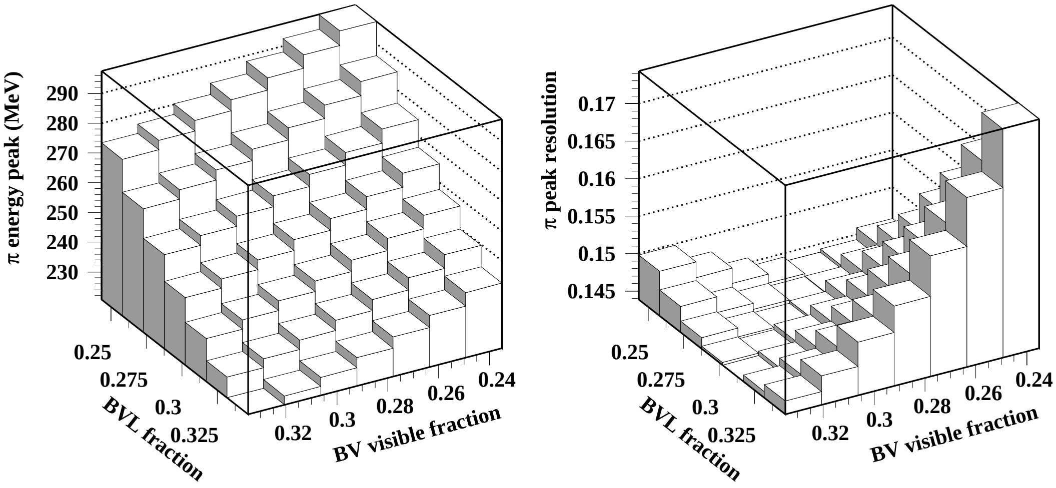

Figure 66: Peak position (left) and width (right) of the reconstructed π^0 energy as a function of the BV and BVL visible fractions. In the right figure, the width was normalized by the absolute peak position. The set of (BV, BVL) visible fractions, that gives the correct π^0 energy and the best resolution, was used as calibration constants.

Table 27: Measured visible fractions of the BV and BVL.

System	Visible fraction
Barrel Veto	0.295
Barrel Veto Liner	0.321

the correct peak position and the best resolution were obtained. The measured result was 0.295 for BV and 0.321 for BVL, as summarized in Table 27.

6.5.2 Obtaining a z position of each photon hit

The BV and BVL were 2-m long scintillator plates and were not segmented in the beam direction. The z hit positions were obtained by comparing energy and/or arrival timing at both ends. From the timing measurement, the z position (z_{time}) was reconstructed as

$$z_{time} = \frac{v}{2}\{T(1) - T(2)\} + A_{time,offset} \tag{30}$$

where v is a calibrated constant of the effective light velocity in the scintillator, $T(i)$ is signal arrival time at the end i (i=1 for downstream, i=2 for upstream). $A_{time,offset}$ is a constant to remove instrumental offsets.

From the energy measurement, the z position (z_{energy}) was reconstructed as

$$z_{energy} = \frac{\lambda}{2} log \frac{E(2)}{E(1)} + A_{energy,offset} \tag{31}$$

where λ is a light attenuation length and $E(i)$ is energy measured at the end i. $A_{energy,offset}$ is a correction to remove an offset away.

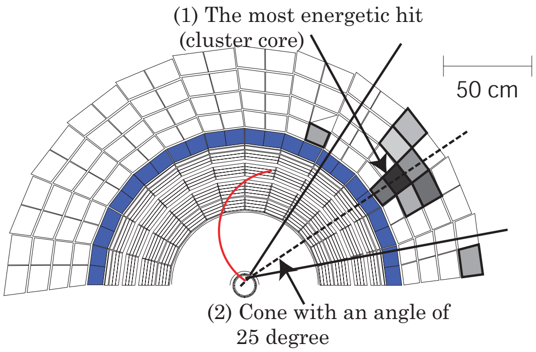

Figure 67: Illustration of the photon clustering method. The most energetic hit, which was indicated by the darkest color, was assigned to the cluster core. A cone was defined with referring to the kaon decay point and the core. Any hit in the cone was collected, assuming that the activities originated from a single photon. Two hits seen outside of the cone were supposed to come from other photons or noises.

Combining the both measurements, the most reliable z position $z_{combine}$ was obtained as

$$z_{combine} = \frac{z_{timing} + z_{energy} \times \sqrt{E/10}}{1 + \sqrt{E/10}} \tag{32}$$

where E is energy sum of both ends. The weight of $\sqrt{E/10}$ is an empirical factor found in the prior studies [42].

6.5.3 Clustering of incident photons

The hit information of the individual counters in the BV and BVL, described in the previous subsection, was gathered to identify photon's cluster, energy, direction and timing. The analysis method is described below.

1. The most energetic hit in the barrel modules was assigned as a cluster core (see Figure 67). The hit timing was employed as cluster reference time.
2. A cone with an angle of 25 degree was defined with assigning the kaon decay position to the cone's vertex and the cluster core to the cone's axis.

   The minimum opening angle of two photons from π^0 of $K_{\pi 2}$ was 60 degree at the kaon rest frame. The cone angle was designed not to include the both photons in the single cone.
3. Any photon activity inside the cone was summed up when the hit time was around ± 3 ns from the cluster reference time.
4. The photon energy was defined as the total energy of the BV and BVL in the cone. The flight direction and timing were computed from the energy weighted mean of each hit.
5. The cone was re-defined with the reconstructed information. The cluster reference timing was updated with the averaged timing. Above sequence was iterated with the updated cone.

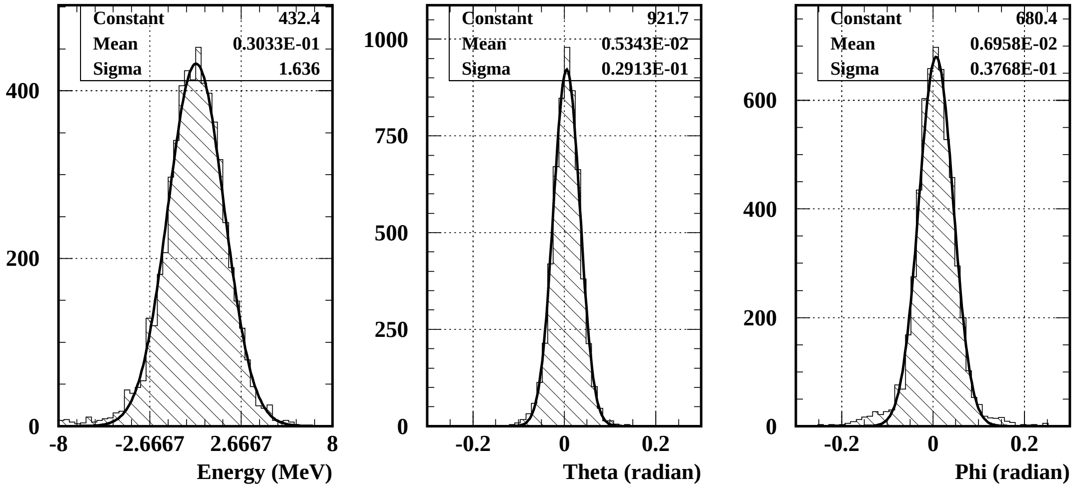

Figure 68: Reconstructed resolutions with the clustering method. All plots were measured with Monte Carlo $K_{\pi 2}$ sample. The left plot is a residual distribution of the reconstructed energy from the true energy. The center (right) plot is a residual of the reconstructed polar (azimuthal) angle from the generated value in the Monte Carlo simulation.

Table 28: Resolutions of the reconstructed variables by the photon clustering method. A sample from the Monte Carlo simulation was used for the evaluation of the clustering method.

Kinematics variables	Resolution (radian)
Polar angle (θ)	0.028
Azimuthal angle (ϕ)	0.039

6.5.4 The reconstruction performance

The performance of the clustering method was examined with a sample of $K_{\pi 2}$ events generated with Monte Carlo simulation. The residual distributions of the photon energy, polar angle and azimuthal angle are plotted in Figure 68. The obtained resolutions are summarized in Table 28. In particular, clustering method showed good azimuthal angle resolution; the obtained resolution of 0.039 radian was equivalent to 1/3 $\sim$ 1/4 of the BV rod.[28].

6.6 Tagging-photon selection criteria

Tagging photon, selected from reconstructed photons, is a photon whose kinematics is used to compute the undetected photon's kinematic variables. Selection criteria for the tagging photon were important not to include fake photons.[29]

---

[28] $1/3 \times 2\pi/48$ modules $= 0.0436$ radian, $1/4 \times 2\pi/48$ modules $= 0.0327$ radian

[29] For example, suppose we were measuring an inefficiency of $10^{-2} \sim 10^{-4}$. If poorly reconstructed tagging photons caused cross talks from the region with 10^{-2} inefficiency to that with 10^{-4}, the region with 10^{-4} inefficiency would be measured as 10^{-2}. This should be suppressed as much as possible by the selection criteria for the tagging photon.

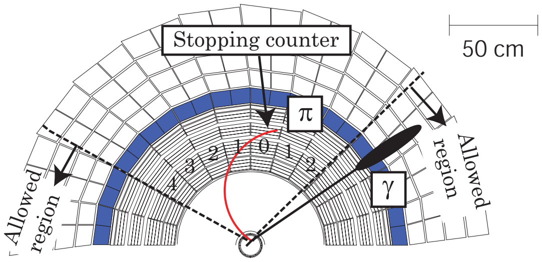

Figure 69: Schematic view of the overlapping photon cut. Any photon cluster, which was placed within 4 (2) sectors from the π^+ stopping counter in the anticlockwise (clockwise) direction, was not used as the tagging photon. Energy from the π^+ and the photon might be mixed up.

1. Timing selection : The cluster time must be within ± 3 ns from the π^+ track time determined by the Range Stack.
2. Energy selection : The cluster energy must be more than 15 MeV.

   Note that the minimum energy of photons from $\pi^0 \to \gamma\gamma$ of $K_{\pi 2}$ is $\sim$ 20 MeV. The cut condition was set considering the energy resolution.
3. Fiducial selection : For a confirmation that all energy was included in the detector with no shower leakage, the following fiducial requirements were imposed.
   - (a) Conversion position : Conversion must begin at inner region of the photon detector. The BVL and the layer 1 of BV must have energy more than 10 MeV in total.
   - (b) Photon flight direction : The photon dip angle of θ must satisfy $|\cos(\theta)| < 0.45$. This condition is to avoid the area where the radiation length is less than $15X_0$, as shown in Figure 18 on page 36.
   - (c) Overlapping photon cuts : The tagging photon must be well separated from a charged track trajectory. As shown in Figure 69, it must be 4 sectors away from the track in the anticlockwise direction, and 2 sectors away in the clockwise direction.

   More details on the cut, together with the distributions of the candidates before imposing the selection criteria, are described in the dedicated section in the Appendix on page 150.

6.7 Full reconstruction of $K_{\pi 2}$ events and missing photon kinematics

The events, which passed $K_{\pi 2}$ selection criteria and had a tagging photon in fiducial, was reconstructed to extract the kinematics of the missing photon. Note that, in addition to the prime aim, the kinematic fitting rejected unrealistic events by imposing physics requirements (constraints). For example, the photon which was emitted to the opposite direction of the π^+, should have a larger energy by the π^0 boost. If smaller energy was observed, energy leakage might occur and the event should be discarded or, if possible, it should be replaced with proper energy by

Table 29: Input variables for kinematical fitting (Monte Carlo data). A total of ten variables were used. For a technical reason, cosine was pre-calculated for θ_{π^+}. Note that the π^+ momentum employed the ideal number of 205 MeV/c with no measurement error.

Variables	Notation	Resolution
- π^+ kinematics -		
Momentum	P_{π^+}	— (ideal)
Polar angle	$\cos(\theta_{\pi^+})$	0.029 (radian)
Azimuthal angle	ϕ_{π^+}	0.028 (radian)
- Tagging photon kinematics -		
Energy	E_{tag}	$1.8\sqrt{E_{tag}}$ (MeV)
Polar angle	θ_{tag}	0.028 (radian)
Azimuthal angle	ϕ_{tag}	0.039 (radian)

the fitting. Actually, the kinematical fit was performed with physical constrains of π^0 invariant mass and momentum conservation with the Lagrange multiplier method.

6.7.1 Kinematical fit with the Lagrange multiplier method

The Lagrange multiplier method is a technique to minimize a given variable, in this case, χ^2 defined as Equation 33, under a set of given constraints. It takes measured variables ($X_{meas,i}$) and their resolutions (σ_i) as inputs and returns the best estimates of the unmeasured variables as well as measured variables ($X_{fig,i}$). The goodness of the kinematical fitting is indicated by the obtained χ^2. Details on the technique are described on page 151 in Appendix.

$$\chi^2 = \sum_i \left(\frac{X_{meas,i} - X_{fit,i}}{\sigma_i} \right)^2 \tag{33}$$

In general, it is difficult to obtain accurate resolutions for measured variables[30]. Thus, the fitting procedure was pre-worked out with Monte Carlo simulation. And with an assumption that the data was not so far from the actual performance of the real detectors, the kinematical fitting was re-worked to real data with the resolutions which were extrapolated from stretch functions.[31]

6.7.2 Full reconstruction with Monte Carlo sample and the performance

Input variables Table 29 shows a list of the input variables and their resolutions which were obtained by the cluster reconstruction (see the table 28). Two π^+ kinematic variables of θ_{π^+} and ϕ_{π^+} and three γ kinematic variables of E_{tag}, θ_{tag} and ϕ_{tag}, totaling five inputs, were employed with the corresponding resolutions. The resolutions were measured with residuals from the Monte Carlo generated values.

---

[30] For the resolution measurements, the ideal reference was required to make the residual plots.

[31] The stretch function is explained in Appendix C.2.

Table 30: Performance of the kinematical fitting performed with Monte Carlo data. The resolutions before (after) the kinematical fitting are listed in the third (rightmost) column.

Variables	Notation	Resolution : Before	Resolution : After
		- π^+ kinematics -	
Polar angle	$\cos(\theta_{\pi^+})$	0.029 (radian)	(not measured)
Azimuthal angle	ϕ_{π^+}	0.028 (radian)	(not measured)
		- Tagging-photon kinematics -	
Energy	E_{tag}	1.6 (MeV)	0.59 (MeV)
Polar angle	θ_{tag}	0.028 (radian)	0.028 (radian)
Azimuthal angle	ϕ_{tag}	0.039 (radian)	0.038 (radian)
		- Missing-photon kinematics -	
Energy	E_{miss}	—	0.89 (MeV)
Polar angle	θ_{miss}	—	0.061 (radian)
Azimuthal angle	ϕ_{miss}	—	0.053 (radian)

Constraints There were four physical constraints. Three were from momentum conservation and the fourth was a constraint on the invariant mass of two photons (M_{γ_1,γ_2}) from $\pi^0 \to \gamma\gamma$:

$$\sum_i P_x^i = 0, \qquad \sum_i P_y^i = 0, \qquad \sum_i P_z^i = 0 \tag{34}$$

$$M_{\gamma_1\gamma_2} = m_{\pi^0} \tag{35}$$

where $P_{x(y,z)}^i$ is the x (y, z) component of the momentum for the particle i ($i = \pi^+$, γ_1, γ_2) and m_{π^0} denotes the π^0 mass.

Fitting performance and the extracted missing photon kinematics Figure 97 on page 153 in Appendix shows the resultant resolutions of the tagging-photon kinematics from the kinematical fitting with the Monte Carlo data. Comparing with the resolutions obtained in the clustered method (Figure 68), significant improvements could be achieved. The improvements were summarized in Table 30 including the resolutions of missing-photon kinematics.

The probability distribution of the minimized χ^2 is plotted in Figure 99 on page 154. The flat distribution indicates that the kinematical fitting worked well.

6.7.3 Kinematical fitting with real data

Stretch functions Stretch function for the i-th variable is constructed with the measured variable $X_{meas,i}$ and the corresponding fitted value $X_{fit,i}$ with an equation of

$$\frac{X_{meas,i} - X_{fit,i}}{\sqrt{\sigma^2_{meas,i} - \sigma^2_{fit,i}}} \tag{36}$$

Table 31: Resolutions of the measured variables (Real data). The third column shows the bridge factors C_i determined from the stretch functions. The fourth column shows the most likely resolutions.

Variables	Notation	Correction (C_i)	σ_{meas}^{real}
- π^+ kinematics -			
Momentum	P_{π^+}	—	— (ideal)
Polar angle	$\cos(\theta_{\pi^+})$	1.185	0.034 (radian)
Azimuthal angle	ϕ_{π^+}	1.196	0.035 (radian)
- Tagging photon kinematics -			
Energy	E_{tag}	1.157	$2.1\sqrt{E_{tag}}$ (MeV)
Polar angle	θ_{tag}	1.203	0.033 (radian)
Azimuthal angle	ϕ_{tag}	1.203	0.046 (radian)

where $\sigma_{meas,i}$ and $\sigma_{fit,i}$ are their resolutions. When the data set is specified, the variables carry a superscript such as $X_{meas,i}^{real}$ or $X_{meas,i}^{MC}$. The stretch function forms a normal Gaussian shape if the $X_{meas,i}$ and $\sigma_{meas,i}$ are proper. Examination of the function shape would tell the correctness or fault of the variables. The peak offset indicates systematic error in the $X_{meas,i}$ measurements, and the wider (narrower) width compared with the normal Gaussian indicates that the $\sigma_{meas,i}$ is underestimated (overestimated).

To determine the unknown resolutions for real data $\sigma_{meas,i}^{real}$ (i=1,$\cdots$5), the stretch functions were employed. Assuming each $\sigma_{meas,i}^{real}$ was close to that of $\sigma_{meas,i}^{MC}$, the kinematical fitting was performed with real data with $\sigma_{meas,i}^{real}$'s which were defining as $\sigma_{meas,i}^{real} \equiv C_i \sigma_{meas,i}^{MC}$ with bridge coefficients of C_i (i = 1, $\cdots$ 5). The process was repeated by changing the coefficients as shown in Figure 70 and the points with a peak width of 1 were selected as the most likely σ_{meas}^{real}. Table 31 shows the resultant coefficients and the σ_{meas}^{real}'s. To check the validity, the χ^2 probability distribution was checked in the subsequent paragraph.

The performance The performance of the kinematical fitting was checked with real data and the estimated $\sigma_{meas,i}^{real}$'s. Figure 71 shows the χ^2 probability distributions obtained by the kinematical fitting for the $K_{\pi 2}(1)$ (left) and 1-gamma (right) sample. Flat distribution in both plots indicates the kinematical fitting worked properly. The cut position was set at the χ^2 probability greater than 0.2. The resultant stretch functions are plotted in Figure 103 on page 157.

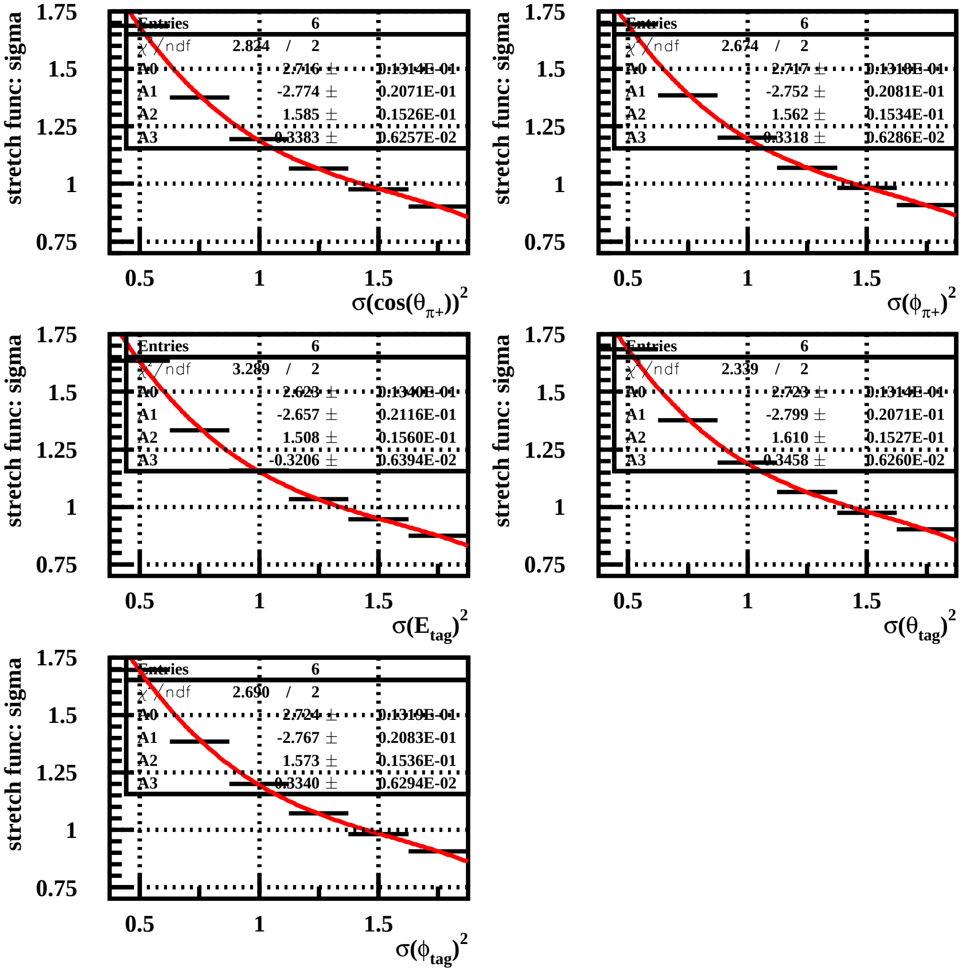

Figure 70: Resolution (σ^{real}_{meas}) measurements with stretch functions. Peak width of each stretch function was plotted as a function of $\sigma^{real}_{meas,i}$ by changing the C_i. Note that the $\sigma^{real}_{meas,i}$ was squared in the plots. The $\sigma^{real}_{meas,i}$ with a peak width of 1 was the most likely value.

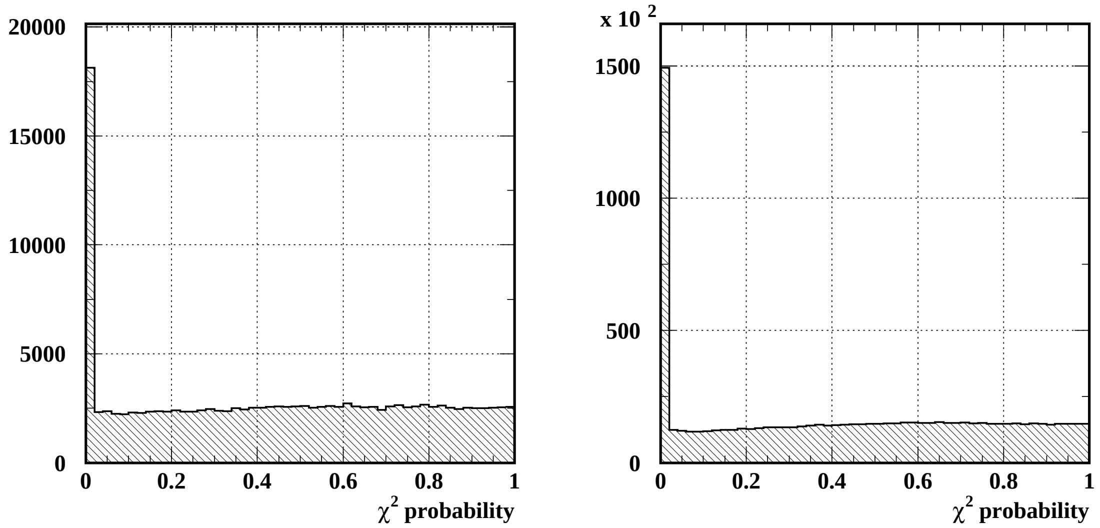

Figure 71: χ^2 probabilities from the kinematical fitting. The left (right) plot was made with a sample of $K_{\pi 2}(1)$ (1-gamma) events which were used for SPI denominator (numerator) map. Both show flat distribution. Peak at the χ^2 probability = 0 was made with events in which tagging photons were faultily reconstructed.

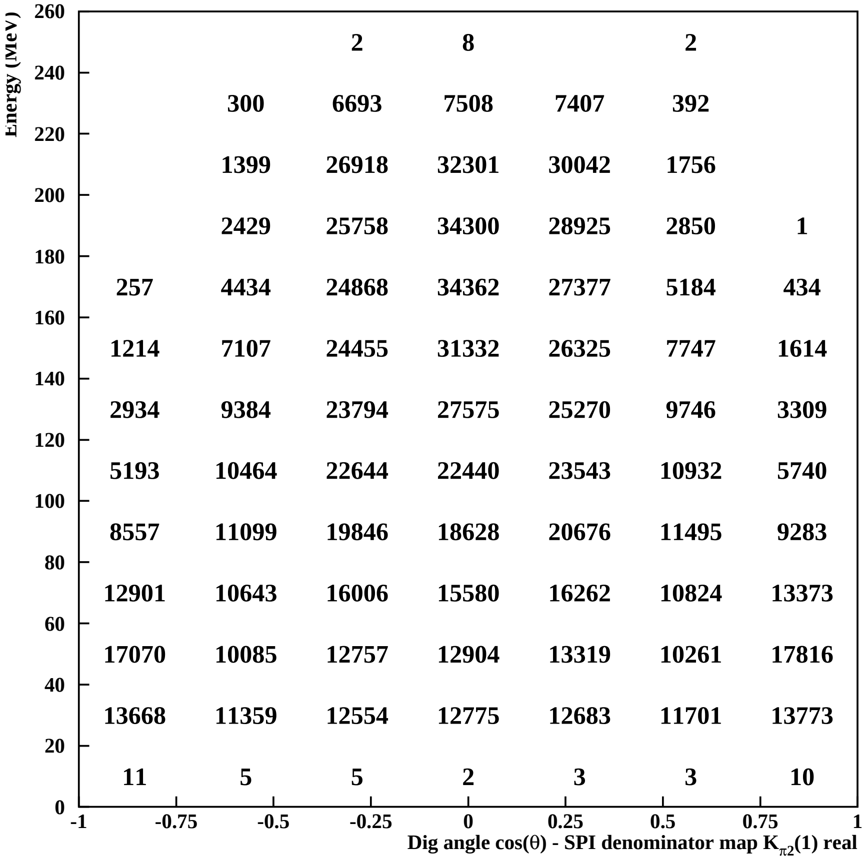

		2	8		2	
	300	6693	7508	7407	392	
	1399	26918	32301	30042	1756	
	2429	25758	34300	28925	2850	1
257	4434	24868	34362	27377	5184	434
1214	7107	24455	31332	26325	7747	1614
2934	9384	23794	27575	25270	9746	3309
5193	10464	22644	22440	23543	10932	5740
8557	11099	19846	18628	20676	11495	9283
12901	10643	16006	15580	16262	10824	13373
17070	10085	12757	12904	13319	10261	17816
13668	11359	12554	12775	12683	11701	13773
11	5	5	2	3	3	10

Figure 72: Measured SPI denominator map. The numbers of photon entries are plotted as a function of the direction and energy. The entries observed in $0 < E_\gamma < 20$ MeV were from the resolution effect.

6.8 The measurement of the SPI denominator map

The SPI denominator map was measured with $K_{\pi2}(1)$ data. The data were purified with the $K_{\pi2}$ selection criteria, and then, the kinematical fitting was performed with clusterized tagging-photons. The denominator map, obtained with events with the χ^2 probability greater than 0.2, is listed in Figure 72. The corresponding plots, sliced along the energy and flight direction, are placed in Figure 100 in Appendix on page 155. The performance of the measurement was examined by comparing the denominator map produced with Monte Carlo data and the map with their generated values. Details are summarized on page 156 in Appendix C.4. In the study, the discrepancy was less than 10 %.

6.9 The measurement of the SPI numerator map

After the missing-photon kinematics was extracted by the kinematical fitting with the 1-gamma events, all energy deposit, belonged to the tagging photons, were removed. The numerator map was measured with the number of entries after applying the photon veto condition. Figure 73 shows the resultant numerator map with the offline photon veto which was used in the $\pi^0 \to \nu\overline{\nu}$ search. Its net rejection was 3.5×10^6 and the acceptance was 11.7 %. As seen in the plot, due to a lack of statistics, the cells in the high energy region were almost empty. When one wanted to estimate the number of $\pi^0 \to \gamma\gamma$ backgrounds accurately, inefficiency measurement for high energy photons was indispensable. As shown later, the dominant casual process of the mis-detection was that the first photon went with very small energy and the second with large energy. Therefore, the uncertainty of the inefficiency for high energy photons would change the background estimation drastically. In order to increase entries of high energy photons, the photon veto was relaxed, having the effective rejection of 5.8×10^5 and the acceptance of 80 % (see Figure 62 on page 91). The resultant map is shown in Figure 74.

In the further analyses, all studies were performed with the relaxed photon veto. Since we could not subtract the $\pi^0 \to \gamma\gamma$ backgrounds from the observed candidates in the $\pi^0 \to \nu\overline{\nu}$ search (described in Section 5), here we built alternate two goals for the further studies.

1. Establish a reliable subtraction method of the $\pi^0 \to \gamma\gamma$ backgrounds, based on real data. Then, show the validity of the method with the relaxed photon veto.
   This promises further improvement in the $\pi^0 \to \nu\overline{\nu}$ search when we will have more data in future.

2. Understand single photon missing mechanisms with the relaxed photon veto.
   The tightness of the relaxed photon veto is fairly close to that of the photon veto used in the $K^+ \to \pi^+\nu\overline{\nu}$ search. After this study, we can tell how and/or where the $K_{\pi 2}$ backgrounds with mis-detected $\pi^0 \to \gamma\gamma$ decays come from. This will bring great feedbacks to the $K^+ \to \pi^+\nu\overline{\nu}$ search and may give a hint for more effective way of the background rejection.

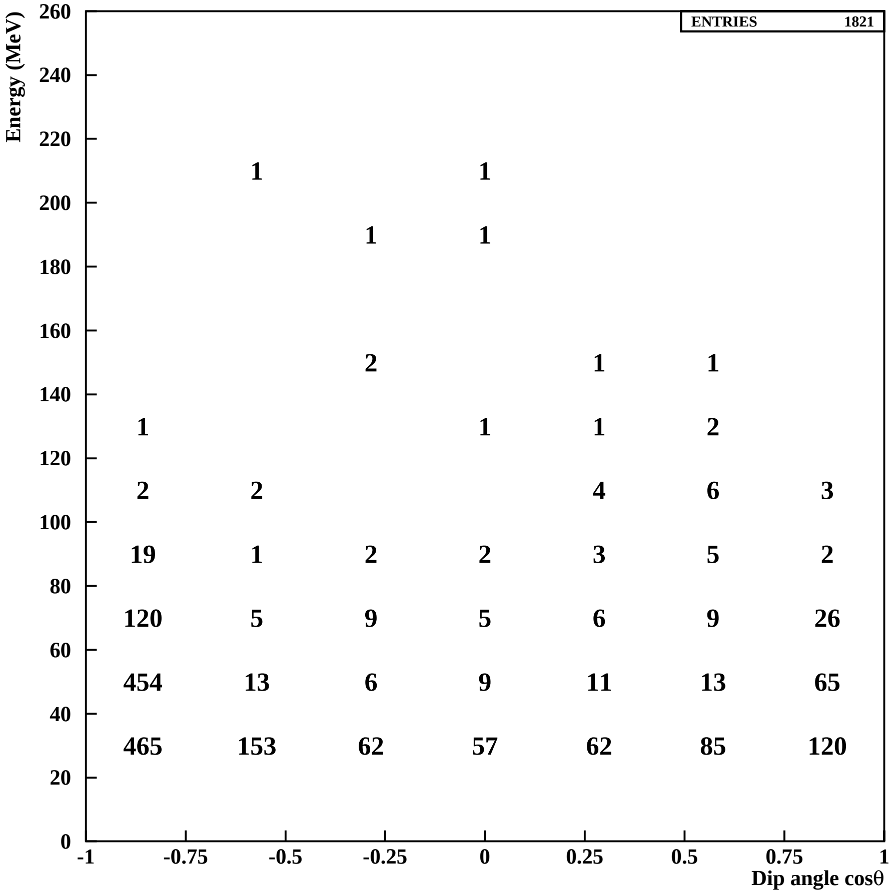

Figure 73: Numerator map measured with the offline photon veto used for the $\pi^0 \to \nu\overline{\nu}$ search. Empty cell indicates no entry. The high energy region are dominated by empty cells.

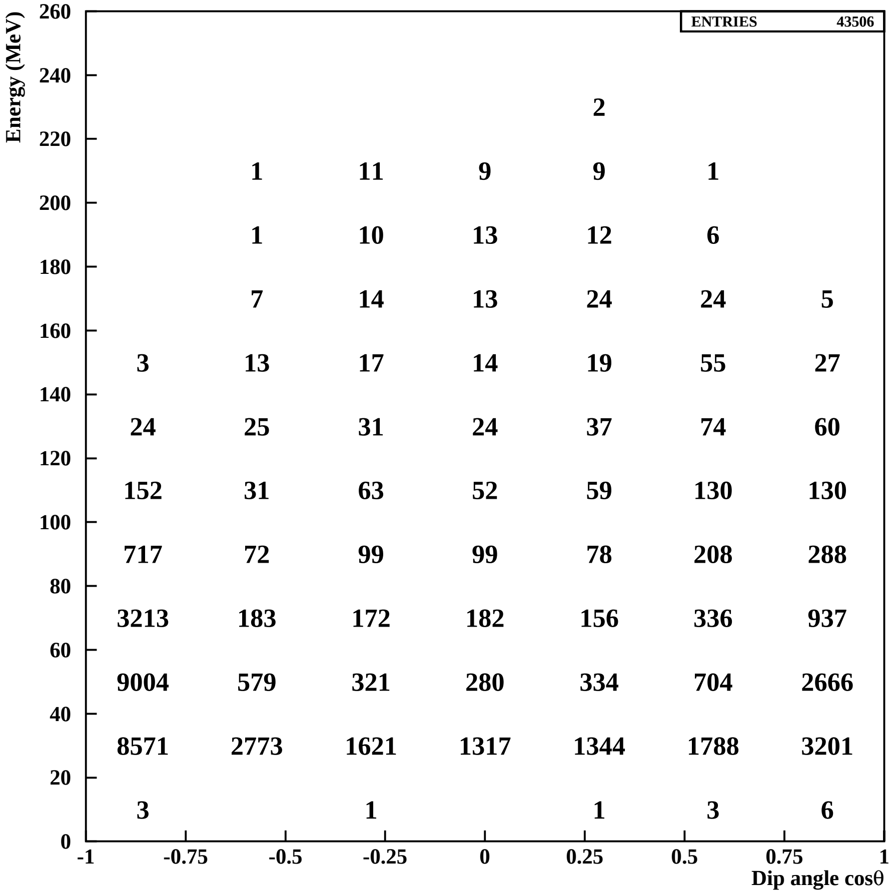

				2		
	1	11	9	9	1	
	1	10	13	12	6	
	7	14	13	24	24	5
3	13	17	14	19	55	27
24	25	31	24	37	74	60
152	31	63	52	59	130	130
717	72	99	99	78	208	288
3213	183	172	182	156	336	937
9004	579	321	280	334	704	2666
8571	2773	1621	1317	1344	1788	3201
3		1		1	3	6

Figure 74: Numerator map measured with the relaxed photon veto. Empty cell indicates null entry. The entries observed in $0 < E_\gamma < 20$ MeV were from the resolution effect.

Table 32: The number of 1-gamma events produced from $K_{\pi 2}(1)$ sample. To see the rejection of the online second photon veto, conditions of $\overline{NG2} \cdot HEX \cdot L12 \cdot \overline{EC}$ were imposed separately.

	# of entries	Acceptance
$K_{\pi 2}(1)$ events		
+ $DC \cdot L11 \cdot BV$		
+ $K_{\pi 2}$ selection criteria	184275	—
+ Tagging photon reconstruction	140063	0.760 ± 0.001
+ Kinematical fit with χ^2 selection	101119	0.722 ± 0.001
+ $\overline{NG2} \cdot HEX \cdot L12 \cdot \overline{EC}$	9117	0.090 ± 0.001

Table 33: The number of 1-gamma events with sequentially imposed selection criteria

	# of entries	Acceptance
1-gamma real data		
+ $K_{\pi 2}$ selection criteria	993162	—
+ Tagging photon reconstruction	839993	0.846 ± 0.001
+ Kinematical fit with χ^2 selection	580389	0.691 ± 0.001

6.10 The measurement of the normalization factor

As explained in section 6.2, different event samples with different trigger conditions were used to extract $N^{\text{numer}}(\theta, E)$ and $N^{\text{denom}}(\theta, E)$. Thus, the normalization factor A_{norm}, which took into account the difference in prescale factor, must be determined to calculate the ratio. The factor was measured with the number of 1-gamma events and that of reproduced 1-gamma events from the $K_{\pi 2}(1)$ sample. The ratio was used as the normalization factor. Table 32 shows the number of 1-gamma events found in the $K_{\pi 2}(1)$ sample. Table 33 shows the entries of 1-gamma events where the same selection criteria were imposed. As seen in the tables, there are 580389 1-gamma events and 9117 reproduced events from $K_{\pi 2}(1)$ sample. The normalization factor A_{norm} was measured to be $(1.57 \pm 0.02) \times 10^{-2}$ (= 9117 / 580389).

6.11 Corrections for the measurements

There were three correction factors for the measurements. The first one was the rejection of "L1.1-afterburner" condition embedded in the L1.2 condition in the 1-gamma trigger. The rejection should be subtracted. The second one was over-vetoing effects caused by split tagging photons. The third one was over-rejection due to accidentals. Each of them is described below.

The measurement of the L1.1-afterburner rejection For the measurement, all 1-gamma trigger conditions except for L1.2 were imposed to the $K_{\pi 2}(1)$ sample. The measurement is summarized in Table 34. With further application of selection criteria and the HEX-afterburner condition, the rejection of 1.140 ± 0.006 was measured with the number of entries before and after the L1.2 application. The correction factor was denoted as $C_{L1.1after}$.

Table 34: Rejection of the L1.1-afterburner cut. HEX-afterburner was emulated with software codes.

	# of entries	Rejection
$K_{\pi 2}(1)$ sample		
+ All 1-gamma trigger conditions except for L1.2		
+ $K_{\pi 2}$ selection criteria		
+ Tagging photon reconstruction		
+ Kinematical fit with χ^2 selection	5115	—
+ HEX-afterburner (simulation)	4382	1.167 ± 0.007
+ L1.2 trigger condition	3845	1.140 ± 0.006

As seen in the table, the resultant HEX-afterburner rejection was 5 % larger than that of $\pi^0 \rightarrow \nu\overline{\nu}$ search in the table 21 on page 78. The difference came from the fact that, in the 1-gamma events, at least, one photon passed through the Range Stack by the trigger condition of BV. This made the HEX-afterburner rejection higher.

Self-vetoing effect by split tagging photons Tagging photons sometimes split during the showering process, and would appear as two or more clusters. An example of the mechanism is illustrated in Figure 75. Once the events were recognized having two or more clusters, they were rejected by the photon veto. Since the self-rejection underestimated the inefficiency, it should be corrected.

The Monte Carlo simulation was employed to estimate this correction factor. In the simulation, those events were generated artificially with the virtual decay mode of $\pi^0 \rightarrow \gamma X$, where X was a massless non-interacting particle. Since the visible final states were π^+ and one photon only, once the tagging photon was removed, the rejection by the photon veto would be due to the split photons. For the reliable measurement, all the processes including kinematical fitting were reprocessed in the estimation. The correction factors were estimated with acceptance loss with the photon veto. Figure 76 shows the resultant correction factors. The plot indicates that low energy region suffers more over-veto. This is because tagging photons with larger energy tended to drop larger energy outside the cluster cone.[32] The correction factors were denoted as $C_{\text{split}}(\theta, E)$.

Over-rejection caused by accidental hits The over-rejection caused by accidental activities should be corrected. The correction factor was measured with the acceptance loss of the $K_{\mu 2}$ events with the photon veto. The technique was described in the $\pi^0 \rightarrow \nu\overline{\nu}$ search in section 4.5.6 on page 86. The correction factor C_{acc} for the relaxed photon veto was 0.80.

6.12 Results on the single photon inefficiency

The single photon detection inefficiency was obtained by Equation 28 with the correction factors :

---

[32] When the tagging photon has larger energy, the coressponding missing photon has lower energy.

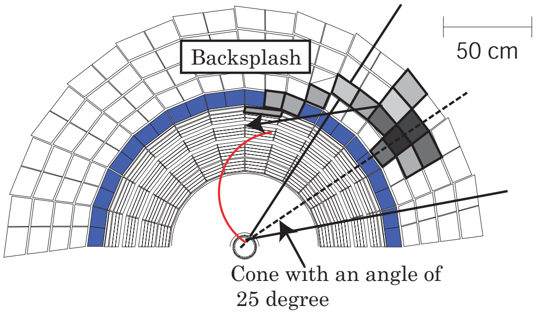

Figure 75: Illustration of the over-veto mechanism caused by the splitting from the tagging photon. The back-splash, observed outside the cluster cone, makes a fake second hit. The event would be rejected by the photon veto even if the second photon is mis-detected in fact.

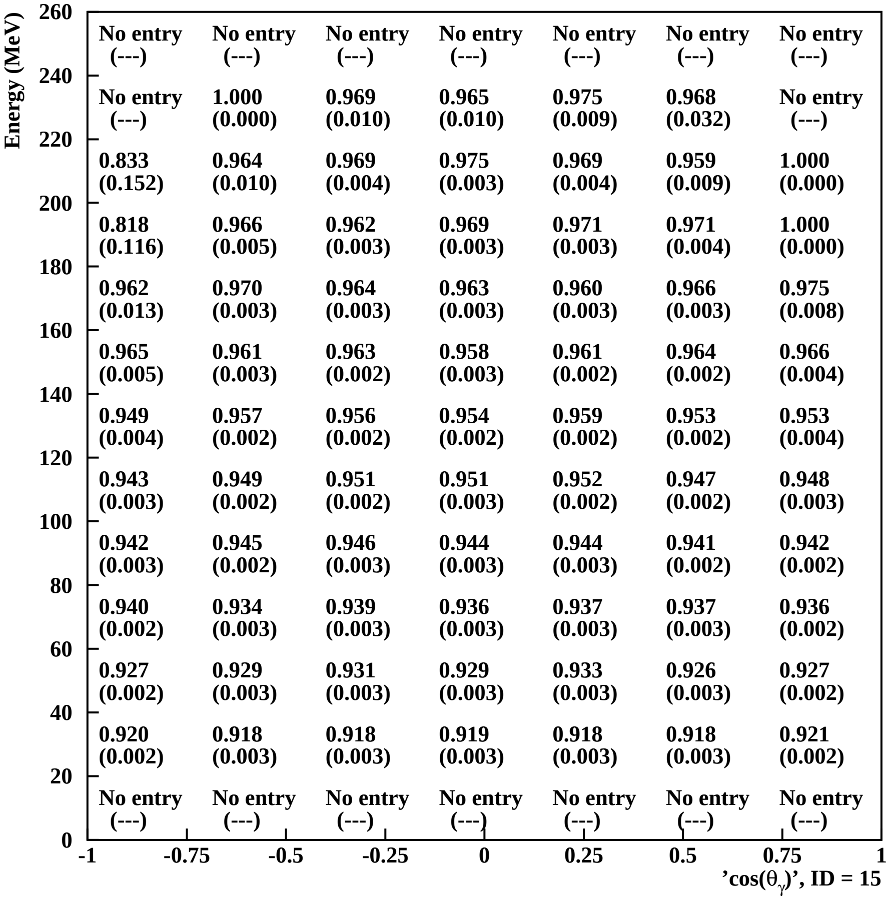

No entry (---)	No entry (---)	No entry (---)	No entry (---)	No entry (---)	No entry (---)	No entry (---)
No entry (---)	1.000 (0.000)	0.969 (0.010)	0.965 (0.010)	0.975 (0.009)	0.968 (0.032)	No entry (---)
0.833 (0.152)	0.964 (0.010)	0.969 (0.004)	0.975 (0.003)	0.969 (0.004)	0.959 (0.009)	1.000 (0.000)
0.818 (0.116)	0.966 (0.005)	0.962 (0.003)	0.969 (0.003)	0.971 (0.003)	0.971 (0.004)	1.000 (0.000)
0.962 (0.013)	0.970 (0.003)	0.964 (0.003)	0.963 (0.003)	0.960 (0.003)	0.966 (0.003)	0.975 (0.008)
0.965 (0.005)	0.961 (0.003)	0.963 (0.002)	0.958 (0.003)	0.961 (0.002)	0.964 (0.002)	0.966 (0.004)
0.949 (0.004)	0.957 (0.002)	0.956 (0.002)	0.954 (0.002)	0.959 (0.002)	0.953 (0.002)	0.953 (0.004)
0.943 (0.003)	0.949 (0.002)	0.951 (0.002)	0.951 (0.003)	0.952 (0.002)	0.947 (0.002)	0.948 (0.003)
0.942 (0.003)	0.945 (0.002)	0.946 (0.003)	0.944 (0.003)	0.944 (0.003)	0.941 (0.002)	0.942 (0.002)
0.940 (0.002)	0.934 (0.003)	0.939 (0.003)	0.936 (0.003)	0.937 (0.003)	0.937 (0.003)	0.936 (0.002)
0.927 (0.002)	0.929 (0.003)	0.931 (0.003)	0.929 (0.003)	0.933 (0.003)	0.926 (0.003)	0.927 (0.002)
0.920 (0.002)	0.918 (0.003)	0.918 (0.003)	0.919 (0.003)	0.918 (0.003)	0.918 (0.003)	0.921 (0.002)
No entry (---)	No entry (---)	No entry (---)	No entry (---)	No entry (---)	No entry (---)	No entry (---)

Figure 76: Over-vetoing effect caused by split tagging photons. The number in each cell indicates acceptance loss. The numbers in brackets indicate the statistical errors.

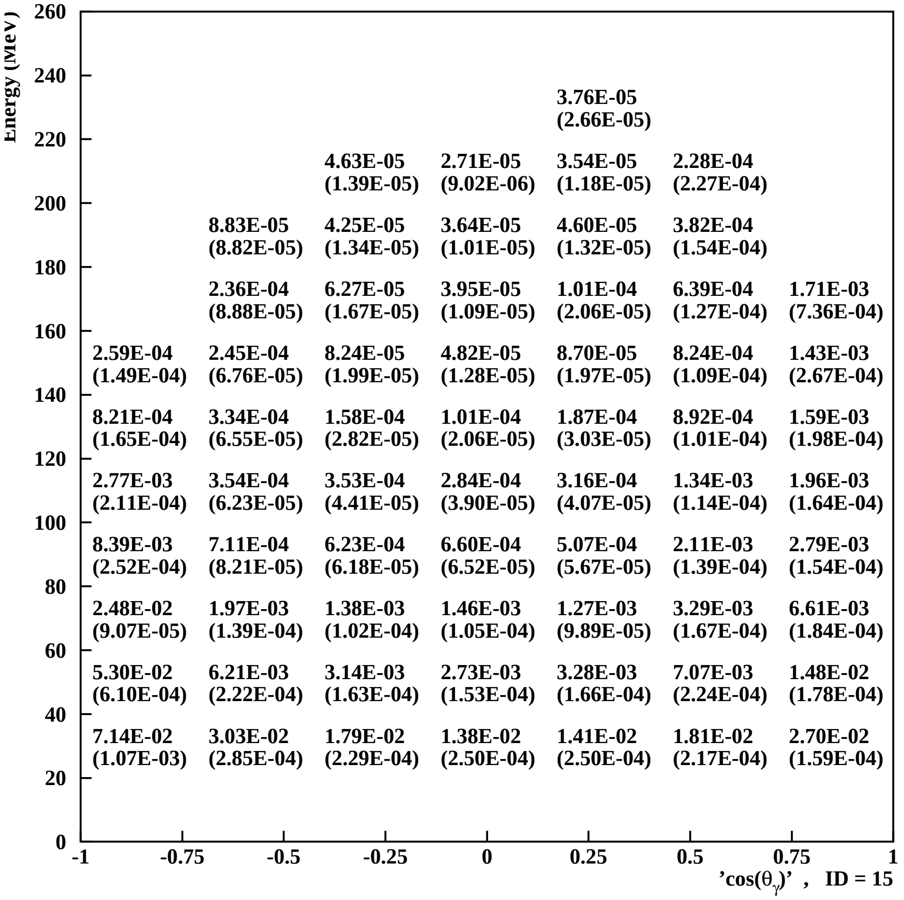

				3.76E-05 (2.66E-05)		
		4.63E-05 (1.39E-05)	2.71E-05 (9.02E-06)	3.54E-05 (1.18E-05)	2.28E-04 (2.27E-04)	
	8.83E-05 (8.82E-05)	4.25E-05 (1.34E-05)	3.64E-05 (1.01E-05)	4.60E-05 (1.32E-05)	3.82E-04 (1.54E-04)	
	2.36E-04 (8.88E-05)	6.27E-05 (1.67E-05)	3.95E-05 (1.09E-05)	1.01E-04 (2.06E-05)	6.39E-04 (1.27E-04)	1.71E-03 (7.36E-04)
2.59E-04 (1.49E-04)	2.45E-04 (6.76E-05)	8.24E-05 (1.99E-05)	4.82E-05 (1.28E-05)	8.70E-05 (1.97E-05)	8.24E-04 (1.09E-04)	1.43E-03 (2.67E-04)
8.21E-04 (1.65E-04)	3.34E-04 (6.55E-05)	1.58E-04 (2.82E-05)	1.01E-04 (2.06E-05)	1.87E-04 (3.03E-05)	8.92E-04 (1.01E-04)	1.59E-03 (1.98E-04)
2.77E-03 (2.11E-04)	3.54E-04 (6.23E-05)	3.53E-04 (4.41E-05)	2.84E-04 (3.90E-05)	3.16E-04 (4.07E-05)	1.34E-03 (1.14E-04)	1.96E-03 (1.64E-04)
8.39E-03 (2.52E-04)	7.11E-04 (8.21E-05)	6.23E-04 (6.18E-05)	6.60E-04 (6.52E-05)	5.07E-04 (5.67E-05)	2.11E-03 (1.39E-04)	2.79E-03 (1.54E-04)
2.48E-02 (9.07E-05)	1.97E-03 (1.39E-04)	1.38E-03 (1.02E-04)	1.46E-03 (1.05E-04)	1.27E-03 (9.89E-05)	3.29E-03 (1.67E-04)	6.61E-03 (1.84E-04)
5.30E-02 (6.10E-04)	6.21E-03 (2.22E-04)	3.14E-03 (1.63E-04)	2.73E-03 (1.53E-04)	3.28E-03 (1.66E-04)	7.07E-03 (2.24E-04)	1.48E-02 (1.78E-04)
7.14E-02 (1.07E-03)	3.03E-02 (2.85E-04)	1.79E-02 (2.29E-04)	1.38E-02 (2.50E-04)	1.41E-02 (2.50E-04)	1.81E-02 (2.17E-04)	2.70E-02 (1.59E-04)

Figure 77: Measured single photon inefficiency. The numbers in brackets are statistical errors.

$$\frac{N^{\text{numer}}(\theta, E)}{N^{\text{denom}}(\theta, E)} \times A_{\text{norm}} \times \frac{C_{\text{L1.1after}}}{C_{\text{split}}(\theta, E) C_{acc}} \tag{37}$$

Figure 77 shows the single photon inefficiency measured with the numerator map in Figure 74 at the photon veto acceptance of 0.80. The table of inefficiencies is presented graphically in Figure 78, where they are sliced with the energy (20 MeV interval). In the plot, geometrical dependency was observed. The inefficiency is worse around the $|\cos(\theta_\gamma)| = 1$. Figure 79 shows inefficiency as a function of energy, sliced with dip angle.

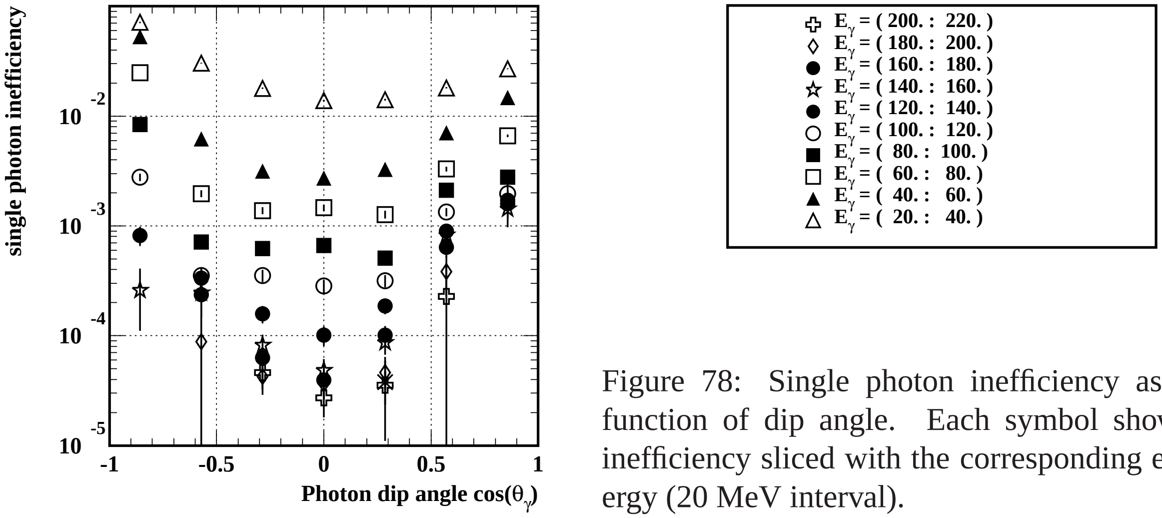

Figure 78: Single photon inefficiency as a function of dip angle. Each symbol shows inefficiency sliced with the corresponding energy (20 MeV interval).

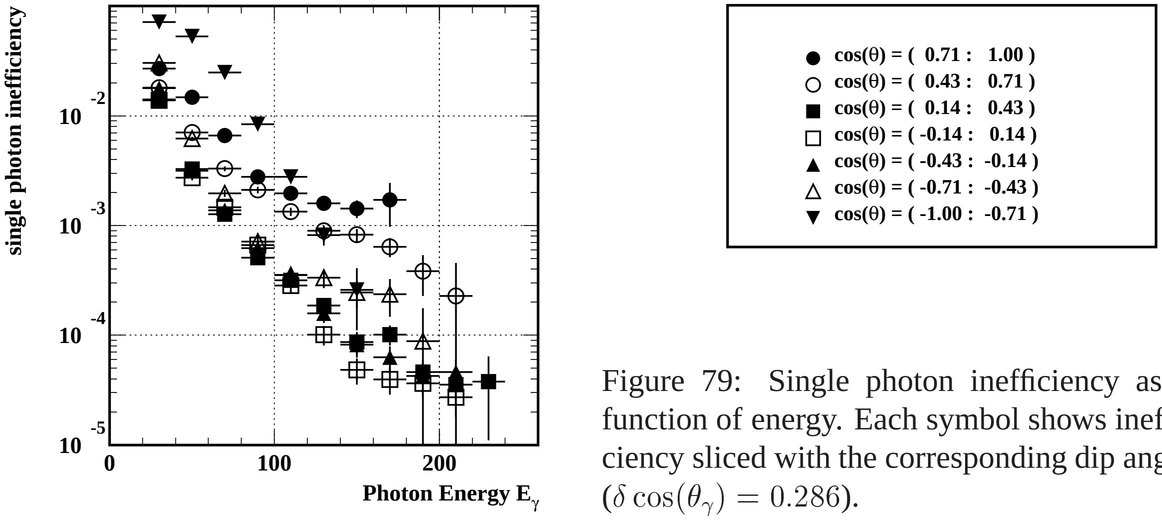

Figure 79: Single photon inefficiency as a function of energy. Each symbol shows inefficiency sliced with the corresponding dip angle ($\delta\cos(\theta_\gamma) = 0.286$).

7 $\pi^0 \rightarrow \gamma\gamma$ Detection Inefficiency

$\pi^0 \rightarrow \gamma\gamma$ miss-detection probability, denoted as $P_{\pi^0\,\text{miss}}$, was estimated by convoluting the single photon missing probability as follows,

$$P_{\pi^0\,\text{miss}} = \sum_{i}^{N} \frac{P_{SPI}(\theta_1^i, E_1^i) P_{SPI}(\theta_2^i, E_2^i)}{N} \tag{38}$$

where $P_{SPI}(\theta, E)$ is the single photon inefficiency, and θ_k^i (E_k^i) is the direction (energy) of the k-th photon in the i-th event. Here, the index "k" takes 1 or 2 to address a photon in $\pi^0 \rightarrow \gamma\gamma$ decay. N is the number of events generated for the estimation, and should be large to avoid a localization of the phase space (θ_k^i, E_k^i). The event number i runs through 1 to N.

7.1 The daughter table method

As seen in the table of single photon inefficiency, each cell consisted of a center value ($P_{SPI}(\theta, E)$) and its uncertainty ($U_{SPI}(\theta, E)$). To obtain an uncertainty of the $\pi^0 \rightarrow \gamma\gamma$ detection inefficiency, the $U_{SPI}(\theta, E)$ should be correctly propagated. In this analysis, a technique called "daughter table method" was employed.

The daughter table method For explanation, we describe the inefficiency table with a matrix notation : $a_{i,j}$, where i (j) addresses i-th (j-th) bin of the dip angle (energy) in the table. Each element $a_{i,j}$ obeys the Binomial distribution because it is defined by the ratio of two numbers, $N^{\text{denom}}(\theta, E)$ and $N^{\text{numer}}(\theta, E)$. We generated, with a binomial random number generator, 300 new values for each $a_{i,j}$ with the measured mean value and its variance.[33] The generated numbers were denoted as $a_{i,j}^k$ (k = 1, 300). A new table, called "daughter table", was made with $a_{i,j}^k$; there were thus 300 tables in total. If the $\pi^0 \rightarrow \gamma\gamma$ inefficiency was estimated with each individual daughter table, a total of 300 different estimations would be obtained. The distribution of the resultant estimations would reflect the uncertainty of the single photon inefficiency. The most likely $\pi^0 \rightarrow \gamma\gamma$ inefficiency (= center value) was extracted from their mean and the uncertainty was extracted from their RMS of the distribution.

7.2 Phase space generation with Monte Carlo simulation

A sample of photon phase space (θ_k^i, E_k^i) was generated with Monte Carlo simulation. Localization of the (θ_k^i, E_k^i) in particular cells could bring a faulty π^0 inefficiency, thus, a large number of 1.2×10^6 events were produced by the simulation. Note that, in the simulation, the π^+ dip angle distribution should reproduce that of real data. This is because the different π^+ dip angle distribution would bring the different distribution of the π^0 boost direction, and would result in biased (θ_k^i, E_k^i) distribution.

---

[33] The mean value is given by $P_{SPI}(\theta, E)$ and the variance by $\left[\frac{1}{N_T} P_{SPI}(\theta, E)(1 - P_{SPI}(\theta, E))\right]^{1/2}$, where N_T is the total number of events.

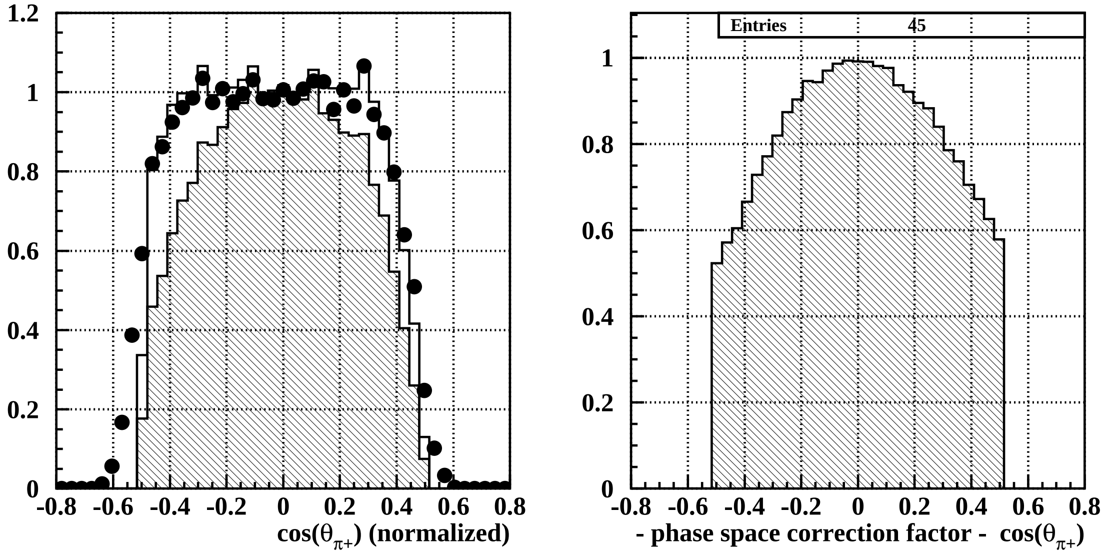

Figure 80: π^+ dip angle distribution made with real data and Monte Carlo simulation (left) and the ratio (right). In the left figure, closed circles show the dip angle distribution of produced π^+s by Monte Carlo simulation. The hatched histogram shows that of real data, where all the selection criteria were applied except for online and offline photon veto. Cut-off at $|\cos(\theta_{\pi^+})| = 0.5$ in the real data was due to offline fiducial cuts. The open histogram shows the distribution of events collected with minimum bias trigger $K_{\pi 2}(1)$, which well agrees with that of the Monte Carlo events except for cut-off. The right figure shows obtained correction factors. One can reproduce the distribution of real data by multiplying the correction factors to that of the Monte Carlo simulation.

The π^+ dip angle correction The π^+ dip angle distribution was examined with the Monte Carlo simulation and real data. As shown in the left plot of Figure 80, however, difference was actually observed at large $|\cos(\theta_{\pi^+})|$ region. Thus, correction factors are introduced to account for the difference. The right plot in Figure 80 shows the actual correction factor.

7.3 Results

7.3.1 The convoluted $\pi^0 \to \gamma\gamma$ detection inefficiency

The $\pi^0 \to \gamma\gamma$ detection inefficiency was estimated using the daughter tables and a list of phase space (θ^i_k, E^i_k) with the correction factors. Figure 81 shows the convoluted inefficiency distribution. Width of the distribution was shaped by the uncertainties in the photon inefficiency table. The most likely inefficiency was 0.99×10^{-6} and the uncertainty was 0.18×10^{-6}. Remind that the table of single photon inefficiency was measured with the relaxed photon veto, whose acceptance was 0.80. The $\pi^0 \to \gamma\gamma$ inefficiency was estimated with various levels of photon veto with the corresponding single photon inefficiency table. The obtained results are shown in Figure 82. For comparison, the inefficiency was transformed to the corresponding π^0 net rejection in the plot. As seen in the plot, the convoluted rejection agreed with that of real data.

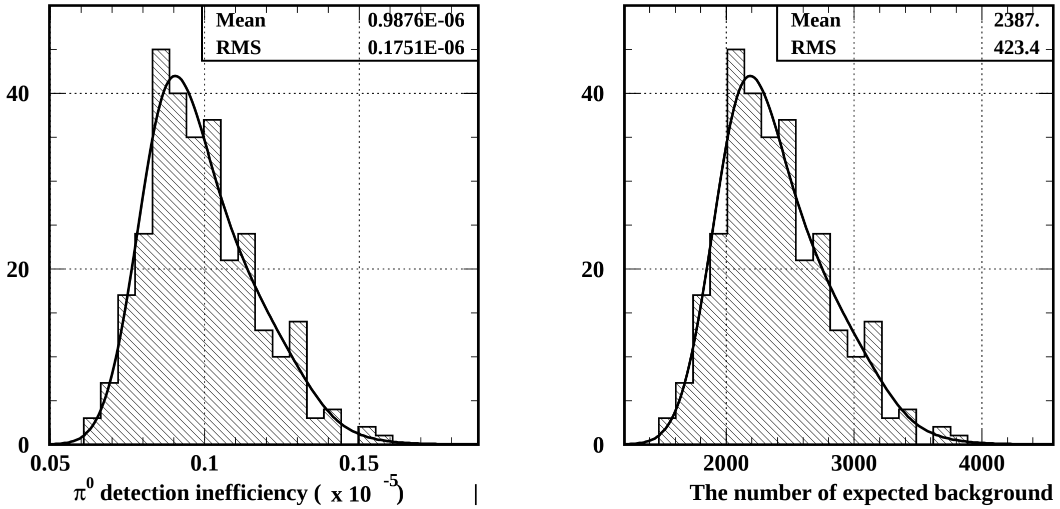

Figure 81: Convoluted $\pi^0 \to \gamma\gamma$ inefficiency (left) with the photon veto condition of acceptance = 0.80. The mean and the RMS were 0.99×10^{-6} and 0.18×10^{-6} respectively. The shape reflected the uncertainty on the inefficiency table. The right plot shows the number of expected $\pi^0 \to \gamma\gamma$ backgrounds when a total of 3.0×10^9 π^0 were accumulated.

7.3.2 The convoluted $\pi^0 \to \gamma\gamma$ rejection as a function of π^+ dip angle

As seen in the table of single photon inefficiency (Figure 78 on page 114), the inefficiency depended on the photon's dip angle. It indicates that the π^0 missing probability would change depending on its boost direction. To investigate it, the $\pi^0 \to \gamma\gamma$ net rejection was plotted as a function of the π^+ dip angle. Figure 83 shows the result. As shown in the plot, smaller rejection at the large $|\cos(\theta_{\pi^+})|$ area was observed. This tendency was observed also in the data used for the $\pi^0 \to \nu\overline{\nu}$ search.

7.4 Background subtraction

7.4.1 Subtraction of the estimated $\pi^0 \to \gamma\gamma$ backgounds

Background subtraction was performed with the number of expected $\pi^0 \to \gamma\gamma$ backgrounds obtained with the relaxed photon veto (acceptance=0.80). In the $\pi^0 \to \nu\overline{\nu}$ search, a total of 4131 $\pi^0 \to \nu\overline{\nu}$ candidates were observed in the signal region with the relaxed photon veto, and the upper limit without the subtraction resulted in $Br(\pi^0 \to \nu\overline{\nu}) < 1.5 \times 10^{-6}$. The right plot of Figure 81 shows the distribution of the expected backgrounds with the daughter map method. Since we did not have the background estimation for other background sources, we took a conservative attitude again and examined the improvement in the upper limit with the subtraction. Assuming the observed events followed Poisson statistics, the signal events after the subtraction were less than 2259 at 90 %C.L. This corresponded to the upper limit of $Br(\pi^0 \to \nu\overline{\nu}) < 8.2 \times 10^{-7}$, and a factor of 1.9 improvement was obtained by the subtraction. One question arose here. What were the remaining ~2000 events? We thought they were the $\pi^0 \to \gamma\gamma$ backgrounds coming through the effects which could not be estimated by the

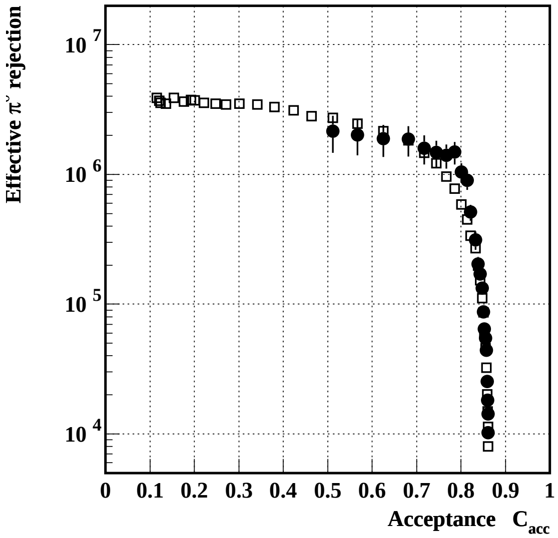

Figure 82: Convoluted $\pi^0 \to \gamma\gamma$ rejection with various levels of photon veto. The plot with closed circles shows the resultant rejections. The plot with rectangles shows the net π^0 rejection measured in the $\pi^0 \to \nu\overline{\nu}$ search.

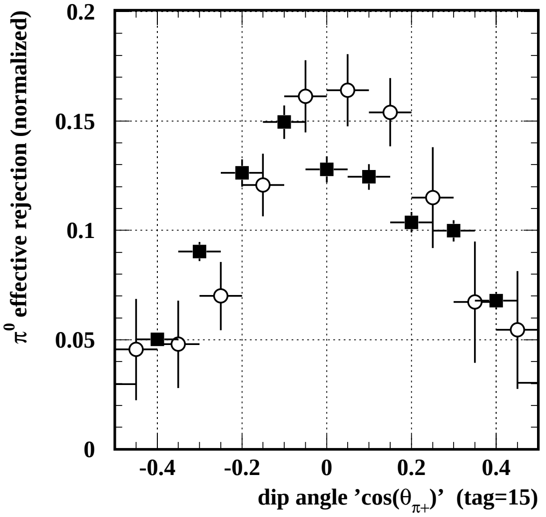

Figure 83: $\pi^0 \to \gamma\gamma$ rejection as a function of π^+ dip angle. The plot with open circles shows the dip angle dependence convoluted from the single photon inefficiency. The plot with rectangular symbols shows that of real data obtained in the $\pi^0 \to \nu\overline{\nu}$ search. In both plots, the rejection drops by a factor of three at the $\cos(\theta_{\pi^+})$ edge.

measurement of the single photon inefficiency. One possible example was the case that both photons in the π^0 decay impinged the same rod of the BV/BVL module (see Figure 54 and 55 on page 83). As shown in the plots, two peaks were observed in the BVL timing distribution. When the photon veto was relaxed, the earlier peak was not fully covered with the veto window. Since the two-photon phenomenon was not taken into account in the study of the single photon inefficiency, the effect would bring a discrepancy in the estimation. As the photon veto got tighter, the discrepancy was expected to be smaller or disappeared thanks for the wider veto window. Also in case of further loosened photon veto, the effect would get negligible, since the two-photon effect no longer dominated the $\pi^0 \to \gamma\gamma$ backgrounds.

The background subtraction was performed at various levels of photon veto. The left plot in Figure 84 shows the resultant upper limit after the background subtraction. The right plot in the figure shows improvement factor brought by the subtraction. As seen in the plot, the subtraction improve the upper limits at least by $\sim$ 1.8.

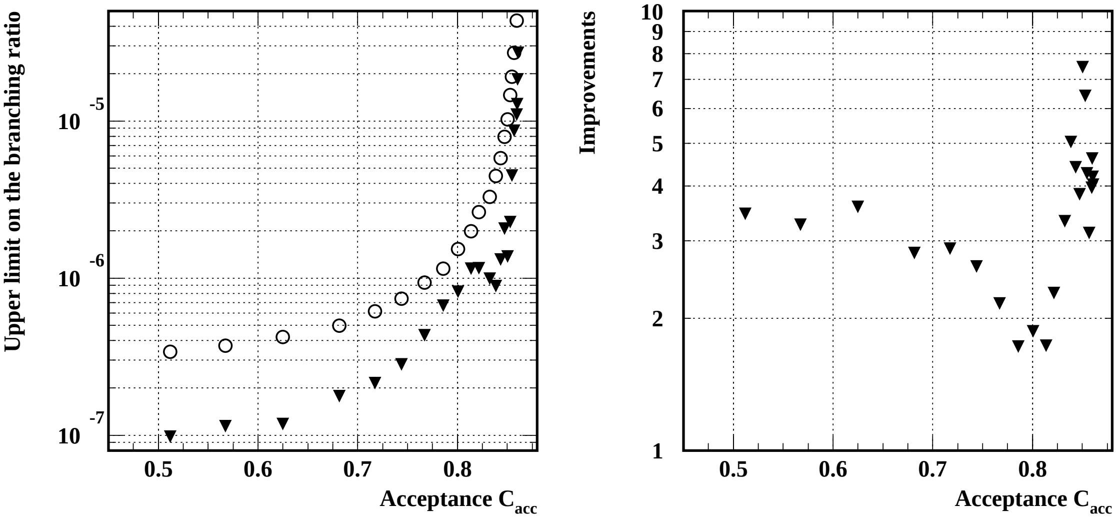

Figure 84: Upper limits before and after the background subtraction. The plot with open circles (closed triangles) in the left figure shows upper limits which were obtained before (after) the background subtraction. The right plot shows improvement factors brought by the subtraction.

7.4.2 Subtraction with π^+ dip angle dependence

In this subsection, we will subtract the $\pi^0 \to \gamma\gamma$ background using the π^+ dip-angle (θ_{π^+}) distribution. Because the θ_{π^+} distribution for the $\pi^0 \to \nu\overline{\nu}$ should not be affected by application of the photon veto, any difference in the θ_{π^+} shape before and after the veto would indicate the existence of the remaining $\pi^0 \to \gamma\gamma$ backgrounds. In fact, as seen in the section 7.3.2, the $\pi^0 \to \gamma\gamma$ rejection did depend on θ_{π^+}. The right plot with circles in Figure 85 shows the original π^+ dip angle distribution measured before the photon veto application. The function was called signal shape function because the $K_{\pi 2}$ decay with $\pi^0 \to \nu\overline{\nu}$ should follow this distribution. The plot with rectangles in the figure shows the background shape function constructed from the table of single photon inefficiency. The χ^2 fitting was performed[34] with a function form of $sS_{shape}(\cos(\theta_{\pi^+})) + bB_{shape}(\cos(\theta_{\pi^+}))$ to the observed candidates (left plot in Figure 85), where $S_{shape}(x)$ and $B_{shape}(x)$ were dip angle distribution (shape function) of the signal and background. The variable s and b were introduced as a free parameter for the fitting. The likelihood distribution is shown in the figure 86. The best fit was obtained with s = 1977 and b = 2154, which meant 48 % being the $\pi^0 \to \nu\overline{\nu}$ signal ($= 1977/4131$). Again, using the χ^2 probability as a likelihood, the number of s at the 90 % C.L. was measured conservatively. The resultant number was $s_{90} = 2449$, which corresponded to the upper limit of $Br(\pi^0 \to \nu\overline{\nu}) < 8.9 \times 10^{-7}$.

We already knew, from our result in section 5, the $Br(\pi^0 \to \nu\overline{\nu})$ was, at least, a factor of three lower than this upper bound. We thought almost all of the “s” came from the poor estimation of the background function shape, mainly caused by the resolution effects in the tagging-photon kinematics and/or kinematical fitting. Correction for the resolution effects would bring further improvement in the method.

---

[34] If the shape function were more accurate, we could have used unbinned extended maximum likelihood method.

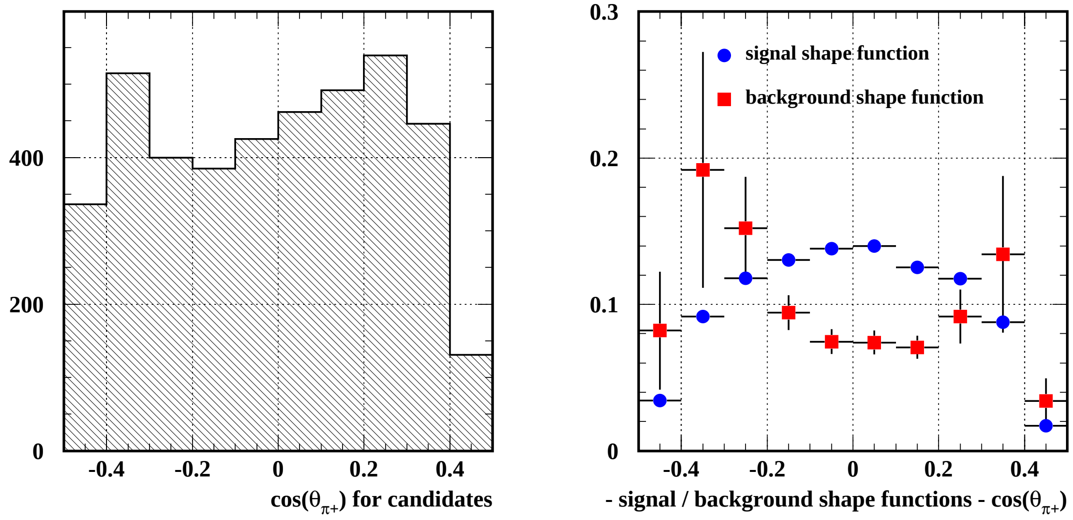

Figure 85: $\cos(\theta_{\pi+})$ distribution of the observed candidates (left) and the corresponding signal and background shape functions (right). As shown in the right figure, the $\pi^0 \to \nu\overline{\nu}$ signal shape function (the plot with circles) had a peak at around $\cos(\theta_{\pi+}) = 0$ and decreased as $|\cos(\theta_{\pi+})|$. This shape was formed by the fiducial constraints for π^+ in the $\pi\nu\overline{\nu}$ trigger and the $K_{\pi2}$ selection criteria. On the other hand, the background shape function had a peak at the shoulders reflecting the geometrical dependence of the single photon inefficiency.

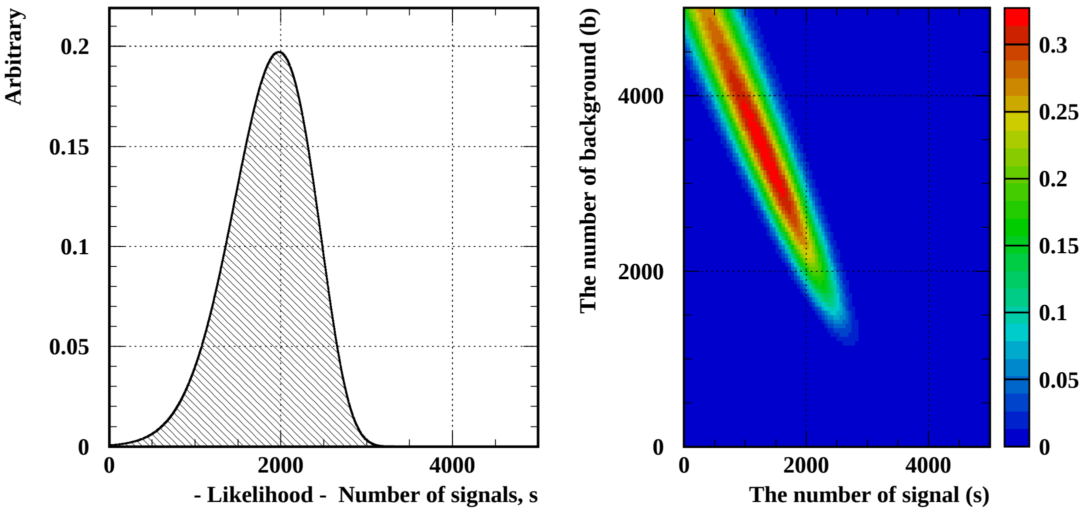

Figure 86: Likelihood distribution constructed from $\cos(\theta_{\pi+})$ dependence. The left plot shows the likelihood as a function of signal s with a constraint of $s + b = 4131$. The most likely numbers were s = 1977 and b = 2154. The right plot shows the likelihood distribution where the s and b behaved as a free parameter. The most likely pair was (s, b) = (1372, 3342).

7.5 Summary

We measured single photon inefficiency with special trigger events and estimated the number of $\pi^0 \to \gamma\gamma$ backgrounds with the resultant photon inefficiency table at various levels of photon veto. With a series of the studies and their results, we made answers for the questions in section 6.1 on page 94.

1. For the question 1. Single photon inefficiency was measured with real data, which was independent from that of $\pi\nu\overline{\nu}$ search. The resultant table quantified the geometrical and/or energy dependent inefficiencies. At $\cos(\theta_\gamma) = 0$ region, comparing with the obtained result and the expectation from the Monte Carlo simulation, it was found that the inefficiency was limited by neither the sampling fluctuation, which was precisely estimated by the electro-magnetic shower simulation, nor the photo-nuclear interaction, whose cross-section was available from the reference [43]. Other studies ([44]) indicated the inefficiency was well reproduced if masking effect by early accidentals was introduced. In terms of the geometrical dependence, inefficient region was observed at the downstream area of $\cos(\theta_\gamma) \sim 1$ (see Figure 78). The region had been pointed out as an inefficient area by the analysis for the $K^+ \to \pi^+\nu\overline{\nu}$ decay [45, 46]. Up to now, it was revealed that dead materials of the drift chamber's end-plate was thought to be one of the known source of inefficiency.

   The measured inefficiency around the beam hole direction was $(7.1 \pm 0.1) \times 10^{-2}$ for photons with $20 \sim 40$ MeV. Supplemental photon detectors at the beam line might improve the inefficiency. However, as seen in the section for photon veto optimization on page 85, they would be exposed by high beam accidentals as the End Cap innermost ring. Timing resolution and second-particle (or multi-particle) detection were the key for effective photon rejection.

2. For the question 2. By convoluting the single photon inefficiency, the number of $\pi^0 \to \gamma\gamma$ backgrounds was estimated. The estimated numbers agreed, to some extent, with the actual numbers of observed candidates at various levels of the photon veto. The errors on the estimations were mainly from the statistical errors of the 1gamma events. As a typical number, the error was 18 % at photon veto of acceptance = 0.80. A factor of 1.9 improvement was achieved in the upper limit by the $\pi^0 \to \gamma\gamma$ background subtraction.

3. For the question 3. It was observed that the π^+ dip angle distribution had a discrimination capability of the signals from the $\pi^0 \to \gamma\gamma$ backgrounds. This was caused by the geometrical dependency of the photon inefficiency. Background subtraction with the π^+ dip angle shape information improved the upper limit by a factor of 1.7 at the photon veto of acceptance $= 0.80$.

4. For the question 4. Figure 87 shows the photon distribution made with the miss-detected $\pi^0 \to \gamma\gamma$. As seen in the figure, the backgrounds were from mis-detection of low energy photons around the beam line direction (and coincident mis-detection of their counterpart of high energy photons). Photon detectors reinforcing these regions (or one of the regions) would improve the $\pi^0 \to \nu\overline{\nu}$ sensitivity. Also, the remained candidates (especially in case of relaxed photon veto) had more photon hits in the back-to-back band region ($\phi_\gamma - \phi_{\pi^+} = \pi$) as seen in Figure 64 on page 93. Introduction of a cut based on the band structure would improve the upper limit. Masking effect caused by preceding accidentals were observed

as seen in Figure 53 on page 82. Data taking under high rate environment needs special care for the effect. For example, waveform digitization and multi-pulse extraction would help to reduce such effects and reject the $\pi^0 \to \gamma\gamma$ backgrounds.

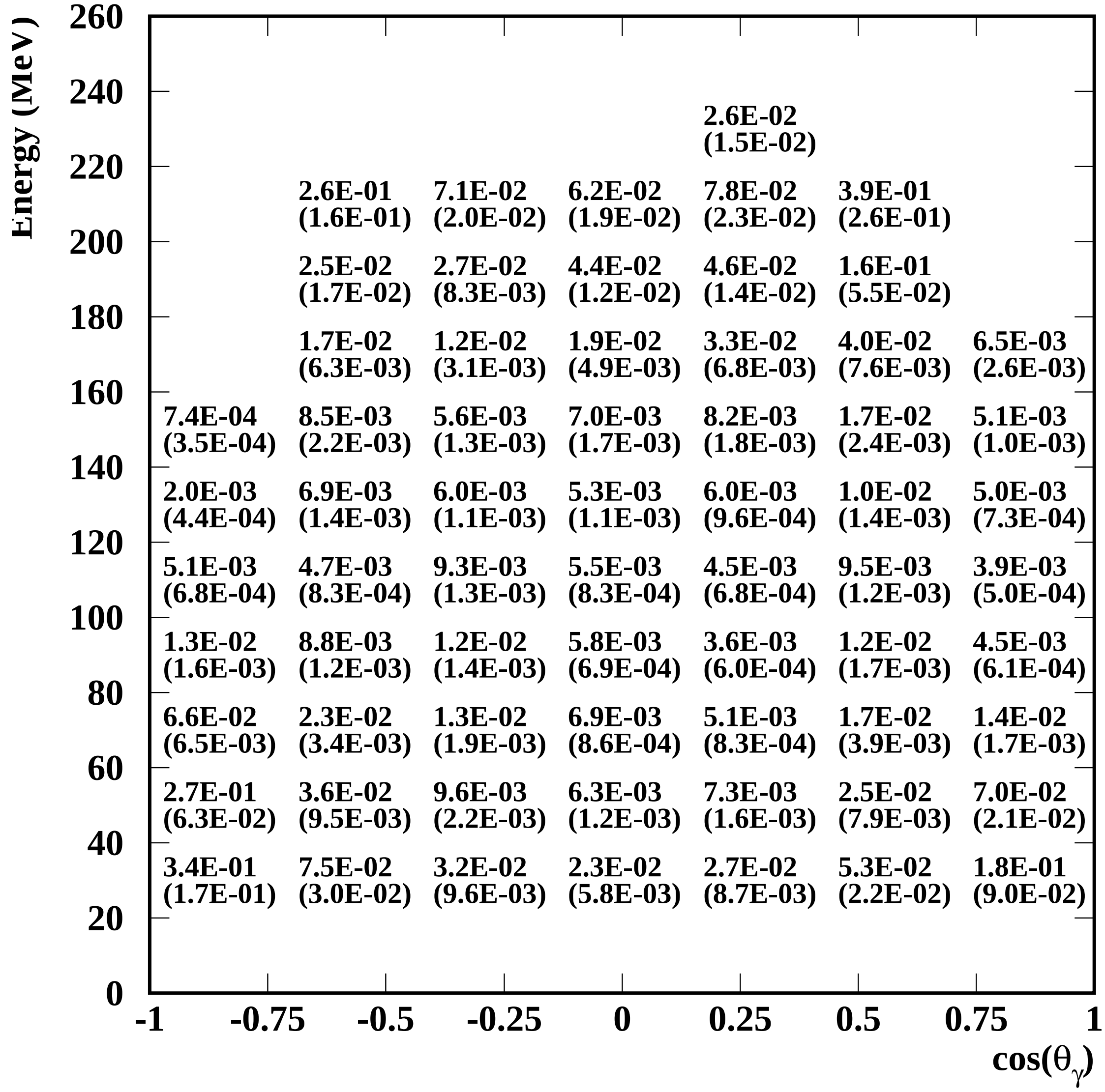

				2.6E-02 (1.5E-02)		
	2.6E-01 (1.6E-01)	7.1E-02 (2.0E-02)	6.2E-02 (1.9E-02)	7.8E-02 (2.3E-02)	3.9E-01 (2.6E-01)	
	2.5E-02 (1.7E-02)	2.7E-02 (8.3E-03)	4.4E-02 (1.2E-02)	4.6E-02 (1.4E-02)	1.6E-01 (5.5E-02)	
	1.7E-02 (6.3E-03)	1.2E-02 (3.1E-03)	1.9E-02 (4.9E-03)	3.3E-02 (6.8E-03)	4.0E-02 (7.6E-03)	6.5E-03 (2.6E-03)
7.4E-04 (3.5E-04)	8.5E-03 (2.2E-03)	5.6E-03 (1.3E-03)	7.0E-03 (1.7E-03)	8.2E-03 (1.8E-03)	1.7E-02 (2.4E-03)	5.1E-03 (1.0E-03)
2.0E-03 (4.4E-04)	6.9E-03 (1.4E-03)	6.0E-03 (1.1E-03)	5.3E-03 (1.1E-03)	6.0E-03 (9.6E-04)	1.0E-02 (1.4E-03)	5.0E-03 (7.3E-04)
5.1E-03 (6.8E-04)	4.7E-03 (8.3E-04)	9.3E-03 (1.3E-03)	5.5E-03 (8.3E-04)	4.5E-03 (6.8E-04)	9.5E-03 (1.2E-03)	3.9E-03 (5.0E-04)
1.3E-02 (1.6E-03)	8.8E-03 (1.2E-03)	1.2E-02 (1.4E-03)	5.8E-03 (6.9E-04)	3.6E-03 (6.0E-04)	1.2E-02 (1.7E-03)	4.5E-03 (6.1E-04)
6.6E-02 (6.5E-03)	2.3E-02 (3.4E-03)	1.3E-02 (1.9E-03)	6.9E-03 (8.6E-04)	5.1E-03 (8.3E-04)	1.7E-02 (3.9E-03)	1.4E-02 (1.7E-03)
2.7E-01 (6.3E-02)	3.6E-02 (9.5E-03)	9.6E-03 (2.2E-03)	6.3E-03 (1.2E-03)	7.3E-03 (1.6E-03)	2.5E-02 (7.9E-03)	7.0E-02 (2.1E-02)
3.4E-01 (1.7E-01)	7.5E-02 (3.0E-02)	3.2E-02 (9.6E-03)	2.3E-02 (5.8E-03)	2.7E-02 (8.7E-03)	5.3E-02 (2.2E-02)	1.8E-01 (9.0E-02)

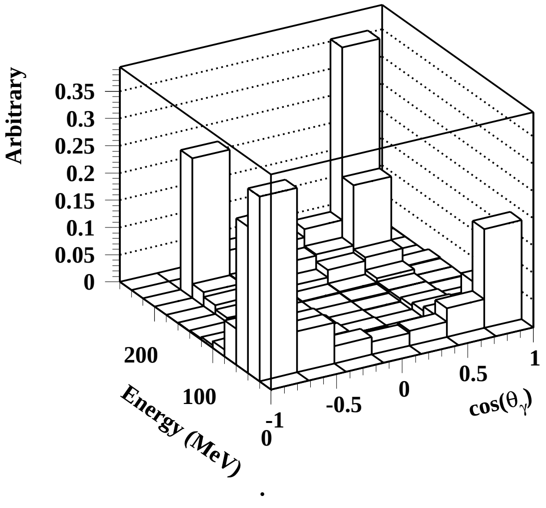

Figure 87: γ distribution of miss-detected $\pi^0 \to \gamma\gamma$ decays shown in texts (up) and in graphically (left). Both are normalized. In the upper plot, the numbers in brackets are the errors. $\pi^0 \to \gamma\gamma$ backgrounds were from a poor detection efficiency of low energy photons at beam line direction and the coincident detection failure of high energy photons.

8 Conclusion

The decay of $\pi^0 \to \nu\overline{\nu}$ was searched with hermetic photon detection system in the E949 experiment. A sample of 3.0×10^9 π^0s of $K_{\pi 2}$ decays was collected with the $K_{\pi 2}$ selection criteria, where the impurity of 10^{-9} was achieved. To suppress the most dominant background $\pi^0 \to \gamma\gamma$, maximization was performed for numerous photon veto parameters using an independent control sample. After application of the optimized photon veto, a total number of 99 candidates were observed in the signal region. As a result, an upper limit of $Br(\pi^0 \to \nu\overline{\nu}) < 2.7 \times 10^{-7}$ (90%C.L.) was obtained. A factor of three improvement was achieved in this analysis. The experiment achieved the best photon detection performance in the world.

The saturation curve observed in the profile plot was a proof that the analysis reached to the best detector performance. It indicated the necessity of the $\pi^0 \to \gamma\gamma$ background subtraction to realize further improvement. Due to difficulties in the reliable estimation of the backgrounds with Monte Carlo simulation, we developed a new technique to measure the detector photon inefficiency with real data.

The technique was performed with a total of 1.7×10^6 $K_{\pi 2}$ sample collected with special 1-gamma trigger. Unfortunately, due to the lack of sufficient event statistics, the inefficiency table with photon veto of the $\pi^0 \to \nu\overline{\nu}$ search was not available. Thus, the inefficiency was measured with the relaxed photon veto. The resultant table quantified the geometrical and/or energy dependence of the photon detection inefficiency.

$\pi^0 \to \gamma\gamma$ missing probability was convoluted from the single photon inefficiency and the number of $\pi^0 \to \gamma\gamma$ backgrounds was estimated. Background subtraction based on the estimation was performed with the observed candidates in the signal region and, as a result, a factor of 1.8 improvement was achieved at the photon veto of acceptance $= 0.80$. The convoluted net π^0 rejection and the π^+ dip angle dependence were found to agree fairly well with that of real data measured in the $\pi^0 \to \nu\overline{\nu}$ search. Background subtraction with the π^+ dip angle distribution was performed and a factor of 1.7 improvement was obtained. These results proved the validity of the technique developed in this thesis for background subtraction.

References

[1] D. Asner *et al.*, Phys. Rev. **D61**, 012002 (2000).

[2] Y. Fukuda *et al.*, Phys. Rev. Lett. **81**, 1562 (1998).

[3] A. Aguilar *et al.*, Phys.Rev. **D64**, 112007 (2001).

[4] Y. Fukuda *et al.*, Phys. Lett. **B539**, 179 (2002).

[5] Q. R. Ahmad *et al.*, Phys. Rev. Lett. **89**, 011302 (2002).

[6] M. H. Ahn *et al.*, Phys. Rev. Lett. 90, 041801 (2003).

[7] T. Araki *et al.*, Phys. Rev. Lett. **94**, 081801 (2005).

[8] T. Kalogeropoulos, J. Schechter, and J. Valle, Phys. Lett. **B86**, 72 (1979); P. Herczeg and C.M. Hoffman, Phys. Lett. **B100**, 347 (1981); L. Arnellos, W.J. Marciano, and Z. Parsa, Nucl. Phys. **B196**, 365 (1982); Robert Shrock, private communication.

[9] Particle Data Group, S. Eidelman *et al.*, Phys. Lett. **B592**, 1 (2004).

[10] K. Assamagan *et al.*, Phys. Rev. **D53**, 6065 (1996).

[11] R. Barate *et al.*, EPJ **C2**, 395 (1998).

[12] P. T. Springer *et al.*, Phys. Rev. **A35**, 679 (1987).

[13] Ch. Weinheimer *et al.*, Phys. Lett. **B460**, 219 (1999).

[14] V. M. Lobashev *et al.*, Phys. Lett. **B460**, 227 (1999).

[15] W.J. Marciano and Z. Parsa, Phys. Rev. **D53**, R1 (1996).

[16] P. Herczeg and C.M. Hoffman, Phys. Lett. **100B**, 347 (1981).

[17] J. Dorenbosch *et al.*, ZPhys. **C40**, 497 (1988).

[18] M.S. Atiya *et al.*, Phys. Rev. Lett. **66**, 2189 (1991).

[19] L. B. Auerbach *et al.*, Phys. Rev. Lett. **92**, 091801 (2004).

[20] See, for example, D.N. Spergel *et al.*, Astrophys. J. Suppl. **148**, 175 (2003).

[21] W. P. Lam and K. -W. Ng, Phys. Rev. **D44**, 3345 (1991).

[22] A. A. Natale, Phys. Lett. **B258**, 227 (1991).

[23] P. P. Jaikumar and M. Prakash, Phys. Rev. **D66**, 063003 (2002).

[24] S. Reddy, M. Sadzikowski, and M. Tachibana Nucl. Phys. **A714**, 337 (2003).

[25] F. Arretche, A. A. Natale and D. N. Voskresensky Phys. Rev. **C68**, 035807 (2003).

[26] P. Abreu *et al*, (DELPHI Collaboration), Phys. Lett. **B274** , 230 (1992).

[27] BABAR Collaboration, B. Aubert *et al.*, Phys. Rev. Lett. **93**, 091802 (2004).

[28] J. Doornbos *et al.*, Nucl. Instr. and Meth. **A444**, 546 (2000).

[29] B. Bassalleck et al., E949 Proposal, BNL-67247, TRI-PP-00-06 (1999), `http://www.phy.bnl.gov/e949/` . E949 is an upgraded version of the E787 experiment.

[30] V.V. Anisimovsky *et al.*, Phys. Rev. Lett. **93**, 031801 (2004).

[31] D. A. Bryman *et al.*, Nucl. Instrum. Meth. **A396**, 394 (1997).

[32] M. Atiya *et al.*, Nucl. Instrum. Meth. **A279**, 180 (1989).

[33] E. W. Blackmore *et al.*, Nucl. Instrum. Meth. **A404**, 295 (1998).

[34] M. Kazumori, Master thesis, Osaka University, March 31 (1997).

[35] I-H. Chiang *et al.*, IEEE Trans. Nucl. Sci. **42**, No.4, 394 (1995).

[36] Saint-Gobain Ceramics & Plastics Inc. URL : http://www.crismatec.com/ .

[37] T. K. Komatsubara *et al.*, Nucl. Instr. and Meth. **A404**, 315 (1998).

[38] Sylgard 527, manufactured by Dow Corning Chemical Company, with a UV cutoff at ~ 240 nm in a wavelength and provide 95% transmission above 350 nm.

[39] The Relativistic Heavy Ion Collider, http://www.bnl.gov/RHIC/ .

[40] T. Yoshioka *et al.*, IEEE Trans. Nucl. Sci. **51**, 334 (2004).

[41] J. B. Birks, Proc. Phys. Soc. **A64** 874 (1951).

[42] T. Nakano *et al.*, E787 Technical Note 310 “A First Measurement of the $\pi\gamma\gamma(2)$ Branching Ratio” (1996).

[43] CDFE Website, Centre for photonuclear experiments data,
(URL) http://cdfe.sinp.msu.ru/cgi-bin/exf2htm?LINK=m0188009 .

[44] Photon veto studies for KOPIO experiments,
(URL) http://www.phy.bnl.gov/ djaffe/KOPIO/VETO/ .

[45] S. Chen *et al.*, E949 Technical Note K-034 “2002 $\pi\nu\overline{\nu}(1)$ Data Analysis” (2003).

[46] S. Chen*et al.*, E949 Technical Note K-038 “Further 2002 $\pi\nu\overline{\nu}(1)$ analysis” (2003).

Acknowledgments

For E949 Japanese Collaborators :

"Well, the E949 experiment . . . ", a person beside me broke the silence, kept walking along the corridor, "may stop . . . ", he continued. The sudden confess was the beginning of my doctor-course life, and the very next moment, two flight tickets to the United States were prepared. Yes, the person who drastically opened the curtain of my research life was Dr. T. Nomura, my supervisor. He and his words gave me a lot of exciting experiences in my research life. I would say the scene was very symbolic, since he was always beside me, and gave me a lot of advices and supported my studies. I would like to express my great appreciations to him.

Prof. S. Sugimoto, who is one of the E949 spokesperson in our group, took care of our research activities and arranged analysis meetings for us. Through the series of meetings, I could get many precious suggestions and/or comments to proceed my analyses. That was a great help to me.

Prof. T. K. Komatsubara. He is an excellent physicist. His comments always casted light on an ambiguous point in my analyses and made the tangled logics clear. I have got thousands of advices in our weekly analysis meetings and all (no single exception) were helpful for my studies. I also would like to thank his tremendous efforts to improve this thesis. I would like to report him this thesis was highly praised in the thesis defense.

Dr. T. Yoshioka, who played an important role in the E949 trigger development, provided me many precious information I required in this analysis. He was, actually, the best teacher who try to teach me how to enjoy beer. The lesson was quite enthusiastic, although I was not good at drinking. But there is no doubt that, having a chat with him was my great pleasure.

Dr. T. Sekiguchi, with whom I sometimes discussed analysis techniques, (once, the discussion grew up in another direction. . . and finally, we built up a virtual experiment in our mind and thought about what kind of detector design should be taken), while taking burgers in the TRIUMF cafeteria. In my private life, he is also one of my great friends. We enjoyed a short trip to Victoria, that was a great memory for me.

Mr. T. Fujiwara, who is now working on the analysis of the BNL-E787 experiment, provided me some references for kinematical fit routines. The kinematical fit codes I made for this analysis were based on the documents.

Dr. T. Tsunemi, who studied $K_{\pi 2}\gamma$ decay with the E787 data set, provided me a Monte Calro kludge code. This useful information helped me to update my codes for my specific use. He has wide interests on the many things in the world. Particularly, his knowledge covers economical issues. Sometimes, that brought me some fresh air. I also would like to say "thank you" to him for continuous e-mail exchanges, sometimes with nice pictures, while I was writing this thesis. I could refresh my brain fatigue.

I would like to thank all Japanese collaborators : Prof. M. Miyajima, Prof. Y. Tamagawa who arranged annual Fukui workshop, Prof. S. Kabe, Prof. M. Kobayashi, Dr. K. Omata, Prof. K. Sato and Prof. Y. Yoshimura, who supported my research life when I was in BNL, Dr. N. Muramatsu, Prof. T. Shinkawa, Prof. M. Nomachi and Prof. T. Nakano.

and

Prof. N. Sasao. He read through this thesis and gave me a lot of suggestions and comments to improve the sentenses without taking new year holidays. I was very glad to have his supports. I will never forget he had cakes sent in to me when I was exhausted with successive all-night works.

For E949 collaborators :
I would like to express my great appreciations to Prof. D.A. Bryman, Dr. J. Hu, Prof. P. Kitching, Dr. A. Konaka, Dr. J. Mildenberger, Dr. T. Numao, Dr. R. Poutissou of TRIUMF, Prof. S. Chen of Tsinghua University, Dr. I-H. Chiang, Dr. M.V. Diwan, Dr. J.S. Frank, Dr. D.E. Jaffe, Dr. S.H. Kettell, Dr. K.K. Li, Dr. L.S. Littenberg, Dr. G. Redlinger and Dr. B. Viren of BNL, Dr. D.V. Vavilov of IHEP, Mr. B. Lewis of University of New Mexico, Miss I.-A. Christidi of Stony Brook University and Prof. P.S. Cooper of FNAL. I also would like to express my acknowledgments to other E949 collaborators.

For all the members in High Energy Group of Kyoto University :

Dr. H. Nanjyo. He was a co-worker when I was in the ATLAS collaboration in my master course and, now is a roommate. I like (and respect) his attitude toward researches, especially when he faces to a problem. His aggressive style inspired me many times. Try and try and try, and then try. I recently get confident that I can manage to do anything if I seriously stand facing toward the problem, thanks for him.

Miss N. Taniguchi. I definitely believe she checks these acknowledgments, searching for her name. Hi, Nanae-san. How's everything going? I have one message to you. Even when you are in trouble, just keep going and going with your best effort. I hope you will have a happy research life. Thank you.

I would like to thank all the members : Prof K. Nishikawa, Prof. T. Nakaya, Dr. M. Yokoyama, Dr. H. Tanaka, Dr. T. Sumida, Dr. M. Hasegawa, Mr. S. Yamamoto, Mr. H. Yokoyama, Mr. H. Morii, Mr. J. Kubota, Mr. K. Hiraide, Mr. K. Ezawa, Mr. Y. Kurimoto, Mr. Y. Kurosawa, Mr. Y. Nakajima, Mr. T. Nobuhara, Mr. M. Taguti, Mr. K. Matsuoka, and people those who was in the group, Prof. R. Kikuchi, Prof. H. Sakamoto, Dr. K. Murakami, Dr. Y. Ushiroda, Dr. H. R. Sakai, Dr. T. Inagaki, Dr. S. Nishida, Dr. Y. Honda, Mr. A. Shima, Mr. E. Shinya, Dr. H. Maesaka, Mr. S. Tsuji, Mr. T. Morita, Mr. K. Hayashi, Mr. T. Sasaki, Mr. S. Ueda, Miss K. Takezawa, and Mr. T. Shirai.

Dr. I. Kato. If I say him in one word, he is a "inspector", definitely. He is now in TRIUMF, but I swear he knows what I'm doing now. I would like to say "thanks" to him for continuous digging of my directories to keep eyes on my research (and private) acitivities. Issei-san, when you will be back to Japan, please let me know. Let's have a great dinner.

Miss K. Uchida, who is one of the best friends. We had studied together when we were undergraduate students and also were master-course students. Kirika-san, I'm very glad when I have heard that you enjoy your research life in the University of Hawaii. I'm looking forward to seeing you and drinking with you when you get your PhD.

Mr. M. Suehiro. I talked a lot with him about recent electronics and softwares. He made kernel-patch codes for a computer cluster used in this analysis. Thanks for the codes, I could use the fastest computers with the given (limited) budget at the time. We also developed a device driver for CAMAC controllers. They are still in use in our laboratory.

Miss A. Nakao. She is a secretary of our group. She is really someone in our group. Not only she supported all our research activities, but also her smile took care of our mental health. We need her. There is no question about it. I would like to say “Everyone, please hand over your receipt to her as soon as possible when you get it”. Thank you.

And Others . . . :
Mr. R. Ichimiya. We developed front-end ASICs for the ATLAS experiment under a lot of pressure, since we could not re-make them easily. Occasionally, after everybody went to home, we started the work until morning because we had own daily duties. I explained every single verilog line and we traced the behavior at every single clock. I can still see the state diagram of the readout sequencer on a whiteboard in the electronics room. I encourage you to keep writing your thesis. And when you finish it, let’s have a meeting and enjoy talking about the electronics again.

I would like to thank all my friends. The thesis writing was very harsh job to me. They sometimes took me to recreations, concerts and so on. Chatting with them really refreshed my brain and removed all my stresses. I hope I can do something for you all.

and

Finally, I would like to express my deepest gratitudes to my parents, sister and brother. They supported my research life with various ways. Without the supports, I could not complete my doctor-course life. I also would like to thank my grandfather and grandmother and their families. They always welcomed me when I went back to my home town.

A Lists of Selection Criteria

A.1 Run selection

1. Data Acquisition Quality (BAD_RUN)
   Runs with a hardware or software problem in the data acquisition are removed.

A.2 Pass 1 selection criteria

The combination of the all entities listed below is called “PASS1-ALL”.

1. Duplicated Event Rejection (DUPEV)
   Duplicated events, which were caused by the parallel data processing in the DAQ, are removed.
2. Trigger Bit Examination (TRBIT)
   Events having the $\pi\nu\overline{\nu}$ trigger record are skimmed out.
3. Level 1.1 (LEV11)
   The Level 1.1 trigger condition is ensured.
4. Level 1.2 (LEV12)
   The Level 1.2 trigger condition is ensured.
5. Trajectory Reconstruction in the Range Stack (RD_TRK)
   At least one positively-charged track should be reconstructed in the Range Stack.
6. Stopping Counter Consistency (STLAY)
   Online stopping counter, which was from a hardware stopping counter finder, must be consistent with that of offline from the track reconstruction routine.
7. Waveform Digitizer Status in the π^+ Stopping Counter (BAD_STC)
   Events are rejected if whose pion stopping counter has a hardware problem at the waveform digitization.
8. Accidental Hit Rejection in the π^+ Stopping Counter (RSHEX)
   This cut rejects events with any accidental activity around the π^+ stopping counter, which would prevent from the π^+ decay chain search. Note that signals form the RS counters are multiplexed when feeding into a waveform digitizer.
9. Track Time Reconstruction in the Range Stack (TRKTIM)
   The track time is successfully reconstructed by averaging the hit times in the track counters.
10. Track Reconstruction in the Drift Chamber (UTC)
    Track fitting in the X-Y and R-Z plane should be succeeded and, at least, one track should be obtained.

11. Track Matching Quality between the Drift Chamber and the Range Stack (RDUTM)
    Extrapolation of the reconstructed track in the drift chamber should agree with the T2 counter in the Range Stack.

12. Momentum Cut in the Drift Chamber (PDC)
    Events with the momentum greater than 280 MeV/c in the drift chamber are rejected. The high momentum tracks would be dominated by the events of beam pions.

13. π^+ Stopping Position in the RSSC (LAY14)
    Charged tracks are rejected if they come to rest at the layer 14 with the dip angle $\cos(\theta_{\pi^+})$ less than -0.5.

14. Further Track Reconstruction Quality Cut in the Drift Chamber (UTC1)

15. Track Range Quality Cut (RANGE1)

16. Sector Crossing Check (RSHEX2)
    Sector crossing between the counters in the same hextant was prohibited in the stopping layer.

17. Track Reconstruction in the Target (TARGET)
    Track reconstruction should be succeeded in the target.

A.3 Pass 2 selection criteria

1. Crude $\pi^+ \to \mu^+$ Double Pulse Fitting in the π^+ Stopping Counter (FITPI)
   π^+ identification is performed using the $\pi^+ \to \mu^+$ double pulse fit to the waveforms in the stopping counter. The resultant χ^2, the muon energy, the pion decay time, and the muon z position relative to that of pion decay are examined.

2. Pion Scattering Cut with Beam Counters (PSCUT)
   Events are rejected if the energy in the B4 counter is smaller than 1.2 MeV or the B4 have a hit within ± 1.5 ns around the track time in the Range Stack, or pion Čerenkov counter have a hit within ± 1.0 ns around the track time with, at least, five pion PMTs firing.

3. Compound Target Reconstruction Cuts (TGCUT)
   Events are rejected if any of the following conditions is violated.

   - Kaon decay vertex is included in the target.
   - The hit time of the B4 hodoscope is consistent with the average kaon fiber time in the target within ± 4 ns.
   - The hit time in the I-Counters is consistent with the average time of the pion fiber hits within ± 5 ns.
   - The energy observed in the I-Counter should be consistent with the dE/dx of pion.

A.4 The box cuts for selection of π^+ from $K_{\pi 2}$

The combination of the following three cuts is called “KP2BOX”.

1. Momentum Selection
   Events are rejected if the momentum is three sigma ($\sigma_P = 2.295$ MeV/c) away from the monochromatic π^+ momentum of 205 MeV/c.
2. Energy Selection
   Events are rejected if the energy is three sigma ($\sigma_E = 3.158$ MeV) away from the monochromatic π^+ energy of 109 MeV.
3. Range Selection
   Events are rejected if the range is three sigma ($\sigma_R = 0.874$ cm) away from the monochromatic π^+ range of 30.3 cm.

A.5 The box cuts for selection of μ^+ from $K_{\mu 2}$

1. The combination of the following two cuts is called KM2BOX.
   (a) Momentum Selection
   Events are rejected if the momentum (P) satisfies the condition of $|P - 236| > 10$ MeV/c.
   (b) Range Selection
   Events with the range less than 37 cm are rejected.

A.6 Kinematical selection criteria

The combination of the all entities in this category is called “KINCUT-ALL”.

1. Fiducial Category
   (a) π^+ Dip Angle Cut (COS3D)
   Event, in which the π^+ dip angle of $\cos(\theta_{\pi^+})$ is greater than 0.5 or less than -0.5 is rejected.
   (b) Stopping Layer Constraint (LAYV4)
   Charged track should come to rest in the RS counters between layer 11 and 18.
   (c) Allowed Z Position in the π^+ Stopping Counter (ZFRF)
   Event, whose π^+ comes to rest at the outside of the allowed region, is rejected. The allowed z region (Z_{stop}) is varied depending on the stopping layer as follows,
      - $|Z_{stop}| \leq 35$ cm for the stopping layers of 11 and 12.
      - $|Z_{stop}| \leq 40$ cm for the stopping layer of 13.
      - $|Z_{stop}| \leq 30$ cm for the stopping layer of 14.
      - $|Z_{stop}| \leq 50$ cm for the stopping layers of 15, 16, 17 and 18.

    (d) Allowed Z Position in the Drift Chamber (ZUTOUT)
    Events are rejected if the trajectory passed through the outside of the fiducial volume of the drift chamber. The track z-position (Z_{DC}) at the outer radius of the drift chamber should be $|Z_{DC}| \leq 25$ cm.

2. Range Stack dE/dx Category
   This category was used in the bifurcation study for $K_{\mu 2}$ background suppression. Details of the cuts are described in the text in the section 4.4.4 on page 65.

    (a) Cut on the Confidence Level of π^+ Identification with the dE/dx in the Range Stack (RSDEDXCL)
    Events are rejected if the confidence level on the dE/dx energy loss in the Range Stack, is less than 0.04. The confidence level is constructed from the logarithmic deviation of the individual counters as,

$$\chi^i \equiv \frac{\log E^i_{exp} - \log E^i_{meas}}{\sigma^i} \tag{39}$$

    where E^i_{exp} is the expected energy and E^i_{meas} is the measured energy. The term of σ^i is the size of the error on the energy measurement. The cut position is tightened to 0.2 when the largest energy deviation is negative.

    (b) Maximum Allowed Energy Deviation in the Range Stack (RSDEDXMAX)
    Events are rejected when any of the track counters (i) has χ^i of $|\chi^2| \geq 4$ in the Range Stack. The χ^i is defined in Equation 39.

    (c) Likelihood based Selection with the Range Stack dE/dx (RSLIKE)
    Events are rejected if the likelihood is greater than 10. The likelihood is computed from the $\Delta(\log E)^i$ of the individual counter, which is defined as

$$\Delta(\log E)^i \equiv \log E^i_{exp} - \log E^i_{meas} \tag{40}$$

3. Range Stack Track Fitting Category

    (a) χ^2 Probability Selection at the Track Fitting (PR_RF)
    Events are rejected if the confidence level from the χ^2 probability in the X-Y track fitting is less than 0.05. The track fitting is performed with sector crossing points, RSSC hit locations and energy deposit in the π^+ stopping counter.

    (b) Track Matching Quality in the X-Y plane with the RS track and the UTC track extrapolation (PR_RF_XY)
    Events are rejected if the confidence level, which is computed from the residual of the UTC track extrapolation and the position of sector crossing and the RSSC hits, is less than 0.05.

    (c) Track Matching Quality in the RSSC Z Measurement (PR_RFZ1)
    Events are rejected if the confidence level, which is computed with the residual of the UTC track extrapolation from the RSSC Z measurements, is less than 0.005.

    (d) Track Matching Quality in the RS Z Measurement (PR_RFZ2)
    Events are rejected if the confidence level, which is computed with the residual of the UTC track extrapolation from the RS Z measurements, is less than 0.005.

4. Target Likelihood Category
    1. (a) Target Combined Likelihood Cut (TGLIKE1)
    Events are rejected if the combined likelihood, which is computed from timing, energy and distance from the UTC-extrapolated track at all pion fibers, is less than $10^{-3.2}$.
    2. (b) Another Target Combined Likelihood Cut (TGLIKE2)
    Events are rejected if the combined likelihood, which is computed from distance from the UTC-extrapolated track at all pion fibers, is less than $10^{-2.3}$.
5. Target Tracking Category
    1. (a) Hit Position Consistency between the Target and the B4 Hodoscope (TGDB4)
    Events are rejected if the closest hit (to kaon fibers) in the B4 Hodoscope is more than 2 cm apart from the kaon fibers in the X-Y plane.
    2. (b) Another Hit Position Consistency between the Target and the B4 Hodoscope (TGDB4TIP)
    Events are rejected if the farthest kaon fiber from the kaon decay vertex is more than 2-cm away from hits in the B4 hodoscope.
    3. (c) Maximum Allowed Gap at the Kaon Decay Vertex with Kaon fibers (TGDVXTIP)
    Events are rejected if the nearest kaon fiber to the kaon decay vertex is more than 0.7 cm apart.
    4. (d) Maximum Allowed Gap at the Kaon Decay Vertex with Pion Fibers (TGDVXXPI)
    Events are rejected if distance from the kaon decay vertex to the closest pion fiber is greater than 1.5 cm.
6. Stopping Counter Confirmation in the Range Stack (ICODEL14)
Events are rejected if the π^+ stopping layer is 14 and the outer RSSC has a prompt hit in the same sector or that of clockwise adjacent.
7. Track Fitting Quality in the Drift Chamber (UTCQUAL)
Events are rejected if the confidence level, which is computed from the residual of all hits including unused hits which are located within 1.5 cm from the reconstructed track, is less than 10^{-5}.
8. Range versus Momentum Consistency (RNGMOM)
Events are rejected if the range deviation $|\chi_R|$ is greater than 2.2. The deviation is defined as
$$\chi_R \equiv \frac{R_{meas} - R_{exp}}{\sigma_R} \tag{41}$$
where R_{meas} is the measured range in the Range Stack and R_{exp} is the expected range from the momentum in the drift chamber. σ_R is the resolution in the range measurement.
9. Maximum Allowed Gap in the Pion Track in the Target (PIGAP)
Events are rejected if a gap in the pion track is greater than 1.6 cm in the target.
10. Maximum Range in the Target (RTGHI)
Events are rejected if the pion path length is greater than 12 cm in the target.
11. Maximum Energy in the Target (ETCHI)
Events are rejected if the pion energy deposit is greater than 28 MeV in the target.

A.7 π^+ decay sequence selection criteria

This category was used for the bifurcation study in this thesis. Details are described in the text in the section 4.4.4 on page 64. The combination of the all cuts in this category is called “TD-ALL”.

1. Double Pulse Finding for $\pi^+ \to \mu^+$ Identification (IPIFLG)
   Events are rejected if the double pulse fitting is failed or the fitted pion time is more than 2.5 ns away from the track time in the Range Stack.
2. $\mu^+ \to e^+$ Decay Search (EV5)
   Events are rejected if the $\mu^+ \to e^+$ decay is not found. Positron candidate is searched around the π^+ stopping counter in the prepared time window expected from the muon lifetime. If the positron candidate has hits on both sides (inner and outer layer) of the stopping counter, the event is rejected.
3. Muon Time Accidental Rejection (TDFOOL)
   Events are rejected if an accidental activity is found at the π^+ decay time in the RS counter in the two prior layer from the stopping counter. Double pulse fitting is performed to the counter and when extracted second pulse is consistent with the muon time in the stopping counter, the event is rejected.
4. Neural Network based $\pi^+ \to \mu^+$ Decay Search (TDVARNN)
   Events are rejected if the neural network output is less than 0.76. The neural network is constructed with (1) the log product of χ^2 from single pulse fit at both ends, (2) log product of the χ^2 ratio of single pulse fit to that of double pulse fit, (3) extracted muon energy, (4) extracted muon time, (5) z position difference between π^+ and μ^+ (6) time difference of the second pulse between both ends.

A.8 Beam background rejection criteria

1. Target Track Quality
   (a) Target Reconstruction Quality (TGQUALT)
   Events are rejected if (1) no kaon cluster is found, or (2) more than five kaon clusters are found, or (3) any of the kaon clusters consists of more than 150 fibers, or (4) no kaon cluster is connected to the pion passage, or (5) no pion track is found even if the kaon cluster is away from the target edge.
   (b) Target Fiducial Region (TGZFOOL)
   Events are rejected if the z position of the kaon decay vertex, which is extrapolated from the UTC track, is less than -15 cm.
   (c) Maximum Allowed Gap between Kaon and Pion Fibers (TARGF)
   Events are rejected if the distance from the kaon cluster to the nearest pion fiber is greater than 0.7 cm.
   (d) Track Matching between Target and Drift Chamber (DTGTTP)
   Events are rejected if the discrepancy between the track in the target and that of the drift chamber is greater than 2.0 cm at the target edge.

(e) Target Path Length Quality (RTDIF)
    Events are rejected if error in the measurement of the pion path length is large.

(f) Scattering Cut in the Target (DRP)
    Events are rejected if a kink is found in the pion track in the target. Events are recognized to have a kink with D_{diff} greater than 0.35, where the D_{diff} is defined as

$$D_{diff} \equiv \frac{D_{max} - D_{min}}{R_{tg}} \tag{42}$$

2. Selection Criteria for the B4 Hodoscope

   Details on selection criteria for two-beam background rejection are described in the section 4.4.6 on page 72.

   (a) $K^+ - \pi^+$ Separation with dE/dx energy loss in the B4 hodoscope (B4DEDX)
       Energy deposit in the B4 hodoscope should be greater than 1.1 MeV.

   (b) Extra Activity Rejection in the Beam Wire Chamber (BWTRS)
       Events are rejected if an extra hit exists in the beam wire chamber within ± 4.5 ns from the π^+ track time.

   (c) CCD Pulse Consistency in the B4 Hodoscope (B4ETCON)
       Energy measured with CCDs should be consistent with that of ADCs within $\pm$ 1.5 MeV. Hit time measured with CCDs should be consistent with that of TDCs within $\pm$ 2.0 ns.

   (d) Extra Activity Rejection in the B4 Hodoscope (B4TRS)
       Events are rejected if an extra activity is found in the TDCs within $\pm$ 2.5 ns from the π^+ track time or, in the CCDs within $\pm$ 1.5 ns from the track time.

   (e) Double Pulse Rejection in the B4 Hodoscope (B4CCD)
       Double pulse fitting is performed to CCD pulses in the B4 Hodoscope. If the time of the second pulse is within $\pm$ 3.5 ns from the π^+ track time, the event is rejected.

3. Selection Criteria for the Čerenkov Counter

   Details on this selection criteria are described in the section 4.4.6 for two-beam background suppression on page 72.

   (a) Extra Activity Rejection in the Pion Čerenkov Counter (CPITRS)
       Extra activity is rejected when its average of TDC and/or CCD timings is within $\pm$ 2ns from the track time.

   (b) Extra Activity Rejection with Pulse Trailing Edge in the Pion Čerenkov Counter (CPITAIL)
       Extra activity is rejected when the average time of the pulse trailing edges in the pion Čerenkov counter is within $\pm$ 2 ns from the pion track time.

   (c) Extra Activity Rejection in the Kaon Čerenkov Counter (CKTRS)
       Extra activity is rejected when the average of the TDC or CCD timings in the Kaon Čerenkov counter is within $\pm$ 2 ns from the pion track time.

(d) Extra Activity Rejection with Pulse Trailing Edge in the Kaon Čerenkov Counter (CKTAIL)
Extra activity is rejected if the average of the pulse trailing times is coincident with the pion track time. The coincident conditions are varied depending on the kaon fiber time (t_K) and that of pion (t_π) as follows,

    i. ± 3 ns from the pion track time if $t_\pi - t_K < 15$ ns.
    ii. ± 3.5 ns from the pion track time if 15 ns $< t_\pi - t_K < 25$ ns.
    iii. ± 2 ns from the pion track time if $t_\pi - t_K \geq 25$ ns.

4. Cuts on Beam Likelihood (B4EKZ)
   A likelihood function is constructed with the energy deposit in the B4 hodoscope, energy sum of the kaon fibers and the kaon decay vertex. Events are rejected if the likelihood is less than 2.0. The cut position is tightened when there is no pion fibers in the target.

5. Kaon and Pion Timing Consistency in the Target (TIMCON)
   The averaged kaon fiber time should be consistent with that of the B4 hodoscope within ± 3 ns. The averaged pion fiber time should be consistent with the charged track time in the Range Stack within ± 4 ns.

6. Consistency of the Kaon Fiber Timings (TGTCON)
   Each of the kaon fiber time should be consistent with the reconstructed kaon time in the target. The allowed discrepancy is varied depending on the energy in the fiber.

7. I-Counter Hit Time Consistency (TIC)
   The I-Counter hit timing should be consistent with the charged track timing in the Range Stack within ± 5 ns.

8. Delayed Coincidence Requirement (DELC)
   This cut was used for single beam background suppression. Details are described in the section 4.4.5 on page 68.

   Events with no significant timing gap between t_K and t_π is rejected, where t_K is the average kaon fiber timing and the t_π is that of pion fibers. The required timing gap is varied, depending on reliability of the timing strobes, as follows.

   - $t_\pi - t_K > 2$ ns if none of the following conditions is satisfied.
   - $t_\pi - t_K > 3$ ns if the number of pion fibers is less than four.
   - $t_\pi - t_K > 3$ ns if beam likelihood is less than 200.
   - $t_\pi - t_K > 4$ ns if there is a kaon fiber whose timing is 2 ns away from the t_K.
   - $t_\pi - t_K > 4$ ns if there is a pion fiber whose timing is 3.5 ns away from the t_π.
   - $t_\pi - t_K > 4$ ns if kaon energy deposit is less than or equal to 50 MeV in the target.
   - $t_\pi - t_K > 5$ ns if the kaon time in the B4 hodoscope is 1 ns away from the t_K.
   - $t_\pi - t_K > 5$ ns if no pion fiber is found.
   - $t_\pi - t_K > 6$ ns if the pion track timing in the Range Stack is 1.5 ns away from the t_π.

9. Cut on the Kaon Decay Vertex in the I-Counter (KIC)
   Events are rejected if the nearest I-Counter to the kaon fibers have a hit at the kaon time. The cut rejects an events with the kaon coming to rest in the I-Counter.

A.8.1 Beam likelihood distribution

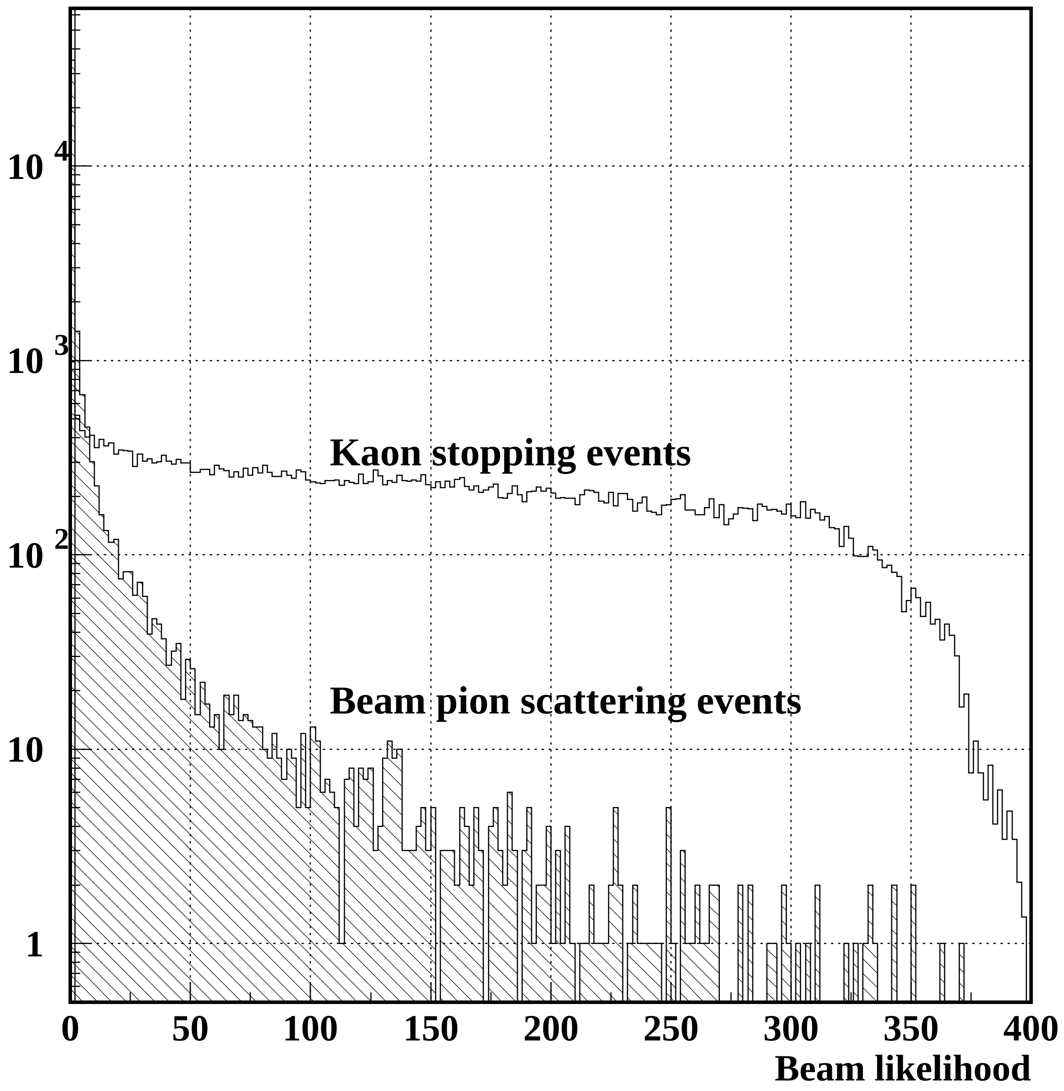

Figure 88: Beam likelihood distribution. The likelihood function was reconstructed from a distribution of the energy deposit in the B4 hodoscope, the kaon stopping Z position expected from the track extrapolation by the drift chamber, and the kaon energy deposit in the scintillator fiber targets. The open histogram was from the Kaon stopping events made with $K_{\mu 2}$ real data and the hatched histogram was from that of the beam pion scattering events.

A.9 $K_{\pi 2}$ selection criteria

The $K_{\pi 2}$ selection criteria are composed of 7 categories, as shown in Table 35. Details of each cut are described in Appendix A on page 130. Brief description for each category is presented below. (1) Run range cuts skimmed stable runs by dropping runs with trigger changes or extremely short runs. Runs with a hardware problem were also discarded. (2) In the PASS 1 selection, crude selection with trigger recorded was performed in offline. Fairly loose offline cuts with reconstructed kinematics were also imposed. (3) In the PASS 2 selection, $K_{\pi 2}$ events were selected. Events which passed the selection were used in the $\pi^0 \rightarrow \nu\overline{\nu}$ analysis. Beam backgrounds and muon backgrounds were also skimmed out in this level. They were used for background studies. (4) This was called "the signal box", which selected monochromatic π^+s with the box cut for momentum, energy and range. (5) These are selection criteria for reconstructed kinematics. (6) This is a list of π^+ decay sequence cuts. They discarded muon events by tracing the π^+ decay sequence. (7) A list of beam background cuts. Single pion beam backgrounds and two-beam backgrounds were rejected.

Table 35: $K_{\pi 2}$ event selection criteria.

(1) Available run range and bad run cuts					
BAD_RUN	$run \geqq 48077$ except for $48540 \leqq run \leqq 48575$				
(2) PASS1 level cuts (a selection of healthy data)					
DUPEV	TRBIT	LEV11	LEV12	RD_TRK	STLAY
BAD_STC	RSHEX	TRKTIM	UTC	RDUTM	PDC
LAY14	UTC1	RANGE1	RSHEX2	TARGET	
(3) PASS2 level cuts and event skimming (Final selection for offline analysis)					
FITPI	PSCUT	TGCUT			
(4) π^+ monochromatic kinematics box cuts : $K_{\pi 2}$ selection					
Momentum :	$\|P - P_{peak}\| < 3\sigma_P$ where $P_{peak} = 205.0$ MeV/c and $\sigma_P = 2.295$ MeV/c				
Energy :	$\|E - E_{peak}\| < 3\sigma_E$ where $E_{peak} = 109.0$ MeV and $\sigma_E = 3.158$ MeV				
Range :	$\|R - R_{peak}\| < 3\sigma_R$ where $R_{peak} = 30.33$ cm and $\sigma_R = 0.8738$ cm				
(5) Kinematics selection criteria					
(A) Fiducial	(B) RS dE/dx	(C) PRRF	(D) TGLIKE	(E) TGDB4	(F) Other
COS3D	RSDEDXCL	PR_RF	TGLIKE1	TGDB4	ICODEL14
LAYV4	RSDEDXMAX	PR_RF_XY	TGLIKE2	TGDB4TIP	UTCQUAL
ZFRF	RSLIKE	PR_RFZ1		TGDVXTIP	RNGMOM
ZUTOUT		PR_RFZ2		TGDVXPI	PIGAP
(6) π^+ decay sequence cuts					
IPIFLG	EV5	TDFOOL	TDVARNN		
(7) Beam background cuts					
(A) TG pattern	(B) B4BWBH	(C) Čerenkov	(D) TG energy	(E) Timing	(F) Other
TGQUALT	B4DEDX	CPITRS	B4EKZ	TIMCON	DELC
TGZFOOL	BWTRS	CPITAIL		TGTCON	KIC
TARGF	B4ETCON	CKTRS		TIC	
DTGTTP	B4TRS	CKTAIL			
RTDIF	B4CCD				
DRP					

A.10 $K_{\mu 2}$ selection criteria

The $K_{\mu 2}$ selection criteria are composed of four categories, as shown in Table 36. In the selection criteria, the same beam background cuts are used as in the $K_{\pi 2}$ selection criteria. π^+ identification cuts such as Range Stack dE/dx cuts and π^+ decay sequence cuts are turned off. The monochromatic μ^+ of the $K_{\mu 2}$ decay is selected by the cut "KM2BOX".

Table 36: The $K_{\mu 2}$ selection criteria.

(1) Available run range and bad run cuts					
BAD_RUN	$run \geqq 48077$ except for $48540 \leqq run \leqq 48575$				
(2) μ^+ monochromatic kinematics box cuts : $K_{\mu 2}$ box					
KM2BOX					
(3) Kinematics cuts					
(A) Fiducial	(B) PRRF	(C) TGLIKE	(D) TGDB4	(E) Other	
COS3D	PR_RF	TGLIKE1	TGDB4	ICODEL14	
ZFRF	PR_RF_XY	TGLIKE2	TGDB4TIP	UTCQUAL	
ZUTOUT	PR_RFZ1		TGDVXTIP	RTGHI	
	PR_RFZ2		TGDVXPI	ETGHI	
				PIGAP	
(4) Beam background cuts					
(A) TG pattern	(B) B4BWBH	(C) Čerenkov	(D) TG energy	(E) Timing	(F) Other
TGQUALT	B4DEDX	CPITRS	B4EKZ	TIMCON	DELC
TGZFOOL	BWTRS	CPITAIL		TGTCON	KIC
TARGF	B4ETCON	CKTRS		TIC	
DTGTTP	B4TRS	CKTAIL			
RTDIF	B4CCD				
DRP					

A.11 Loosened $K_{\pi 2}$ selection criteria for single photon inefficiency study

The loosened $K_{\pi 2}$ selection criteria for the studies of the single photon inefficiency are presented. The cut definitions, which are described with the abbreviations in brackets, are shown in the section A on page 130. Run range selection criteria are summarized in Table 37 on page 142.

1. Fiducial selection criteria for π^+
   (a) the π^+ stopping layer should be greater than 7 and smaller than 17.
   (b) π^+ dip angle condition (COS3D).
2. Successful track reconstruction in the target (TARGET).
3. Timing strobe consistency
   (a) Kaon time consistency
   The average kaon fiber time should be consistent with that of the B4 hodoscope within 3.7 ns.

   (b) Pion time consistency
      The average pion fiber time should be consistent with that of the track time in the Range Stack within 5.4 ns.

4. Fiducial selection criteria for the kaon decay vertex (TGZFOOL)

5. Maximum allowed gap in the target
   Gap between the kaon fiber and the nearest pion fiber should be less than 1.5 cm.

6. Track time consistency with the I-Counter
   The I-Counter hit time should be consistent with the track time in the Range Stack within 3 ns.

7. Track matching quality between the target and the drift chamber (DTGTTP)

8. Double pulse finding for $\pi^+ \rightarrow \mu^+$ decay (IPIFLG)

9. $K^+ - \pi^+$ separation with dE/dx energy loss in the B4 hodoscope (B4DEDX)

10. Delayed conincidence
    The pion fiber time t_π should be, at least, 2 ns later than that of kaon fiber time.

11. Extra activity rejection in the Čerenkov counter

    (a) Events are rejected if there is a hit in the kaon Čerenkov counter within 1.2 ns from the track time in the Range Stack.
    (b) Events are rejected if there is a hit in the pion Čerenkov counter within 4.3 ns from the track time in the Range Stack.

12. Extra activity rejection in the beam wire chambers
    Events are rejected if the beam wire chamber-1 (-2) has a hit within 1.9 ns (1.3 ns) from the track time in the Range Stack.

13. Extra activity rejection in the B4 hodoscope
    Events are rejected if the B4 hodoscope has a hit within 3.0 ns from the track time in the Range Stack. The condition is unactivated when the hit time is within 10 ns from the kaon beam time.

14. Monochromatic $K_{\pi 2}$-π^+ selection
    Events are accepted if the π^+ momentum (P) is $195 < P < 215$ MeV/c, the energy (E) is $94 < E < 114$ MeV, and the range (R) is $27 < R < 35$ cm.

Table 37: Run conditions for the data used in the single photon inefficiency study. The 1gamma data were accumulated from run-47592 to run-48975. Problematic runs for this study should be removed. Runs before 40877 were removed due to the hardware problems. A total of 14 % of the data was lost by the run range cut.

Run range	Description
47592 ∼ 47719	Analog sum modules were used for online photon veto.
48003 ∼ 48975	Mean-timer modules were used for online photon veto.
47592 ∼ 48975	NG2 was generated from the online BV veto
47592 ∼ 48076	L1.2 was broken.
48077 ∼ 48134	L1.2 did not fully function.
47592 ∼ 48231	EC discriminator was unplugged.

B Details on none-$K_{\pi 2}$ background suppression

Details on the studies of the background suppression are presented in this section. Since the studies involve many selection criteria, the criteria are denoted with the abbreviations. The abbreviation “PV” means the photon veto cuts, and other abbreviations are described in the section A on page 130.

In the bifurcation method, background estimation is performed with two measurements of “B” and “R” in Equation 19 on page 61. Each of the background analysis (single-beam, two-beam and muon backgrounds) is branched to the two measurements. The first branch for the measurement of “R” is called “rejection branch” and that of “B” is called “normalization branch”.

B.1 Single beam background suppression

The bifurcation study for the single beam background was performed with B4DEDX and DELC.

Rejection branch The bifurcation chart for the rejection branch is shown in Figure 89. Since the DELC rejection was large, setup cuts, which correspond to the (1), (2) and (3) in the figure, were relaxed to increase the usable statistics. The DELC rejection was measured with the number entries before and after its application (see (6) in the figure).

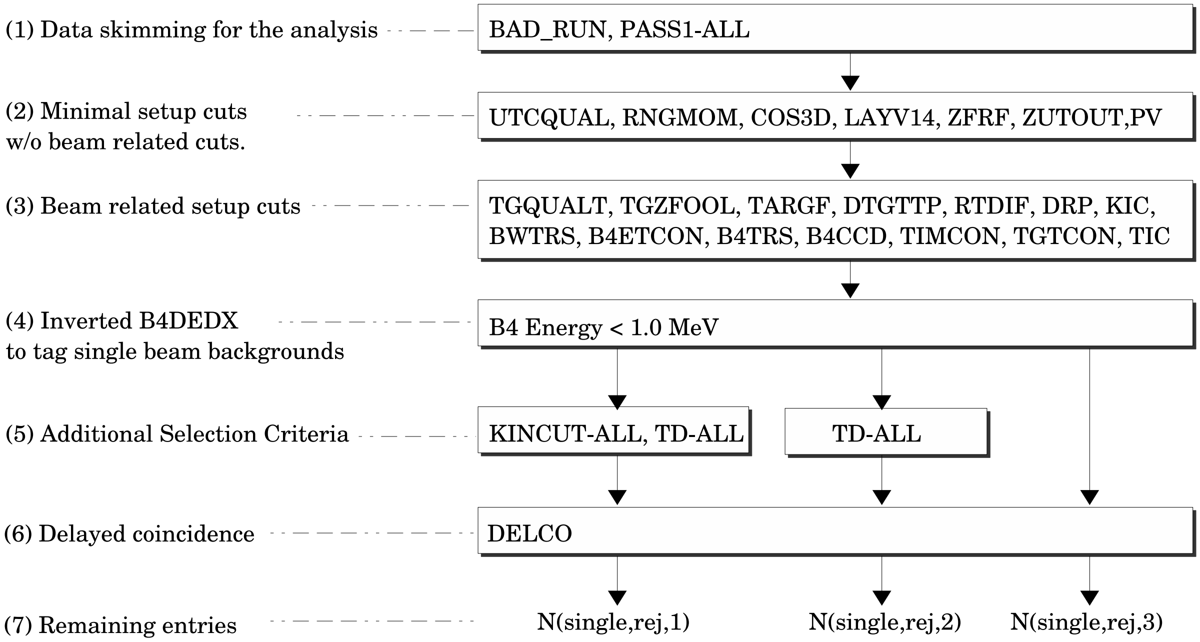

Figure 89: Analysis flow chart for the rejection branch in the single beam background study.

Normalization branch The measurement of the normalization branch was further branched with the cuts for Čerenkov counter hits (see the cut-(5) in Figure 90). With the application of CKTRS and CKTTAIL, which corresponded to the kaon Čerenkov counter veto, the number of single π^+ beam backgrounds in the normalization branch was individually measured. With the application of CPITRS and CPITAIL, single π^+ beam backgrounds, which involved kaon decays in flight, was measured. The normalization factor was obtained with the number of entries after all the cut application except for inverted DELC (see (4) in the figure).

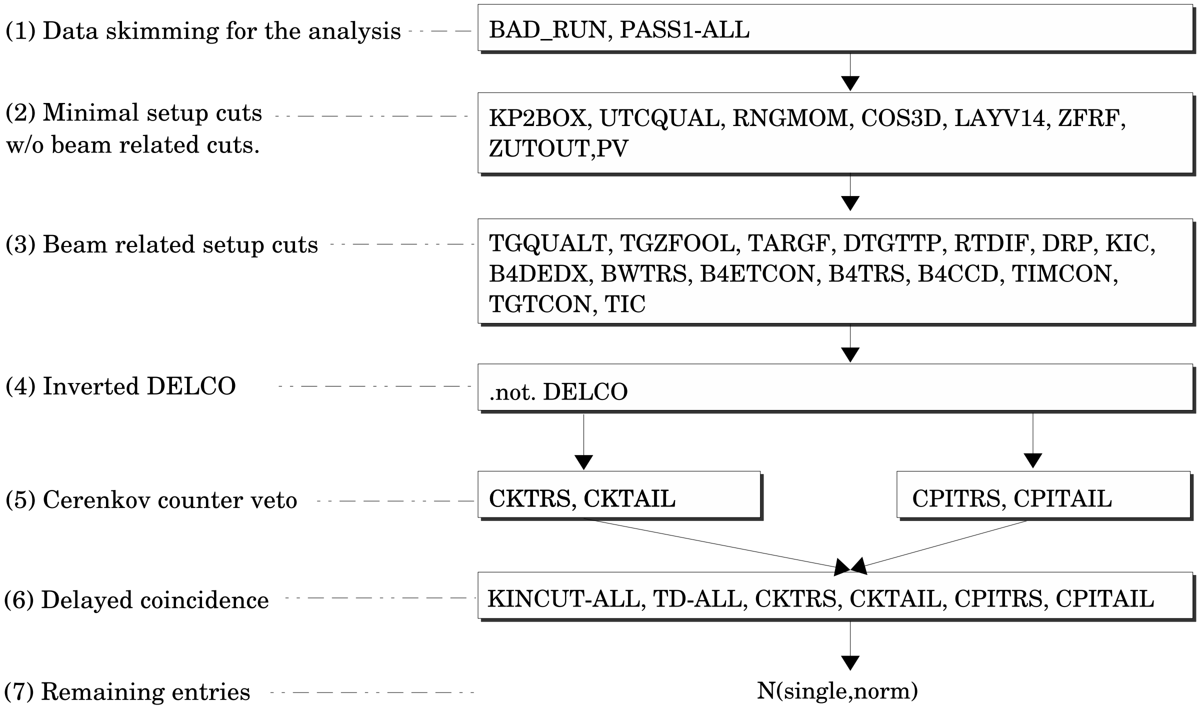

Figure 90: Analysis flow chart for the normalization branch in the single beam background study.

B.2 Two-beam background suppression

The bifurcation study for the two-beam backgrounds was performed with the extra beam cuts by the B4 hodoscope (B4TRS, B4CCD) and that of Čerenkov counters and Beam wire chambers (BWTRS, CKTRS, CKTAIL, CPITRS, CPITAIL).

Rejection branch In the rejection branch, rejection factors for π^+ beams and K^+ beams were individually measured with the sample tagged with inverted B4TRS and B4CCD cuts, as shown in Figure 91. In the measurement, kaons were tagged with the pion Čerenkov counter veto (CPITRS, CPITAIL) and larger B4 energy deposit (see cut-(5) and (6) in the figure). Pions were tagged with CKTRS, CKTAIL and the condition of the B4 energy smaller than 1.1 MeV.

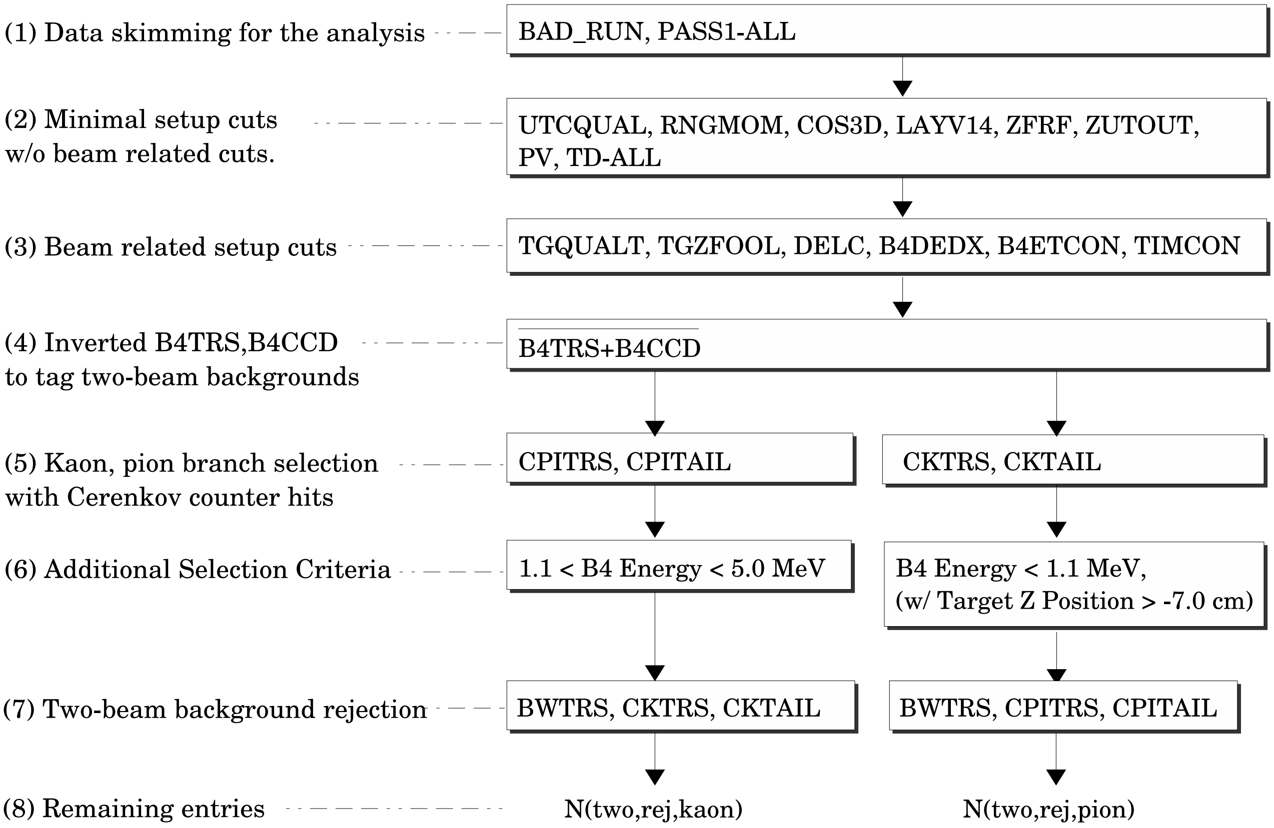

Figure 91: Analysis flow chart for the rejection branch in the two-beam background study.

Normalization branch In the normalization branch, the normalization factor for kaon beam was measured with the number of remaining entries after the application of inverted BWTRS, CKTRS and CKTAIL to the kaon events. They were tagged with pion Čerenkov counter veto (see the cut-(4) and (5) in Figure 92). The normalization factor for pion beam was measured by applying the inverted BWTRS, CPITRS and CPITAIL to the pion events tagged with kaon Čerenkov counter veto.

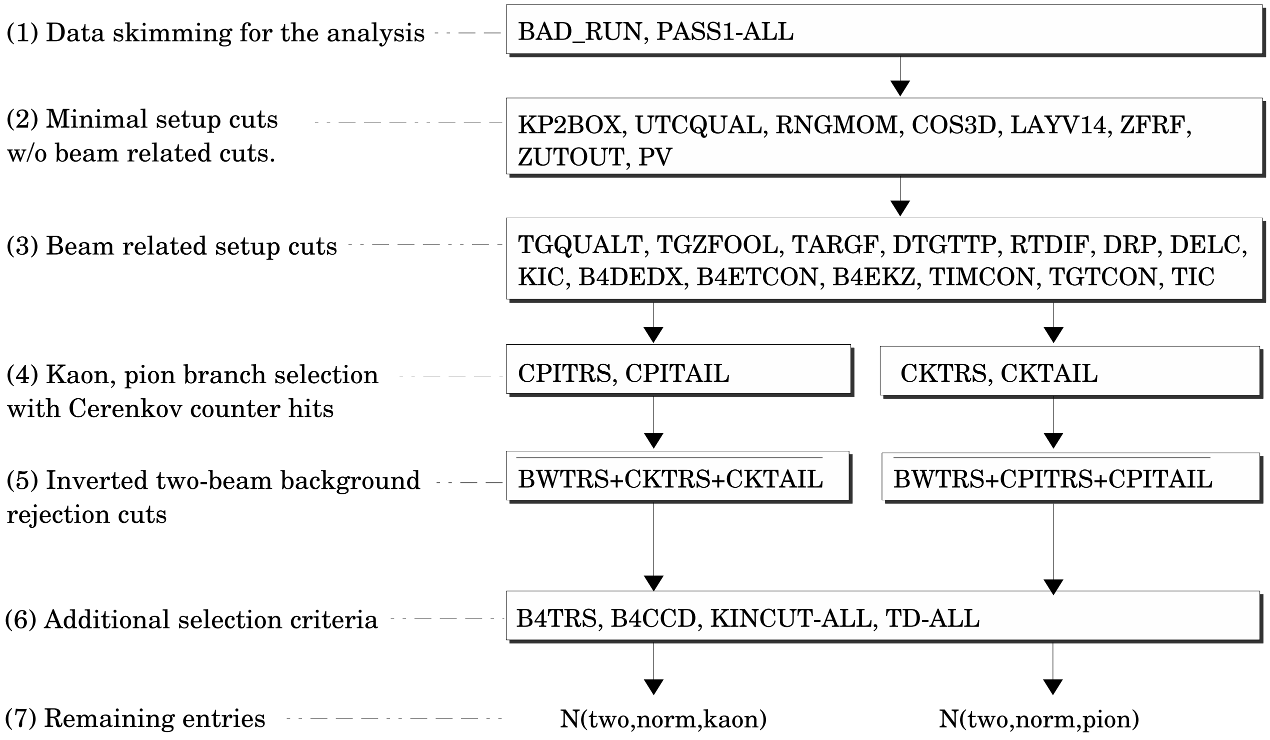

Figure 92: Analysis flow chart for the rejection branch in the two-beam background study.

B.3 Muon background suppression

Bifurcation studies for the muon backgrounds were performed with the Range Stack dE/dx cut (RSDEDX) and pion decay sequence cut (TD-ALL).

Rejection branch In the rejection branch, the rejection of TD-ALL was measured with the sample tagged with the inverted RSDEDX cut. The rejection measurement was branched for events in the muon band and $K_{\mu 2}$ range tail (see Figure 25 on page 45) to see the consistency. The analysis flow is illustrated in Figure 93.

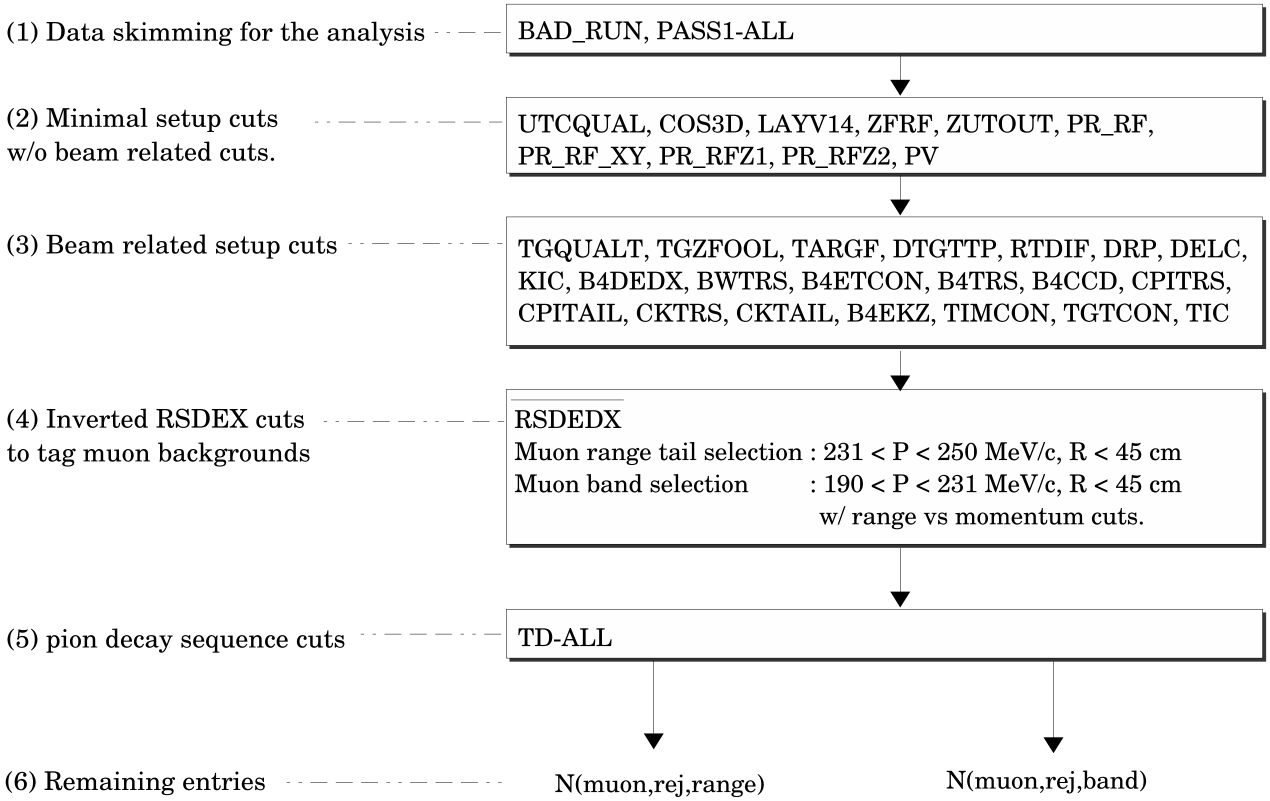

Figure 93: Analysis flow chart for the rejection branch in the muon background study.

Normalization branch In the normalization branch, the normalization factor was measured with the number of entries after the application of the inverted TD-ALL, where all $K_{\pi 2}$ selection criteria except for the TD-ALL were imposed to the sample. The analysis flow is illustrated in Figure 94.

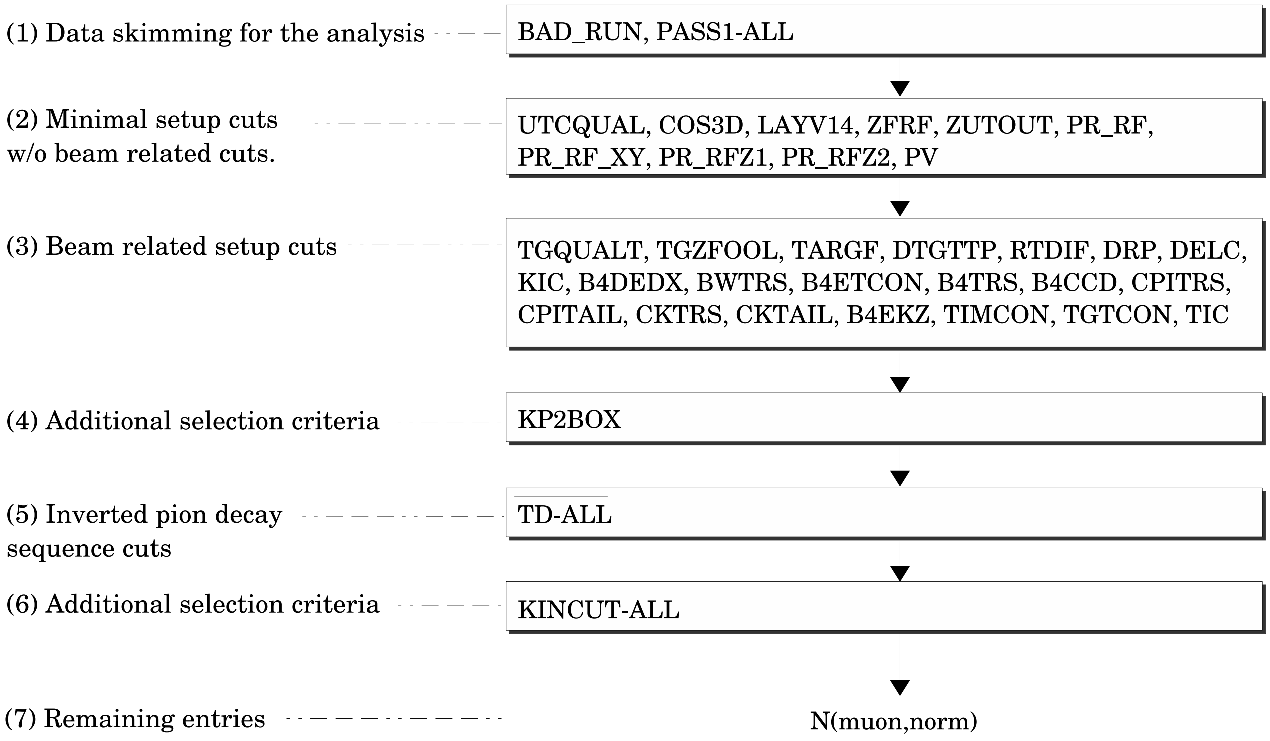

Figure 94: Analysis flow chart for the normalization branch in the muon background study.

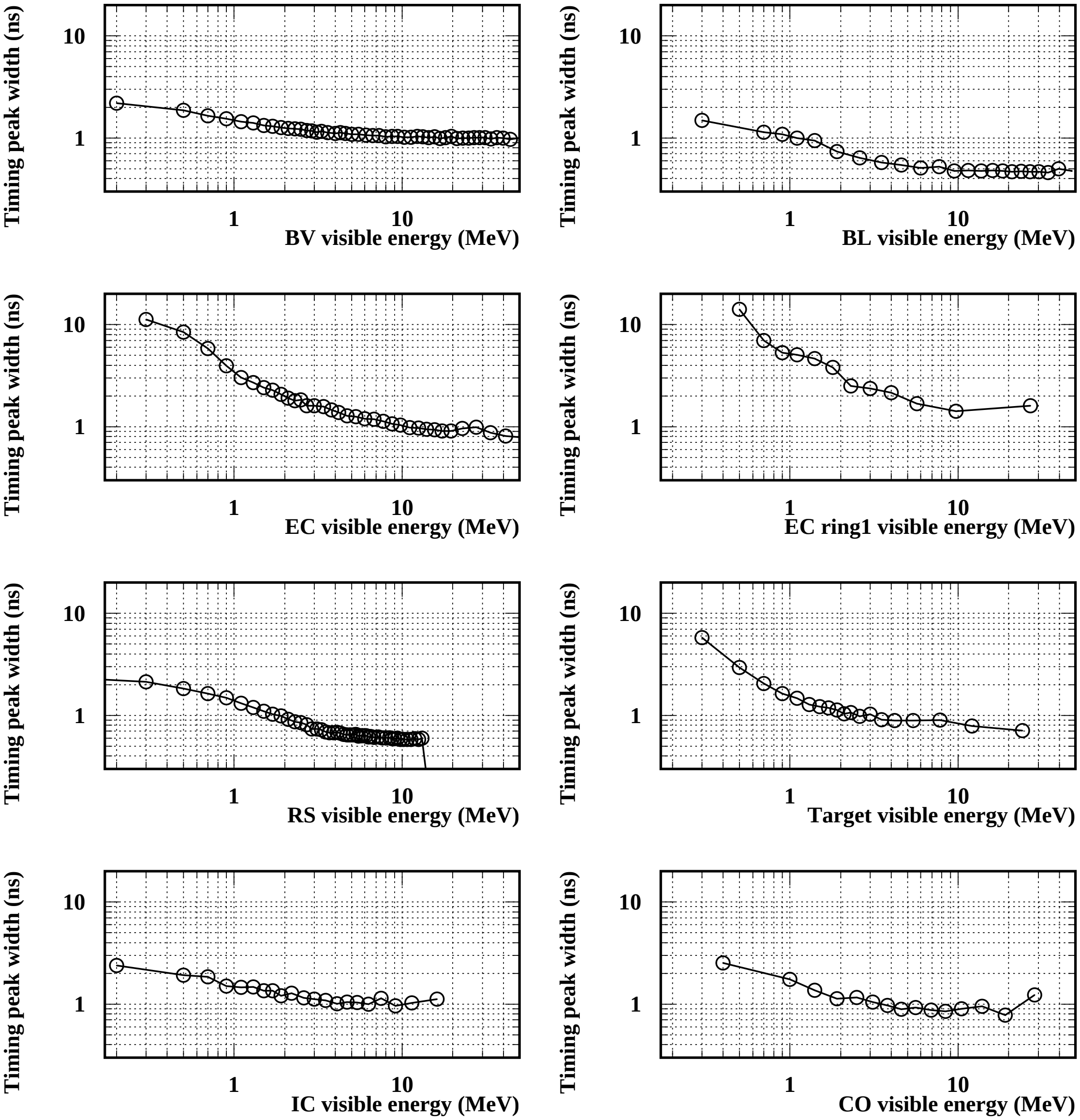

Figure 95: The measured peak width (timing resolution) as a function of hit energy in the various photon detectors. Abbreviations; BV = Barrel Veto, BVL = Barrel Veto Liner, EC = End cap CsI detector, RS = Range Stack, IC = I-Counters, CO = Collar counters. The plots for V-counter and Micro-Collar counter was not available due to the statistical shortage from low hit occupancy.

C Photon reconstruction and kinematical fitting

C.1 The fiducial cuts for tagging photons

Not to use poorly reconstructed tagging photons in the kinematical fitting, fiducial constraints were developed to confirm their energy was fully contained in the detector volume. Distribution of the observed energy in the BVL and the BV first layer was produced with reconstructed photons by the clustering method (see left plot in Figure 96). To reject events with shower leakage, it was confirmed that the conversion process started in the BVL or BV layer 1 by requiring the energy deposit greater than 15 MeV in the modules. Photon dip angle cut was also developed to discard photons went to the 45-degree region. This is because the radiation lengths of the photon detectors were not enough around the region. In addition to it, the region was a boundary between the End Cap Calorimeters and the barrel photon detectors (BV and BVL). The clustering method might have separated two clusters, if a photon went to the direction. The cut position was set at $|\cos(\theta_\gamma)| = 0.45$, taking into account the resolution. Acceptance loss by imposing the both cuts was ~0.85.

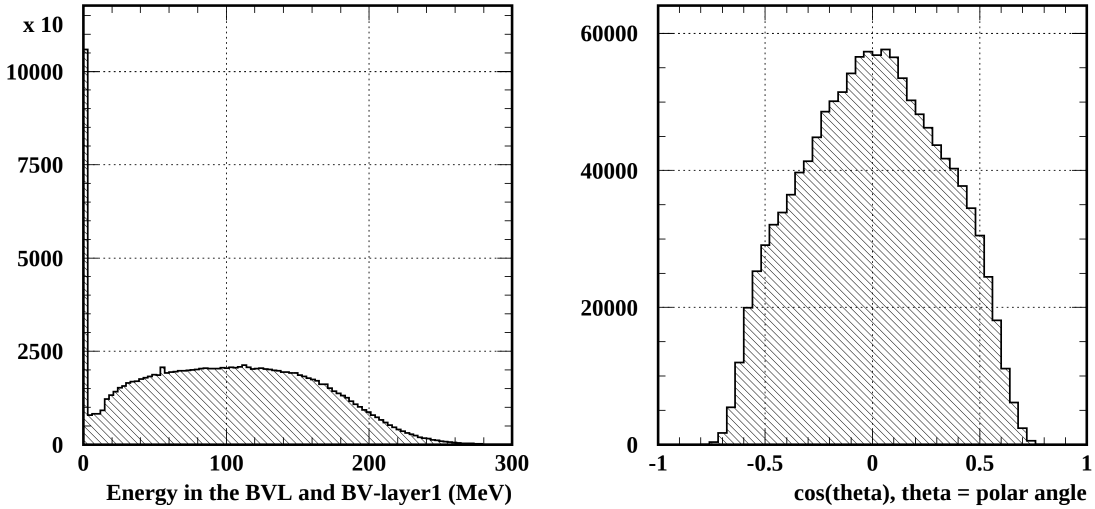

Figure 96: Miscellaneous plots on the fiducial cuts for tagging photons. In the left plot, distribution of the total energy deposit in the BVL and BV layer 1 is shown. Peak standing at the origin (Energy=0) comes from events with no photon conversion in the BV / BVL modules. The right plot shows the flight direction ($\cos(\theta)$) of the reconstructed photons.

C.2 Lagrange multiplier technique

Suppose that there are N measureable variables $y_1, y_2, \cdots, y_N$ and J un-measureable variables $\xi_1, \xi_2, \cdots, \xi_J$ in your experiment, and when the event reconstruction, all of them (y_i and ξ_i) are required. Constraints on physics (conservation laws ...) provide the K number of relations to the y_i and ξ_i for the reconstruction. In this section, the technique of the kinematical fitting with the Lagrange multiplier method is presented, explaining how to obtain the ξ_i and the best fitted values η_i for the N measured variables.

The N dimensional column-wise vector $\mathbf{y}$ and J dimensional vector of ξ are defined as arrays of the measured and unmeasured variables; $\mathbf{y} = (y_1, \cdots, y_N)^T$ and $\xi = (\xi_1, \cdots, \xi_J)^T$. The best fitted result to the $\mathbf{y}$ is denoted as η (N dimension). The K number of constraint functions are denoted with a vector notation : $\mathbf{f}(\eta, \xi) = 0$. The primal goal of the kinematical fitting is to minimize the χ^2 defined as

$$\chi^2(\eta, \xi) = (\mathbf{y} - \eta)^T V^{-1} (\mathbf{y} - \eta) \tag{43}$$

and to obtain sets of η and ξ at the point where they satisfy the constraints of $\mathbf{f}(\eta, \xi) = 0$. In above equation, V is a covariance matrix consisted of errors in the measurements. The mathematical solution of the minimization is provided by the Lagrange Multiplier method. The method extends the prior χ^2 equation as follows, by introducing K coefficients of λ (K dimensional vector),

$$\chi^2(\eta, \xi, \lambda) = (\mathbf{y} - \eta)^T V^{-1} (\mathbf{y} - \eta) + 2\lambda^T \mathbf{f}(\eta, \xi) \tag{44}$$

At the minimum-χ^2 point, the differential coefficients for each variable should be zero;

$$-2V^{-1}(\mathbf{y} - \eta) + 2\mathbf{F}_\eta^T \;=\; 0 \;:\; \frac{\partial \chi^2}{\partial \eta} \tag{45}$$

$$\mathbf{F}_\xi^T \lambda \;=\; 0 \;:\; \frac{\partial \chi^2}{\partial \xi} \tag{46}$$

$$\mathbf{f}(\eta, \xi) \;=\; 0 \;:\; \frac{\partial \chi^2}{\partial \lambda} \tag{47}$$

where the matrices $\mathbf{F}_\eta$ and $\mathbf{F}_\xi$ are defined as $(\mathbf{F}_\eta)_{kn} \equiv \frac{\partial f_k}{\partial \eta_n}$, $(\mathbf{F}_\xi)_{kj} \equiv \frac{\partial f_k}{\partial \xi_j}$. Below, we take an iterative procedure to solve the equation of the matrices. Assuming the solutions of ν-th iteration have already been obtained (denoted as η^ν, ξ^ν and λ^ν), Equation 47 is described in a Taylor expansion style as below with supposing ν+1-th order of solutions are close to that of ν-th.

$$f_k^\nu + \sum_{i=1}^{N} \left(\frac{\partial f_k}{\partial \eta_i} \right) (\eta_i^{\nu+1} - \eta_i^\nu) + \sum_{j=1}^{J} \left(\frac{\partial f_k}{\partial \xi_j} \right) (\xi_j^{\nu+1} - \xi_j^\nu) + \cdots = 0 \quad \text{for k = 1, K.} \tag{48}$$

Ignoring the higher order term, above equation is written as follows in the vector notation :

$$\mathbf{f}^\nu + \mathbf{F}_\eta^\nu (\eta^{\nu+1} - \eta^\nu) + \mathbf{F}_\xi^\nu (\xi^{\nu+1} - \xi^\nu) = 0 \tag{49}$$

With the ν+1-th solutions of Equation 45, $\eta^{\nu+1}$ is written as

$$\eta^{\nu+1} = -V(\mathbf{F}_\eta^T)^\nu \lambda^{\nu+1} + \mathbf{y} \tag{50}$$

where the $(\mathbf{F}_\eta^T)^{\nu+1}$ is assumed not to be changed from $(\mathbf{F}_\eta^T)^\nu$ in the lowest order. Substituting Equation 50 to Equation 49, we have

$$\mathbf{F}_\xi^\nu(\xi^{\nu+1} - \xi^\nu) = S\lambda^{\nu+1} - r \tag{51}$$

where new variables S and r are defined as

$$\begin{aligned} S &\equiv \mathbf{F}_\eta^\nu V(\mathbf{F}_\eta^T)^\nu, &(52)\\ r &\equiv \mathbf{f}^\nu + \mathbf{F}_\eta^\nu(\mathbf{y} - \eta^\nu). &(53)\end{aligned}$$

Note that both are described with ν-th order variables only. To remove $\lambda^{\nu+1}$, Equation 46 is substituted to Equation 50 with replacing $(\mathbf{F}_\xi^T)^{\nu+1}$ with $(\mathbf{F}_\xi^T)^\nu$. The obtained equation is

$$\xi^{\nu+1} = \xi^\nu - \left[(\mathbf{F}_\xi^T)^\nu S^{-1}\mathbf{F}_\xi^\nu\right]^{-1}(\mathbf{F}_\xi^T)^\nu S^{-1} r \tag{54}$$

Now $\xi^{\nu+1}$ is derived only with the ν-th order solutions. And substituting above equation to Equation 51,

$$\lambda^{\nu+1} = S^{-1}\left[r + \mathbf{F}_\xi^\nu(\xi^{\nu+1} - \xi^\nu)\right]. \tag{55}$$

Subsequently, the $\eta^{\nu+1}$ is obtained as

$$\eta^{\nu+1} = \mathbf{y} - V\mathbf{F}_\eta^T\lambda^{\nu+1} \tag{56}$$

Now the all ν+1-th solutions are obtained from the ν-th variables. The iteration starts with initial parameters of $\mathbf{y}$ as η^0 and ξ^0 are from the constraints and $\mathbf{y}$. The process is continued until no significant improvement is observed between $(\chi^2)^{\nu+1}$ and $(\chi^2)^\nu$ or the iteration reaches to the limited number of repetitions.

Stretch functions The stretch function s_i for the i-th measurement is defined as

$$s_i = \frac{y_i - \eta_i}{\sqrt{\sigma^2(y_i) - \sigma^2(\eta_i)}}. \tag{57}$$

If the kinematic reconstruction works properly with reasonable errors $\sigma(y_i)$ of the measurements, the stretch functions form a normal Gaussian. The stretch functions with a normal Gaussian shape and flatness of the χ^2 probability indicate success of the kinematical fitting.

C.3 Performance of the kinematical fitting

To check the performance of the kinematical fitting, the residual plots were made with outputs from the kinematical fitting and the Monte Carlo generated values. Figure 97 shows the residual plots for tagging photons. Figure 98 shows that for missing photons. Observed tail in the polar and azimuthal angle distribution were from low energy photons. Figure 99 show the χ^2 distribution.

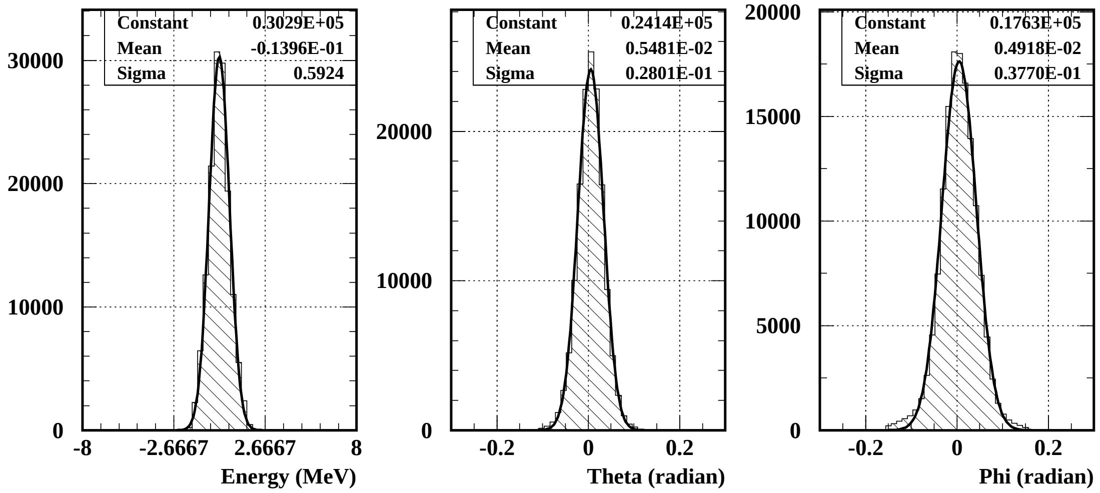

Figure 97: Resultant resolutions of the tagging photons after the kinematical fitting. All plots were measured with Monte Carlo $K_{\pi 2}$ sample. The left plot is a residual distribution of the photon energy from the generated values. The center (right) plot is a residual of the best fitted polar (azimuthal) angle from the generated values.

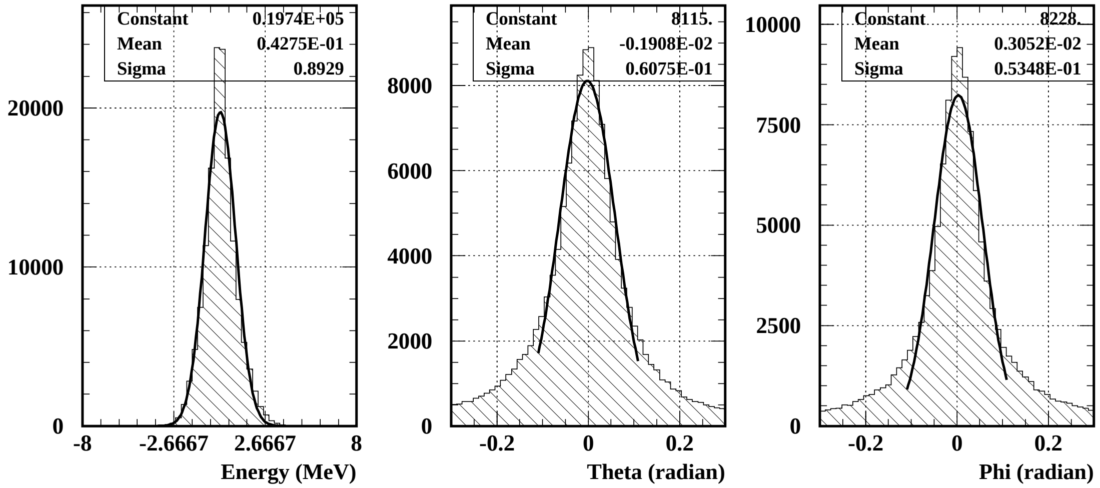

Figure 98: Resultant resolutions of the extracted missing-photon kinematics from the kinematical fitting (MC). All plots were produced with Monte Carlo $K_{\pi 2}$ sample. The left plot is a residual distribution of expected missing energy from the generated missing energy. The center (right) plot is a residual of the expected polar (azimuthal) angle from the Monte Carlo generated value.

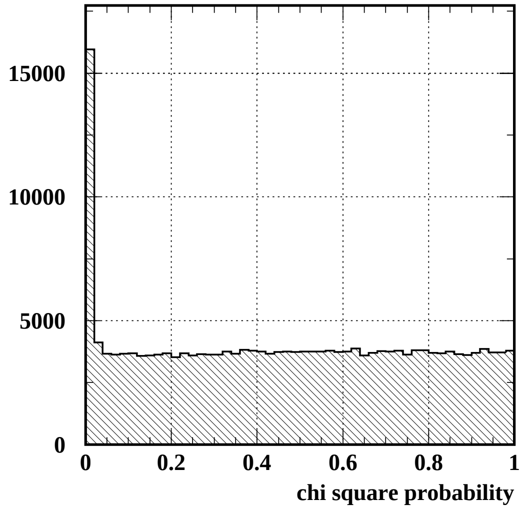

Figure 99: χ^2 probability obtained in the kinematical fitting with Monte Carlo data. Flat distribution indicates the kinematical fitting worked well.

The SPI denominator map

The measured SPI denominator map is plotted graphically, as shown in Figure 100.

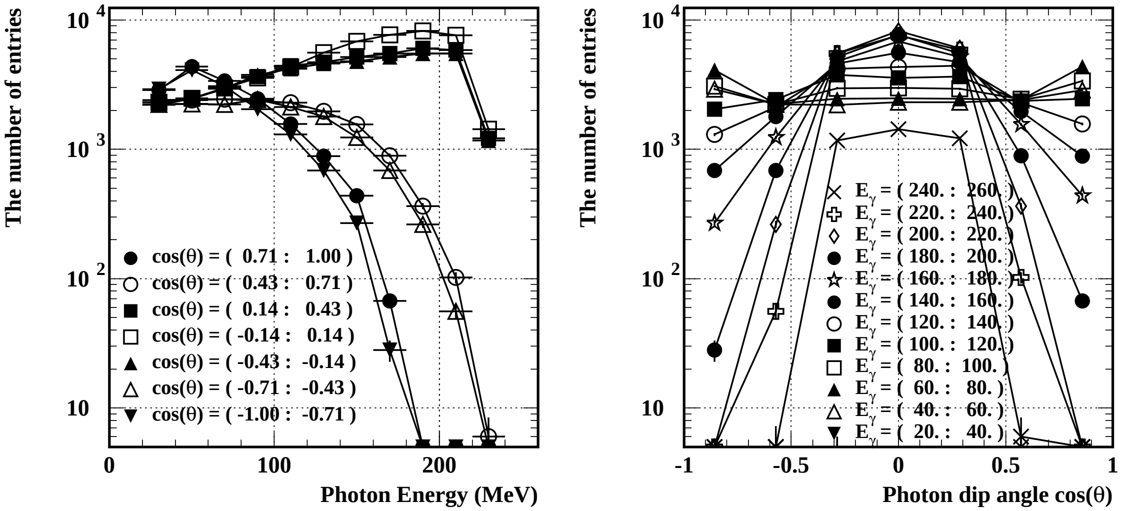

Figure 100: Obtained SPI denominator map (real data). The numbers of photon entries are plotted as a function of photon energy (left) and flight direction (right).

C.4 Performance checks of the denominator maps measurement

Validity and the performance of the denominator map measurements were checked with Monte Carlo samples. The left plot in Figure 101 shows the obtained denominator map with Monte Carlo sample, where all sequences (clustering, kinematical fitting) were processed as done in real data. The right plot of the figure shows the distribution of the generated values in the Monte Carlo simulation (Monte Carlo truth). Figure 102 shows a ratio of the measured map to the Monte Carlo truth. It shows good agreement with less than 10 % discrepancy.

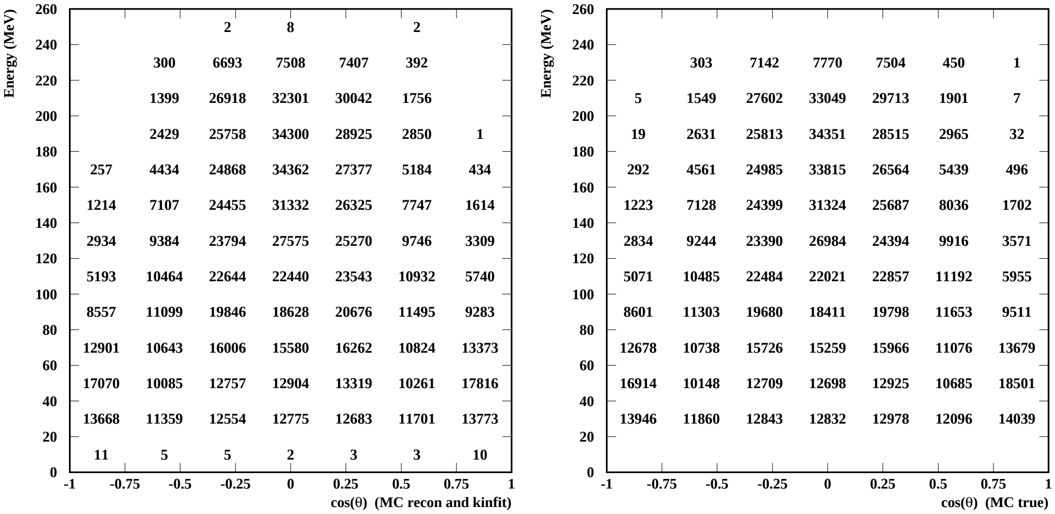

Figure 101: Measured denominator map with Monte Carlo data (left) and Monte Carlo generated values (right). Empty cell means null entry. The left figure has entries in the cell with energy of less than 20 MeV. They come from a resolution effect at the photon reconstruction and kinematical fitting.

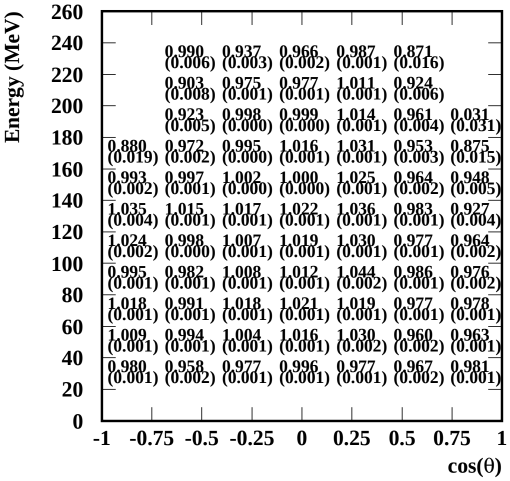

Figure 102: Ratio of the Monte Carlo denominator map to the truth. The plot is obtained with a ratio of the left plot to the right plot in Figure 101. Numbers in brackets are statistical errors. Good agreements within $\pm 10\%$ are achived except for boundary areas where resolution effect is seen.

Outputs from stretch functions (Real data)

To confirm the estimated resolutions ($\sigma^{real}_{meas,i}$) were not erroneous, outputs from the stretch functions were checked. Figure 103 shows the resultant distributions. It was confirmed that there was no peak offset and the width was close to 1 in each plot.

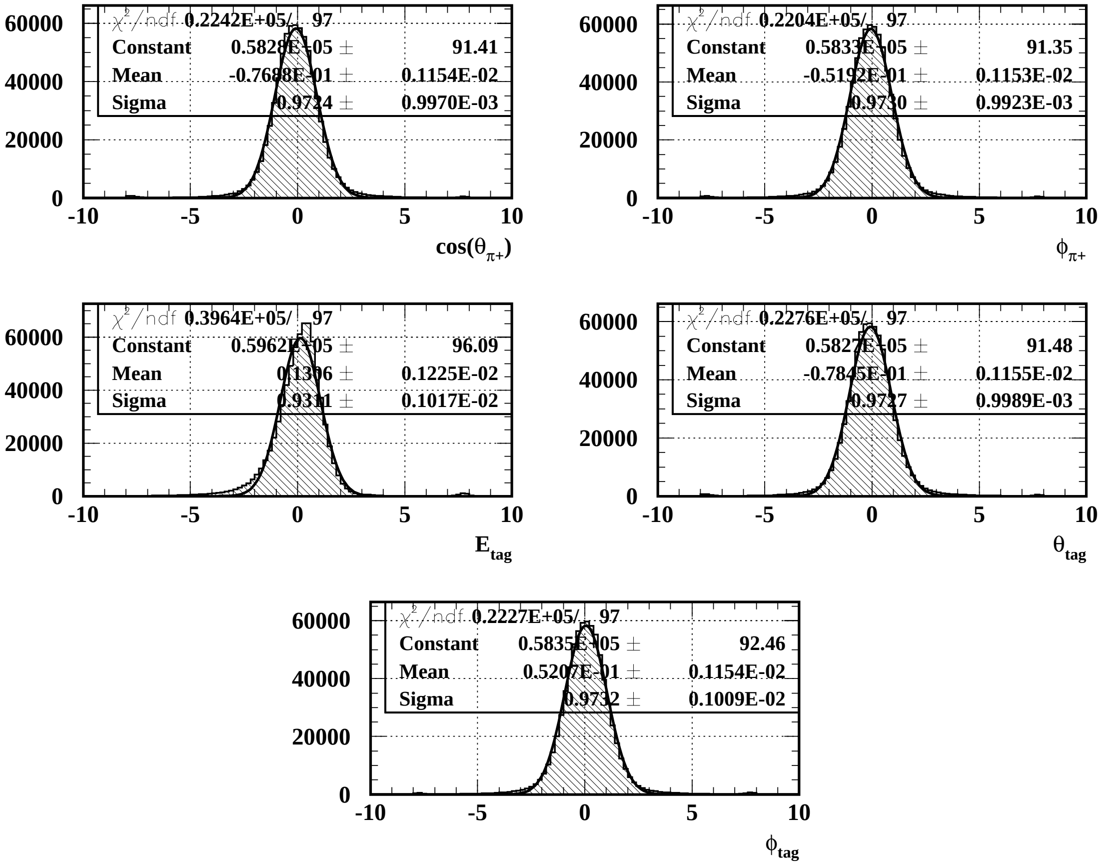

Figure 103: Stretch functions measured with real data.

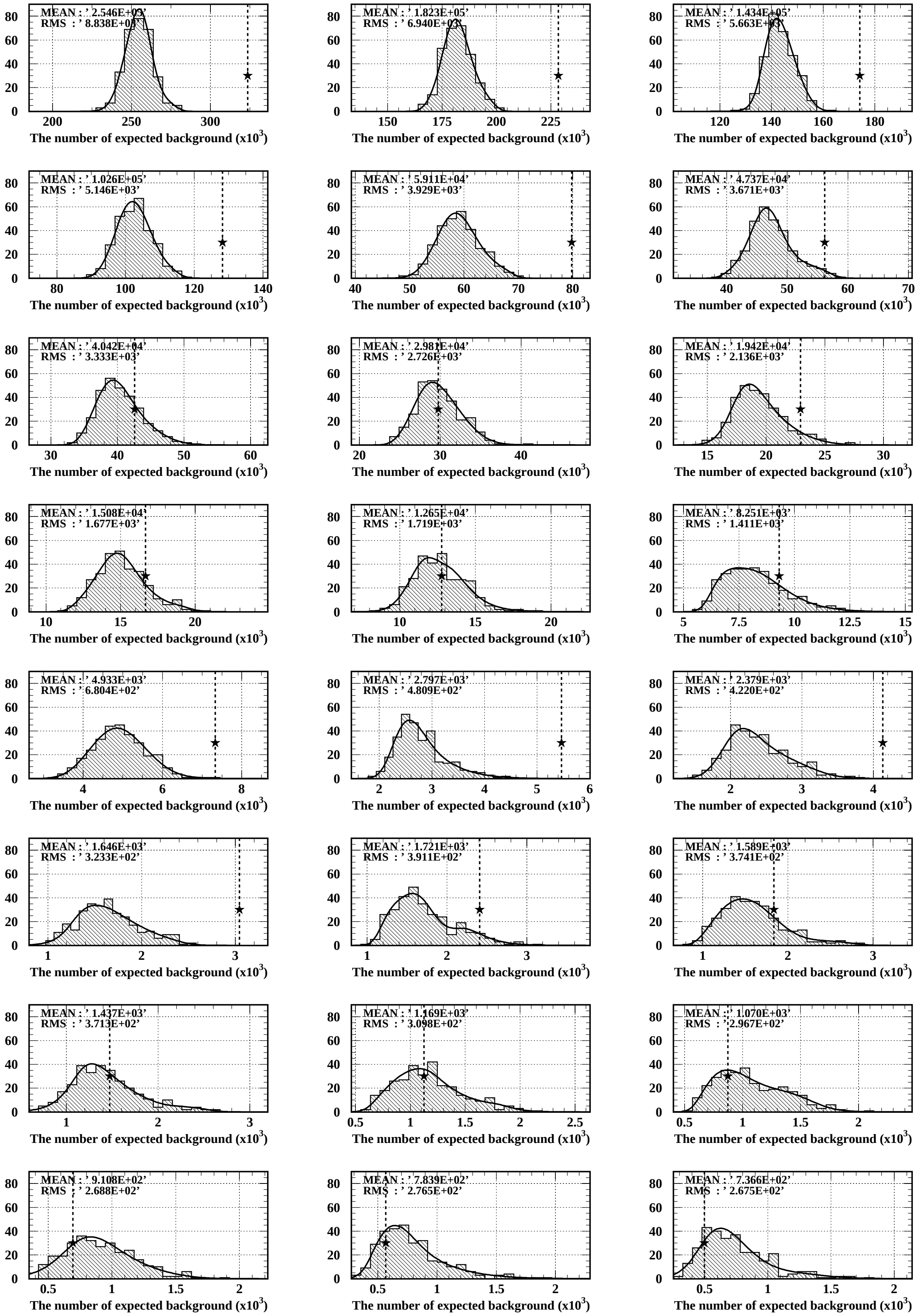

Figure 104: The number of expected $\pi^0 \to \gamma\gamma$ backgrounds and candidates in the signal region.

D Acronyms and Abbreviations

- BV : Barrel Veto : Photon detection counter placed in Barrel region.
- BVL : Barrel Veto Liner : Supplemental photon detector newly installed in Barrel region.
- CO : Collar counter : Photon detection counters covering the small dip angle area from the beam line.
- CM : Micro-Collar : Supplemental beam line photon vetoes settled at downstream end.
- EC : End Cap Calorimeters : Photon detection device located at upstream and downstream End cap region, which was made with an array of CsI cristals.
- IC : I-Counters : Fiducial decision counters, which is surrounding the scintillator fiber target.
- RS : Range Stack : scintillator layer-stack detector to measure the energy and range of charged particles in the barrel region.
- TD : Transient Digitizer : wave form recorder for $\pi^+ \to \mu^+ \to e^+$ decay sequence trace
- TG : Scintillator fiber target : Kaon stopping target made with fine segmented plastic scintillator fibers.
- VC : V-Counters : scintillator counters covering the I-Counter's light guide.